Steady State Thermal Hydraulic Analysis of Hydride Fueled BWRs

by

Paolo Ferroni

B.S. Nuclear Engineering
Polytechnic of Torino, 2004

SUBMITTED TO THE DEPARTMENT OF NUCLEAR ENGINEERING IN PARTIAL FULFILLMENT OF THE REQUIREMENTS FOR THE DEGREE OF

MASTER OF SCIENCE IN NUCLEAR ENGINEERING
AT THE
MASSACHUSETTS INSTITUTE OF TECHNOLOGY

MAY 2006
[June 2006]

Signature of Author: _____
Department of Nuclear Engineering
May 12, 2006

Certified By: _____
Neil E. Todreas
KEPCO Professor of Nuclear Engineering, Professor of Mechanical Engineering
Thesis Supervisor

Read By: _____
Pavel Hejzlar
Principal Research Scientist
Thesis Reader

Accepted By: _____
Jeffrey A. Coderre
Chairman, Department Committee on Graduate Students

Steady State Thermal Hydraulic Analysis of Hydride Fueled BWRs

by
Paolo Ferroni

Submitted to the Department of Nuclear Engineering on May 12, 2006 in partial fulfillment of the requirements for the degree of Master of Science in Nuclear Engineering

Abstract

This thesis contributes to the Hydride Fuel Project, a collaborative effort between UC Berkeley and MIT aimed at investigating the potential benefits of hydride fuel use in Light Water Reactors (LWRs). Considerable work has already been accomplished on hydride fueled Pressurized Water Reactor (PWR) cores. This thesis extends the techniques used in the PWR analysis to examine the potential power benefits resulting from the implementation of the hydride fuel in Boiling Water Reactors (BWRs). This work is the first step towards the achievement of a complete understanding of the economic implications that may derive from the use of this new fuel in BWR applications. It is a whole core steady-state analysis aimed at comparing the power performance of hydride fueled BWR cores with those of typical oxide-fueled cores, when only thermal-hydraulic constraints are applied. The integration of these results with those deriving from a transient analysis and separate neutronic and fuel performance studies will provide the data required to build a complete economic model, able to identify geometries offering the lowest cost of electricity and thus to provide a fair basis for comparing the performance of hydride and oxide fuels.

Core design is accomplished for two types of reactors: one smaller, a BWR/5, which is representative of existing reactors, and one larger, the ESBWR, which represents the future generation of BWRs. For both, the core design is accomplished in two ways: a "Backfit" approach, in which the ex-bundle core structure is identical to that of the two reference oxide cores, and a "New Core" approach, in which the control rods are inserted into the bundles in the form of control fingers and the gap between adjacent bundles is fixed optimistically at 2 mm. The benefits of the latter approach are evident since the space occupied by the bypass channel for cruciform control rod insertion becomes available for new fuel and a higher power can be achieved.

The core power is constrained by applying thermal-hydraulic limits that, if exceeded, may induce failure mechanisms. These limits concern Minimum Critical Power Ratio (MCPR), core pressure drop, fuel average and centerline temperature, cladding outer temperature and flow-induced vibrations. To limit thermal-hydraulic instability phenomena, core power and coolant flow are constrained by fixing their ratio to a constant value. In particular, each BWR/5 core has been analyzed twice, each time with a different pressure drop limit: a lower limit corresponding to the pressure drop of the reference core and an upper limit 50% larger.

It has been demonstrated that, in absence of neutronic constraints and with the maximum allowed pressure drop fixed at the upper limit, the implementation of the hydride fuel yields power gain percentages, with respect to oxide cores chosen as reference, of the order of 23% when its implementation is performed following the "Backfit" approach and even higher (50-70%) when greater design freedom is allowed in the core design, i.e. in the "New Core" approach. Should the maximum allowed pressure drop be fixed at the lower limit, the power gain percentage of the "Backfit" approach would decrease to 17%, while that of the "New Core" approach would remain unchanged, i.e. 50-70%.

Since the results obtained in the main body of the analysis account only for thermal-hydraulic constraints, an estimate of the power reduction due to the application of neutronic constraints is also performed. This investigation, focused only on the "New Core" cases, is coupled with an increase of the thickness of the gap separating adjacent bundles from 2 to 5 mm. Under these more conservative conditions, the power gain percentages are lower, ranging between 24% and 43% (depending on the discharge burnup considered acceptable) for the upper pressure drop limit, and between 17% and 32% for the lower pressure drop limit.

Thesis Supervisor: Neil E. Todreas
Title: KEPCO Professor of Nuclear Engineering, Professor of Mechanical Engineering

Thesis Reader: Pavel Hejzlar
Title: Principal Research Scientist

Acknowledgements

I would like to express my sincere gratitude to my supervisor, Professor Neil E. Todreas, for his guidance, help and support. I appreciated his depth of knowledge and especially his humility in referring me to others when the answer was not apparent to him.

I also want to thank Professor Jacopo Buongiorno, for his continuous availability in giving valuable suggestions, not only related to this thesis, but also in helping me navigate life as an international student.

Special thanks also to Dr. Pavel Hejzlar. Aside from the help he gave me to improve and correct the performance of VIPRE, he gave me a deeper understanding of the interplay between neutronics and thermal-hydraulics through his integrated mastery of these two fields.

Professor Ehud Greenspan of UCB gave me important suggestions to improve the quality and consistency of the thermal-hydraulic analysis that I performed, which proved extremely insightful.

I gratefully acknowledge the support of Chris Handwerk, who helped me to start my research work. I really wish him all the best for his career and, especially, for his nice and growing family.

My studies at MIT would be impossible without the encouragement of my parents, Fabio and Gina. I miss them every day, and I look forward to being closer to them and the mountains where I grew up.

I dedicate this thesis to my wife, Francesca. Although she only has a vague idea about what hydride fuel may be, her support is invaluable, more than any other. I am looking forward to spending much time together.

The financial support for this work was provided by US Department Of Energy (DOE) through the Nuclear Energy Research Initiative (NERI) project, and partly by Tokyo Electric Power Company (TEPCO).

Table of Contents

Chapter 1: Introduction 15
1.1- Background 15
1.2 – Objective of the Present Analysis 15
1.3 – Organization of the Work 15
1.3 – Analysis Approach 17
1.4 – Computational Tools 17
1.5 – Reference Parameters 18
Chapter 2: Cases Analyzed and Constraints Applied 23
2.1 – Case Summary 23
2.2 – Constraints 29
2.2.1 – Power Constraints 29
2.2.2 – Structural Constraints 33
Chapter 3: Analysis Assumptions 38
3.1 – Common Assumptions 38
3.2 – Case 0: VIPRE Core Modeling Validation 42
3.2.1 – Strategy Employed 42
3.2.2 – Assumptions for Case 0 43
3.2.3 – Case 0: Validation Results 49
3.3 – Alternate Core Designs 52
3.3.1 – Case Ox-Backfit-5, Hyd-Backfit-5 and Ox-Backfit-ES 52
3.3.2 – Case Hyd-NewCore-5 and Case Hyd-NewCore-ES 56
Chapter 4: Results 65
4.1 – Case Ox-Backfit-5 65
4.1.1 – Achievable Power 65
4.1.2 – Fuel Matrix 69
4.1.3 – Constraints on Achievable Power 70
4.1.4 – Quality and Bypass Flow 73
4.2 – Case Hyd-Backfit-5 75
4.2.1 – Achievable Power 75
4.2.2 – Fuel Matrix 78
4.2.3 – Constraints on Achievable Power 78
4.2.4 – Quality and Bypass Flow 81
4.3 – Case Hyd-NewCore-5 82
4.3.1 – Achievable Power 82
4.3.2 – Fuel Matrix and Structural Constraints 85
4.3.3 – Constraints on Achievable Power 88
4.3.4 – Quality 91
4.4 – Case Ox-Backfit-ES 91
4.4.1 – Achievable Power 91
4.4.2 – Fuel Matrix 94
4.4.3 – Constraints on Achievable Power 95
4.4.4 – Quality and Bypass Flow 96
4.5 – Case Hyd-NewCore-ES 98
4.5.1– Achievable Power 98

4.5.2 – Fuel Matrix and Structural Constraint 100
4.5.3 – Constraints on Achievable Power 102
4.5.4 – Quality 104
4.6 – Comparison Between Cases 104
4.6.1 – Case Ox-Backfit-5 and Case Hyd-Backfit-5 104
4.6.2 – Case Ox-Backfit-5 and Case Hyd-NewCore-5 107
4.6.3 – Case Ox-Backfit-ES and Case Hyd-NewCore-ES 110
Chapter 5: Conclusions 113
Chapter 6: Future Work 122
6.1 Transient Power Performance Analysis 122
6.2 Analysis of Other Economics-related Issues 123
Appendix A 125
A1. Comparison Between Oxide and Hydride Bundles Via Subchannel Analysis 125
A1.1. Motivation for the Analysis 125
A1.2. Analysis Objective 125
A1.3. Reference Bundle Design 126
A1.4. Bundles Examined 127
A1.5. Thermal Hydraulic Constraints 127
A1.6. Operating Conditions and Pin-by-Pin Power Distributions 129
A1.7. Bundle Geometry Assumptions 132
A1.8. Comparisons Performed 136
A1.9. Results 137
Appendix B 145
B1. Rod Vibration Magnitude in Two-phase Flow: Development of the Corrected Païdoussis Correlation 145
Appendix C 160
C1. Investigation of the Influence of the Ratio Between Core Power and Coolant Flow Rate on the Maximum Achievable Power 160
Appendix D 167
D1. Development of a Simplified Relation to Predict the Hydride Bundle Weight... 167
Appendix E 172
E1. Supplemental Comments on Case Assumptions 172
E1.1. Common Assumptions 172
E1.2. Assumptions for Case 0 (VIPRE Core Modeling Validation) 178
E1.3. Assumptions for Case Ox-Backfit-5, Hyd-Backfit-5, Ox-Backfit-ES 182
E1.4. Assumptions for Case Hyd-NewCore-5 and Case Hyd-NewCore-ES 186
Appendix F 187
F1. Investigation of the Pitch Influence on the LHGR 187
Appendix G 192
G1. Investigation of the LHGR of Oxide and Hydride Bundles 192
G1.1. Motivation for the Analysis 192
G1.2. Characteristics of the Bundles Examined 192
G1.3. Comparisons Performed 193
G1.4. Results 194
Appendix H 196
H1. Grid Spacer Loss Coefficients Calculation: In's Correlation 196

H2. Correction of In's Correlation for BWR Application 197
Appendix I 199
I1. Channel Numbering for VIPRE Reference Core Modeling 199
Appendix J 203
J1. Material Properties 203
References 205

List of Figures

FIGURE 1.1: FLOWCHART OF THE METHODOLOGY USED TO PERFORM THE ANALYSIS ([3]) ... 18
FIGURE 1.2: GE11 9×9 ([12]) AND GE14 10×10 ([13]) FUEL BUNDLE DESIGNS ... 20
FIGURE 3.1: PERIPHERAL BLOCKED REGION ... 39
FIGURE 3.2: 1/8TH SECTION OF BWR/5 OXIDE CORE AND OF ESBWR OXIDE CORE ... 43
FIGURE 3.3: AXIAL POWER PROFILES USED FOR BWR/5 AND ESBWR ... 47
FIGURE 3.4: CORE RADIAL PEAKING FACTORS FOR REF. BWR/5 AND REF. ESBWR ... 48
FIGURE 3.5: GAP CONDUCTANCE AS A FUNCTION OF COLD DIAMETRAL GAP ([17]) ... 49
FIGURE 3.6: GEOMETRIC MEANING OF H_{CORE} ... 57
FIGURE 3.7: BUNDLE LAYOUT FOR EVEN AND ODD CORES ... 59
FIGURE 3.8: "NEWCORE" STRUCTURE ... 60
FIGURE 3.9: CONTROL GUIDE TUBE LOCATIONS FOR ODD AND EVEN MATRIX INDEX ([6]) ... 62
FIGURE 4.1: CASE OX-BACKFIT-5 POWERMAPS (LEFT: ΔP_{LIMIT} = 24.5 PSIA; RIGHT: ΔP_{LIMIT} =36 PSIA) ... 65
FIGURE 4.2: CASE OX-BACKFIT-5 (ΔP_{LIMIT} = 24.5 PSIA): POWER, LHGR AND NUMBER OF ROD RATIOS BETWEEN THE EXAMINED OXIDE CORE CONFIGURATIONS AND THE REFERENCE BWR/5 CORE ... 67
FIGURE 4.3: CASE OX-BACKFIT-5 (ΔP_{LIMIT} = 36 PSIA): POWER, LHGR AND NUMBER OF ROD RATIOS BETWEEN THE EXAMINED OXIDE CORE CONFIGURATIONS AND THE REFERENCE BWR/5 CORE ... 68
FIGURE 4.4: WHOLE CORE FLOW RATE (CASE OX-BACKFIT-5, ΔP_{LIMIT} = 36 PSIA) ... 69
FIGURE 4.5: FUEL MATRIX (N×N) SIZE (CASE OX-BACKFIT-5) ... 70
FIGURE 4.6: LIMITING EFFECT EXERTED BY CONSTRAINTS (CASE OX-BACKFIT-5, ΔP_{LIMIT} = 24.5 PSIA) ... 71
FIGURE 4.7: LIMITING EFFECT EXERTED BY CONSTRAINTS (CASE OX-BACKFIT-5, ΔP_{LIMIT} = 36 PSIA) ... 72
FIGURE 4.8: INFLUENCE AREAS OF THE LIMITING CONSTRAINTS (CASE OX-BACKFIT-5. LEFT: ΔP_{LIMIT} = 24.5 PSIA; RIGHT: ΔP_{LIMIT} = 36 PSIA) ... 72
FIGURE 4.9: CORE AVERAGE EXIT QUALITY, BUNDLE AVERAGE EXIT QUALITY AND HOT BUNDLE EXIT QUALITY (CASE OX-BACKFIT-5, ΔP_{LIMIT} = 36 PSIA) ... 73
FIGURE 4.10: BYPASS FLOW PERCENTAGE (CASE OX-BACKFIT-5, ΔP_{LIMIT} = 36 PSIA) ... 74
FIGURE 4.11: CASE HYD-BACKFIT-5 POWERMAP (LEFT: ΔP_{LIMIT} = 24.5 PSIA; RIGHT: ΔP_{LIMIT} = 36 PSIA) ... 75
FIGURE 4.12: CASE HYD-BACKFIT-5 (ΔP_{LIMIT} = 24.5 PSIA): POWER, LHGR AND NUMBER OF ROD RATIOS BETWEEN THE EXAMINED HYDRIDE CORE CONFIGURATIONS AND THE REFERENCE BWR/5 OXIDE CORE ... 76
FIGURE 4.13: CASE HYD-BACKFIT-5 (ΔP_{LIMIT} = 36 PSIA): POWER, LHGR AND NUMBER OF ROD RATIOS BETWEEN THE EXAMINED HYDRIDE CORE CONFIGURATIONS AND THE REFERENCE BWR/5 OXIDE CORE ... 77
FIGURE 4.14: WHOLE CORE FLOW RATE (CASE HYD-BACKFIT-5, ΔP_{LIMIT} = 36 PSIA) ... 77
FIGURE 4.15: FUEL MATRIX (N×N) SIZE (CASE HYD-BACKFIT-5) ... 78
FIGURE 4.16: LIMITING EFFECT EXERTED BY CONSTRAINTS (CASE HYD-BACKFIT-5, ΔP_{LIMIT} = 24.5 PSIA) ... 79
FIGURE 4.17: LIMITING EFFECT EXERTED BY CONSTRAINTS (CASE HYD-BACKFIT-5, ΔP_{LIMIT} = 36 PSIA) ... 80
FIGURE 4.18: AREAS OF INFLUENCE OF THE LIMITING CONSTRAINTS (CASE HYD-BACKFIT-5. LEFT: ΔP_{LIMIT} = 24.5 PSIA; RIGHT: ΔP_{LIMIT} = 36 PSIA) ... 80
FIGURE 4.19: BYPASS FLOW PERCENTAGE (CASE HYD-BACKFIT-5; ΔP_{LIMIT} = 36 PSIA) ... 81
FIGURE 4.20: CASE HYD-NEWCORE-5 POWERMAPS (LEFT: ΔPLIMIT =24.5 PSIA; RIGHT: ΔPLIMIT = 36 PSIA) ... 82
FIGURE 4.21: CASE HYD-NEWCORE-5 (ΔP_{LIMIT} = 24.5 PSIA): POWER, LHGR AND NUMBER OF ROD RATIOS BETWEEN THE EXAMINED HYDRIDE CORE CONFIGURATIONS AND THE REFERENCE BWR/5 CORE ... 83

FIGURE 4.22: CASE HYD-NEWCORE-5 (ΔP_{LIMIT} = 36 PSIA): POWER, LHGR AND NUMBER OF ROD RATIOS BETWEEN THE EXAMINED HYDRIDE CORE CONFIGURATIONS AND THE REFERENCE BWR/5 CORE *84*
FIGURE 4.23: WHOLE CORE FLOW RATE (CASE HYD-NEWCORE-5, ΔP_{LIMIT} = 36 PSIA) *85*
FIGURE 4.24: FUEL MATRIX (N×N) SIZE (CASE HYD-NEWCORE-5, ΔP_{LIMIT} = 36 PSIA) *86*
FIGURE 4.25: STRUCTURAL CONSTRAINTS (CASE HYD-NEWCORE-5, ΔP_{LIMIT} = 36 PSIA) *86*
FIGURE 4.26: BUNDLE WIDTH RATIO (CASE HYD-NEWCORE-5, ΔP_{LIMIT} = 36 PSIA) *87*
FIGURE 4.27: TOTAL CORE CROSS SECTIONAL AREA (CASE HYD-NEWCORE-5, ΔP_{LIMIT} = 36 PSIA) *88*
FIGURE 4.28: LIMITING EFFECT EXERTED BY CONSTRAINTS (CASE HYD-NEWCORE-5, ΔP_{LIMIT} = 24.5 PSIA) *89*
FIGURE 4.29: LIMITING EFFECT EXERTED BY CONSTRAINTS (CASE HYD-NEWCORE-5, ΔP_{LIMIT} = 36 PSIA) *90*
FIGURE 4.30: REGIONS OF INFLUENCE OF LIMITING CONSTRAINTS (CASE HYD-NEWCORE-5. LEFT: ΔP_{LIMIT} = 24.5 PSIA; RIGHT: ΔP_{LIMIT} = 36 PSIA) *90*
FIGURE 4.31: CASE OX-BACKFIT-ES POWERMAP *91*
FIGURE 4.32: CASE OX-BACKFIT-ES: POWER, LHGR AND NUMBER OF ROD RATIOS BETWEEN THE EXAMINED OXIDE CORE CONFIGURATIONS AND THE REFERENCE ESBWR CORE *93*
FIGURE 4.33: TOTAL CORE FLOW RATE (CASE OX-BACKFIT-ES) *94*
FIGURE 4.34: FUEL MATRIX (N×N) SIZE (CASE OX-BACKFIT-ES) *94*
FIGURE 4.35: LIMITING EFFECT EXERTED BY CONSTRAINTS (CASE OX-BACKFIT-ES) *95*
FIGURE 4.36: AREAS OF INFLUENCE OF THE LIMITING CONSTRAINTS (CASE OX-BACKFIT-ES) *96*
FIGURE 4.37: CORE AVERAGE EXIT QUALITY, BUNDLE AVERAGE EXIT QUALITY AND HOT BUNDLE EXIT QUALITY (CASE OX-BACKFIT-ES) *96*
FIGURE 4.38: BYPASS FLOW PERCENTAGE (CASE OX-BACKFIT-ES) *97*
FIGURE 4.39: CASE HYD-NEWCORE-ES POWERMAP *98*
FIGURE 4.40: CASE HYD-NEWCORE-ES: POWER, LHGR AND NUMBER OF ROD RATIOS BETWEEN THE EXAMINED HYDRIDE CORE CONFIGURATIONS AND THE REFERENCE ESBWR CORE *99*
FIGURE 4.41: WHOLE CORE FLOW RATE (CASE HYD-NEWCORE-ES) *100*
FIGURE 4.42: FUEL MATRIX (N×N) SIZE (CASE HYD-NEWCORE-ES) *101*
FIGURE 4.43: STRUCTURAL CONSTRAINT (CASE HYD-NEWCORE-ES) *101*
FIGURE 4.44: BUNDLE WEIGHT RATIO (CASE HYD-NEWCORE-ES) *102*
FIGURE 4.45: LIMITING EFFECT EXERTED BY POWER CONSTRAINTS (CASE HYD-NEWCORE-ES) *103*
FIGURE 4.46: AREAS OF INFLUENCE OF LIMITING CONSTRAINTS (CASE HYD-NEWCORE-ES). *103*
FIGURE 4.47: POWER RATIO: HYD-BACKFIT-5 / OX-BACKFIT-5 ..... *105*
(LEFT: ΔP_{LIMIT} = 24.5 PSIA; RIGHT: ΔP_{LIMIT} = 36 PSIA) *105*
FIGURE 4.48: LHGR RATIO AND NUMBER OF ROD RATIO (HYD-BACKFIT-5 / OX-BACKFIT-5) .. *106*
FIGURE 4.49: CORE POWER RATIO AND LHGR UNITY LINE *106*
(LEFT: ΔP_{LIMIT} = 24.5 PSIA; RIGHT: ΔP_{LIMIT} = 36 PSIA) *106*
FIGURE 4.50: CORE POWER RATIO: HYD-NEWCORE-5 / OX-BACKFIT-5 ..... *107*
FIGURE 4.52: CORE POWER RATIO AND LHGR UNITY LINE (HYD-NEWCORE-5 / OX-BACKFIT-5) *108*
FIGURE 4.53: CORE CROSS SECTIONAL AREA RATIO (HYD-NEWCORE-5 / OX-BACKFIT-5) *109*
FIGURE 4.54: MATRIX INDEX RATIO (HYD-NEWCORE-5 / OX-BACKFIT-5) *110*
FIGURE 4.55: CORE POWER RATIO: HYD-NEWCORE-ES / OX-BACKFIT-ES *111*
FIGURE A.1: PIN BY PIN POWER-TO-AVERAGE POWER RATIO FOR FRESH BUNDLE *130*
OXIDE FUEL WITH GD (FROM FIGURE 4 OF [2], RE-NORMALIZED TO 74 RODS) *130*
FIGURE A.2: PIN BY PIN POWER-TO-AVERAGE POWER RATIO FOR 10×10 OXIDE BUNDLE *130*
(POWER DISTRIBUTION OF FIGURE A.1 ARBITRARLY EXTENDED TO 10×10 LATTICE) *130*
FIGURE A.3: PIN BY PIN POWER-TO-AVERAGE POWER RATIO FOR 10×10 OXIDE BUNDLE, ("BEST CASE" OF FIGURE A.5 ARBITRARILY EXTENDED TO AN OXIDE 10×10 BUNDLE) . *131*
FIGURE A.4: PIN BY PIN POWER-TO-AVERAGE POWER RATIO FOR FRESH BUNDLE *131*
HYDRIDE FUEL WITH GADOLINIA (FROM FIGURE 13 OF [2]) *131*
FIGURE A.5: PIN BY PIN POWER-TO-AVERAGE POWER RATIO FOR FRESH BUNDLE *131*
HYDRIDE FUEL WITH IFBA (FROM FIGURE 40 OF [2]) *131*

FIGURE A.6: PIN BY PIN POWER-TO-AVERAGE POWER RATIO FOR HYDRIDE 12×12 BUNDLE ("BEST CASE" OF FIGURE A.5 ARBITRARILY EXTENDED TO 12×12 LATTICE) 132
FIGURE B.1: PEAK VIBRATION RATIO DEPENDENCE ON QUALITY AND MASS FLUX, PAÏDOUSSIS CORRELATION 149
FIGURE B.2: PAÏDOUSSIS CORRELATION – QUINN'S DATA COMPARISON 150
FIGURE B.3: RMS VIBRATION RATIO DEPENDENCE ON QUALITY AND MASS FLUX, TSUKUDA CORRELATION 154
FIGURE B.4: PAÏDOUSSIS - TSUKUDA VIBRATION RATIO COMPARISON 155
FIGURE B.5: PAÏDOUSSIS - TSUKUDA VIBRATION RATIO COMPARISON (RESTRICTED G RANGE) 155
FIGURE B.6: PAÏDOUSSIS - TSUKUDA VIBRATION RATIO COMPARISON (RESTRICTED G RANGE) 156
FIGURE B.7: FINAL VIBRATION RATIO COMPARISON 158
FIGURE C.1: LOCATIONS OF THE ASSEMBLY CONFIGURATIONS EXAMINED FOR $\dot{Q}/\dot{m}$ *RATIO INVESTIGATION* 161
FIGURE D.1: CORRECTIVE FACTOR F VS N 168
FIGURE D.2: PELLET DIAMETER AS A FUNCTION OF D (HYDRIDE FUELED ROD) 170
FIGURE D.3: $(D^2 - D_{ci}^2)$ *AS A FUNCTION OF D (HYDRIDE FUELED ROD)* 170
FIGURE E.1: PIN-BY-PIN POWER DISTRIBUTION USED FOR ALL THE BUNDLE DESIGNS 174
FIGURE E.2: ORIGINAL PIN-BY-PIN POWER DISTRIBUTION USED TO OBTAIN FIGURE E.1 174
FIGURE E.4: CENTRAL (WHITE) AND PERIPHERAL (GREY) BUNDLES IN THE BWR/5 CORE (LEFT) AND ESBWR CORE (RIGHT) 179
FIGURE F.1: LEFT: LHGR RATIO (=LHGR/REFERENCE LHGR). RIGHT: AREAS OF INFLUENCE OF LIMITING CONSTRAINTS (CASE OX-BACKFIT-5, ΔP_{LIMIT}*=36).* 187
FIGURE F.2: LEFT: WHOLE CORE FLOW RATE RATIO (FLOW RATE / REFERENCE FLOW RATE); RIGHT: HOT BUNDLE EXIT QUALITY RATIO (QUALITY / REFERENCE QUALITY). CASE OX-BACKFIT-5 (ΔP_{LIMIT} 189
FIGURE F.3: LHGR RATIO (CASE OX-BACKFIT-5, ΔP_{LIMIT} *=36 PSIA) AND ISO-PITCH LINES* 190
FIGURE G.1: NON-UNIFORM PIN-BY-PIN POWER DISTRIBUTION USED FOR OXIDE BUNDLE.. 193
FIGURE I.1: REFERENCE BWR/5 OXIDE CORE MODELING MAP FOR VIPRE INPUT DECK ([3]) 201
FIGURE I.2: REFERENCE ESBWR OXIDE CORE MODELING MAP FOR VIPRE INPUT DECK 202

List of Tables

TABLE 1.1: REFERENCE CORE PARAMETERS 20
TABLE 1.2: REFERENCE ASSEMBLY KEY PARAMETERS 21
TABLE 1.3: KEY BUNDLE GEOMETRIC DATA USED FOR ALL THE CORE CONFIGURATIONS 22
TABLE 2.1: CASE SUMMARY 23
TABLE 2.2: KEY CASE CHARACTERISTICS 28
TABLE 2.3: THERMAL-HYDRAULIC CONSTRAINTS 29
TABLE 2.4: STRUCTURAL CONSTRAINTS 37
TABLE 3.1: PARAMETER COMPARISON FOR CORE MODELING VALIDATION: BWR/5 CORE 50
TABLE 3.2: PARAMETER COMPARISON FOR CORE MODELING VALIDATION: ESBWR CORE 51
TABLE 5.1: OVERALL MAXIMUM ACHIEVABLE POWER NOT ACCOUNTING FOR NEUTRONIC CONSTRAINTS 114
TABLE 5.2: MAXIMUM ACHIEVABLE POWER FOR THE REFERENCE ASSEMBLY CONFIGURATIONS 114
TABLE 5.3: MAXIMUM ACHIEVABLE POWER (SUBCHANNEL ANALYSIS, APPENDIX A) 115
TABLE 5.4: OVERALL MAXIMUM ACHIEVABLE POWER FOR HYDRIDE NEWCORE CASES ACCOUNTING FOR PRELIMINARY NEUTRONIC RESULTS 116
TABLE A.1; SUBCHANNEL ANALYSIS THERMAL HYDRAULIC CONSTRAINTS 128
TABLE A.2: BUNDLE KEY GEOMETRIC PARAMETERS 135
TABLE A.3: BUNDLE COMPARISON BASIS 136
TABLE A.4: BUNDLE COMPARISON 1 (SAME X_{OUT} = 26.8%). NONE OF THE CONSTRAINTS ARE EXCEEDED 138
TABLE A.5: BUNDLE COMPARISON 2 (SAME PRESSURE DROP = 34.0 PSIA). NONE OF THE CONSTRAINTS ARE EXCEEDED. 139
TABLE A.6: BUNDLE COMPARISON 3A (SAME PRES. DROP = 34.0 PSIA + ANOTHER HARD CONSTRAINT MATCHED). NO LIMIT FOR X_{OUT}. 140
TABLE A.7: BUNDLE COMPARISON 3B (SAME PRES. DROP = 22.6 PSIA, SAME MCHFR = 1.158). NO LIMIT FOR X_{OUT}. 141
TABLE A.8: BUNDLE COMPARISON 4 (SAME X_{OUT} = 26.8%, SAME MCHFR = 1.158). MCHFR IS THE ONLY CONSTRAINT. 142
TABLE A.9: POWER DIFFERENCE PERCENTAGES WITH RESPECT TO THE OXIDE 9×9 REFERENCE CASE 143
TABLE C.1: ASSEMBLY CONFIGURATIONS EXAMINED FOR POWER/FLOW RATIO INVESTIGATION 161
TABLE C.2 : COMPARISON BETWEEN "RELATIVE" MAXIMUM POWER AND "OVERALL" MAXIMUM POWER 163
TABLE C.3: "RELATIVE" MAXIMUM ACHIEVABLE POWERS FOR ASSEMBLY A 164
TABLE C.4 : "RELATIVE" MAXIMUM ACHIEVABLE POWERS FOR ASSEMBLY B 164
TABLE C.5: "RELATIVE" MAXIMUM ACHIEVABLE POWERS FOR ASSEMBLY C 165
TABLE C.6: "RELATIVE" MAXIMUM ACHIEVABLE POWERS FOR ASSEMBLY D 165
TABLE C.7: "RELATIVE" MAXIMUM ACHIEVABLE POWERS FOR ASSEMBLY E 166
TABLE C.8: "RELATIVE" MAXIMUM ACHIEVABLE POWERS FOR ASSEMBLY F 166
TABLE D.1 : CORRECTIVE FACTOR F 168
TABLE D.2: HYDRIDE FUELED ROD GEOMETRY 169
TABLE E.1: BUNDLE LOSS COEFFICIENTS 181
TABLE E.2: COEFFICIENTS FOR FRICTIONAL PRESSURE DROP CORRELATIONS 182
TABLE E.3: FUEL PELLET DIAMETER COMPARISON FOR OXIDE AND HYDRIDE FUELED RODS 185
TABLE G.1: LHGR COMPARISON OXIDE-HYDRIDE 194
TABLE I.1: BYPASS CHANNEL AREA AND PERIMETER 200
TABLE J.1 : MATERIAL PROPERTIES 203

Chapter 1: Introduction

1.1- Background

The proposal to fuel a BWR core with hydride rather than the common oxide fuel arises from considerations concerning the integral hydrogen content of this new type of fuel. In particular, the hydrogen concentration is comparable to that in liquid water of LWR cores at operating conditions ([1]). Therefore $UZrH_{1.6}$ behaves both as fuel and as moderator, allowing the elimination of water rods and bypass channels, that are present in a typical BWR core for providing extra neutron moderation. As a consequence, the volume occupied by the special moderator zones would become available for new fuel, and a higher core power could be achieved.

1.2 – Objective of the Present Analysis

The objective of the present analysis is to compare the power achievable in a hydride fueled core with that of an oxide fueled core, when both are loaded in a vessel having same size and only thermal-hydraulic constraints are applied. Once coupled with a comparable analysis based on neutronic constraints, such a comparison will form the basis to identify the assembly configuration, or the configuration range, which should assure achievement of the most significant power benefits from the use of the new fuel type.

The study searches for the particular combination of fuel rod diameter (D), pitch (P) and fuel bundle matrix[1] (n) that lead to the maximum achievable power which does not exceed some thermal-hydraulic constraints. The hydride core configurations are analyzed with bypass control rod channels and with control fingers in fuel rod positions (i.e. without bypass channels). Conversely, water rods are not contained in any of the hydride core configurations examined.

1.3 – Organization of the Work

The work is divided into three main parts, which are sequentially described in the central sections of this report:

[1] Throughout the whole analysis, the size of the rod array will be referred to as "matrix".

- Validation of the core modeling technique: this step is fundamental in order to verify the accuracy of the procedure used and the assumptions made to model the various core geometries examined. It is performed by analyzing a model of an existing oxide core and the recent ESBWR (so-called "reference cores") and comparing the results obtained with the core performance characteristics found in the literature;
- Steady state analysis of alternative oxide and hydride core configurations over the ranges: $0.6 \leq D \leq .6$ cm and $1.1 \leq P/D \leq .6$. In the analysis of some hydride configurations a third range, the matrix index n varying from 8 to 20, is also considered.
- Comparison of the power attainable from different core configurations.

To simplify the programming and limit the computational time, the wide spectrum of core geometries examined in the whole core analysis required the elaboration of several simplifying assumptions that are listed and described in Chapter 3. Moreover, except for the oxide bundles taken as reference, which are used in current plants and therefore there is a valid proof of their feasibility, none of the other assembly geometries has been here subjected to neutronic calculations. Thus, the results provided by the **whole core** analysis must not be considered as "final" since the maximum power that this analysis has proved to be achievable by each *D-P/D* may drop after the application of neutronic constraints[2]. For this reason the whole core analysis was followed by a subchannel analysis of a very restricted number of oxide and hydride bundle designs, for which a neutronic analysis together with the related "optimization" has also been separately performed ([2]). Consistent with the purpose of the whole core analysis, the subchannel analysis is also aimed at comparing the power performance resulting from the use of hydride vs oxide fuel. The subchannel analysis is not contained in the main body of this report, but is fully described in Appendix A.

[2] An estimate of the measure of this achievable power reduction is performed directly on the final results provided by the whole core analysis. The application of neutronic constraints causes several *D-P/D* pairs to be excluded from the search for the assembly configuration yielding the maximum power since they are not feasible from the neutronic viewpoint. As a consequence, the maximum power is not only lower, but is also achieved at different *D-P/D* combinations than those resulting from the use of thermal-hydraulic constraints only. These results are described in Chapter 5.

1.3 – Analysis Approach

The search for the maximum achievable power is performed by assigning conservative limit or constraint values to some crucial parameters. A constraint is therefore a thermal-hydraulic parameter that, if exceeded, may induce a failure mechanism: a situation that must obviously be avoided. Once a core is geometrically defined, its thermal power is increased starting from a low value. For each power level, a thermal-hydraulic analysis is performed, and its results are compared to the established constraints. If they are not exceeded, the power is further increased till one of them reaches a value between 99.9% and 100.0% of the corresponding limit value (between 100.0% and 100.1% for the MCPR). The core power which led to this situation is recorded as the maximum achievable power for the geometry just examined. The whole procedure is repeated for all the core geometries within the analysis range. Figure 1.1 shows the flowchart of the methodology used ([3]).

1.4 – Computational Tools

The thermal-hydraulic analysis is performed using the well known VIPRE code ([4]). However, the particular nature of the present work would make VIPRE use tedious in pursuit of the final goal since VIPRE is designed to analyze a single core with a fixed thermal power entered as input. Instead, the present work is aimed at establishing the maximum achievable power among hundreds of different core candidates. This implies the need to iteratively vary the input power for each core configuration, and then automatically shift to the next core geometry. This "management role" is performed by MATLAB, which generates the VIPRE input file, executes VIPRE and manages the output data (see Figure 1.1). The interface between the two programs is called VAMPIRE (VIPRE And MATLAB Programming InteRfacE). It was developed for PWRs by Blair ([5]) and Malen ([6]), and adjusted for applications to BWRs by Handwerk ([3]).

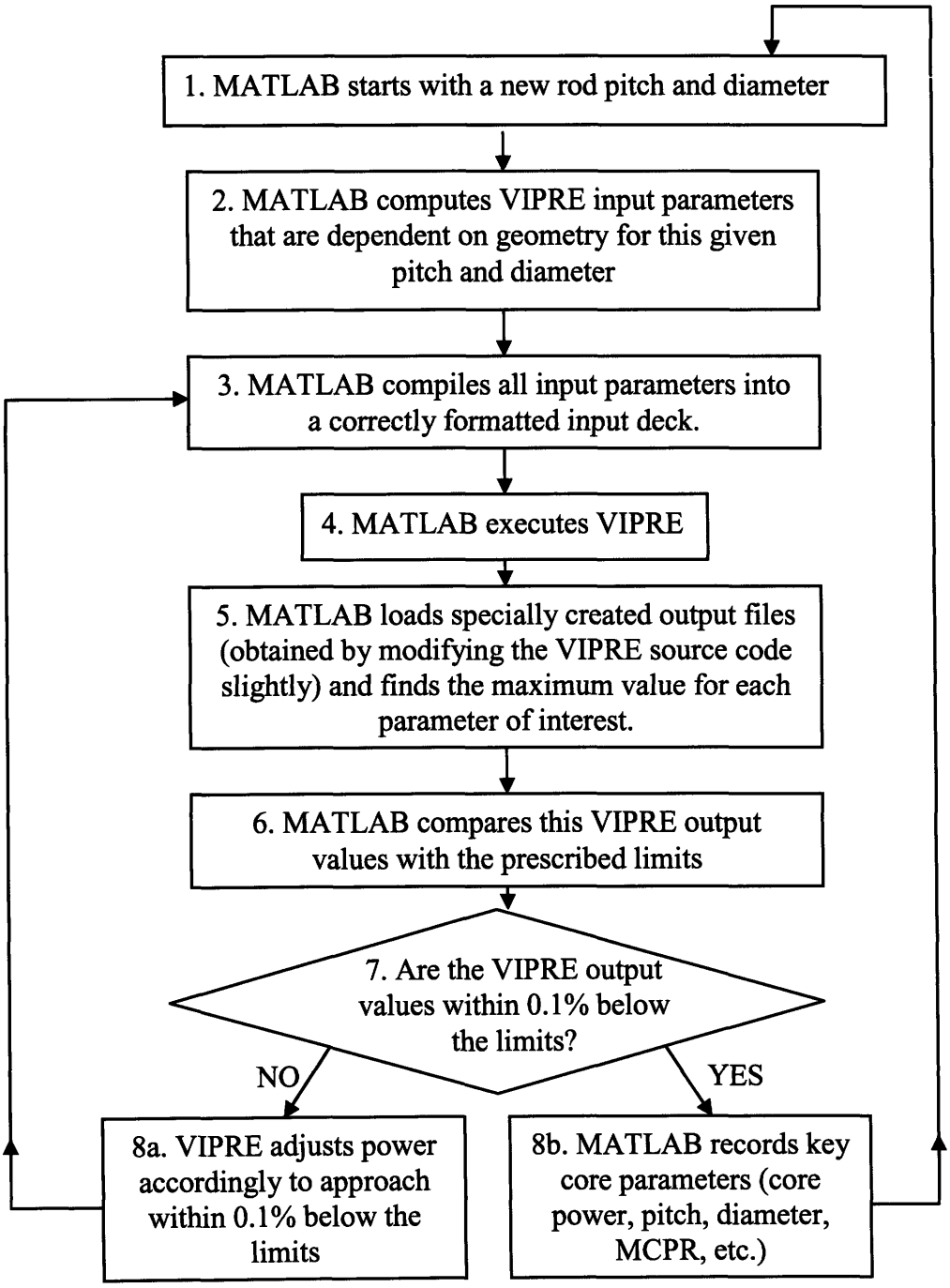

Figure 1.1: Flowchart of the Methodology Used to Perform the Analysis ([3])

1.5 – Reference Parameters

The predicted core performance derived from the implementation of the new fuel type and/or from the modification of the lattice parameters D and P, will be often compared to

those of two "reference cores". These "reference cores" do not exactly represent any existing core, although most of their features are in common with the General Electric BWR/5 of Nine Mile Point Unit 2 (NMP2), and with the recent GE ESBWR respectively[3]. This is basically due to the lack of some data which has been consequently replaced with values derived from different but consistent sources. For example, while parameters like the core power, coolant flow rate, number of bundles and system pressure for the two reference cores correspond exactly to those of NMP2 and of the ESBWR, the bundle geometries chosen are different. In fact, NMP2 is loaded with 8×8 assemblies ([7], Table 1.3-1) while the reference BWR/5 core contains 9×9 lattice assemblies (GE11 type), consistent with the current tendency to use bundles having a larger number of rods. It is important to stress that, in spite of the different number of rods, the fuel channel size is practically unchanged:

- NMP2 fuel channel size: 5.48×5.48 inches ([7], Table 1.3-1)
- GE11 fuel channel size: ~5.42×5.42 inches

Contrary to the choice made for the reference BWR/5 oxide core, the bundle design used for the reference ESBWR oxide core does not differ significantly from that actually designed for this reactor, i.e. the GE14 bundle design ([8]). Due to the incompleteness of the data sources, some of the bundle geometric characteristics refer to the GE14 design, while some others to the GE12 design. In spite of the different designations, the two designs are very similar.

Consistent with the nomenclature used for the two reference cores, the bundle designs modeled are called "reference bundle designs", i.e. reference BWR/5 bundle and reference ESBWR bundle respectively.

The reference core key parameters are listed in Table 1.1.

[3] The choice of the BWR/5 and the ESBWR as "reference reactors" was not made randomly. The former represents a model of an existing plant, for which the implementation of the hydride fuel, to be economically acceptable, should account for the presence of pre-existing structures and components, designed in view of an oxide-fueled core. Vice versa, the ESBWR represents a model of a future plant, for which the design of all the components is performed to accomodate hydride fuel. Since the ESBWR is not "pre-existing", its core can be designed with a greater freedom, such that all the potential advantages deriving from the use of the new fuel can be actually obtained.

Table 1.1: Reference Core Parameters				
Parameter	***Reference BWR/5***		***Reference ESBWR***	
	Value	***Source***	***Value***	***Source***
Core shroud radius, in (m)	102.56 (2.605)	[9]	120.36 (3.057)	Estimated from [10][4]
Number of fuel bundles	764	Table 1.3-1 in [7]	1132	Table 1.3-1 in [8]
Whole core flow rate, Mlbm/hr (kg/s)	108.5 (13671)	Table 4.4-1 in [11]	79.388 (10003)	Table 1.3-1 in [8]
System pressure, psia (MPa)	1035 (7.136)	Table 4.4-1 in [11]	1050 (7.240)	Table 4.4-1 in [8]
Core inlet temperature, F (°C)	533 (278.3)	Table 4.4-1 in [11]	520 (271.1)	Table 4.4-1 in [8]
Thermal output power, MW	3323	Table 1.3-1 in [11]	4500	Table 1.3-1 in [8]

Figure 1.2 shows the GE11 fuel design, which was chosen as assembly design of the reference BWR/5 oxide core, and the GE14 bundle design, that the present analysis attempts to model approximately to use as the bundle design for the reference ESBWR core.

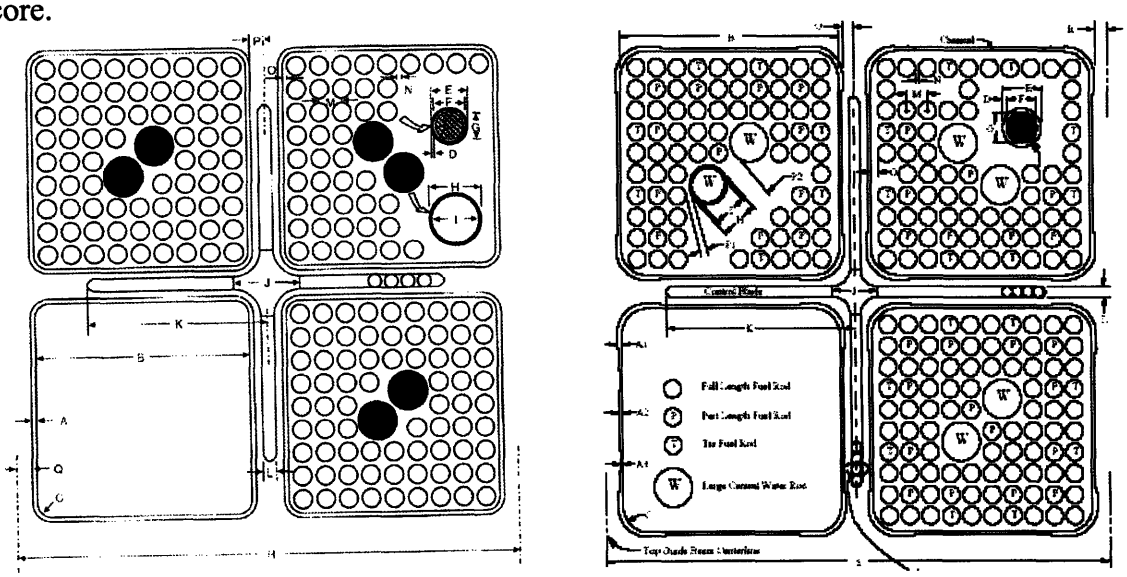

Figure 1.2: GE11 9×9 ([12]) and GE14 10×10 ([13]) Fuel Bundle Designs

[4] Figure 7 of [10] shows the overall ESBWR core layout. If a hypothetical infinite bundle array is assumed to occupy all the available space within the shroud, exactly 28 bundles would lie on the 45° symmetry line that diagonally cuts the core. Of these bundles, 26 are actually present, while the remaining two, i.e. the most peripheral ones, if present would touch the shroud inner surface with their upper left/bottom right corners respectively. Since the bundle pitch and the fuel channel outer width are known (P_b= 6.1" from [10], l_{bo} = 5.52" from Table 1.3-1 of [8]), the shroud radius can be calculated as: $R_{shroud}^{ESBWR} = 0.5 \cdot \left(27 \cdot \sqrt{2} \cdot P_b + \sqrt{2} \cdot l_{bo}\right) = 120.36"$.

Numerical values used for the two reference bundle designs are shown in Table 1.2. Most of the GE11 design values are not displayed since they are GE proprietary. Conversely, those used to represent the reference ESBWR fuel bundle derive from the coupling of GE12 and GE14 geometric data available in the open literature.

Table 1.2: Reference Assembly Key Parameters

	Reference BWR/5 bundle design (GE11-type)		***Reference ESBWR bundle design***	
	Value	***Source***	***Value***	***Source***
Number of fuel rods	74	[12]	92	[13]
Number of water rods	2		2	[13]
Fuel rod outer diameter, in (cm)	-		0.4039 (1.0260)	[14]
Fuel rod inner diameter, in (cm)	-		0.3441 (0.8740)	Calculated using clad thickness algorithms (see Section E1.3. of Appendix E)
Fuel pellet diameter, in (cm)	-		0.3386 (0.8600)	Calculated using gap thickness algorithms (see Section E1.3. of Appendix E)
Fuel rod pitch, in (cm)	-		0.5098 (1.2950)	[15]
Water rod outer diameter, in (cm)	-		1.0322 (2.6218)	Calculated using data in this table
Water rod wall thickness, in (cm)	-		-	Assumed to be the same as in GE11
Bundle outer width, in (cm)	-		5.52 (14.0208)	Table 1.3-1 of [8]
Bundle wall thickness, in (cm)	-		0.120 (0.3048)	Table 1.3-1 of [8]
Bundle active flow area, in^2 (cm^2)	-		14.4150 (93.0)	Table 4.4-1a of [8]
Bundle pitch, in (cm)	-		6.1 (15.4940)	[10]
Gap width between bundles, in (cm)	-		0.58 (1.4732)	Calculated using bundle pitch and bundle outer width

Geometric data used for all the core configurations analyzed, regardless of the values of the lattice parameters D and P and the type of fuel, are listed in Table 1.3.

Table 1.3: Key Bundle Geometric Data Used for All the Core Configurations

	Cases adopting BWR/5-size vessel		***Cases adopting ESBWR-size vessel***	
Parameter	***Value***	***Source***	***Value***	***Source***
Fuel bundle total length, in (cm)	164.567 (418.0)	[3]	149.1 (378.7)	Table 1.3-1 in [8]
Fuel bundle heated length, in (cm)	145.98 (370.8)	[3]	120 (304.8)	Table 1.3-1 in [8]
Number of grid spacers	7	[15]	8	[15]

Chapter 2: Cases Analyzed and Constraints Applied

2.1 – Case Summary

The validation of the core modeling technique is designated Case 0. The designation of the other whole core cases, i.e. Case 1, Case 2,..., Case 5, adopts nomenclature describing the most important features of each case. This nomenclature consists of three parts:

- the abbreviation "Ox" or "Hyd" for the type of fuel used;
- the acronym "Backfit" or "NewCore" to identify the core layout (Backfit ≡ core provided with large bypass channels for the cruciform control rod insertion; NewCore ≡ core without bypass channels and provided with control fingers directly inserted into the bundles);
- the number "5" or the initials "ES", to identify the vessel size (5 ≡ BWR/5, ES ≡ ESBWR).

As mentioned in Section 1.3, the whole core analysis was followed by a subchannel analysis focused on a restricted number of oxide and hydride bundle designs, which is presented in Appendix A.

The various cases are summarized in Table 2.1, which is followed by a detailed description of Case 0 through Case 5.

Table 2.1: Case Summary

Case #	Case Designation
0	0
1	Ox-Backfit-5
2	Hyd-Backfit-5
3	Hyd-NewCore-5
4	Ox-Backfit-ES
5	Hyd-NewCore-ES
6	Subchannel Analysis

Two oxide fueled cores are analyzed: a BWR/5 core (Case Ox-Backfit-5) and the

ESBWR core (Case Ox-Backfit-ES). Although of different core radii, these cases have the same general structure and, in particular, both are provided with water rods and large bypass channels. The corresponding achievable power ratings are used as reference for comparison to those of the hydride core configurations.

The implementation of hydride fuel into a BWR/5 vessel is analyzed following two different strategies: the first, examined in Case Hyd-Backfit-5, considers a hydride core provided with bypass channels having size and disposition identical to those modeled in Case Ox-Backfit-5. Although this design does not maximize the power benefits potentially achievable with the new fuel, it does not require a complete rearrangement of the structure of a core that had been previously fueled with oxide. This translates into a significant economic saving. The only design modification required for the transition from oxide to hydride would be the elimination of the water rods, and their replacement with fuel rods. The second strategy, analyzed in Case Hyd-NewCore-5, examines a hydride core without water rods and bypass channels. Control rods are no longer in the form of cruciform rods, but in the form of control fingers directly inserted through guide tubes into the bundles. Except for the presence of the fuel channels, such a core configuration has a characteristic PWR appearance.

The implementation of the hydride fuel into an ESBWR-size vessel is examined following the NewCore approach only (Case Hyd-NewCore-ES). In fact, the oxide ESBWR is still in the design phase, and the design of a first-of-a-kind hydride ESBWR is considered more likely than the adoption of the hydride fuel into a core just designed to house oxide fuel.

The cases examined are described below in the order they are presented in the report.

Case 0: VIPRE CORE MODELING VALIDATION - REFERENCE BWR/5 OXIDE CORE AND REFERENCE ESBWR OXIDE CORE: the subdivision of the diameter and *P/D* ranges[5] performed for the "wide geometry spectrum" analyses (400 assembly configurations examined in a single VAMPIRE analysis) does not include *D-P/D* pairs that exactly match those of the reference assembly geometries. In particular, the closest configurations are within ±1% both for the

[5] $0.6 \leq D \leq .6$ cm, $1.1 \leq P/D \leq .6$.

reference BWR/5 bundle and for the reference ESBWR bundle. Moreover, once *D* and *P/D* are entered as input, the algorithms[6] implemented in VAMPIRE would use these two parameters to calculate the clad thickness and the pellet diameter. Since these algorithms have been designed to perform such a task for hundreds of different configurations, even if the exact values of *D* and *P/D* of the two reference assemblies were entered, the resulting pellet diameter and clad thickness would still differ slightly from the actual values. For this reason, each of the reference oxide cores is analyzed with a single VIPRE run, i.e. without the use of the VAMPIRE interface, with all the necessary geometric data (together with power and flow rate) entered "manually" in a VIPRE input file. The reference geometry analysis is fundamental for two reasons:

- it establishes a validation base, i.e. it compares the most important VIPRE thermal-hydraulic output data (exit quality, pressure drop etc.) to those found in the literature. This comparison gives an indication of the accuracy of the core model and the feasibility of the assumptions made
- it determines the two values of Minimum Critical Power Ratio (MCPR) that characterize the reference cores during normal operation. As explained in Section 2.2.1, the MCPR is not subject to any comparison with the corresponding values found in the literature. Conversely, they are the MCPR limits that the core configurations analyzed here, i.e. BWR/5 types and ESBWR types, cannot exceed.

Case Ox-Backfit-5: BWR/5 core, fueled with UO_2, provided with water rods and bypass channels. The thermal-hydraulic analysis was performed over 400 different assembly configurations[7], that is 400 *D-P/D* pairs, maintaining the fuel channel size unchanged[8]. Consequently, rod pitch *P* and fuel matrix *n* are related by a one-to-one correspondence.

---

[6] Introduced in Section 3.3.1 (point "b" of "Bundle structure assumptions") and described in detail in Section E1.3. of Appendix E (point "b" of "Bundle structure assumptions").

[7] Through the whole report, the term "assembly configuration" indicates a geometry characterized by a particular rod diameter *D* and a particular *P/D* ratio, where *P* is the rod pitch.

[8] Contrary to PWRs, typical boiling reactors have control rods outside the bundles, in the form of cruciform rods. Their effectiveness would be strongly affected by any change in the fuel channels size and therefore a

Case Hyd-Backfit-5: same BWR/5 core as that examined for case Ox-Backfit-5, except for the different fuel and the absence of water rods inside the bundles (replaced with fuel rods). 400 *D-P/D* pairs are analyzed. *P* and *n* are related through a one-to-one correspondence.

Case Hyd-NewCore-5: the same vessel used in the three previous cases is assumed loaded with a hydride core, without water rods and bypass channels. The analysis is performed over the 400 assemblies configurations already examined for Case Ox-Backfit-5. In this case, however, the fuel channel size is not constrained. As a consequence, once the rod pitch is chosen, the choice of the fuel matrix is no longer univocal. For each *D-P/D* pair such a choice is made through two sequential steps. First some matrixes are excluded since they would imply exceeding physical limits (related to the features of the existing plant) such as the assembly weight and their total number. Then, all the remaining matrixes are examined, and the choice of the best solution was based on the maximum achievable power criterion.

Case Ox-Backfit-ES: ESBWR core, fueled with UO_2, provided with water rods and bypass channels. The analysis was performed over the 400 *D-P/D* pairs examined for Case Ox-Backfit-5, with the fuel channel size constrained to the value chosen for the reference 10×10 bundle. Again, a one-to-one correspondence exists between *P* and *n*.

Case Hyd-NewCore-ES: ESBWR-size core, fueled with $UZrH_{1.6}$, examined in 400 different *D-P/D* pairs. As for Case Hyd-NewCore-5, the fuel channel size is not constrained and the same procedure is used to choose the fuel matrix to couple to each *D-P/D* pair. However, since a new plant like the ESBWR will be provided with a crane suited for the bundle weight, the bundle weight limit is no longer applied.

---

control rod remodeling would be required. However, the present analysis treats the oxide core using a backfit approach, that is assuming different assembly configurations loaded in an existing core and vessel having a fixed geometry.

Conversely, the limit concerning the maximum allowed number of bundles is maintained and is the same as that used in Case Hyd-NewCore-5.

The key characteristics for each case are summarized in Table 2.2.

Table 2.2: Key Case Characteristics

Case	Objective	# of assembly config. analyzed	Computational technique	Main geometric input parameters		Power-related input	Main output parameters [9]
				In-bundle	*Ex-bundle*		
0	VIPRE core modeling validation. MCPR and pressure drop limit determination	1 for reference BWR/5, 1 for reference ESBWR	VIPRE (single run)	D, P/D, matrix index, pellet D, clad thickness, fuel channel width, water rod D	# of bundles, bypass channel area, orificing coefficients	Power, flow, power axial and radial profile	Thermal-hydraulic parameters of the reference BWR/5 and ESBWR core; MCPR for both
Ox-Backfit-5	Max achievable power for the BWR/5 Oxide Backfit Core	400	VAMPIRE	D, P/D, fuel channel width, k_{flow} [10]	# of bundles, bypass channel area, orificing coefficients	Power axial and radial profile, power/flow ratio	Maximum power
Hyd-Backfit-5	Max achievable power for the BWR/5 Hydride Backfit Core	400	VAMPIRE	D, P/D, fuel channel width	# of bundles, bypass channel area, orificing coefficients	Power axial and radial profile, power/flow ratio	Maximum power
Hyd-NewCore-5	Max achievable power for the BWR/5 Hydride NewCore	400	VAMPIRE	D, P/D	Core size, NO orificing	Power axial and radial profile, power/flow ratio	Maximum power
Ox-Backfit-ES	Max achievable power for the ESBWR Oxide Backfit Core	400	VAMPIRE	D, P/D, fuel channel width, k_{flow} [9]	# of bundles, bypass channel area, orificing coefficients	Power axial and radial profile, power/flow ratio	Maximum power
Hyd-NewCore-ES	Max achievable power for the ESBWR Hydride NewCore	400	VAMPIRE	D, P/D	Core size, NO orificing	Power axial and radial profile, power/flow ratio	Maximum power
Subchannel Analysis	Max. achievable power of a restricted number of oxide and hydride bundles	6	VIPRE (subchannel analysis)	Complete and detailed bundle description	Not Applicable	Axial Power profile, pin-by-pin power distribution	Maximum power

[9] Table 2.2 lists the main output parameters for each case. Many others are obtained during the analysis. Although they will be subject to several observations in Chapter 4, according to the purpose of Table 2.2 they are considered here of secondary importance.

[10] k_{flow} is the ratio between the water rod flow area and the active bundle flow area (water rods excluded).

2.2 – Constraints

The constraints chosen in the present analysis are classified as *power constraints* and *structural constraints*. While the former are used for all the cases examined, the latter characterize the Hydride NewCore analyses only (Case Hyd-NewCore-5 and Case Hyd-NewCore-ES). In the NewCore approach the fuel channel size is not constrained: this greater freedom allowed in the core construction consequently requires the existence of some structural constraints.

2.2.1 – Power Constraints

The parameters chosen as power limiting constraints assure the existence of an adequate safety margin for all the core configurations analyzed. Table 2.3 summarizes these power constraints specifying the limit values chosen for each one.

Table 2.3: Thermal-Hydraulic Constraints

Case	Fuel centerline T (°C)	Fuel avg T (°C)	Core pres. drop (psi)	MCPR	$\dot{Q}/\dot{m}$ (kW/(kg/s))	Clad surface T (°C)	Vibration ratio
0	2805	1400	Output*	Output*	Input*	349	0.021
Ox-Backfit-5	2805	1400	24.5 36.0	1.015	243.07		
Ox-Backfit-ES	2805	1400	11.0	1.018	449.87		
Hyd-Backfit-5 Hyd-NewCore-5	750	N.A.	24.5 36.0	1.015	243.07		
Hyd-NewCore-ES	750	N.A.	11.0	1.018	449.87		

N.A. ≡ Not Applied

* Case 0 is used to obtain the minimum allowed CPRs as well as the core pressure drop limits. Core power and coolant flow rate are entered as input data.

The limit values chosen derive from considerations described below.

i. *MCPR*. The particular nature of this parameter, together with the strong influence it exerts on the maximum achievable power, forced the present analysis to fix the minimum acceptable MCPR in an unusual way compared to the strategy used for the other constraints. In fact, the MCPR is around 1.25 for a typical BWR/5 during normal operational conditions (see Table 4.4-1 of [11]): thus, fixing the MCPR limit to this value could seem the best choice. However it is not. The approximate core modeling which characterizes the present analysis, together with the

conservative character of the correlation used, makes the MCPR prediction inaccurate. Reverse engineering the process by entering all the data provided in Table 1.1 (core power and flow included), Table 1.2 and Table 1.3 as input, by means of the Hench-Gillis correlation ([16]) VIPRE delivers a MCPR of 1.015 for the reference BWR/5 core and 1.018 for the reference ESBWR core, compared to a more reasonable value which may be, as mentioned, 1.25. However, as long as these values are consistently used as a constraint for the BWR/5-type cores and ESBWR-type cores respectively, a fair and accurate comparison between hydride fuel and oxide fuel can be assumed. For this reason the MCPR limits were set to 1.015 and 1.018, even though they are not representative of the actual values. The reverse approach just mentioned is nothing else then Case 0 analysis (VIPRE Core Modeling Validation). It is important to note that the same MCPRs have been separately obtained by means of a VIPRE subchannel analysis of the hot bundle, using the flow rate delivered by Case 0 (which is a whole-core analysis). This means that the underestimate of such a parameter is not due to the bundle lumping approach used in the whole core analysis, but to the conservative nature of the Hench-Gillis correlation coupled with the simplifying assumptions made in modeling advanced bundle designs[11].

ii. *Fuel centerline/average temperature.* While UO_2 requires two different limits, that is 2805°C as peak temperature to prevent melting and a maximum average temperature of 1400°C to keep the fission gas release below 5% ([17]), the hydride fuel does not melt[12] and, as Malen states in 3.3 of [6], is not subject to a significant

[11] The bundle designs currently used in BWRs are provided with features that increase the margin to dryout. The most well known examples are Partial Length Fuel Rods (PLFRs) and advanced grid spacer designs. No one of the bundle designs examined in this analysis is assumed to contain PLFRs, and the grid spacers are not explicitly accounted for in the Hench-Gillis correlation (even though the pressure drop of the grids is modeled as form pressure losses in a calculation separate from the CPR calculation). In fact, after developing this correlation, Hench and Gillis stated: "*The spacer design can have a strong influence on CHF. The data used in the correlation were taken with a variety of spacers, whose design details are unknown to us. We must therefore, assume that most fuel rods spacers fall into a "benign zone" in which there is no significant spacer effect on CHF, and that it must be assumed that the fuel bundles whose CHF would be predicted using this correlation also have "benign" spacers*" ([16]).

[12] Paragraph 4.4 of [1] states: "Fuel melting of the hydride fuel is not likely to occur because the hydride does not have a defined melting temperature". Moreover, in paragraph 5.1.3 Petrovic and Garkisch state: "*Hydride fuel does not melt because the hydrogen will dissociate and be released. However, the remaining*

fission gas release. However, as the temperature increases, $UZrH_{1.6}$ dissociates releasing hydrogen which can contribute to clad corrosion and internal pressurization of the fuel rod. The value of 750°C was suggested by Westinghouse ([1]) as the appropriate hydride temperature limit.

iii. *Clad surface temperature.* During the LOCA severe accident, the maximum allowed oxidation level is fixed at 17% of the clad thickness ([18]). During normal operational conditions the clad temperature has to be limited in order to assure enough margin between the oxide thickness that unavoidably tends to form and the 17% limit. This limit was set to 349°C.

iv. *Core pressure drop.* In a BWR operating under forced convection conditions, the maximum allowed core pressure drop is fixed by the recirculation pump head limit. The pumps have to overcome the total pressure drop existing in the whole loop, of which a significant contribution is due to the core. In the cases modeling a core contained in a BWR/5 reactor, two limits are applied: 24.5 psia and 36 psia. The former is a value slightly above the core pressure drop calculated in Case 0 (24.33 psia), and therefore represents a close approximation of the pressure drop predicted by VIPRE for the reference BWR/5 oxide core[13]. It can be interpreted as the maximum allowed core pressure drop for an existing BWR, for which no pump design improvements are implemented. However, since the hydride core is still in early design stages, and pumping technologies will have improved by the time it is in the final design stage, the present analysis also assumes that a 50% increase in the core pressure drop is a reasonable estimate of the maximum value that will be achieved in the near future. The upper limit, i.e. 36 psia, is the result of this assumption ($24.33 \times 1.5 \approx 36$ psia). The considerations made so far can not be applied to the oxide and hydride fueled ESBWR core, since such a reactor is not provided with pumps and operates in natural convection regime. Thus, in Case Ox-Backfit-ES and Case Hyd-NewCore-ES the limit on the core pressure drop was set close to the value predicted by VIPRE in modeling the thermal-hydraulic conditions of the

---

Zirconium-Uranium fuel can melt at temperatures between 1135°C, melting point for U, and 1855 °C, melting point for Zr".

[13] Table 4.4-1 of [11] shows that the core pressure drop for Nine Mile Point Unit 2 is actually very close to the value delivered by the modeling of the reference BWR/5, i.e. 24.74 psia vs 24.33 psia.

reference oxide ESBWR, i.e. 11.0 psia (the value actually predicted for the core pressure drop is 10.65 psia).

v. *Vibration ratio*. This less common parameter is defined as $\frac{y_{max}}{D}$ where y_{max} is the peak transversal rod vibration amplitude while D is the rod diameter. The vibration motions have to be carefully monitored since they induce wear phenomena on the contact points between rods and grid spacers. As a consequence, the cladding thickness may locally decrease, compromising the structural integrity of the rods. Contrary to the other power constraints, the vibration ratio is not a VIPRE output. This fact, together with the unexplored nature of the vibration field in two-phase flow, required a careful choice both of the most suitable correlation to compute the vibrations magnitude and of the vibration ratio limit. In particular, the correlation chosen is a modified version of the Païdoussis correlation ([19]), while the maximum allowed vibration ratio, 0.021, derives from a careful comparison of this correlation with the Tsukuda correlation ([20]) and with a typical PWR limit value found in the literature. The considerations that led to these choices are described in depth in Appendix B.

vi. $\dot{Q}/\dot{m}$. To limit the average exit quality, and thereby to avoid two-phase instability phenomena[14], the ratio between the core power and the coolant flow rate is maintained constant regardless of the lattice configuration analyzed. Such a ratio assumes two different values depending on the type of core modeled. For the cases modeling the thermal hydraulic conditions of oxide and hydride cores contained in a BWR/5-size vessel $\dot{Q}/\dot{m}$ is fixed to 243.07 kW/(kg/s), which corresponds to the ratio $\dot{Q}/\dot{m}$ for the reference BWR/5 oxide core (see Table 1.1). However, in Case Ox-Backfit-ES and Case Hyd-NewCore-ES the mentioned ratio is fixed to 449.86 kW/(kg/s), i.e. the value of $\dot{Q}/\dot{m}$ of the reference ESBWR oxide core (see Table 1.1). The decision to couple power and coolant flow by means of this constraint

[14] Limiting the average exit quality is only one of the preventive measures necessary to avoid two-phase instability phenomena. Usually, the four key variables leading to enhanced thermal-hydraulic stability are: long fuel time constant, low negative void coefficient, high single to two phase pressure drop ratio and low power to flow ratio.

may seem inconsistent with the need to determine the maximum achievable power for each core configuration. In fact, one may reasonably think that, given a core configuration, the maximum achievable power is that coupled with a coolant flow which does not satisfy the relation $\dot{Q}/\dot{m}=const.$ In other words, the search of the maximum achievable power should be performed on a wider spectrum of power-flow combinations. As a matter of fact, it has been found (see Appendix C) that taking even more freedom in the choice of the flow rate to core power ratio, the maximum achievable power is never higher than 105% of the maximum power derived with power/flow ratio constrained to a fixed value. Moreover, the 5% gain in power would be coupled with a significant increase in pressure drop, which can be 40% higher than the pressure drop of the configuration characterized by the maximum power among all those satisfying the ratio $\dot{Q}/\dot{m}=const.$

Although not used as computational constraint, the total coolant flow rate for case Ox-Backfit-5, Hyd-Backfit-5 and Hyd-NewCore-5 was qualitatively monitored in order to avoid core configurations characterized by flow rates not technically achievable. The modern ABWRII ([21]) is provided with 10 recirculation pumps having a flow rate of 1725 kg/s each. With the assumed enhancement of the pump performance, together with the possibility to increase their number make the prediction of 50% more flow availability in the next 5-10 years a reasonable assumption. Therefore, the maximum achievable flow rate is assumed around 25875 kg/s.

2.2.2 – Structural Constraints

As previously mentioned, the hydride core construction faced the problem of choosing the right fuel matrix for each assembly configuration. This choice was made rejecting all the matrixes that exceed particular parameters, here defined as "structural constraints". These constraints are determined by the type of plant in which the hydride fuel is assumed to be implemented. As previously stated, an existing plant requires that the bundle design (regardless the type of fuel) does not exceed certain limits. In case of a new plant designed jointly with the new fuel, some of these limits can be well exceeded. Two structural constraints exist which are described below together with specifications for the hydride case to which they are applied.

i. *Assembly weight*

Such a constraint is applied only in Case Hyd-NewCore-5. In fact, Case Hyd-NewCore-ES models a non-preexisting plant that will be provided with a crane suited for the bundle weight.

The weight limit is represented by means of the relation:

$$M \leq 1.4 \cdot M^{ref} \tag{2-1}$$

where M is an approximate value for the hydride assembly mass, and M^{ref} is a representative mass of the reference oxide assembly (GE 11 type). Both these parameters do not account for the mass of canister and grid spacers, and all the rods are assumed to be full length rods. In particular, assuming UO_2 pellets having 96% of the theoretical density:

$$M^{ref} = M_{UO2} + M_{Zr}^{clad} + M_{Zr}^{WR} = N_{FR}\pi\frac{D_{fo}^2}{4}L_H\rho_{UO2} + N_{FR}\pi\left(\frac{D^2 - D_{ci}^2}{4}\right)L\rho_{Zr} + \\ + N_{WR}\pi\left(\frac{D_{WRo}^2 - D_{WRi}^2}{4}\right)L\rho_{Zr} \cong 258kg \tag{2-2}$$

The values assigned to the parameters present in equation (2-2) derive from Table 1.2, Table 1.3 and Table J.1 and have the following physical interpretation:

- N_{FR} : number of fuel rods in the GE11 oxide reference assembly
- D_{fo} : pellet diameter
- D : fuel rod diameter
- D_{ci} : cladding inner diameter
- N_{WR} : number of water rods in the reference assembly
- D_{WRo} : water rods outer diameter
- D_{WRi} : water rods inner diameter
- L_H : fuel rod heated length
- L : fuel rod total length
- ρ_{Zr} : cladding density
- ρ_{UO2} : oxide fuel density (= $\rho_{UO2,theor} \times 0.96$)

For the hydride assembly mass an approximate relation is used, which is shown below and described in detail in Appendix D. In fact, the purpose of the present study is to

express the bundle mass as a function of the rod diameter D and of the bundle matrix n. By coupling this relation with (2-1) and (2-2), for each pair "rod diameter - rod pitch" it will be possible to choose, from among a wide spectrum of bundle matrixes, only those resulting in a bundle mass below the maximum allowed value. In such a way, the application of scaling relations for clad thickness, fuel pellet diameter and number of control rod guide tubes can be avoided, allowing a shorter computational time and easier programming. This means that the weight limit is not applied at the end of the analysis, i.e. by rejecting the core configurations already analyzed but characterized by an excessive bundle weight. Instead, it is applied before starting the analysis by using the mentioned relation which allows rejection of all the combinations D-n yielding an excessive bundle weight.

Using the same assumptions made for the reference oxide bundle mass calculation, the mass of a hydride bundle is:

$$M = M_{UZrH1.6} + M_{Zr} = N_{FR}\frac{\pi}{4}D_{fo}^2 L_H \rho_{UZrH1.6} + N_R \frac{\pi}{4}\left(D^2 - D_{ci}^2\right)L\rho_{Zr} \qquad (2\text{-}3)$$

where N_R is the total number of rods contained in the bundle, while N_{FR} is the number of fuel rods. Because of the presence of control rod guide tubes: $N_R > N_{FR}$. Moreover, recalling the meaning of the bundle matrix n, it is evident that $N_R = n^2$. By introducing a corrective coefficient $f < 1$ it is possible to express N_{FR} as a function of n:

$$N_{FR} = (n \cdot f)^2 \qquad (2\text{-}4)$$

Based on the VAMPIRE algorithm establishing the control rod guide tubes disposition (see Section 3.3.2, point "b" of "Bundle structure assumptions"), when n ranges between 8 and 20, f shows an oscillating behavior, ranging between 0.916 and 0.968. The average value, $\bar{f} = 0.944$, will be used for all the hydride bundles, regardless the value assumed by n.

By using the scaling correlations for hydride fueled rods (introduced in Section 3.3.1, point "b" of "Bundle structure assumptions"), a best fit of numerical data led to the following relations, which express both the fuel pellet diameter D_{fo} and the difference $\left(D^2 - D_{ci}^2\right)$ as functions of the rod diameter D:

$$D_{fo} = 0.8571D - 0.0004 \tag{2-5}$$

$$D^2 - D_{ci}^2 = 0.264D^2 - 0.0004D + 5 \cdot 10^{-6} \tag{2-6}$$

where D is expressed in meter.

Introducing $\bar{f}$, (2-5) and (2-6) into (2-3), we get:

$$M = n^2 \bar{f}^2 \frac{\pi}{4}(0.8571D - 0.0004)^2 L_H \rho_{UZrH1.6} + n^2 \frac{\pi}{4}(0.264D^2 - 0.0004D + 5 \cdot 10^{-6}) L \rho_{Zr} \tag{2-7}$$

Assigning to the parameters present in (2-7) the corresponding values from Table 1.3 and Table J.1, and using the average value for f, the expression becomes:

$$M = (21416.4D^2 - 23.3D + 0.111) \cdot n^2 \tag{2-8}$$

Combining the relations (2-1), (2-2) and (2-8) one obtains:

$$(21416.4D^2 - 23.3D + 0.111) \cdot n^2 \leq 361.2 \tag{2-9}$$

that is:

$$n \leq \sqrt{\frac{361.2}{21416.4D^2 - 23.3D + 0.111}} \tag{2-10}$$

which is the analytical expression of the assembly weight constraint for Case Hyd-NewCore-5, written in a useful form.

ii. *Total number of bundles*

Such a constraint is applied both in Case Hyd-NewCore-5 and in Case Hyd-NewCore-ES. An excessive number of bundles leads to excessive fuel handling and a consequent long refueling time. In the present analysis the maximum allowed number of bundles is $1.6N^{ref}$, where N^{ref} represents the number of bundles in the reference BWR/5 oxide core[15]. Since N^{ref} is equal to 764, the maximum allowed number of bundles is 1222.

Table 2.4 summarizes the structural constraints applied to Case Hyd-NewCore-5 and Case Hyd-NewCore-ES.

[15] The limit chosen, $1.6N^{ref}$, comes from considerations concerning the ESBWR core. In fact, it contains 1132 bundles ([10]), that is $1.48N^{ref}$ assemblies. Assigning to this reactor the role of reference plant for the next generation of BWRs, and also assuming a further possible increase in the number of bundles, the change in multiplying factor from 1.48 to 1.6 is considered reasonable.

Table 2.4: Structural Constraints		
Case	Maximum number of bundles	Analytical expression limiting the assembly weight*
Hyd-NewCore-5	1222	$n \leq \sqrt{\frac{361.2}{21416.4D^2 - 23.3D + 0.111}}$
Hyd-NewCore-ES		not applied

* D is expressed in m.

Chapter 3: Analysis Assumptions

3.1 – Common Assumptions

The modeling of all the core types examined throughout the analysis requires several VIPRE input files which contain all the necessary input data that describe the core geometry and the thermal-hydraulic conditions. Whenever one encounters:

- a parameter too complex to be exactly modeled and/or
- reduced interest in a particular nuclear aspect

the analysis can be simplified by means of assumptions. They can be conveniently grouped in seven categories:

- core structure assumptions
- bundle structure assumptions
- pressure drop assumptions
- coolant flow assumptions
- power distribution assumptions
- critical power determination assumptions
- other assumptions and considerations

Each category contains a number of different assumptions. Some of them are so general as to be common with all the cases examined, while others differ strongly from case to case. Those shared by all cases are listed and briefly described below. Whenever a more detailed description is required it will be presented in Appendix E, using the same categorization and numbering with letters. Conversely, the assumptions specifically referred to the single cases are presented in the relevant sections.

Core structure assumptions

a) The core peripheral region included between the outermost bundle ring and the core shroud (dashed in the sketch aside) is modeled as completely blocked, i.e. no coolant flows axially through it.

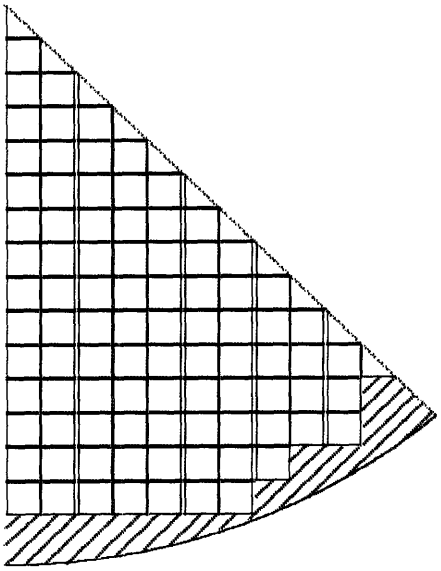

Figure 3.1: Peripheral Blocked Region

Bundle structure assumptions

a) The whole-core approach used to perform the analyses models $1/8^{th}$ of the core, and each bundle as a single channel provided with a flow area, wetted and heated perimeter equal to the sum of the areas, wetted and heated perimeters of all the subchannels.

b) For the loss coefficient calculation, the grid spacers are assumed to have a thickness of 0.45 mm and height of 40 mm, which are typical values for these components.

c) The present analysis neglects the presence of Partial Length Fuel Rods (PLFRs), which are actually present both in the GE11 and in the GE14 fuel designs. All the rods contained in each assembly are assumed to be full length rods. Other than to simplify the analysis of the wide spectrum of bundle geometries assessed, this assumption is forced by the CPR correlation used, i.e. the Hench-Gillis correlation. It is not suited to analyze bundles with PLFRs since it was developed using experimental data deriving from "old" bundle designs, which used only Full Length Fuel Rods. Moreover, if the whole core analysis accounted for the PLFRs, the J_1

factor entered in the whole core VIPRE input file would vary axially, but such an option is not permitted by the VIPRE code (see Section E1.1. in Appendix E for details).

Pressure drop assumptions

a) Although a real bundle has a total length larger than the heated length, this analysis was performed assuming they are equal. This is due to the VIPRE inability to predict correctly the power of each bundle. It has been verified that, both for whole core and subchannel analysis, when the two lengths are different VIPRE overestimates the thermal power of each bundle. Conversely, when the total length is set to be equal to the heated length the bundle power prediction is correct. However, because of the assumption made, the core pressure drop delivered by VIPRE is underestimated by a factor 1.046 for the BWR/5-type cores, and 1.131 for the ESBWR-type cores. Such multipliers are accounted for throughout the whole study, and all the core pressure drop values delivered by VIPRE are automatically multiplied by them. In such a way, the values calculated are representative of the real pressure drop characterizing the core types under examination.

b) The axial friction factor needed for the calculation of the pressure drop through the fuel bundles is determined from the Blasius relation:

$$f_F = a\,\mathrm{Re}^b \tag{3-1}$$

where the coefficients a and b are computed by using the Cheng-Todreas friction factor correlations for square arrays having P/D ≥ 1.1 ([22]). See Table E.2 in Appendix E for the numerical values.

c) The form loss coefficient of the grid spacers is computed by a modified form of the In's correlation ([23]). See Appendix H for details.

Coolant flow assumptions

There are no assumptions common for all cases.

Power distribution assumptions

a) The axial power profile is assumed to be independent of the bundle radial position in the core. Thus, given a core type (BWR/5-type or ESBWR-type), all the bundles are assumed to have the same axial power profile. The power profiles used are described in the sections relative to each case.

b) Consistently with the lumping approach used for the subchannels forming each bundle, the radial power distribution inside them is not described in detail, i.e. the local peaking factors of each rod are not entered as input. However, the non-uniformity that characterizes the power distribution among the fuel rods is accounted for by entering, for each bundle[16], the maximum J_l factor of the pin-by-pin power distribution under examination. A common pin-by-pin power distribution is considered for all the cases analyzed, regardless of the type of fuel and the bundle geometry. Such a power distribution is characterized by a maximum local peaking factor of 1.26 and a maximum J_l factor of 1.198 located on a side rod (see Figure E.1). It is important to note that, because of the subchannel-lumping approach used, such an assumption does not mean that all the bundle designs examined throughout the analysis have the same fuel pin local peaking factors. Instead, it means that all the bundle designs are characterized by the same maximum localized non-uniformity in the pin-by-pin power distribution. Important comments about this assumption are presented in Section E1.1. of Appendix E.

Critical power determination assumptions

a) The calculation of the MCPR is performed by VIPRE using the Hench-Gillis correlation ([16], [4]). Important comments concerning the use of this relation are presented in Section E1.1. of Appendix E.

[16] Since the pin-by-pin power distribution is assumed to be independent of the bundle position in the core, all the bundles have the same maximum J_l factor.

Other assumptions and considerations

a) The vibration ratio calculation was performed using the so-called *Païdoussis Corrected Correlation*. A detailed description of the approach used to analyze the vibration mechanisms in two-phase flow is presented in Appendix B. Except for those concerning the development of the vibration correlation itself, the main assumption made consists of analyzing the fuel rods as they were hollow tubes, i.e. neglecting the presence of the fuel and, for the hydride fueled rods, of the liquid metal (see next assumption). This is a conservative assumption since the absence of these heavy materials makes the rod weight smaller and therefore the vibrations amplitude larger. Moreover, the *Païdoussis Corrected Correlation* was not applied to the whole rod length, but only to the last section, that is the assembly portion included between the last grid spacer and the upper tie plate. In fact, because of the higher quality, this section is subjected to the most significant vibration motions. Given a core configuration, the calculation was performed for all the bundles, and the maximum vibration ratio calculated was compared with the limit value fixed in Table 2.3.

3.2 – Case 0: VIPRE Core Modeling Validation

3.2.1 – Strategy Employed

As specified in Section 2.1, Case 0 is analyzed in a simplified way, at least from the computational viewpoint. A single VIPRE run for each reference core was sufficient to obtain all the results required both for the VIPRE core modeling validation and for fixing the MCPR and the pressure drop limits.

Contrary to all the other cases, in Case 0 core power and coolant flow rate are entered as known input data, together with all the other independent parameters needed to describe as realistically as possible the thermal-hydraulic operational condition of the reference oxide cores. However, the complex structure of the core forces the analysis to make a set of assumptions: their reasonability will be proven by comparison of the VIPRE output data to the values found in literature. Since many assumptions as well as the thermal-hydraulic code used, i.e. VIPRE, are in common with the other cases examined, the validation basis provided for the reference BWR/5 Oxide Core and for the reference

ESBWR Oxide Core can be considered as a validation of all the cases investigated in the present analysis.

3.2.2 – Assumptions for Case 0

Besides the common assumptions listed in Section 3.1, those applied to this case are briefly described below[17]. Although Case 0 consists actually of the analysis of two core types, i.e. the reference BWR/5 oxide core and the reference ESBWR oxide core, the qualitative features of the assumptions made are the same, and therefore are presented together. Quantitative differences will be eventually described as well. The assumption classification is consistent with the category nomenclature presented in Section 2.1. If no specific assumptions are made for a given category, the category is not displayed.

Core structure assumptions

a) The fuel channel size, their number and the width of the gap that separates each from its neighbor reflect the dimensions of the designs listed in Table 1.2 and Table 1.3. The core structures are schematically represented in Figure 3.2, which clearly shows the larger size of the ESBWR core.

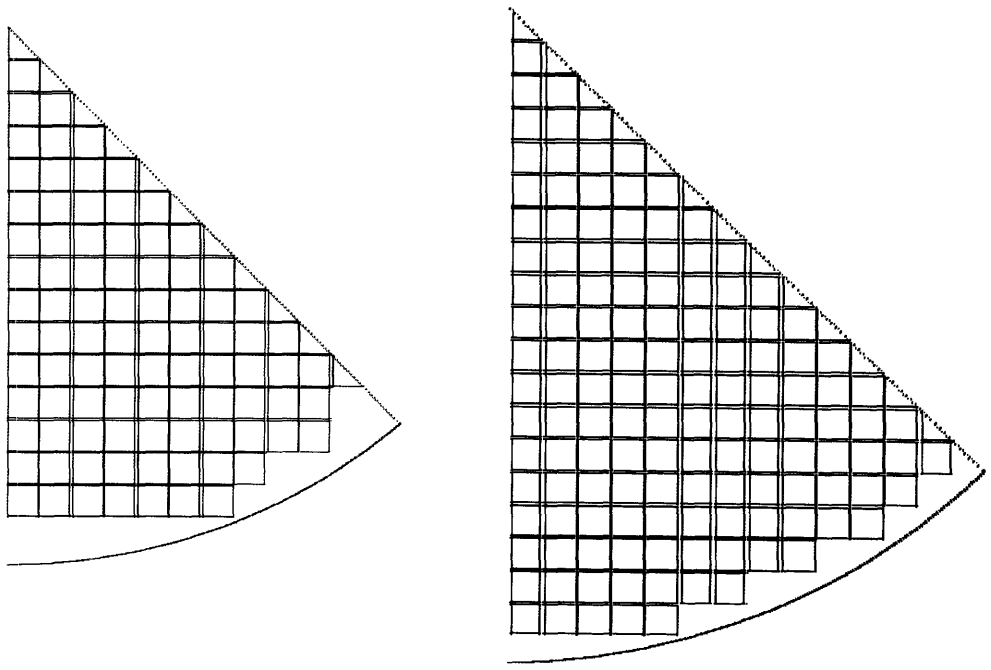

Figure 3.2: 1/8th Section of BWR/5 Oxide Core and of ESBWR Oxide Core

[17] It has to be stressed that some of these assumptions are also applied to Case Ox-Backfit-5 and Case Ox-Backfit-ES, as described later in the Section 3.3.1.

b) The cruciform control rods are assumed completely withdrawn. As a consequence, for both the bypass channel flow area calculation and for the pressure drop calculation their influence is neglected. See Section E1.2. in Appendix E for details.

Bundle structure assumptions

a) The geometric data concerning the bundle structure are entered directly in the VIPRE input file and exactly reflect those summarized in Table 1.2 and Table 1.3. The only exception concerns the number of water rods since the modeling performed with VIPRE assumes a single water rod contained in each bundle (so-called "dummy" water rod) modeled as a hollow tube, i.e. no coolant flows axially through it. Its outer diameter D_{DWRo} and wall thickness t_{DWR} are chosen such that the water rod inner and outer cross sectional areas are preserved with respect to the real bundle. Thus, the following conditions must be satisfied:

$$\left[2\cdot\frac{\pi}{4}\cdot(D_{WRo}-2t_{WR})^2\right]_{real\_bundle}=\frac{\pi}{4}(D_{DWRo}-2t_{DWR})^2 \tag{3-2}$$

$$\left[2\cdot\frac{\pi}{4}\cdot D_{WRo}^2\right]_{real\_bundle}=\frac{\pi}{4}D_{DWRo}^2 \tag{3-3}$$

where D_{WRo} and t_{WR} are the outer diameter and the wall thickness of the water rods present in the real bundle (see Table 1.2). Such conditions yield a "dummy" water rod outer diameter of 1.38590" for the reference BWR/5 bundle, and 1.45975" for the reference ESBWR bundle. The thickness of the "dummy" water rod is equal to 0.0424" for both the reference bundles.

Pressure drop assumptions

a) In order to divert most of the coolant flow through the higher power fuel bundles the core inlet is orificied. Three different orificing coefficients are applied: a large coefficient for the bypass channels and two smaller coefficients for the central and peripheral bundles. The values used are listed as follows:

BWR/5: Bypass channels: 270
Central bundles: 21.089
Peripheral bundles: 182.049

ESBWR: Bypass channels: 394

Central bundles: 21.028

Peripheral bundles: 181.527

The methodology used to calculate the orificing coefficients for the bundles is described in Section E1.2. of Appendix E and is consistent with the directions given in [24]. Instead, the orificing coefficients for the bypass channels were chosen in a way such that 10% of the total coolant flow is diverted through them.

b) Bypass channels and fuel bundles are modeled as channels connected only at plena, and therefore have the same pressure drop. Concerning the fuel bundles, the form losses accounted for are: inlet orificing, lower tie plate, grid spacers (7 for BWR/5, 8 for ESBWR) and upper tie plate. Instead, the bypass channels have a single form loss located at $z = 0$ due to the inlet orificing.

While the correlation used for the frictional pressure drop through the fuel bundles is common to all the cases and has already been mentioned (see Section 3.1, point "b" of "Pressure drop assumptions"), the bypass channel friction factor is computed by means of the Blasius and McAdams correlations for laminar and turbulent flow respectively ([17]). See Section E1.2. in Appendix E for details.

Coolant flow assumptions

a) The flow rate entered in the VIPRE input file is equal to 96% of the value shown in Table 1.1. This is due to the presence of the water rods, through which 4% of the coolant is assumed to flow (consistent with [24]). Since for most of the bundle length the coolant contained in the these rods has mainly a moderation function, and not a cooling function, the "dummy" water rod contained in each bundle is modeled as a hollow tube and the percentage of coolant which actually flows through it is simply deducted from the total coolant inventory.

b) The analysis models bypass channels with dimensions are significantly smaller than the real ones. In particular, their flow area and wetted perimeter are, respectively, ½ and 1/8 of the real values. This is due to the need to reduce the computational time. It

has been verified that, if the bypass channels are modeled realistically, a very large[18] inlet orificing coefficient must be applied in order to preserve the flow splitting percentage described under point a) of "Pressure drop assumptions". Under such conditions, the computational time VIPRE requires to complete the analysis is excessive, especially in view of the other cases examined throughout the analysis, for which 400 different core configurations are analyzed by means of a single VAMPIRE run. Although this assumption may seem quite drastic, it does not significantly affect the results. In fact, because of the fractions chosen, i.e. ½ for the areas and 1/8 for the perimeters, the friction pressure drop through the bypass channels has the same value it would have if the channels were modeled realistically. In fact:

$$\left(\Delta p_{friction}\right)_{real} \propto \left(\frac{G^2}{D_{eq}}\right)_{real} = \left(\frac{\dot{m}}{A_{real}}\right)^2 \frac{P_{w,real}}{4A_{real}} = \frac{\dot{m}^2}{4}\frac{P_{w,real}}{A_{real}^3} = \frac{\dot{m}^2}{4}\frac{8P_{w,\mathrm{mod}\,eled}}{\left(2A_{\mathrm{mod}\,eled}\right)^3} = \frac{\dot{m}^2}{4}\frac{P_{w,\mathrm{mod}\,eled}}{A_{\mathrm{mod}\,eled}^3} \tag{3-4}$$

The only drawback of the approach used is the consequent increase of the heat transfer coefficient across the interface bundle box-bypass channel. It has been verified that such phenomenon results in an increase lower than 0.5°C in the coolant temperature at the exit of the bypass channels, and in a reduction of about 0.4% of the hot bundle exit quality.

See Appendix I for details concerning the numerical values used for the bypass channel dimensioning.

Power distribution assumptions

a) The axial power profiles used for the two reference cores are shown in Figure 3.3. The one used for the reference BWR/5 core is a typical axial power profile for a BWR/5 loaded with GE11 bundles, at Beginning Of Cycle (BOC) ([9]). It is characterized by a maximum peaking factor of 1.47. Instead, that used for the reference ESBWR core has a maximum peaking of 1.44 and reflects the axial power profile of the "real" ESBWR at BOC (from Table 4.4-4-b of [8]). Both are bottom peaked, consistent with a typical BWR axial profile at BOC (see Figure 4D-2 of [8] for an example of the shifting of the axial profile peak during the fuel cycle).

[18] For the BWR/5 core the orificing coefficient for real-dimensioned bypass channels is 1100.

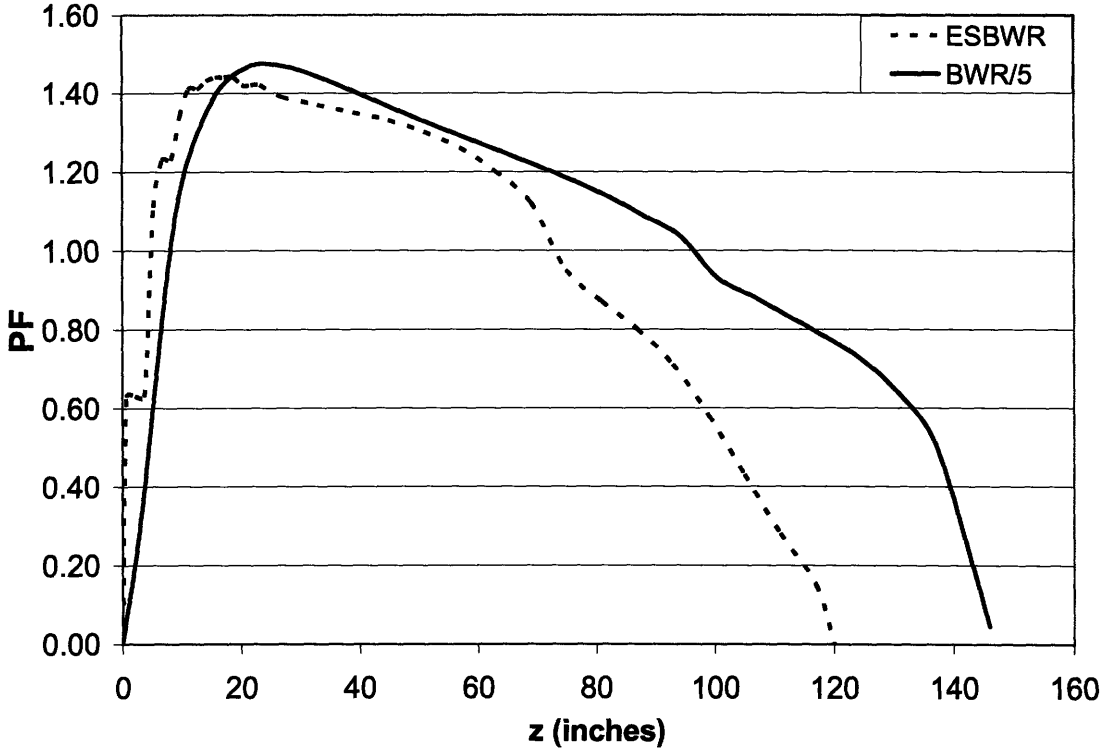

Figure 3.3: Axial Power Profiles used for BWR/5 and ESBWR

b) The non-uniform radial core power distribution is modeled by assigning a radial peaking factor to each bundle. To be consistent with the choice made for the axial power profile, the core radial power distribution should also be referred to the BOC. However, this analysis assigns an End Of Cycle (EOC) power distribution to the reference BWR/5 core. This is due to the lack of a detailed map at BOC, whereas a complete BWR/5 EOC core power map was provided in [25]. Such an assumption is conservative, since the maximum bundle peaking factor is usually higher at EOC than at BOC. According to data provided in ([25]), a typical maximum BOC bundle peaking factor is 1.41, while it increases to 1.51 at EOC. Such an assumption is not applied to the reference ESBWR since a complete set of BOC and EOC data is available in the public literature. Thus, the distribution used for this reactor is the BOC power distribution of the "real" ESBWR (from Figure 4A-1d of [8]), which has a maximum peaking of 1.29. The complete maps of the peaking factors are shown in Figure 3.4.

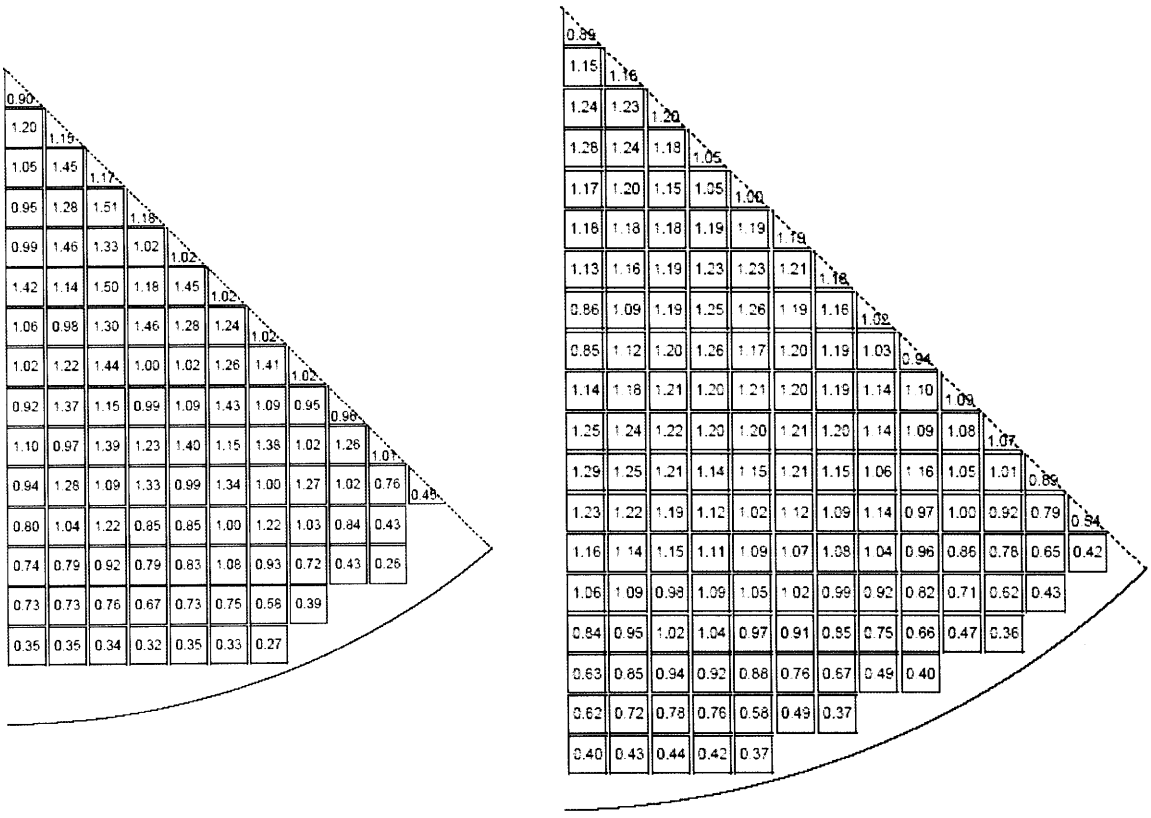

Figure 3.4: Core Radial Peaking Factors for Ref. BWR/5 and Ref. ESBWR

Other assumptions and considerations

a) The Helium-filled gap that separates the oxide fuel from the cladding is assumed to have a constant conductance equal to 1000 Btu/hr ft^2 F (5682.6 W/m^2 K). Such a value has been chosen using Figure 8-22 of [17], which is reproduced and elaborated in Figure 3.5. It shows the gap conductance as a function of the Linear Heat Generation Rate and of the gap thickness. By using the available data it is possible to locate in the figure the points corresponding to the "hot spot" operating conditions of the two reference cores. In particular, the two "hot spot" LHGRs are:

$$LHGR_{ref\_BWR/5}^{hot\_spot} = \frac{\dot{Q}_{core}}{N_{bundles}} \cdot f_{radial}^{\max} \cdot \frac{f_{local}^{\max} \cdot f_{axial}^{\max}}{N_{rods/bundle} \cdot L_H} = \frac{3323 \cdot 10^6}{764} \cdot 1.51 \cdot \frac{1.26 \cdot 1.47}{74 \cdot 370.8} \cdot \cong 443 \frac{W}{cm} \quad (3\text{-}5)$$

$$LHGR_{ESBWR}^{hot\_spot} = \frac{\dot{Q}_{core}}{N_{bundles}} \cdot f_{radial}^{\max} \cdot \frac{f_{local}^{\max} \cdot f_{axial}^{\max}}{N_{rods/bundle} \cdot L_H} = \frac{4500 \cdot 10^6}{1132} \cdot 1.29 \cdot \frac{1.26 \cdot 1.44}{92 \cdot 304.8} \cong 332 \frac{W}{cm} \quad (3\text{-}6)$$

Such values, coupled with the cold diametral gap of the two reference cores (see Table 1.2), identify the two points shown in Figure 3.5. Since the curves present in the original figure do not extend below a diametral gap of 0.10 mm, a rough extrapolation (dashed line) has been necessary for the ESBWR reference core, whose diametral gap is equal to 0.07 mm.

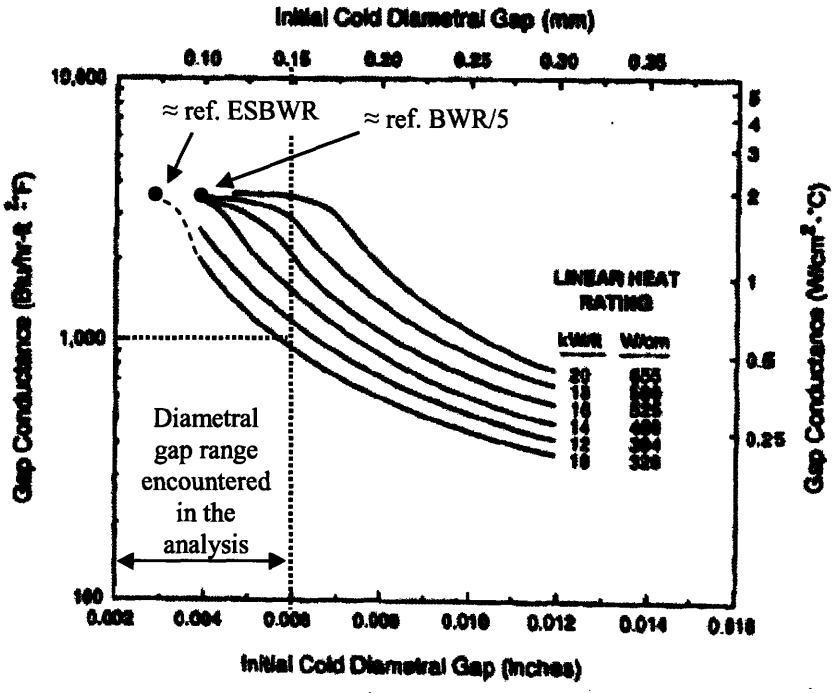

Figure 3.5: Gap conductance as a function of cold diametral gap ([17])

It can be seen that for both reference cores the gap conductance at the hot spot is significantly higher than 1000 Btu/hr ft^2 F, and therefore the choice of this value is conservative.

3.2.3 – Case 0: Validation Results

The most important VIPRE output data are summarized in Table 3.1 and Table 3.2 together with the reference values found in literature. The former contains the results for the reference BWR/5, while the latter for the reference ESBWR. The comparison of the two sets of data gives an indication of the reliability of the core model and the reasonablness of the assumptions made. However, while core power, coolant flow rate, core inlet temperature and system pressure reflect exactly the Nine Mile Point Unit 2 and

the ESBWR core characteristics, many other parameters have been assumed (see Section 3.2.2) and therefore do not correspond to those actually existing in the reference plants.

Table 3.1: Parameter Comparison for Core Modeling Validation: BWR/5 core

Output parameter	VIPRE output	Reference value	Diff. %	Source of the reference value
Total core pressure drop, psi (kPa)	24.33 (167.75)	24.74 (170.58)	-1.5	Table 4.4-1 of [11]
Average orifice pressure drop, central region, psi (kPa)	6.4 (44.1)	6.0 (41.4)	+6.7	Table 4.4-1 of [11]
Average orifice pressure drop, peripheral region, psi (kPa)	17.4 (120.0)	16.0 (110.3)	+8.8	Table 4.4-1 of [11]
Average orifice pressure drop, bypass channels, psi (kPa)	19.95 (137.55)	Not found	N.A.	N.A.
Hot bundle mass flux, kg/s m^2	1568	Not found	N.A.	N.A.
Average bundle mass flux, kg/s m^2	1659	Not found	N.A.	N.A.
Average bypass channel mass flux, kg/s m^2	872	Not found	N.A.	N.A.
Core maximum exit voids, %	81.5	76.2	+7.0	Table 1.3-1 of [11]
Hot bundle exit quality, %	26.7	23.7	+12.6[19]	Table 4.4-3 of [11]
Core average exit quality, %	13.91	13.10	+6.2	Table 1.3-1 of [11]
Flow rate % through bypass channels	10.0	Not found[20]	N.A.	N.A.
Maximum LHGR, kW/ft (kW/m)	13.1[21] (43.1)	13.4 (44.0)	-2.2	Table 4.4-1 of [11]
Maximum fuel temperature, F (°C)	2663.9 (1462.2)	3435 (1890.5)	-22.6[22]	Table 4.4-1 of [11]
Maximum average fuel temperature, F (°C)	1766.1 (963.4)	Not found	N.A.	N.A.
Maximum cladding outside temperature, F (°C)	583.3 (306.3)	Not found	N.A.	N.A.
MCPR	1.015	1.24	-18.1	Table 1.3-1 of [11]

N.A.≡ Not Applicable

[19] The hot bundle exit quality is function of the maximum radial peaking factor in the core: although the radial peaking factor value used in the modeling of the reference core refers to a BWR/5 and derives from a reliable source ([25]), it may not coincide with that of NMP2 and, above all, that of NMP2 yielding an exit quality of 23.7% may not be the End Of Cycle peaking factor, as assumed in this analysis.

[20] For a typical BWR this value is around 10% (water rod flow excluded) ([24]).

[21] Since VIPRE lumps all the rods contained into a bundle in a single rod, the output file does not give any information on the fuel pin having the highest local peaking factor. VIPRE delivers the hot spot linear power as kW per foot of bundle (772 kW/ft for the ref. BWR/5, 674 kW/ft for the ref. ESBWR). Using the maximum local peaking factor shown in Figure E.1, i.e.1.26, it is possible to calculate the hot spot LHGR "per rod" as: 772×1.26/74 = 13.1 kW/ft for the BWR/5, 674×1.26/92=9.2 kW/ft for the ESBWR.

[22] The inconsistency in the maximum fuel temperature may be due to the different rod diameter of the original NMP2 bundle design. As mentioned in Section 1.5, NMP2 was originally loaded with 8×8 bundles, for which it is reasonable to assume a larger rod diameter.

Table 3.2: Parameter Comparison for Core Modeling Validation: ESBWR core				
Output parameter	**VIPRE output**	**Reference value**	**Diff. %**	**Source of the reference value**
Total core pressure drop, psi (kPa)	10.6 (73.1)	10.2 (70.3)	+3.9	Table 4.4-1 of [8]
Average orifice pressure drop, central region, psi (kPa)	1.5 (10.3)	2.9 (20.0)	-48.3	Table 4.4-1 of [8]
Average orifice pressure drop, peripheral region, psi (kPa)	6.0 (41.4)	5.4 (37.2)	+11.1	Table 4.4-1 of [8]
Average orifice pressure drop, bypass channels, psi (kPa)	6.7 (46.2)	Not found	N.A.	N.A.
Hot bundle mass flux, kg/s m^2	777	Not found	N.A.	N.A.
Average bundle mass flux, kg/s m^2	815	Not found	N.A.	N.A.
Average bypass channel mass flux, kg/s m^2	407	Not found	N.A.	N.A.
Core maximum exit voids, %	88.0	90.0	-2.2	Table 4.4-1 of [8]
Hot bundle exit quality, %	43.2	44.0	-1.8	Table 4.4-3b of [8]
Core average exit quality, %	25.5	17.0	+50.0[23]	Table 1.3-1 of [8]
Flow rate % through bypass channels	10.0	Not found	N.A.	N.A.
Maximum LHGR, kW/ft (kW/m)	9.2[21] (30.2)	13.4 (44.0)	-31.3	Table 1.3-1 of [8]
Maximum fuel temperature, F (°C)	2042.1 (1116.7)	Not found	N.A.	N.A.
Maximum average fuel temperature, F (°C)	1452.9 (789.4)	Not found	N.A.	N.A.
Maximum cladding outside temperature, F (°C)	578.1 (303.4)	Not found	N.A.	N.A.
MCPR	1.018	1.20	-15.2	Table 4.4-3 of [8]

N.A.≡ Not Applicable

The substantial agreement between the values of the total core pressure drop, core exit quality and bypass flow percentage (and consequently bundle flow rate) is extremely important since these parameters are strongly tied to the power constraints listed in Section 2.2.1, which have a significant influence on the maximum achievable power. Therefore, the numerical models used to perform the core thermal-hydraulic analysis are correct, and the assumptions made reasonable. Moreover, as specified in Section 2.2.1,

[23] The core average exit quality found in [8] is inconsistent with other data found in the same source. In fact, based on a simple heat balance of the core: $\dot{Q}_{core} = \dot{m}\left(h_f - h_{in} + \bar{x}_{core}^{out} h_{fg}\right)$ for $\dot{Q}_{core} = 4500\,\mathrm{MW_t}$, $\dot{m} = 10003\,\mathrm{kg/s}$, h_f=1280 kJ/kg, h_{in}=1188 kJ/kg and h_{fg}=1489 kJ/kg, the core average exit quality should be 24%. This value is far from that shown in [8], i.e. 17%.

the MCPR values found for the reference cores, i.e. 1.015 and 1.018, are set as the MCPR limits to use throughout the analysis.

3.3 – Alternate Core Designs

In this section the cases examining the "wide geometry spectrum", i.e. $0.6 \leq D \leq .6$ cm, $1.1 \leq P/D \leq .6$, are listed and described sequentially. The choice of the geometry limits for D and P/D is the same as that made in the neutronic analyses of BWR hydride fueled bundles ([26]). Consequently, in order to make the fuel comparison consistent, the oxide cases are also analyzed over this range, which abundantly bounds the typical BWR geometries with some margin. The cases described in this section are grouped as follows:

- Case Ox-Backfit-5, Case Hyd-Backfit-5 and Case Ox-Backfit-ES;
- Case Hyd-NewCore-5 and Case Hyd-NewCore-ES.

While for the "Backfit" cases the description basically consists of a simple list of assumptions, for the "NewCore" cases the presence of the structural constraints requires clarification of how these constraints are computationally implemented and how they influence the choice of the fuel matrix.

3.3.1 – Case Ox-Backfit-5, Hyd-Backfit-5 and Ox-Backfit-ES

Because of the similarity of the qualitative aspects that characterize the Backfit cases, such cases are described together. Whenever present, differences will be highlighted.
Besides the common assumptions listed in Section 3.1, those developed for these cases are briefly described below. Whenever an assumption description requires a further investigation, this is performed in Appendix E. If no specific assumptions are made for a given category, the category is not displayed.

Core structure assumptions

a) The fuel channel width, the number of fuel bundles and the width of the gap that separates each bundle from the neighboring ones are maintained constant regardless of the values chosen for D and P/D. For Case Ox-Backfit-5 and Case Hyd-Backfit-5 such "ex-bundle" dimensions reflect exactly those used for the reference BWR/5 in Case 0 (VIPRE Core Modeling Validation). Likewise, Case Ox-Backfit-ES models

core configurations having the same ex-bundle core structure as that of the reference ESBWR core modeled in Case 0. The dimensions of the BWR/5 bundle and of the ESBWR bundle are listed in Table 1.1 and Table 1.2, while the arrangement of the two cores is shown in Figure 3.2. Thus, the 400 *D-P/D* pairs analyzed in each case differ from each other only in array geometry, that is for the rod diameter D, pitch P and matrix index n.

b) For each *D-P/D* pair the corresponding matrix index n is calculated as:

$$n = floor\left(\frac{l_{bi} + D - P}{P}\right) \tag{3-7}$$

where "*floor*" is a function that rounds down the term in brackets to the lower integer, while l_{bi} is the bundle inner width (from Table 1.2).

c) In agreement with the assumption made for Case 0 (VIPRE Core Modeling Validation), the cruciform control rods are assumed as completely withdrawn. As a consequence, for both the bypass channel flow area calculation and for the pressure drop calculation their influence is neglected.

Bundle structure assumptions

a) In agreement with the modeling of the reference bundles performed in Case 0 (VIPRE Core Modeling Validation), all the assembly configurations modeled in Case Ox-Backfit-5 and Case Ox-Backfit-ES contain a single "dummy" water rod. While its wall thickness is the same as that used in Case 0 (0.0424"), its outer diameter is chosen such that the ratio between the water rod flow area and the bundle active flow area is constant and equal to the values used in Case 0 for the two reference cores, i.e. 0.0921 for Case Ox-Backfit-5 and 0.1030 for Case Ox-Backfit-ES. The iterative algorithm used to calculate the "dummy" water rod diameter given the bundle inner width, the fuel rod diameter D and the fuel rod pitch P was developed by Handwerk ([3]) and is described in Section E1.3. of Appendix E.

   The assumption described above was not applied to Case Hyd-Backfit-5 since the hydride bundles do not contain water rods.

b) For each assembly configuration, once D and P/D are entered as input, the clad and gap thickness are automatically calculated using scaling relations provided by Westinghouse ([27]) and presented in Section E1.3. of Appendix E. While the same correlation is used for the clad thickness regardless of the type of fuel, two different correlations are used for the fuel-clad gap thickness, depending on the type of fuel. In particular, the correlation used for the hydride fuel accounts for the more significant swelling that affects such a fuel, yielding a thicker gap.

Pressure drop assumptions

a) The orificing coefficient of the bypass channels is a function of the rod pitch P expressed in cm. For Case Ox-Backfit-5 and Hyd-Backfit-5 the following relation was applied:

$$C_{bypass}^{orif} = 139.19P^3 - 682.66P^2 + 788.09P + 131.21 \qquad (3\text{-}8)$$

while for Case Ox-Backfit-ES the relation is given by the coupling of the following:

$$C_{bypass}^{orif} = 141.59P^3 - 610.99P^2 + 443P + 350 \qquad \text{if } P/D>1.4 \text{ and } D<1.1 \text{ cm}$$

$$C_{bypass}^{orif} = 141.59P^3 - 610.99P^2 + 443P + 537.46 \qquad \text{otherwise} \qquad (3\text{-}9)$$

Such relations are purely empirical and derived from the following observation. If the bypass channel orificing coefficients were set equal to the values used for the two reference cores (270 for BWR/5-type cores, 394 for ESBWR-type cores, see Section 3.2.2), for several D-P/D pair the bypass flow percentage would be very far from the value of 10% suggested in [24]. It has been observed that, should the mentioned assumption be applied, the bypass flow percentage would decrease as the rod pitch increases. Based on this observation, the bypass channel orificing coefficient was regulated using the above relations, which:

- yield a coefficient of 270 and 394 for the reference BWR/5 and the reference ESBWR respectively;
- reduce the number of D-P/D pair characterized by bypass flow percentages which differ significantly from the reference value of 10%.

Conversely, the orificing coefficients used for the central and peripheral bundles depend on the active bundle flow area (which is a function of the rod diameter D and the fuel matrix size n), and are calculated using the methodology described in Section E1.2. of Appendix E (point "a" of "Pressure drop assumptions").

b) The type and location of the form losses modeled in Cases Ox-Backfit-5 and Case Hyd-Backfit-5 are the same as those used for the modeling of the reference BWR/5 core in Case 0 (VIPRE Core Modeling Validation). Likewise, type and location of the form losses accounted for in Case Ox-Backfit-ES reflect those used for the modeling of the reference ESBWR core in Case 0. However, the numerical values differ, and are function of the bundle active flow area (see Section E1.2. of Appendix E, point "a" of "Pressure drop assumptions").

   The friction factor correlations used for the bypass channels are common to all three cases and are identical to those used in Case 0.

Coolant flow assumptions

a) Core power and coolant flow rate are each constrained by keeping their ratio constant and equal to the values listed in Table 2.3 ($\dot{Q}_{core} / \dot{m}$ = 243.07 kW/(kg/s) for Case Ox-Backfit-5 and Case Hyd-Backfit-5, $\dot{Q}_{core} / \dot{m}$ = 449.87 kW/(kg/s) for Case Ox-Backfit-ES). Thus, the coolant flow can be interpreted as a consequence of the core power which is iteratively entered as an input value to verify that the power constraints are respected (see Figure 1.1).

b) In agreement with the strategy used for the two reference cores in Case 0 (VIPRE Core Modeling Validation), for the two oxide cases the coolant flow rate entered by VAMPIRE in the VIPRE input files is equal to 96% of the value derived from the ratio mentioned at point a). This accounts for the flow rate through the water rods, that are modeled as hollow tubes. Conversely for Case Hyd-Backfit-5 the flow rate entered as VIPRE input matches exactly the value deriving from the *power/flow* ratio since the water rods are not present.

c) In agreement with the assumption made in Case 0 (VIPRE Core Modeling Validation), the dimensions of the bypass channels differ from those characterizing

the reference plants. In particular, the geometry of the bypass channels modeled in Case Ox-Backfit-5 and in Case Hyd-Backfit-5 is the same as in the reference BWR/5 modeled in Case 0. Likewise, the bypass channels modeled in Case Ox-Backfit-ES are identical to those of the reference ESBWR analyzed in Case 0.

Power distribution assumptions

a) The core axial and radial power distributions used in Case Ox-Backfit-5 and Case Hyd-Backfit-5 reflect those used for the reference BWR/5 in Case 0 (VIPRE Core Modeling Validation). Likewise, the core axial and radial power profiles used for Case Ox-Backfit-ES are those of the reference ESBWR. Figure 3.3 and Figure 3.4 show such power distributions.

Other assumptions and considerations

a) Case Ox-Backfit-5 and Case Ox-Backfit-ES assumes that the conductance of the Helium-filled gap that separates the oxide fuel from the cladding is constant, regardless of the gap thickness, and equal to 1000 Btu/hr ft^2 F (see Section 3.2.2, point a) of "Other assumptions and considerations"). Conversely, Case Hyd-Backfit-5 assumes a liquid metal filled gap, having a geometry-dependent conductance equal to:

$$h_g = \frac{k_{LM}}{\frac{D_{fo}}{2}\ln\left(\frac{D_{ci}}{D_{fo}}\right)} \tag{3-10}$$

where k_{LM} is the liquid metal thermal conductivity (see Table J.1), D_{fo} is the pellet diameter and D_{ci} is the inner clad diameter[24]. Some interesting comments concerning this atypical solution are presented in Section E1.3. of Appendix E (point "a" of "Other assumptions and considerations").

3.3.2 – Case Hyd-NewCore-5 and Case Hyd-NewCore-ES

Except for the vessel size and the structural constraints used, Case Hyd-NewCore-5 and Case Hyd-NewCore-ES are analyzed in the same way. The geometry range investigated

[24] The conductance calculated with this formula is an optimistic estimate of the actual conductance of the fuel-clad gap. In fact, it has been experimentally demonstrated ([28]) that the contact resistance across the interfaces with the fuel and with the clad causes the gap conductance to drop significantly.

in the analysis is the same as for the cases described in Section 3.3.1, i.e. $0.6 \leq D \leq 1.6$ cm and $1.1 \leq P/D \leq 1.6$. However, as specified in Section 2.1, the approach used for the "NewCore" cases implies the bundle matrix n to be no longer identified univocally by the choice of the rod pitch P. For this reason, besides D and P, n was also preventively subjected to the choice of a variation range to enter in VAMPIRE as input data. This range[25] was $8 \leq n \leq 20$.

Before presenting the list of the assumptions made for the NewCore cases, we describe the two most important features that make the NewCore approach so different from the Backfit approach: the algorithms aimed at constructing the core given P and n as input data, and the methodology used to couple a single matrix index n to each D-P/D pair.

Core construction algorithms

The core construction procedure computes first the number of rows of bundles contained in 1/8th of the core by means of the relation:

$$R_{1/8th} = floor\left(\frac{H_{core}}{nP + P - D + 2t + t_{gap}}\right) \tag{3-11}$$

where "*floor*" is a function that rounds down the term in brackets to the lower integer, H_{core} has the physical meaning shown in Figure 3.6, t is the bundle wall thickness (equal to ~2.54 mm for the bundle reproducing the GE11 design (from Figure 1.2), 3.048 mm for that reproducing the GE14 design ([8])), and t_{gap} is the width of the gap that separates adjacent bundles. Since hydride cores do not need bypass channels for control rod insertion, t_{gap} is very small but sufficient to allow insertion and withdrawn of the fuel channels themselves. The present analysis optimistically assumes such a gap to be 2 mm thick.

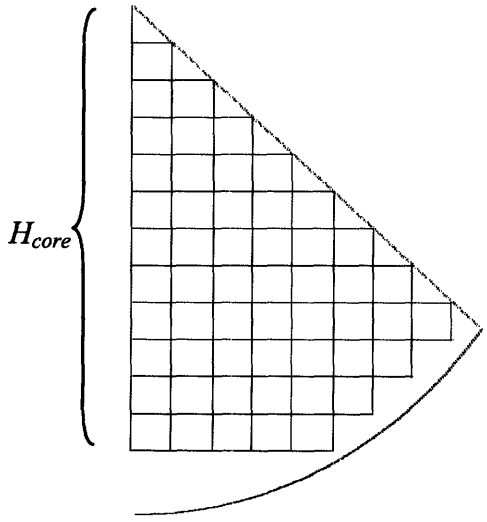

Figure 3.6: Geometric Meaning of H_{core}

[25] Although fuel matrixes larger than 12×12 are not typical for BWRs, the unexplored nature of the hydride cores allows considering matrixes typical of the PWR technology. Current and future bundle designs are abundantly enveloped within this range.

H_{core} varies with the type of vessel in which the hydride core is assumed to be loaded. While for Case Hyd-NewCore-5 this parameter is equal to H_{core} of the reference BWR/5 Oxide Core[26] ($H_{core}^{ref\_BWR/5}$ = 2.278 m), for Case Hyd-NewCore-ES a larger space is available. In fact, the larger size of the ESBWR vessel (D_{ESBWR} = 7.061 m ([8]) versus $D_{BWR/5}$ = 6.3754 m ([11])) allows $H_{core}^{ref\_ESBWR}$ to be 2.936 m[27].

Summarizing:

$H_{core} = H_{core}^{ref\_BWR/5}$ = 2.278m for Case Hyd-NewCore-5

$H_{core} = H_{core}^{ref\_ESBWR}$ = 2.936m for Case Hyd-NewCore-ES

Other than to calculate the number of bundle rows contained in 1/8th of the core, equation 3-11 is important since the parity of $R_{1/8th}$ is used to establish how the 1/8th fraction of the core is actually "cut". If $R_{1/8th}$ is an even number, the core will be referred to as even, and if $R_{1/8th}$ is an odd number the core will be referred to as odd. The difference between even and odd cores is evident from Figure 3.7. Each bundle is displayed as a number, which is representative of the fraction of bundle that is actually modeled in the analysis of 1/8th of the core. In particular:

- 1: 1/8th of bundle cut diagonally
- 2: half bundle cut vertically
- 3: half bundle cut diagonally
- 4: whole bundle

---

[26] This value derives from the relation:
$H_{core}^{ref\_BWR/5} = R_{1/8th}^{ref,ox} \cdot l_{bo} + N_{gaps\_1/8th}^{ref,ox} \cdot t_{gap} = 15 \cdot 13.7541 \cdot 10^{-2} + 14.5 \cdot 1.4859 \cdot 10^{-2}$ m, where $R_{1/8th}^{ref,ox}$ is the number of bundle rows in 1/8th of the reference core, l_{bo} is the bundle side length, $N_{gaps\_1/8th}^{ref,ox}$ is the number of intra-assembly gaps and t_{gao} is the corresponding width. The values used for these parameters are from Figure 3.2 and Table 1.2.

[27] Figure 7 of [10] shows the overall ESBWR core layout. Although it does not represent the last version of the core structure, it is useful to calculate (at least approximately) the value assumed by H_{core} for the ESBWR. Using the bundle pitch and the gap thickness provided in Table 1.2 (6.1"and 0.58" respectively), H_{core} can be easily computed as: $H_{core} = 19P_{bundle} - 0.5t_{gap}$ = 115.61" =2.936 m.

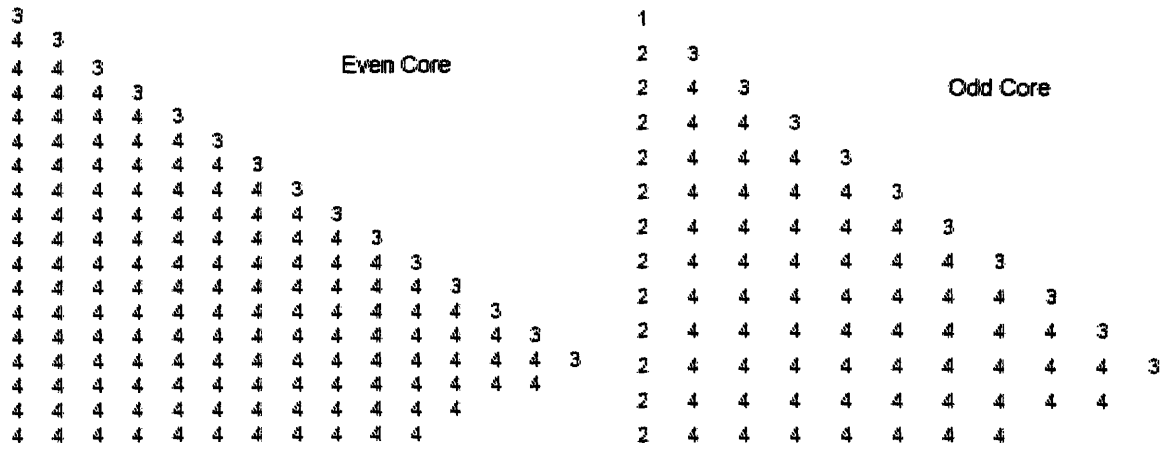

Figure 3.7: Bundle Layout for Even and Odd Cores

Both the core structures shown in Figure 3.7 are BWR/5 Hydride NewCores having the reference BWR/5 *D-P/D* pair. The root cause of the fact that they fall into opposite categories is the size of the fuel matrix adopted. In fact, the even core contains 8×8 bundles, while the odd one contains 11×11 bundles. The larger size of the latter results in a smaller number of bundle rows, i.e. 12.5 versus 18.

The MATLAB algorithm used to construct the core was developed for PWRs, and is described in detail in [6]. It is important to say that, after calculating $R_{1/8th}$ to establish what type of bundle fractions must be used, the bundles are automatically stacked side by side beginning at the center of the core. Each time the algorithm attempts to stack a new bundle, it verifies that such an action does not result in exceeding the available space, which is defined by the core shroud radius (from Table 1.1) and by the number of bundle rows previously calculated by means of equation 3-11.

Algorithm for the choice of the fuel matrix index n to associate to each D-P/D pair

Figure 3.8 shows the typical structure of a BWR Hydride NewCore. Notice that the large bypass channels needed, in the cases examined in Section 3.2 and 3.3, for the cruciform control rod insertion, are no longer present. As a consequence, the overall structure has an evident PWR resemblance, except for the presence of the bundle boxes that eliminate transverse motion of the two-phase coolant. Given a *D-P/D* pair to analyze, the lack of cruciform geometry-fixed control rods together with the experimental nature of this type of core give freedom in changing the bundle width in search of the most suitable one. Such searching implies the need to examine all the fuel matrix indexes n in the interval chosen, i.e. $8 \leq n \leq 20$, and choose the best one.

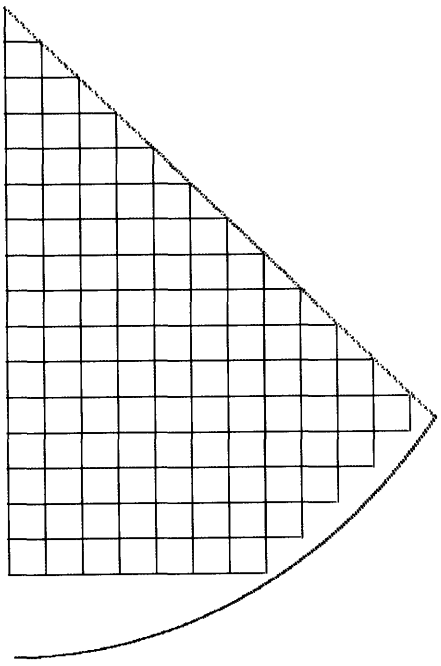

Figure 3.8: "NewCore" Structure

Such a choice is performed through two sequential steps, described as follows.

1) *Comparison to the structural constraints*: each combination of diameter, pitch and matrix index is accepted as long as it does not exceed the limit values chosen for the structural constraints. These limits, i.e. the maximum number of bundles and the maximum bundle weight, were developed in Section 2.2.2 and are summarized in Table 2.4. The core construction algorithm is used to verify that the triplet *D-P-n* under examination does not result in an excessive number of bundles. The core shroud radius, H_{core}, D, n and P are the most important input parameters for this calculation. If the algorithm delivers a total number of bundles larger than the limit fixed, i.e. 1222, the index n is rejected. Conversely, if the bundle number is below the limit, the index n is further checked in order to verify that the bundle weight limit is not exceeded. To do this, it is verified that the rod diameter D and the index n satisfy the inequality shown in Table 2.4. If this does

not occur, the index n is rejected. As already mentioned, Case Hyd-NewCore-ES uses the number of bundles as the only structural constraint. Therefeore, for only this case, the bundle weight verification is not performed.

2) *Maximum power criterion.* Each one of the matrixes surviving the previous selection is then subject to a complete core thermal-hydraulic analysis. The matrix leading to the maximum power is chosen as the best matrix for the pair *D-P/D* under examination. Should different matrixes lead to the same power, the code chooses the one with the smaller index n.

Besides those described in Section 3.1, the following are the assumptions and specifications referred to Case Hyd-NewCore-5 and to Case Hyd-NewCore-ES. Even though they usually apply to both, whenever the two cases tend to differ from each other, this will be clearly highlighted. The assumption classification is consistent with the category nomenclature presented in Section 2.1. If no specific assumptions are made for a given category, the category is not displayed.

Core structure assumptions

a) The 2-mm thick bypass channels that separate adjacent bundles is neglected, i.e. it is not modeled, and all the coolant is assumed to flow through the fuel bundles.

Bundle structure assumptions

a) Once D is entered as input, the scaling relations used to calculate the thickness of the clad and the width of the fuel-clad gap are the same as those used for Case Hyd-Backfit-5. Both derive from [27] and are presented in Section E1.3. of Appendix E (see point "b" of "Bundle structure assumptions").

b) All the fuel bundles contain a certain number of control rod guide tubes, located in some of the positions of the $n \times n$ grid. The guide tube location criterion is different depending whether the matrix is odd or even numbered, as shown in Figure 3.9. In particular, if n is odd, a control rod is placed in the middle of the bundle. If n is even, four control rods are placed equidistant from one another in the center of the bundle.

In both cases, control rods are vertically and horizontally separated by two fuel rods. The algorithm used for their arrangement was developed for PWRs by Malen ([6]).

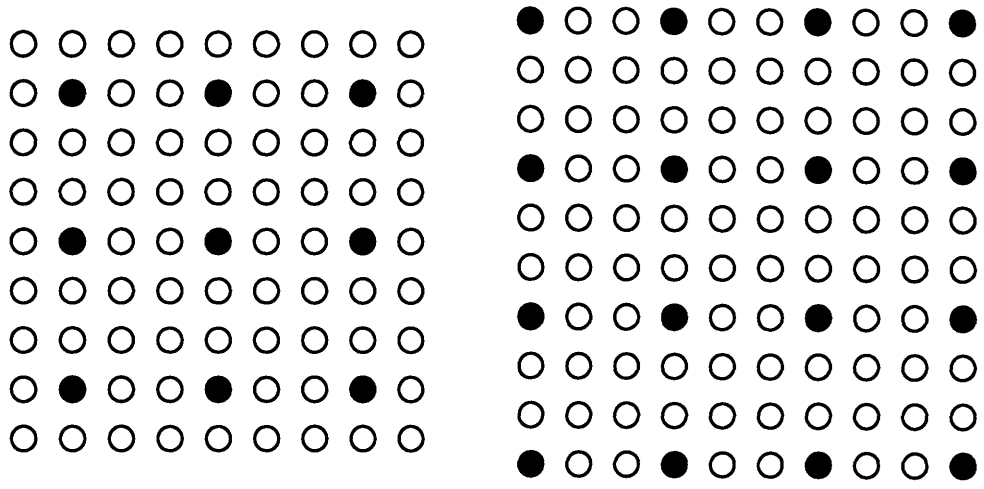

Sample assembly with an odd number of rods per side (9x9)

Sample assembly with an even number of rods per side (10x10)

● control rod guide tube

○ fuel rod

Figure 3.9: Control Guide Tube Locations for Odd and Even Matrix Index ([6])

The diameter of the control guide tubes is calculated by means of the same scaling relation used by Malen in [6]. Such a relation expresses the guide tube outer diameter D_{guide_tube} as a function of the rod pitch P:

$$D_{guide\_tube} = \left[\left(\frac{D_{guide\_tube}}{P}\right)_{ref[5]}\right] P = \left(\frac{12.24}{12.60}\right) P \qquad (3\text{-}12)$$

The term in brackets is the ratio between the guide tube diameter and the rod pitch of the PWR bundle used in [6] as reference, i.e. 12.24 and 12.60 mm respectively.

It is important to stress that, because of the wide variation range analyzed for D and P, the number and location of the control rods is not the result of a bundle optimization from the neutronic point of view. It has been demonstrated ([2]) that an accurate optimization of a hydride 10×10 bundle would result in the use of only 4 control rods, versus the 16 control rods that the mentioned algorithm "inserts" into a

10×10 bundle. For this reason, the maximum achievable power that VAMPIRE delivers for the NewCore cases can be defined as a conservative estimate of the power potentially achievable.

Pressure drop assumptions

a) Both Case Hyd-NewCore-5 and Case Hyd-NewCore-ES do not model any inlet orificing. Regarding the bypass channels, such an assumption is reasonable since the cores examined do not contain large bypass channels like those modeled in the "Backfit" cases, and therefore all the coolant flows spontaneously through the bundles without the need to occlude some paths. Instead, the choice of not modeling any bundle orificing was primarily driven by the simplified core radial power profile assumed for the "NewCore" cases (see next "Power distribution assumptions"). In fact, the flat power profile assumed does not require a model for unequal flow splitting among the bundles.

b) Except for the inlet orificing, the type and location of the form losses modeled are the same as those used in Case 0 (VIPRE Core Modeling Validation). In particular, Case Hyd-NewCore-5 adopts those of the reference BWR/5 core, while Case Hyd-NewCore-ES those of the reference ESBWR. However, the numerical values of the form losses differ, since they are function of the bundle active flow area. The analytical relation between the form loss coefficient and the bundle flow area is common to all the other cases analyzed, and is described in detail in Section E1.2. of Appendix E (point "a" of "Pressure drop assumptions").

c) Since the 2-mm thick bypass channels that separate adjacent bundles are not modeled, the core pressure drop is uniquely due to the fuel bundles.

Coolant flow assumptions

a) In agreement with the procedure used for all the cases, core power and coolant flow rate are constrained by keeping their ratio constant and equal to the values listed in Table 2.3 ($\dot{Q}_{core} / \dot{m}$ = 243.07 kW/(kg/s) for Case Hyd-NewCore-5, $\dot{Q}_{core} / \dot{m}$ = 449.87 kW/(kg/s) for Case Hyd-NewCore-ES). Thus, the coolant flow can be interpreted as a

consequence of the core power which is iteratively entered as input value to verify that the power constraints are respected (see Figure 1.1).

Power distribution assumptions

a) The core axial power distribution used in Case Hyd-NewCore-5 reflect that used for the reference BWR/5 in Case 0 (VIPRE Core Modeling Validation). Likewise, the axial power profile used for Case Hyd-NewCore-ES is that of the reference ESBWR. Figure 3.3 shows such power distributions.

b) The radial power distribution is modeled in a very simplified way: the only bundle which has a non-unity peaking factor is the hot bundle, located at the centre of the core, for which the peaking factor is equal to 1.51 and 1.29 in Case Hyd-NewCore-5 and Case Hyd-NewCore-ES respectively. These peaking factors are the same as the maximum radial peaking factors of the two reference cores. The reason of such a simplification lies in the difficulty of creating a computational model able to correctly assign different peaking factors to bundles which are part of a core having an un-predefined structure. In fact, contrary to the "Backfit" cores for which the number of bundles is constant regardless of the *D-P/D* pair under examination, the "NewCores" have a structure strongly dependent on the lattice parameters. The number, size and location of the bundles are automatically generated by VAMPIRE once D and P are provided as input data.

Other assumptions and considerations

a) In agreement with all the cases modeling a hydride fueled core, the gap that separates the hydride fuel from the cladding is assumed to be filled with a liquid metal. The gap conductance, a function of the gap thickness, is calculated as in Case Hyd-Backfit-5. Some comments concerning this atypical solution are presented in Section E1.3 of Appendix E (point "a" of "Other assumption and considerations").

Chapter 4: Results

Results are presented in the form of maps, showing the dependence of various thermal-hydraulic parameters on the bundle geometry configuration, i.e. *D* and *P/D*.

4.1 – Case Ox-Backfit-5

4.1.1 – Achievable Power

The most interesting result is the maximum achievable power for each geometrical configuration analyzed, which is shown in Figure 4.1 for the two pressure drop limits adopted.

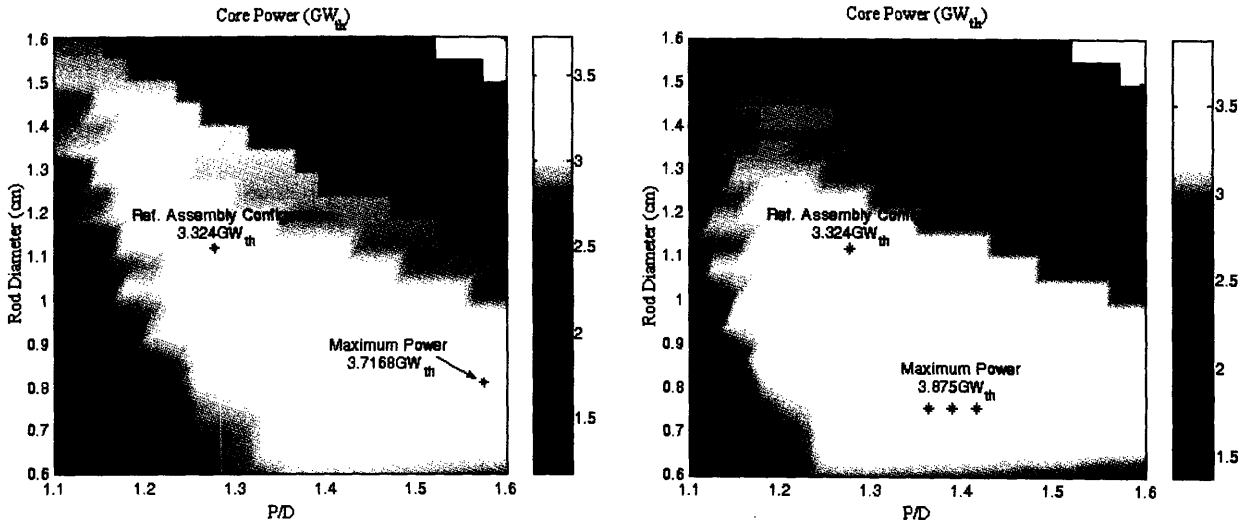

Figure 4.1: Case Ox-Backfit-5 Powermaps (Left: Δp_{limit} = 24.5 psia; Right: Δp_{limit} =36 psia)

Observations from the maps are as follows.

a) The assembly configurations characterized by small rod diameter (0.7 $\leq D \leq$0.9 cm) and medium-large pitch (1.3 $\leq P/D \leq$ 1.6) yield the highest power levels. In particular, the maximum powers are 3717 MW_t and 3875 MW_t for the lower and upper pressure drop limit respectively. Such values are 12% and 16.5% higher than the reference[28] core power (3324 MW_t).

[28] Although the MCPR limit has been established by means of a reverse engineering analysis of the reference BWR/5 core, the maximum achievable power predicted by VAMPIRE for the reference *D-P/D* pair, 3324 MW_t, does not match exactly the reference value shown in Table 1.1, i.e. 3323 MW_t. Such a

b) The possibility to achieve higher power levels in the lower part of the maps is due to a larger number of fuel rods, and is easily verifiable from Figure 4.2 and Figure 4.3. These figures compare the power, the Linear Heat Generation Rate (LHGR) and the number of fuel rods of the core configurations examined with those of the reference BWR/5. In particular, the lines appearing in the first three plots, called "unity lines", divide the maps in two regions: that characterized by a ratio larger than one, and that with a ratio below unity. The last plot, which derives from the superposition of the previous three, shows the location of the high power region[29] with respect to the unity lines corresponding to the LHGR and to the number of fuel rods. Even though the high power core configurations are almost equally distributed above and below these unity lines, the core configurations yielding the overall maximum power are located where the ratio between the number of fuel rods is larger than 1. This is particularly evident from comparison of Figure 4.3 to Figure 4.2 since the lower pressure drop limit of adopted in Figure 4.2 causes these configuration to be shifted to the right. Therefore, the contribution given by a very large number of rods is even more significant than that deriving from the combination of a larger number of rods AND a higher LHGR that characterizes the narrow region included between the two unity lines of subplots b) and c), i.e. the maximum power is not located in this narrow region. The fuel matrix size n, which determines the number of fuel rods in the core, is presented in Figure 4.5.

c) The assembly configurations having very small rod diameter are not included in the high power region. This happens because the reduced diameter makes the rods less stiff and therefore the vibrational motions tend to be significant and limit the power.

d) The lack of data in the blank portion of the map is not a concern since the high power region is not located within this portion of the graph[30].

---

negligible difference is simply due to the 0.1% margin allowed in matching the limit values chosen for the thermal hydraulic constraints (see algorithm in Figure 1.1).

[29] In plot a), the region enclosed by the black unity line is called "high power region" since it contains all the core configurations delivering powers higher than the reference oxide core.

[30] This blank region is a consequence of the inability of VAMPIRE to resolve the core configurations characterized by very large rod pitch. This is not due to the pitch itself, but to the particular combination of bundle and bypass orificing coefficients characterizing such core configurations. In fact, as specified in Section 3.3.1, the bypass channel orificing coefficient is a function of the rod pitch, and tends to decrease

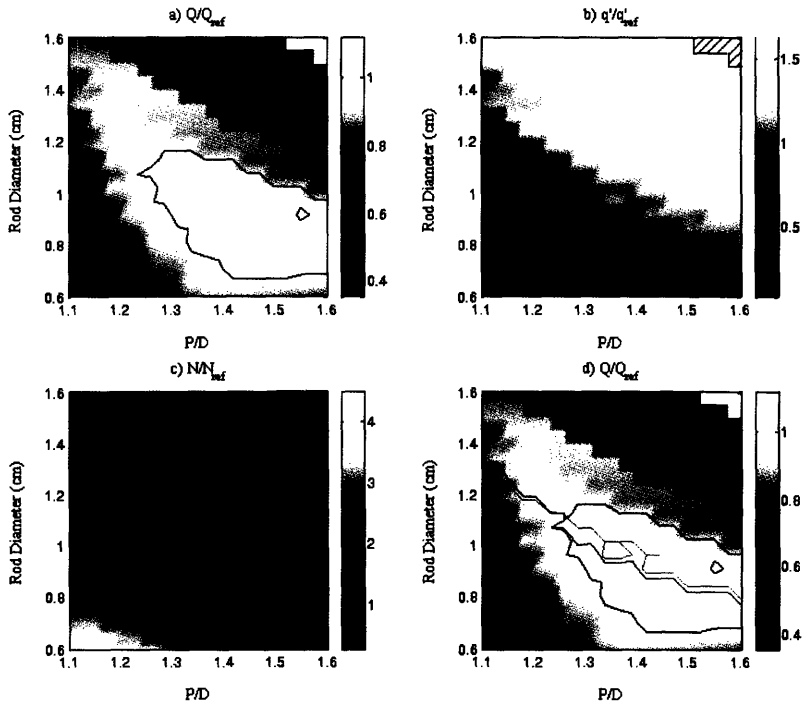

Figure 4.2: Case Ox-Backfit-5 (Δp_{limit} = 24.5 psia): Power, LHGR and Number of Rod Ratios Between the Examined Oxide Core Configurations and the Reference BWR/5 Core
(the lines represent unity ratios)

---

as the pitch increases. Thus, the mentioned core configurations have very low orificied bypass channels. At the same time, the orificing coefficient for the bundles is quite large, since it is a crescent function of the bundle flow area and the bundles having the largest *P/D* also have large active flow area. In such a situation, VIPRE is able to find an analytical solution, i.e. the flow rate split among all the channels that leads to a uniform pressure drop, only if the total flow rate is above a certain value. Because of the relation existing between power and flow rate (power/flow rate = constant), an analytical solution exists only if the core power is above a certain power level. However, for the top-right hand corner core configurations, the power levels which would allow VIPRE to find a solution yield output parameters that exceed the thermal hydraulic constraints, and therefore are automatically reduced. Such a reduction results in trial power levels below the minimum power for which a solution exists, and therefore no solution is provided for these core configurations. However, while no thermal-hydraulic parameters are available for such core configurations, their geometric structure is known. For this reason, plot c) of Figure 4.2 and Figure 4.3, as well as Figure 4.5 do not show any blank region.

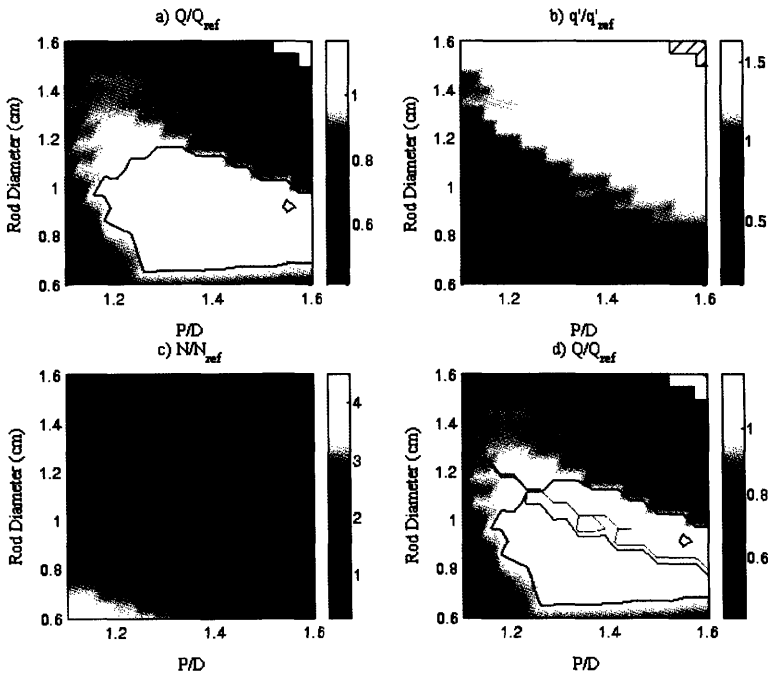

Figure 4.3: Case Ox-Backfit-5 (Δp_{limit} = 36 psia): Power, LHGR and Number of Rod Ratios Between the Examined Oxide Core Configurations and the Reference BWR/5 Core
(the lines represent unity ratios)

From plot b) of Figure 4.3 it can be noticed that the unity line diagonally cuts the plot area. Since the MCPR is the limiting parameter in the central region of the map (see Figure 4.8), this means that only the assembly configurations located above the unity line have better thermal performance than the reference assembly configuration, i.e. a higher LHGR. This can be analytically demonstrated using some simple heat balance relations, referred to the hot bundle, as shown in Appendix F. In this Appendix it is demonstrated that the LHGR variation with assembly geometry is dominated by pitch, although a slight influence is also exerted by the difference in coolant flow rate. Thus, from the thermal viewpoint, assembly geometries having rods well spaced from each other are preferable.

The coolant flow rates corresponding to Case Ox-Backfit-5 with Δp_{limit}= 36 psia (right plot of Figure 4.1) are very far from exceeding the flow rate limit of 25875 kg/s mentioned at the end of Section 2.2.1. In particular, the maximum flow rate examined, 15941 kg/s, is about 62% of this limit, as shown in Figure 4.4.

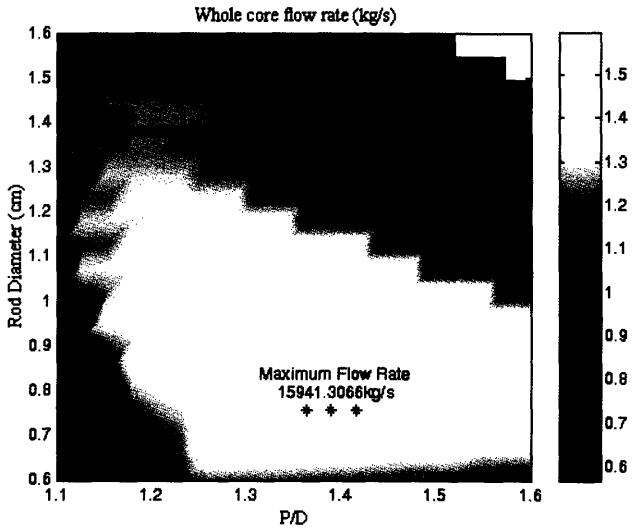

Figure 4.4: Whole Core Flow Rate (Case Ox-Backfit-5, Δp_{limit} = 36 psia)

4.1.2 – Fuel Matrix

Figure 4.5 presents the matrix characterizing each of the 400 assembly configurations analyzed. For the case of the lower pressure drop limit, the *D-P/D* pair yielding the maximum power is coupled with a 10×10 matrix. Instead, for the upper pressure drop limit, the three assembly configurations yielding the maximum power have a 12×12 matrix. It can be noticed that the high power region (enclosed in the black line, i.e. where the power is higher than the reference value of 3323 MW_t) corresponds to fuel matrixes in the range from 8×8 to 15×15. This wide range encompasses typical BWR fuel matrixes as well as geometries having higher index *n*, consistent with the tendency in current practice to increase the number of fuel rods per assembly in order to reduce the LHGR.

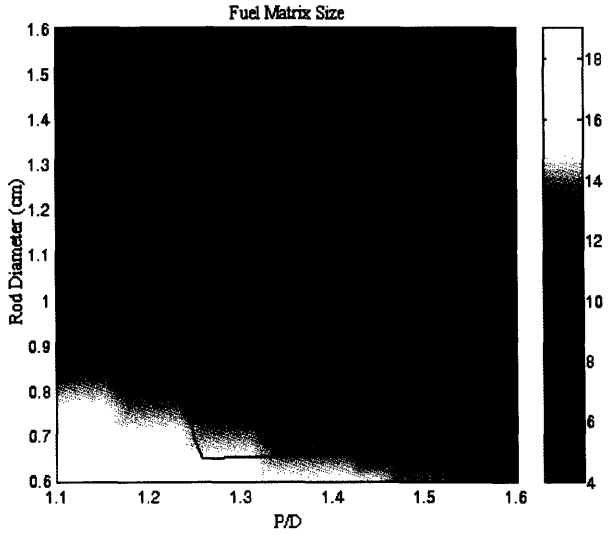

Figure 4.5: Fuel Matrix ($n \times n$) Size (Case Ox-Backfit-5)
(the colored scale indicates the matrix index n; upper green line: n=7, lower green line: n=12; black line: high power region for the case of Δp_{limit} = 36 psia)

4.1.3 – Constraints on Achievable Power

Figure 4.6 and Figure 4.7 show[31] that although six constraints have been applied in the analysis, only four are actually limiting. The fuel centerline and the clad surface temperature are always below the corresponding limit values. The core configurations whose power is limited by the MCPR are located within a broad band that runs along the map diagonal; the average fuel temperature and the core pressure drop exert a limiting effect for medium-large D and P/D and for medium-small D and P/D respectively; the vibration ratio limits the power for configurations having small rod diameter (< 0.75 cm) and medium-large P/D. Such areas of influence are shown clearly in Figure 4.8.

[31] The plots of Figure 4.6 and Figure 4.7 show the value of the thermal hydraulic constraints over the whole geometry range. The procedure followed to construct these plots is such that wherever the constraint is limiting the plot appears white.

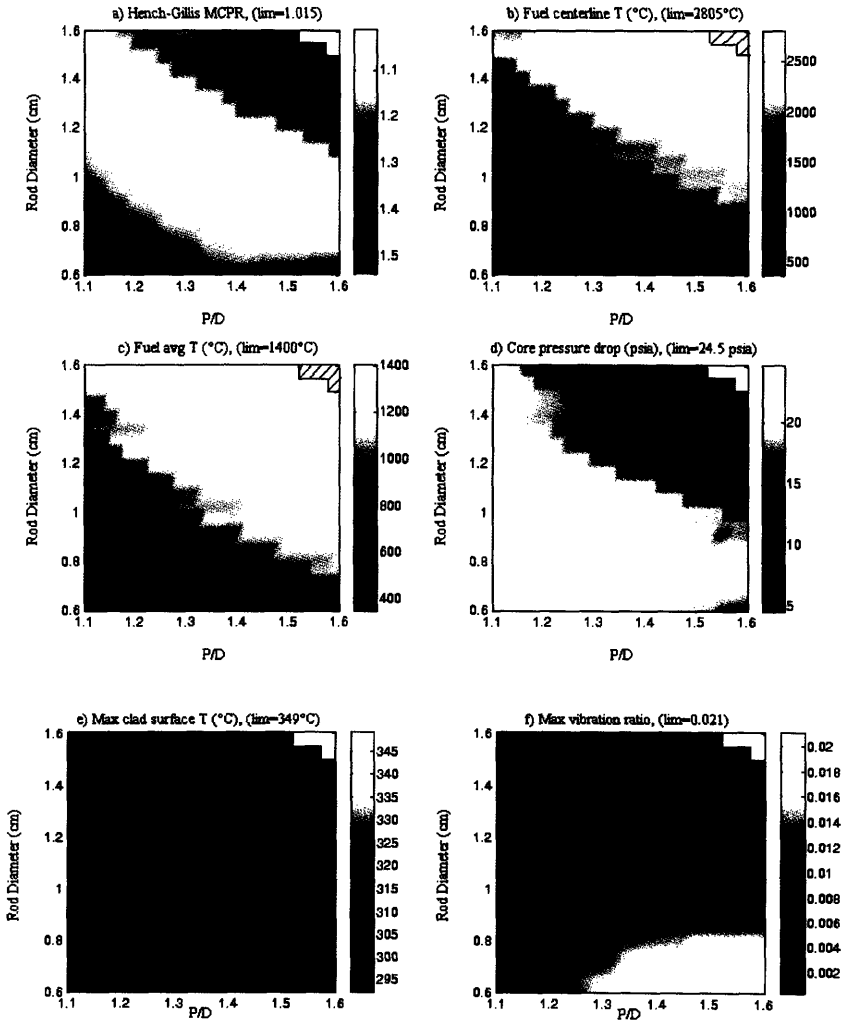

Figure 4.6: Limiting Effect Exerted by Constraints (Case Ox-Backfit-5, Δp_{limit} = 24.5 psia)

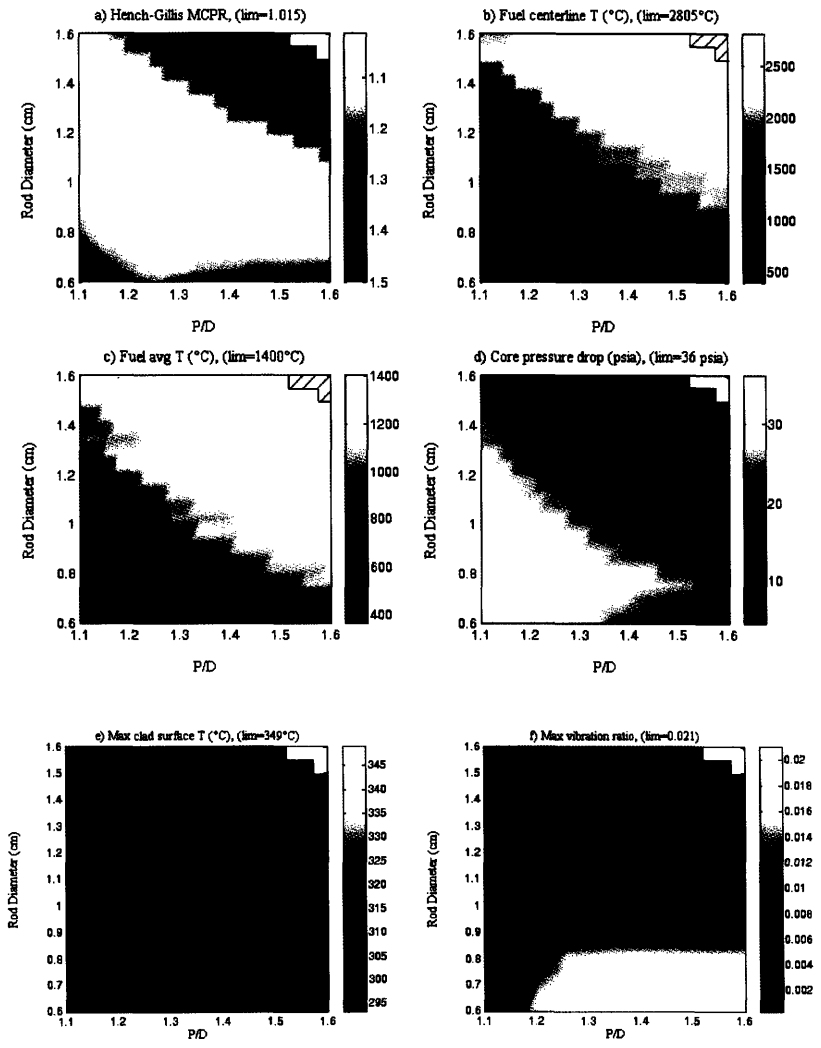

Figure 4.7: Limiting Effect Exerted by Constraints (Case Ox-Backfit-5, Δp_{limit} = 36 psia)

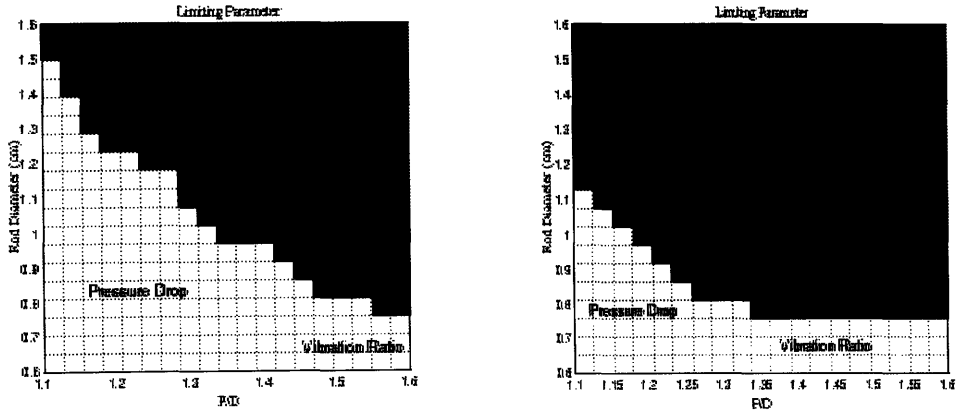

Figure 4.8: Influence Areas of the Limiting Constraints (Case Ox-Backfit-5. Left: Δp_{limit} = 24.5 psia; Right: Δp_{limit} = 36 psia)

4.1.4 – Quality and Bypass Flow

While the results presented so far were focused on the maximum achievable power and on the influence exerted by the related parameters, the following maps show the variation of some important thermal-hydraulic parameters for the various configurations analyzed. Although two are the pressure drop limits adopted, all the maps presented below refer to the upper limit, i.e. 36 psia. This is justified by the fact that this type of map is qualitatively similar regardless of the pressure drop limit applied. Figure 4.9 shows the core average exit quality, bundle average exit quality and hot bundle exit quality. Although the geometry range over which the analysis was performed is quite large, these parameters assume reasonable values for most configurations. This is a consequence of the constraint applied to the relation between power and flow rate, i.e. power/flow = constant, and to the control of the bypass channel orificing coefficients which, for most configurations, prevents the bypass flow percentage from falling outside the range 8-12%. Most of the configurations have core average exit quality around 14%, bundle average exit quality between 15.5% to 17%, and hot bundle exit quality between 26% to 30%. The continuous lines in the second and third plot of Figure 4.9 correspond to 17% and 30% quality respectively.

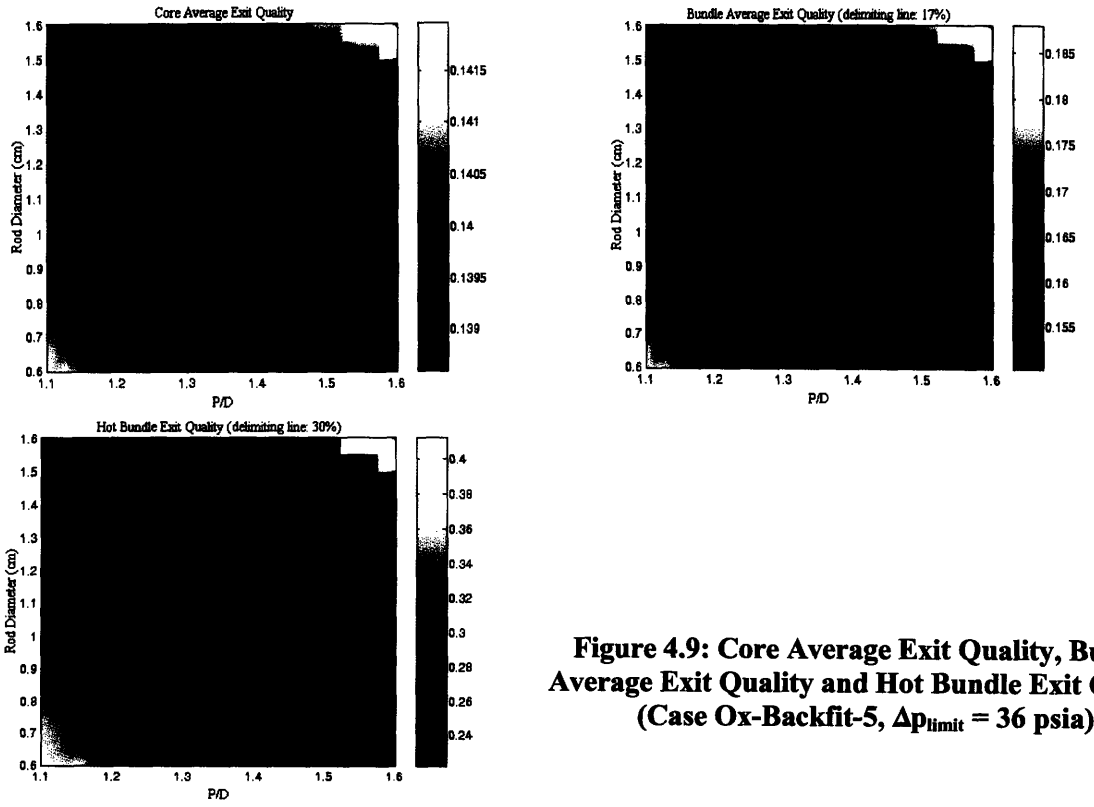

Figure 4.9: Core Average Exit Quality, Bundle Average Exit Quality and Hot Bundle Exit Quality (Case Ox-Backfit-5, Δp_{limit} = 36 psia)

However, it can be noticed that the pressure limited region shown in Figure 4.7, i.e. small-medium *D* and *P/D*, is characterized by higher quality. This is due to the bypass flow percentage which is larger than the value used as reference, i.e. 10%. In spite of this localized effect, the methodology used to vary the orificing coefficients for bundles and bypass channels gives good results since the most interesting portion of the map, i.e. the central region, is characterized by bypass flow percentages close to the reference value. This is clearly shown in Figure 4.10.

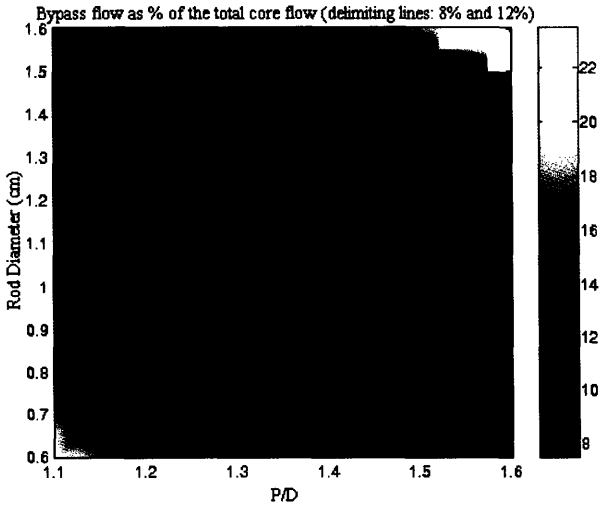

Figure 4.10: Bypass Flow Percentage (Case Ox-Backfit-5, Δp_{limit} = 36 psia)

4.2 – Case Hyd-Backfit-5

4.2.1 – Achievable Power

The maximum power achievable by the various core configurations is shown in Figure 4.11 for the two pressure drop limits, i.e. Δp_{limit} = 24.5 psia and Δp_{limit} = 36 psia.

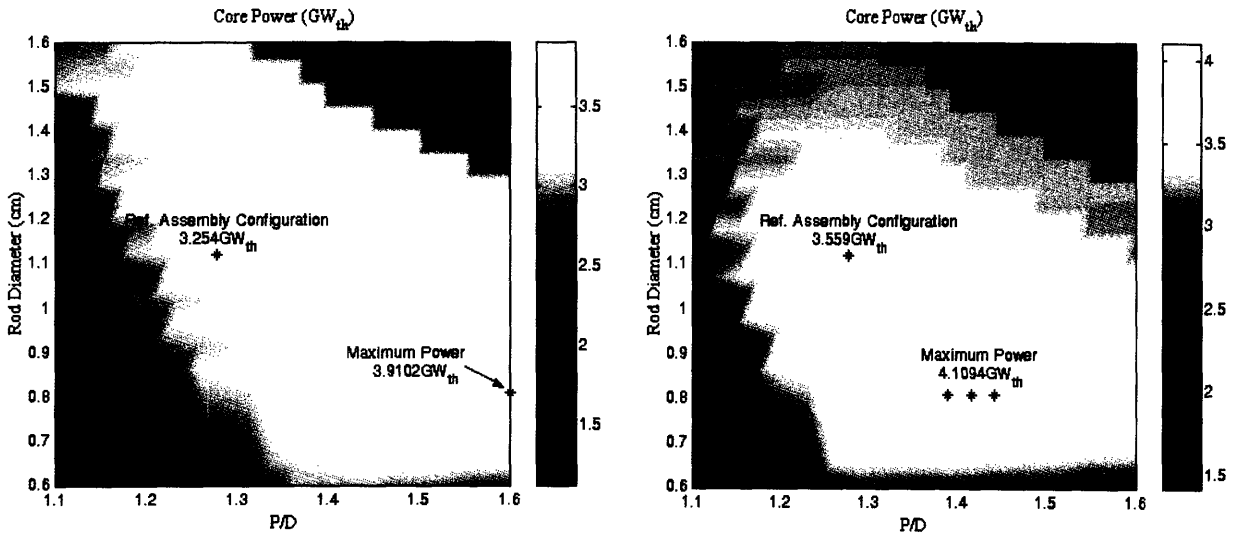

Figure 4.11: Case Hyd-Backfit-5 Powermap (Left: Δp_{limit} = 24.5 psia; Right: Δp_{limit} = 36 psia)

Observations from the maps are as follows.

a) When the pressure drop limit is fixed at 24.5 psia, the hydride core configuration characterized by the reference *D-P/D* pair delivers 2% less power than the same configuration fueled with oxide, i.e. 3254 MW_t versus 3324 MW_t. This is due to the larger number of rods contained in the hydride bundle, i.e. 81 versus 76, which yields a slightly larger pressure drop which impinges the 24.5 pressure drop limit. However, if the pressure drop limit is set to the upper value, for the reference *D-P/D* pair the use of hydride fuel results in a maximum achievable power of 3559 MW_t, which is 7% higher than the power delivered by the reference oxide core (3324 MW_t).

b) The overall maximum power achievable by a hydride backfit configuration is equal to 3910 MW_t and 4109 MW_t for the lower and upper pressure drop limit respectively. Such values correspond to a gain in power of 17.6% and 23.6% with respect to the power delivered by the reference oxide core (3324 MW_t), and of 20.2% and 15.4%

respectively if the power used as reference is that corresponding to the reference *D-P/D* fueled with hydride.

c) As found in the analysis of Case Ox-Backfit-5, the core configurations yielding the maximum power are characterized by small rod diameter and medium-large *P/D*. Again, this is the result of the larger number of rods that characterize such core configurations. This is proved by plot d) of Figure 4.12 and is even more evident in plot d) of Figure 4.13. They show that the core configurations yielding the maximum power are located where the ratio between the number of fuel rods is above unity, while the LHGR ratio is around or less than 1.

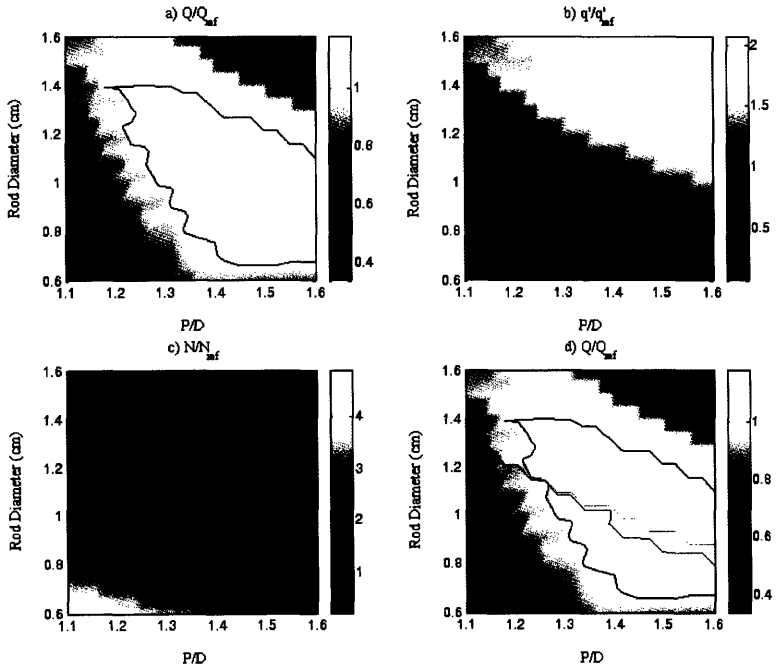

Figure 4.12: Case Hyd-Backfit-5 (Δp_{limit} = 24.5 psia): Power, LHGR and Number of Rod Ratios Between the Examined Hydride Core Configurations and the Reference BWR/5 Oxide Core (the lines represent unity ratios)

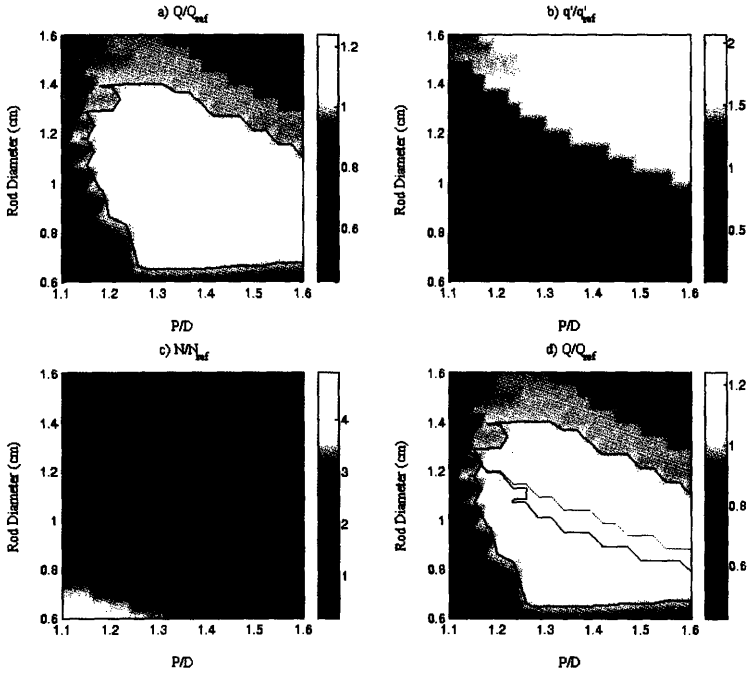

Figure 4.13: Case Hyd-Backfit-5 (Δp_{limit} = 36 psia): Power, LHGR and Number of Rod Ratios Between the Examined Hydride Core Configurations and the Reference BWR/5 Oxide Core (the lines represent unity ratios)

The coolant flow rates corresponding to Case Hyd-Backfit-5 with Δp_{limit}= 36 psia (right plot of Figure 4.11) are shown in Figure 4.14. They do not exceed the flow rate limit of 25875 kg/s mentioned at the end of Section 2.2.1. In particular, the maximum flow rate examined is 16905 kg/s, which is about 65% of this limit.

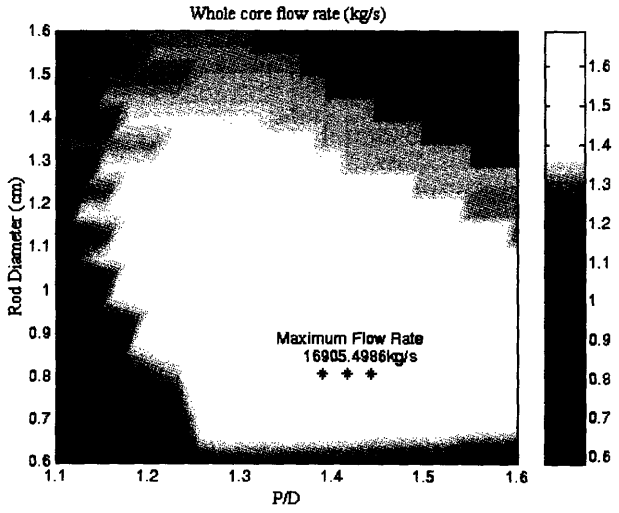

Figure 4.14: Whole Core Flow Rate (Case Hyd-Backfit-5, Δp_{limit} = 36 psia)

4.2.2 – Fuel Matrix

Because of the backfit structure of the core, the fuel matrix size $n \times n$ associated with each *D-P/D* pair is the same as that corresponding to Case Ox-Backfit-5 (see Figure 4.5). In this case, however, the high power region includes a broader range of fuel lattices, i.e. from 7×7 to 15×15, as shown in Figure 4.15. For the case of the lower pressure drop limit adopted, the *D-P/D* pair yielding the maximum power is coupled with a 9×9 matrix. Instead, for the upper pressure drop limit, the three assembly configurations yielding the maximum power have an 11×11 matrix.

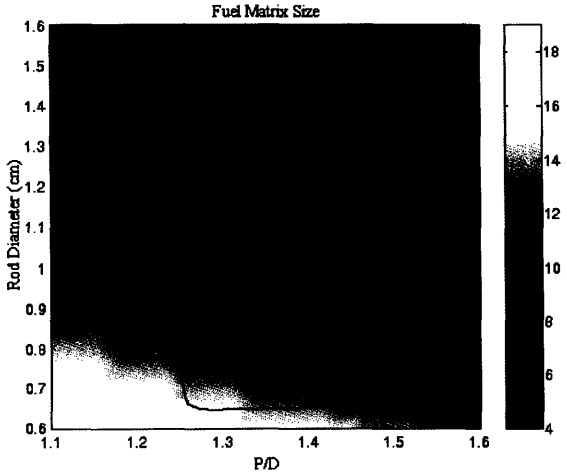

Figure 4.15: Fuel Matrix ($n \times n$) Size (Case Hyd-Backfit-5)
(the colored scale indicates the matrix index n; upper green line: n=7, lower green line: n=12; black line: high power region for the case of Δp_{limit} = 36 psia)

4.2.3 – Constraints on Achievable Power

The values of the thermal hydraulic constraints for the various core configurations examined are shown in Figure 4.16 and Figure 4.17 for the two pressure drop limits adopted. As for Case Ox-Backfit-5, the clad temperature is never limiting. Conversely, all the remaining constraints including now the maximum fuel temperature are somewhere limiting, and the relative areas of influence are shown in Figure 4.18. Recall there is no constraint applied to hydride fuel on average temperature.

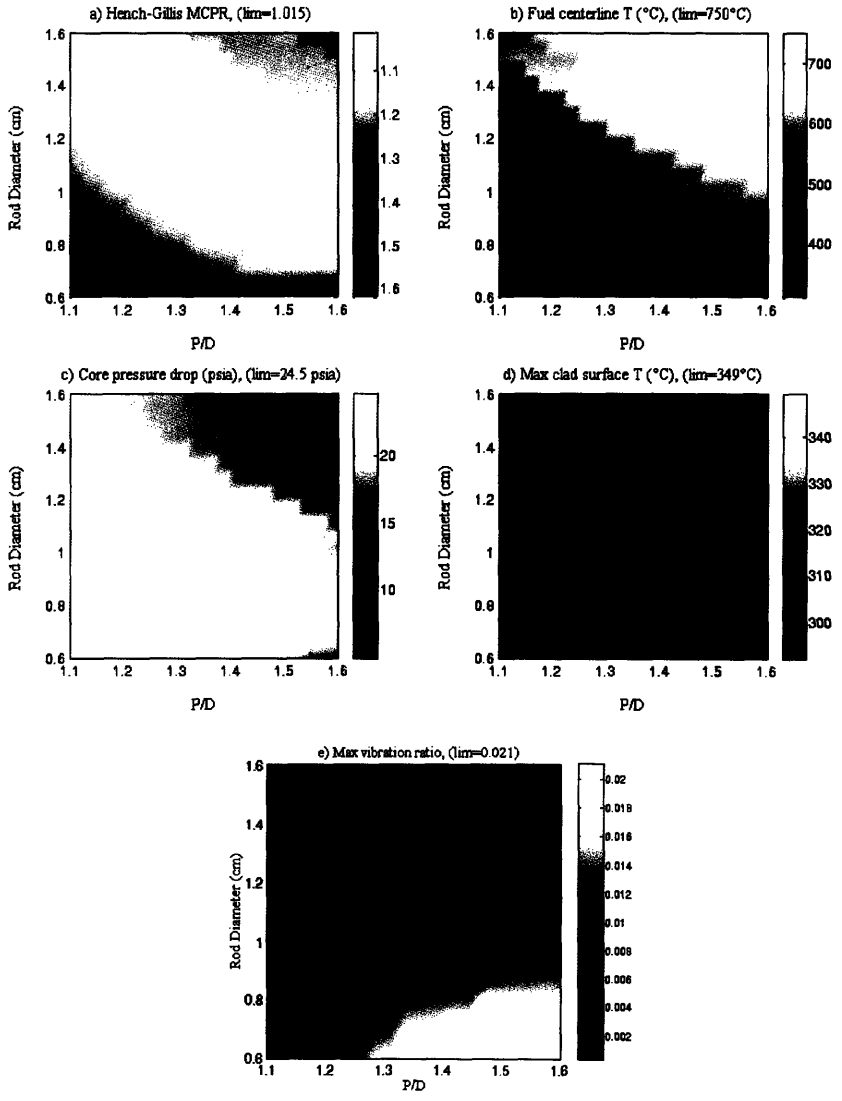

Figure 4.16: Limiting Effect Exerted by Constraints (Case Hyd-Backfit-5, Δp_{limit} = 24.5 psia)

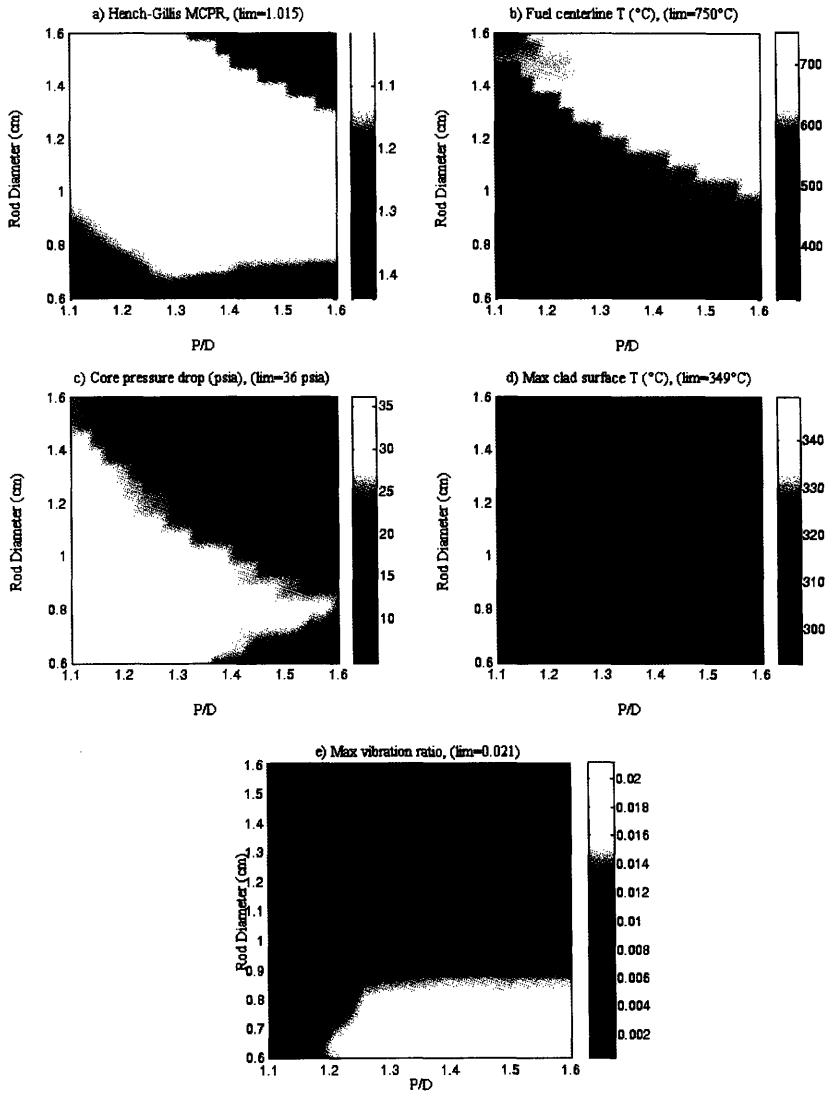

Figure 4.17: Limiting Effect Exerted by Constraints (Case Hyd-Backfit-5, Δp_{limit} = 36 psia)

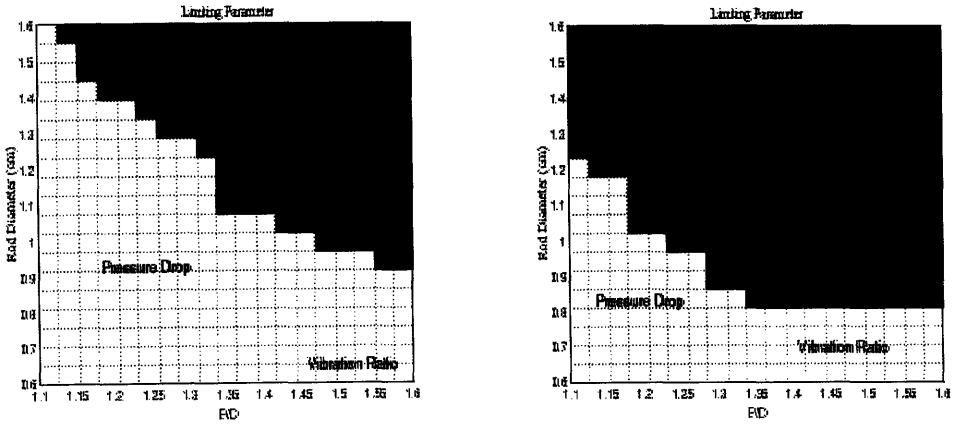

Figure 4.18: Areas of Influence of the Limiting Constraints (Case Hyd-Backfit-5. Left: Δp_{limit} = 24.5 psia; right: Δp_{limit} = 36 psia)

4.2.4 – Quality and Bypass Flow

As for Case Ox-Backfit-5, the steam qualities at the core exit assume reasonable values for most of the configurations examined. In particular, for both pressure drop limits, the core average exit quality is around 13.5%, the bundle average exit quality between 14.5% and 16%, and the hot bundle exit quality between 23% and 30%. Again, this is due both to the relation existing between power and flow, i.e. power/flow = constant, and to the control of the bypass channel orificing coefficients which prevents the percentage of coolant flowing through the bypass channels to be outside the range 8-12%, as shown in Figure 4.19.

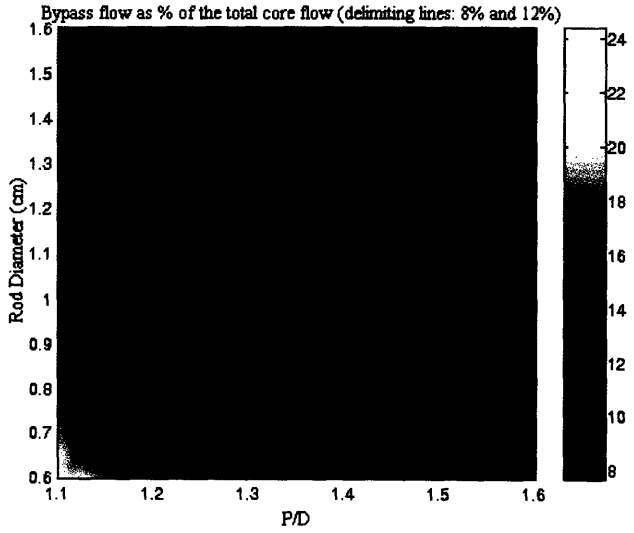

Figure 4.19: Bypass Flow Percentage (Case Hyd-Backfit-5; Δp_{limit} = 36 psia)

4.3 – Case Hyd-NewCore-5

4.3.1 – Achievable Power

The maximum achievable power as a function of the rod diameter and pitch is shown in Figure 4.20 for both the pressure drop limits adopted.

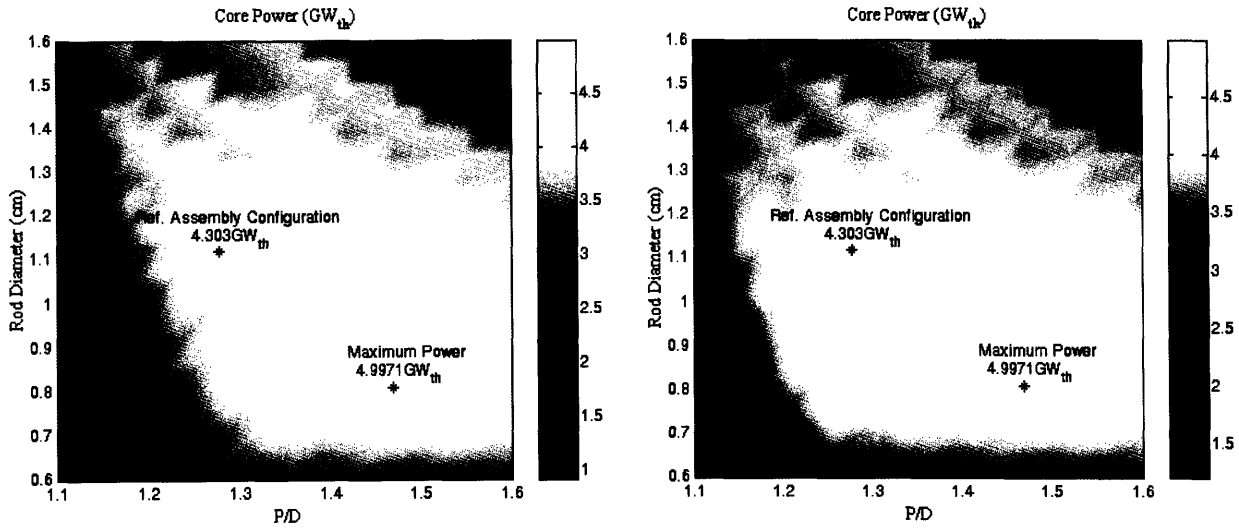

Figure 4.20: Case Hyd-NewCore-5 Powermaps (Left: Δplimit =24.5 psia; Right: Δplimit = 36 psia)

Observations from the maps are as follows.

a) The maximum achievable power of most of the core configurations is the same regardless of the pressure drop limit applied.

b) The ratio between the power of the hydride new core configurations and the reference oxide core power (3323 MW_t) is above unity almost everywhere in the powermap. As is also evident from plot a) of Figure 4.21 and Figure 4.22, the maximum achievable power delivered by the core configuration characterized by the reference *D-P/D* pair is 29% higher than that of the reference oxide core, i.e. 4303 MW_t versus 3323 MW_t, while the highest power, 4997 MW_t, is even 50% higher.

c) The geometrical configurations which lead to the highest power levels have small-medium diameter (although > 0.75 cm) and medium-large *P/D*.

d) With respect to the reference BWR/5 oxide core, the larger number of fuel rods is the reason of the high power achieved by the configurations mentioned at point c). As

observed for all the previous cases, here it is even more evident that the contribution given by a very large number of rods dominates over a larger number of rods and a larger LHGR occurring simultaneously, i.e. the highest power levels are not located between the two unity lines in the last plot of Figure 4.21 and Figure 4.22, but below the LHGR ratio unity line.

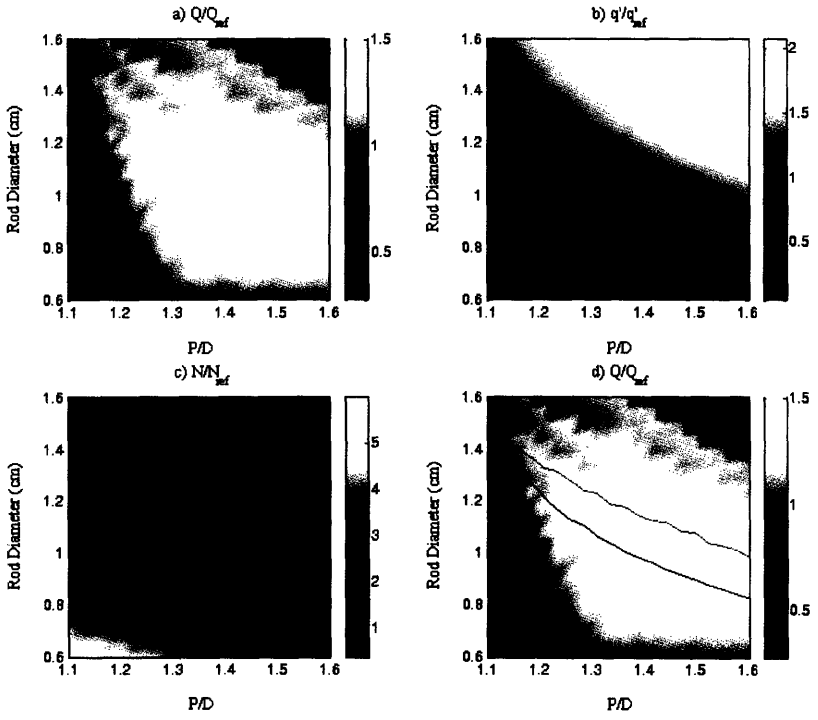

Figure 4.21: Case Hyd-NewCore-5 (Δp_{limit} = 24.5 psia): Power, LHGR and Number of Rod Ratios Between the Examined Hydride Core Configurations and the Reference BWR/5 Core
(the lines represent unity ratios)

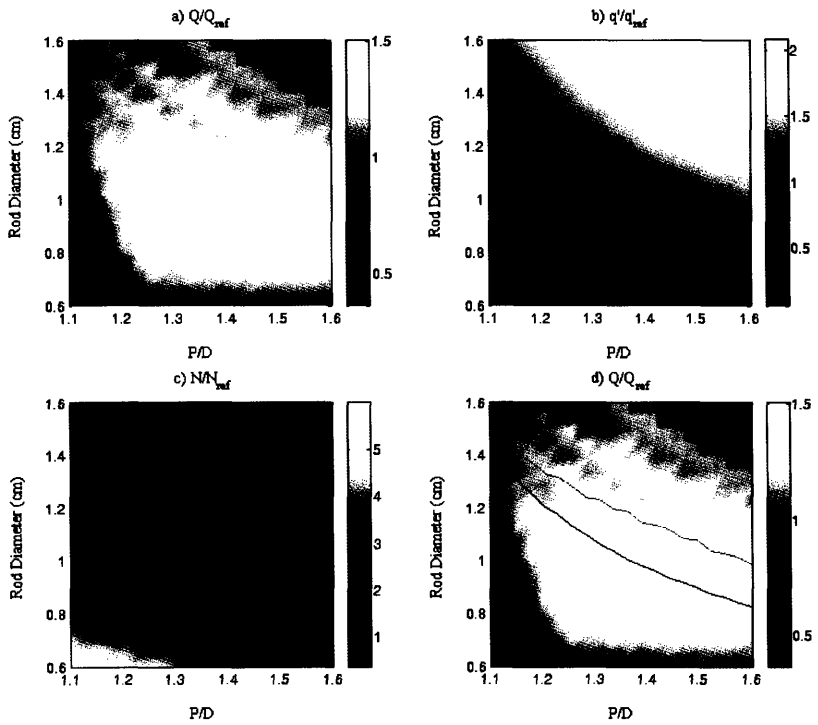

Figure 4.22: Case Hyd-NewCore-5 (Δp_{limit} = 36 psia): Power, LHGR and Number of Rod Ratios Between the Examined Hydride Core Configurations and the Reference BWR/5 Core
(the lines represent unity ratios)

The coolant flow rates corresponding to Case Hyd-NewCore-5 with Δp_{limit}= 36 psia (right plot of Figure 4.20) are shown in Figure 4.23. Even though higher than those of the backfit cases, they do not exceed the flow rate limit of 25875 kg/s mentioned at the end of Section 2.2.1. In particular, the maximum flow rate examined is 20557 kg/s, which is about 80% of this limit.

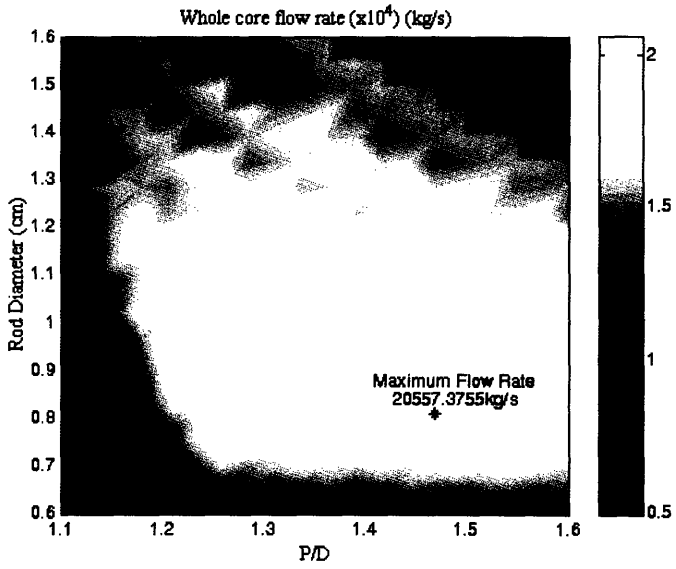

Figure 4.23: Whole Core Flow Rate (Case Hyd-NewCore-5, Δp_{limit} = 36 psia)

4.3.2 – Fuel Matrix and Structural Constraints

Because of the greater design freedom that characterizes the core construction in the "NewCore Approach", the fuel matrix variation within the powermap is more irregular than in the cases using the "Backfit Approach". In particular, it is no longer a function of the rod pitch only, and therefore it does not show the regularity evident in Figure 4.15, where core configurations having same rod pitch have also same fuel matrix. For the pressure drop limit of 36 psia, the methodology used to choose the fuel matrix index to couple to each *D-P/D* pair, i.e. the application of the structural constraints and of the "maximum power criterion" described in Section 3.3.2, results in the fuel matrix map shown in Figure 4.24. The reference *D-P/D* pair has matrix 8×8, while that yielding the maximum power has matrix 11×11 (for both pressure drop limits). It can be noticed that large fuel matrixes are concentrated only at the bottom of the map. In fact, should they be coupled with large diameter rods, the bundle weight limit would be exceeded. The map referred to the lower pressure drop limit is very similar and therefore is not displayed.

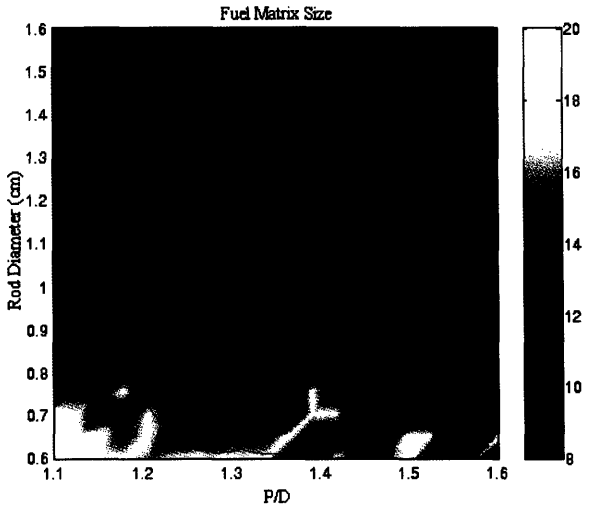

Figure 4.24: Fuel Matrix ($n \times n$) Size (Case Hyd-NewCore-5, Δp_{limit} = 36 psia)
(the colored scale indicates the matrix index n; green line encloses the high power region)

It is interesting to note that power levels higher than the reference oxide core power are achievable employing a wide range of matrixes. However, looking at Figure 4.20 and Figure 4.24, it can be seen that the *D-P/D* pairs characterized by the highest power levels are coupled with fuel matrixes ranging between 12×12 and 14×14.

All the triplets *D-P-n* plotted in Figure 4.24, as well as those referred to the lower pressure drop limit, do not exceed the structural constraints described in Section 2.2.2 (maximum number of bundles and maximum bundle weight). This is shown in Figure 4.23: the first plot shows that the total number of bundles is never larger than the structural constraint fixed as $1.6\,N^{ref}$, while the second plot proves that the hydride assembly weight is never larger than 1.4 times the oxide reference assembly weight. Analogous plots have been obtained when the pressure drop limit is fixed at 24.5 psia.

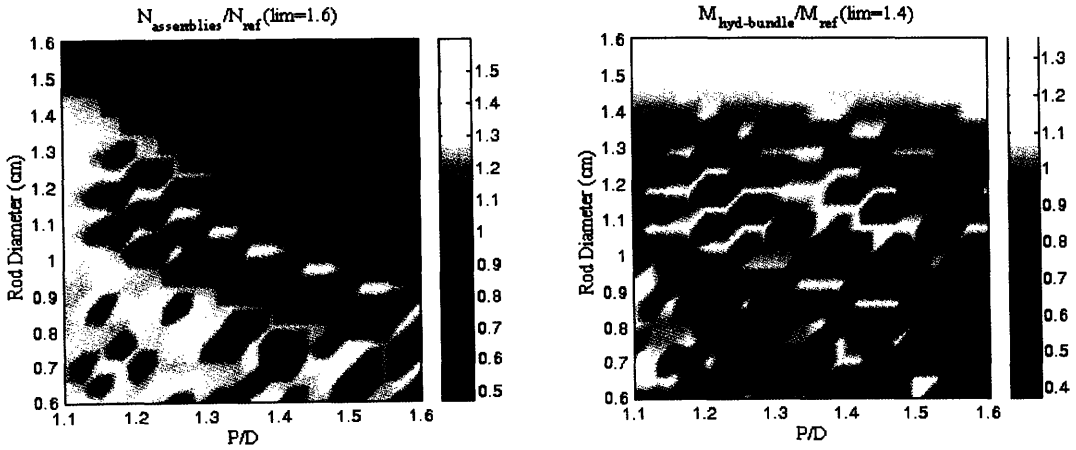

Figure 4.25: Structural Constraints (Case Hyd-NewCore-5, Δp_{limit} = 36 psia)

Figure 4.26 gives an idea about the size of the bundles corresponding to each *D-P/D* pair. It plots the ratio between the bundle outer width of the various configurations examined and that of the reference BWR/5 bundle (from Figure 1.2). The green line represents a unity ratio. In particular, for the reference *D-P/D* pair the ratio is 0.8898, while the *D-P/D* pair yielding the maximum power is characterized by a ratio of 1.0164. Although there is no a definite regular behavior, it can be noticed that almost all the configurations having rod pitch larger than the reference one[32] (~1.43 cm) have bundle size ratio above unity. Conversely, for most of the bundles having smaller pitch this ratio is below unity.

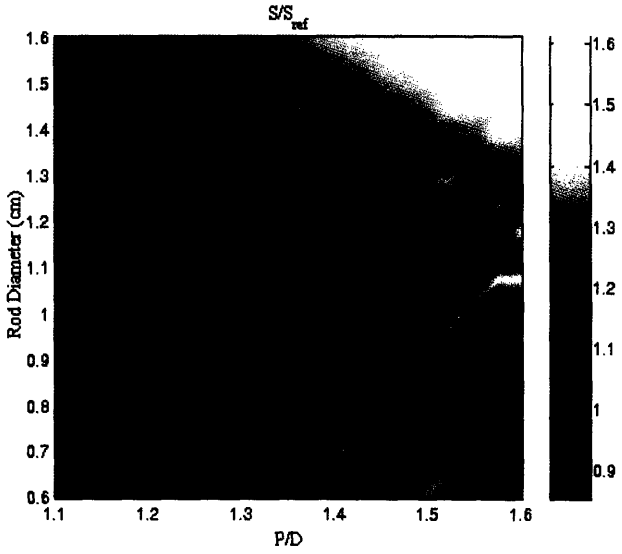

Figure 4.26: Bundle Width Ratio (Case Hyd-NewCore-5, Δp_{limit} = 36 psia)

The fact that the upper part of Figure 4.26 is dominated by large bundles has an important effect of the total cross sectional area of the core. In fact, since the core shroud circular while the bundles are square, some empty spaces exist at the core periphery. The total area of these "unoccupied" zones increases as the bundle size increases. This is shown in Figure 4.27, where the *D-P/D* pairs located in the upper part of the map are characterized by a smaller core cross sectional area. For each core configuration, the efficiency in filling the space potentially available can be estimated by comparing the values shown in Figure 4.27 with the total area enclosed within the core shroud, i.e. ~29×10^4 in^2.

[32] In the *D-P/D* maps, iso-pitch lines are hyperboles. See right plot in Figure F.3 (Appendix F).

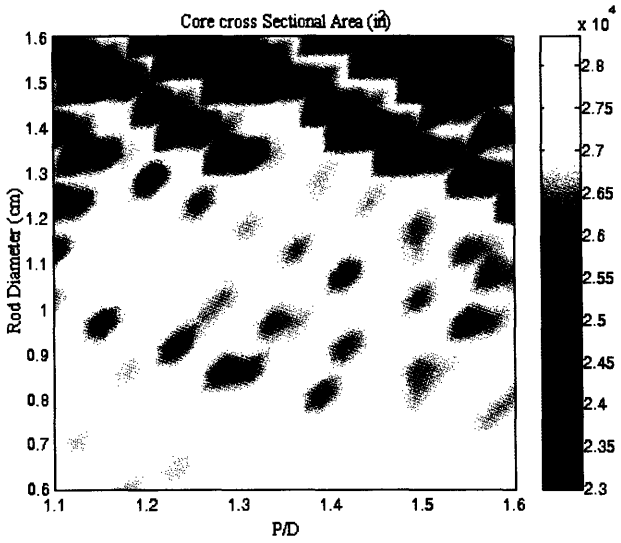

Figure 4.27: Total Core Cross Sectional Area (Case Hyd-NewCore-5, Δp_{limit} = 36 psia)

4.3.3 – Constraints on Achievable Power

As for the previous cases, all constraints do not equally limit the power. The most limiting parameter is the MCPR, while the fuel centerline temperature and the pressure drop tend to limit the power for large *D* and *P/D* and for small *P/D* respectively. The clad surface temperature is never limiting while the vibration ratio limits the power for configurations having rod diameter lower than 0.8 cm and *P/D* above 1.2-1.3. It is interesting to note that the limiting effect exerted by the vibration ratio effects configurations having slightly larger diameters than those found in Case Ox-Backfit-5. This is mainly due to the larger coolant flow rate which characterize the hydride new core bundles (due to the larger power), which results in enhanced vibrational motion. The limiting effects are represented in Figure 4.28 and Figure 4.29 for the two pressure drop limits adopted. The regions of influence of the limiting constraints are shown in Figure 4.30.

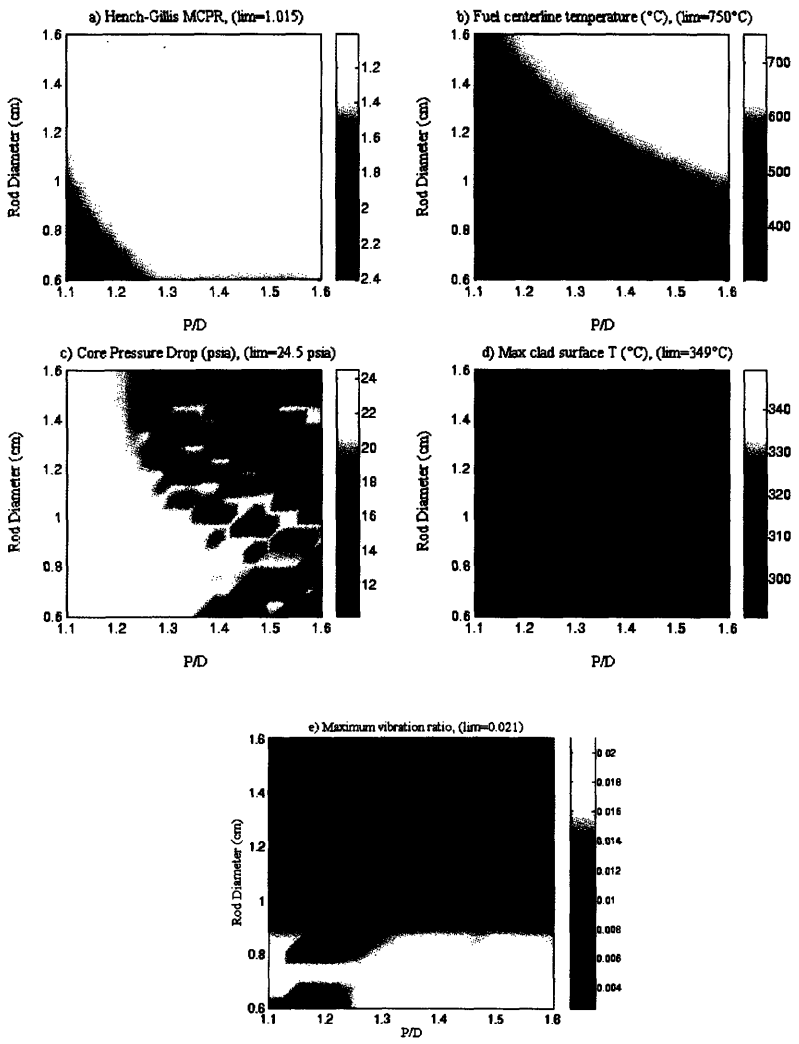

Figure 4.28: Limiting Effect Exerted by Constraints (Case Hyd-NewCore-5, Δp_{limit} = 24.5 psia)

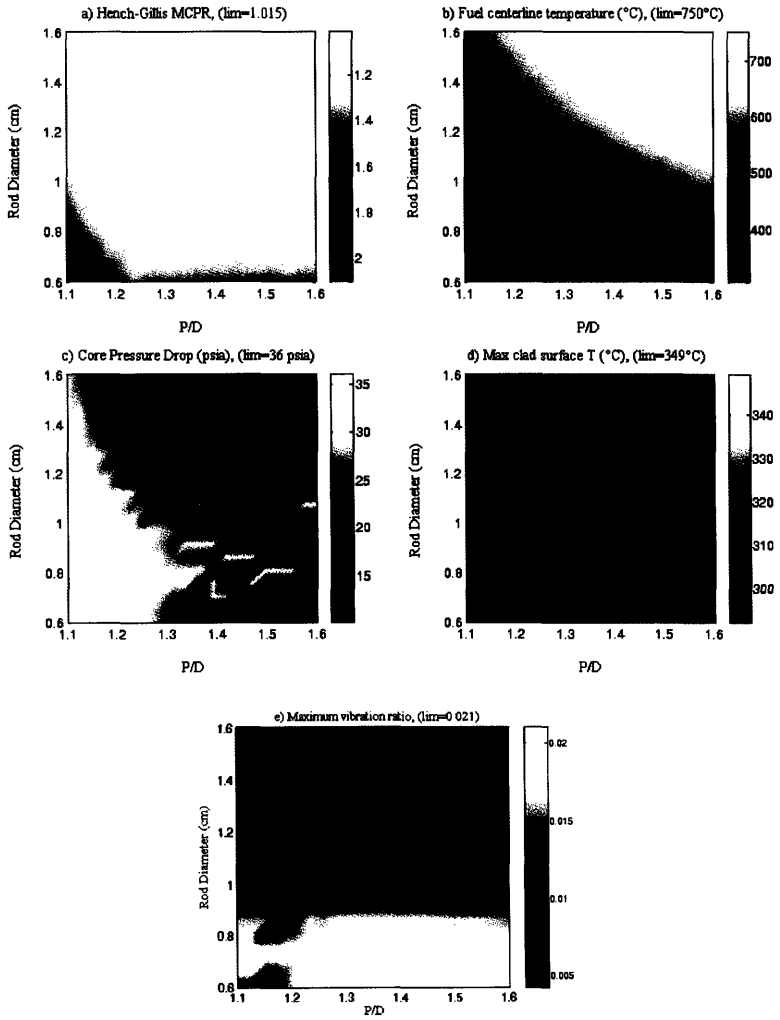

Figure 4.29: Limiting Effect Exerted by Constraints (Case Hyd-NewCore-5, Δp_{limit} = 36 psia)

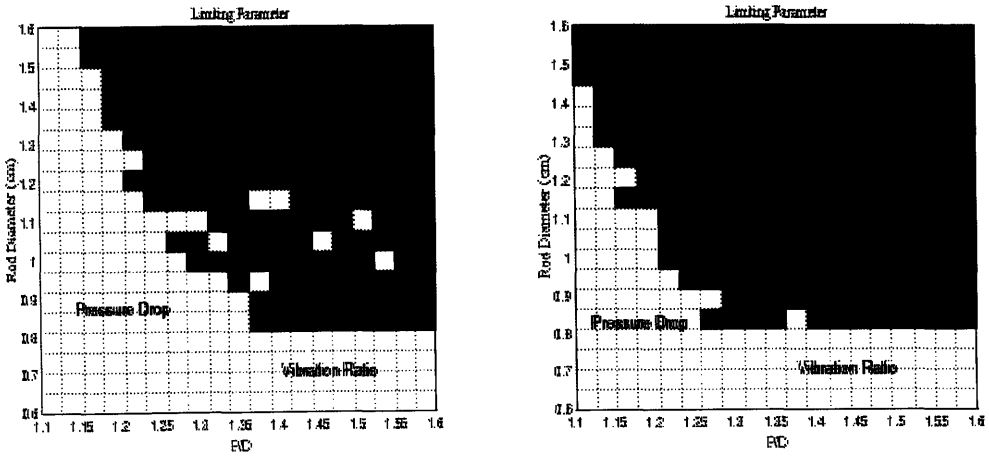

Figure 4.30: Regions of Influence of Limiting Constraints (Case Hyd-NewCore-5. Left: Δp_{limit} = 24.5 psia; Right: Δp_{limit} = 36 psia)

4.3.4 – Quality

The constraint which relates core power and flow rate together with the absence of bypass channels and the flat radial power distribution (except for the hot bundle) make the core average exit quality and the hot bundle exit quality quite constant over the whole geometry range. In particular, for both pressure drop limits, the former is around 13.2%, while the latter around 21.5%.

4.4 – Case Ox-Backfit-ES

4.4.1 – Achievable Power

The maximum achievable power as a function of the rod diameter and pitch is shown in Figure 4.47.

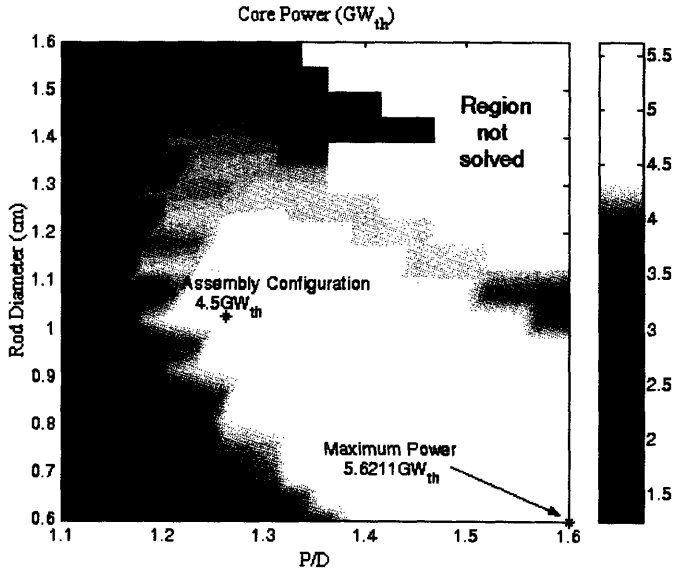

Figure 4.31: Case Ox-Backfit-ES Powermap

As for Case Ox-Backfit-5, the top right hand corner of the map remains unsolved. However, this is not a concern since the high power region is not located in this part of the map. See footnote 30 in Section 4.1.1 for details.

Observations from the map are as follows:

a) The assembly configurations characterized by a very small rod diameter ($0.6 \leq D \leq 0.8$ cm) and medium-large pitch ($1.4 \leq P/D \leq 1.6$) yield the highest power levels. In

particular, the maximum power is 5621 MW_t, which corresponds to a 25% increase with respect to the reference ESBWR (4500 MW_t).

b) The possibility to achieve higher power levels in the lower part of the map is due to a larger number of fuel rods, and is easily verifiable from Figure 4.32. This figure compares the power, the Linear Heat Generation Rate (LHGR) and the number of fuel rods of the core configurations examined with those of the reference ESBWR. According to the scheme used so far, the lines appearing in the plots, called "unity lines", divide them in two regions: that characterized by a ratio larger than one, and that with a ratio below unity. The last plot, which derives from the superposition of the previous three, shows the location of the high power region with respect to the unity lines corresponding to the LHGR and to the number of fuel rods. Even though the high power core configurations are almost equally distributed above and below these unity lines, the core configuration yielding the overall maximum power is located where the ratio between the number of fuel rods is larger than 1. Therefore, as found for Case Ox-Backfit-5, the contribution given by a very large number of rods is even more significant than that deriving from the combination of a larger number of rods AND a higher LHGR that characterizes the narrow region included between the two unity lines of subplots b) and c), i.e. the maximum power is not located in this narrow region.

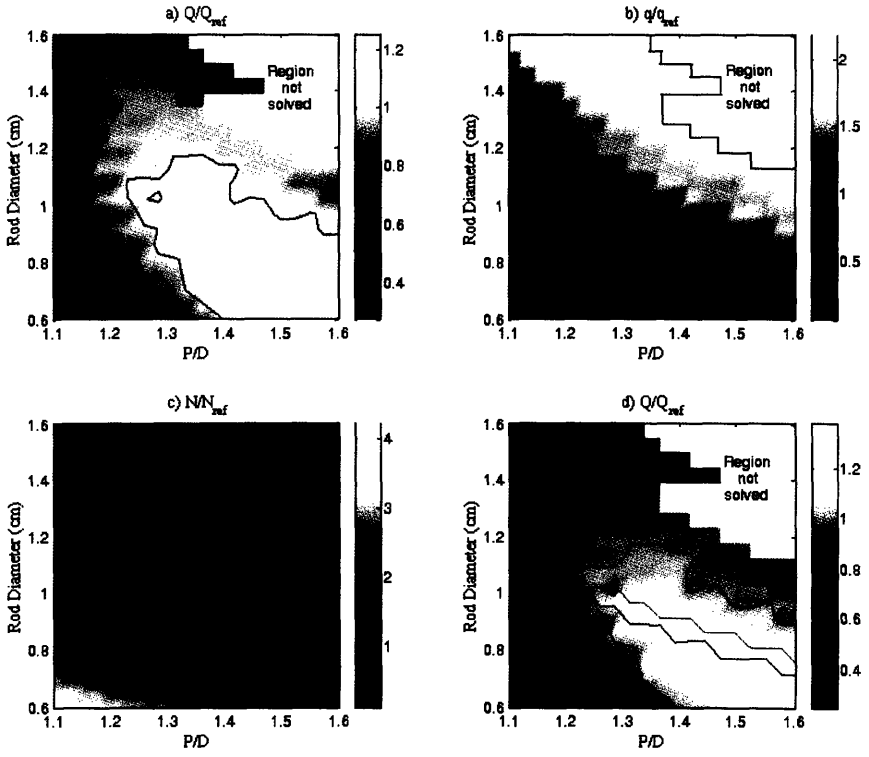

Figure 4.32: Case Ox-Backfit-ES: Power, LHGR and Number of Rod Ratios Between the Examined Oxide Core Configurations and the Reference ESBWR Core
(the lines represent unity ratios)

Contrary to Case Ox-Backfit-5, the high power region shown in plot a) of Figure 4.32 also includes the assembly configurations characterized by very small rod diameter, i.e. D<0.8 cm. This is due to the relatively small flow rates characterizing the various core configurations, which prevent the vibration ratio from limiting the maximum achievable power. As shown in Table 2.3, the need to assure adequate natural circulation inside an ESBWR-type reactor forces the power/flow ratio to be almost two times higher than that of the BWR/5-type reactors, in which the desired coolant circulation is achieved by means of pumps. Figure 4.33 shows that the maximum core flow rate is equal to 12495 kg/s, a value which is below the flow rate of all the core configurations achieving, for each case, the maximum power.

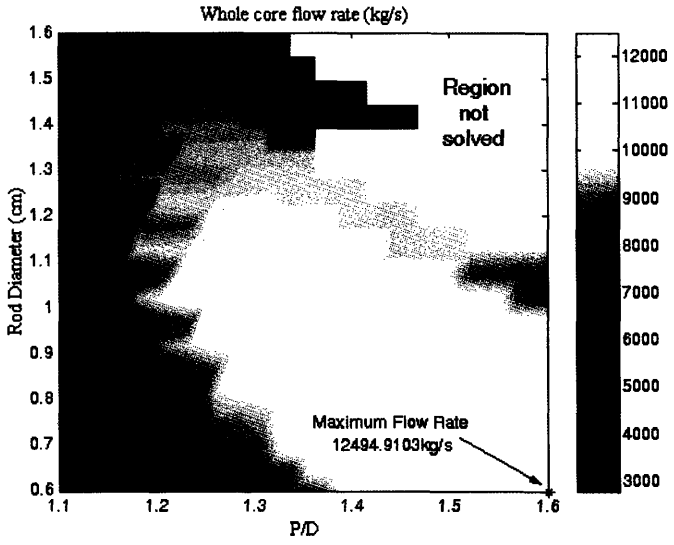

Figure 4.33: Total Core Flow Rate (Case Ox-Backfit-ES)

4.4.2 – Fuel Matrix

Figure 4.34 presents the matrix characterizing each of the 400 assembly configurations analyzed. The black line encloses the high power region, while the upper and lower green lines represent the matrix indexes 7 and 12 respectively. The *D-P/D* pair yielding the maximum power, i.e. 5621 MW_t, is coupled with a 13×13 matrix. It can be noticed that the high power region, i.e. where the power is higher than the reference value of 4500 MW_t, corresponds to fuel matrixes in the range from 9×9 to 14×14.

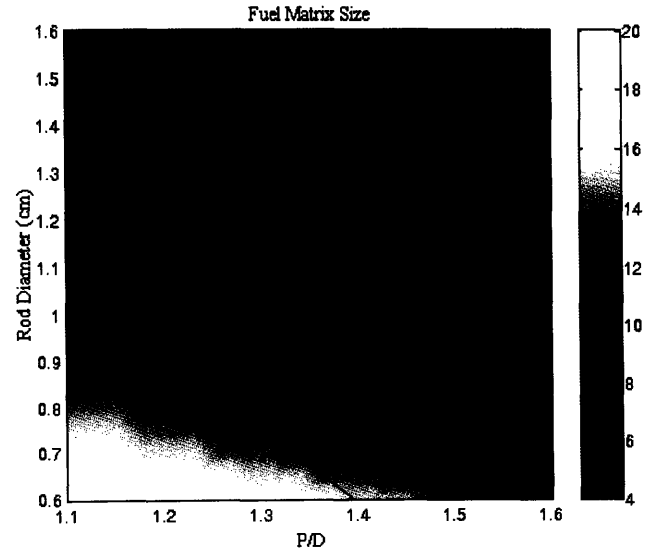

Figure 4.34: Fuel Matrix (n×n) Size (Case Ox-Backfit-ES)

4.4.3 – Constraints on Achievable Power

Figure 4.35 shows the value of the various thermal-hydraulic constraints over the whole geometry range. Again, whenever one of them actually limits the power, the plot appears white (except for the unsolved region).

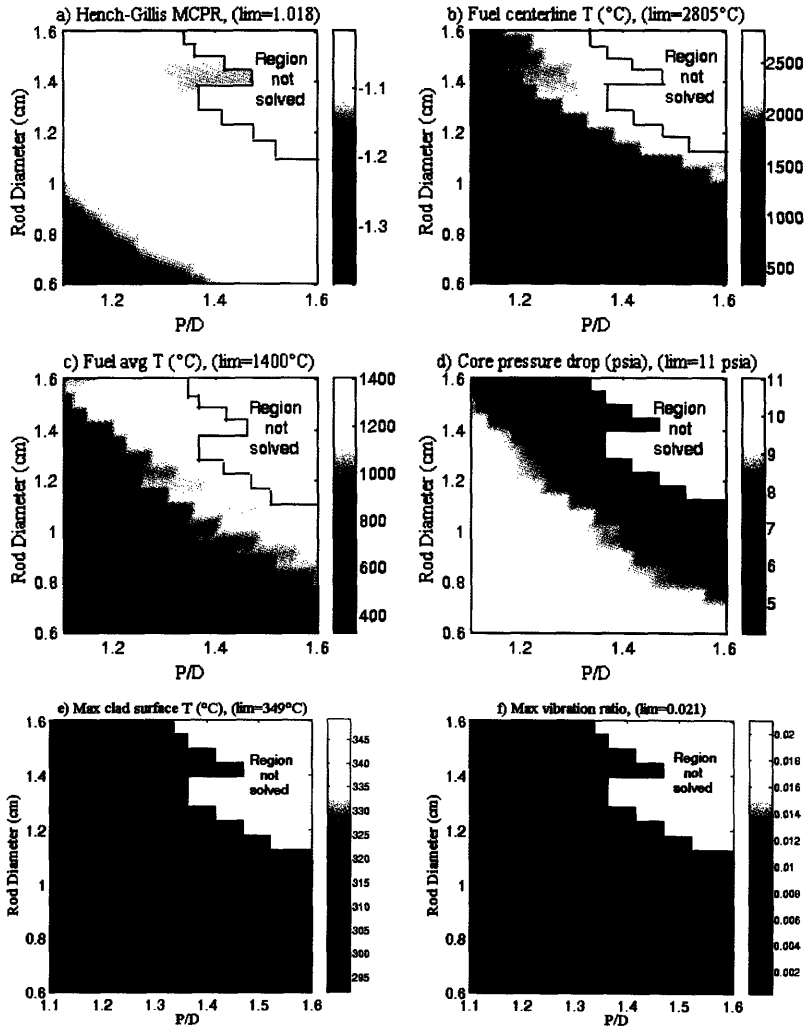

Figure 4.35: Limiting Effect Exerted by Constraints (Case Ox-Backfit-ES)

Figure 4.35 shows that, although six are the constraints applied, only 3 are actually limiting, i.e. the MCPR, the fuel average temperature and the pressure drop. The area of influence of each is evident from Figure 4.36.

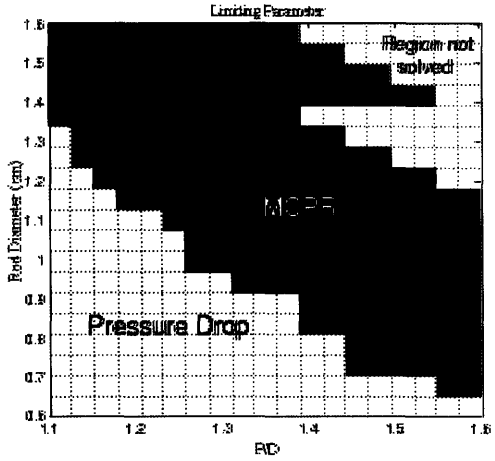

Figure 4.36: Areas of Influence of the Limiting Constraints (Case Ox-Backfit-ES)

4.4.4 – Quality and Bypass Flow

Figure 4.37 shows the core average exit quality, bundle average exit quality and hot bundle exit quality associated with each assembly configurations.

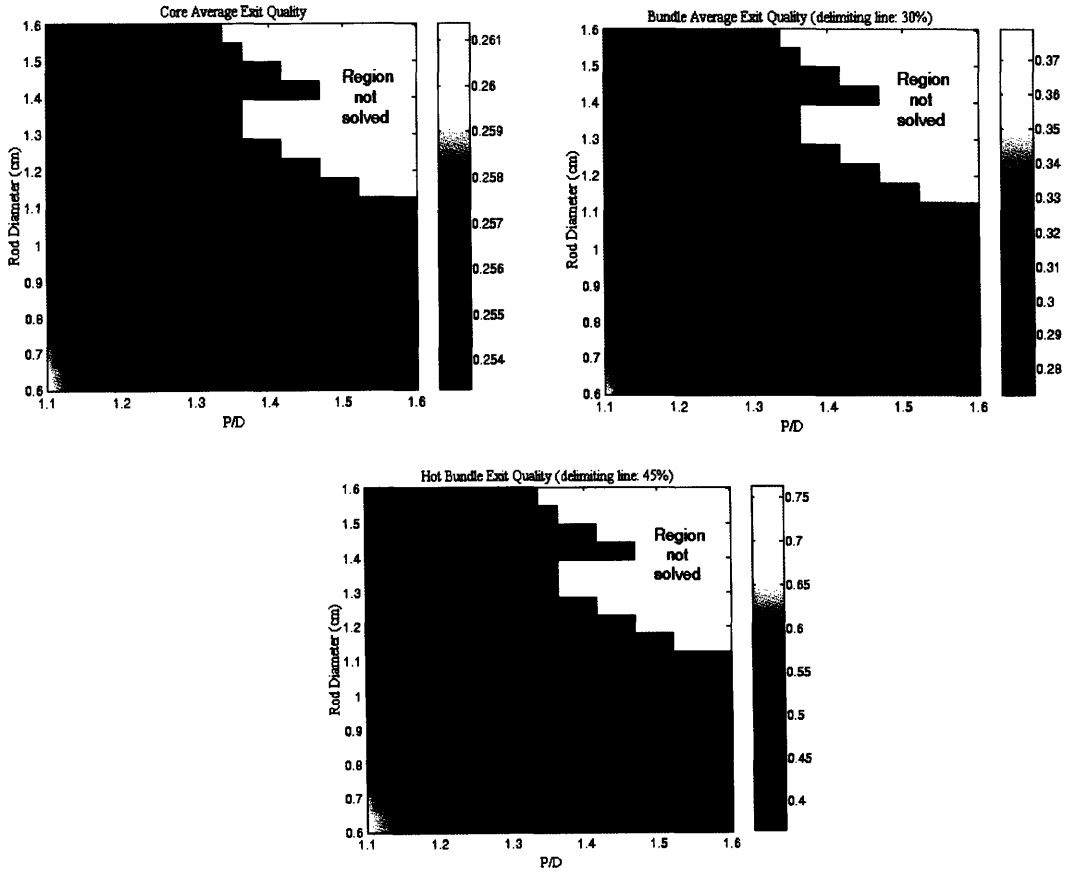

Figure 4.37: Core Average Exit Quality, Bundle Average Exit Quality and Hot Bundle Exit Quality (Case Ox-Backfit-ES)

Because of the constraint relating core power and total coolant flow, i.e. power/flow = constant, most of the *D-P/D* pairs are characterized by core average exit quality ranging between 25.5% to 25.8%, bundle average exit quality between 29% to 30%, hot bundle exit quality between 42% to 45%. The weak discontinuities that appear in the first two plots at *P/D*=1.4 and *D*=1.1 cm are due to the use of two different relations to calculate the bundle inlet orificing coefficient (see equation 3-9 in Section 3.3.1). The use of a single relation, for example the second of equation 3-9, would have yielded a smoother variation of the qualities across the lines *P/D*=1.4 and *D*=1.1 cm. However, the bypass flow percentage in the bottom left hand corner of the map would drop well below the recommended value of 10% ([24]). The use of a different relation in this important region of the map allows the maintainance of a flow percentage around 10%, as shown in Figure 4.38.

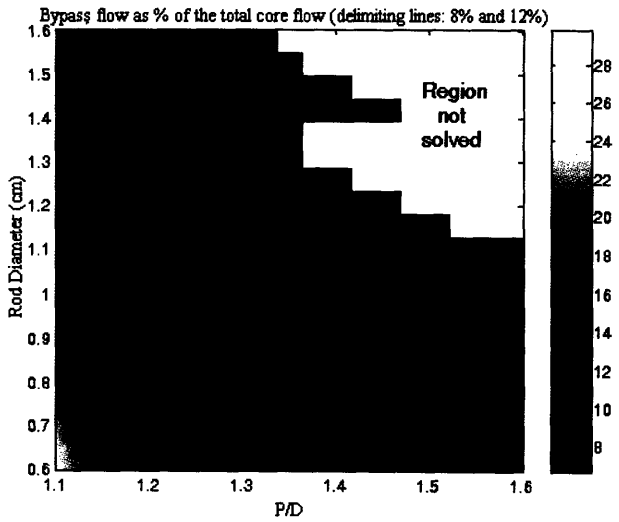

Figure 4.38: Bypass Flow Percentage (Case Ox-Backfit-ES)

4.5 – Case Hyd-NewCore-ES

4.5.1– Achievable Power

The maximum achievable power as a function of the rod diameter and pitch is shown in Figure 4.39.

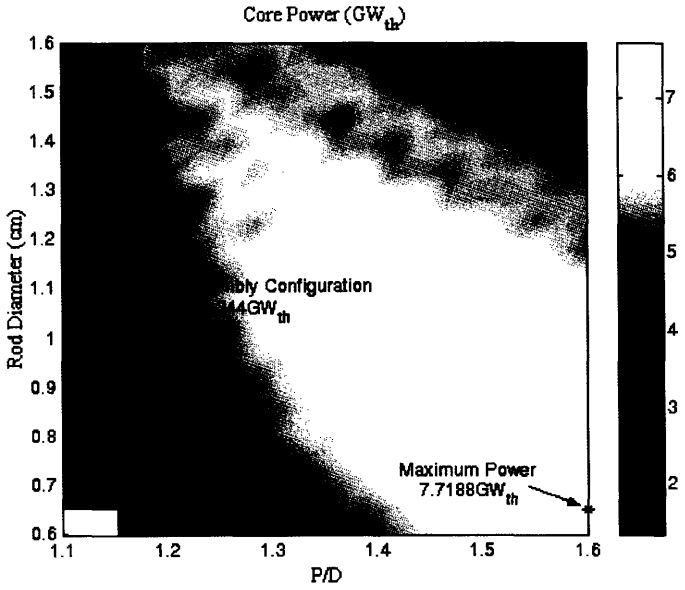

Figure 4.39: Case Hyd-NewCore-ES Powermap

Observations from the map are as follows:

- The large vessel size together with the greater design freedom characterizing the NewCore approach yield a maximum achievable power of 7719 MW_t, which corresponds to a 71% increase with respect to the reference ESBWR power (4500 MW_t). The assembly configuration yielding this power has a rod diameter of about 6.5 mm and a *P/D* of 1.6.
- The maximum achievable power corresponding to the reference configuration is 19% higher than the reference power, i.e. 5344 MW_t versus 4500 MW_t.
- The high power region, i.e. the region of the map characterized by power levels higher than the reference power, occupies a very large portion of the map. This is evident from plot a) of Figure 4.40, which shows the ratio between the power corresponding to the various assembly configurations and that of the reference (backfit) configuration. The shape of this region is quite similar to that shown in plot a) of Figure 4.22: this means that the power comparison between the

NewCore approach and the Backfit approach is weakly dependent on the type of reactor to which it is referred.

- The overall maximum achievable power is a consequence of the larger number of rods contained in the core. This is evident from plot d) of Figure 4.40, which derives from the superposition of the unity lines of plot b) and plot c) on plot a). It can be seen that the assembly configuration yielding the maximum power is located below the unity line corresponding to the number of rod ratio, i.e. where the number of rods is larger than that corresponding to the reference ESBWR core. The LHGR ratio associated with that configuration is practically unity since it is located just across the LHGR ratio unity line.
- The blank region located in the bottom left hand corner results from the application of the only structural constraint used for the NewCore approach, that is the maximum number of bundles. In fact, assembly configurations characterized by very small rod pitch yield a large number of bundles even when the associated matrix index is equal to the maximum allowed value, i.e. 20.

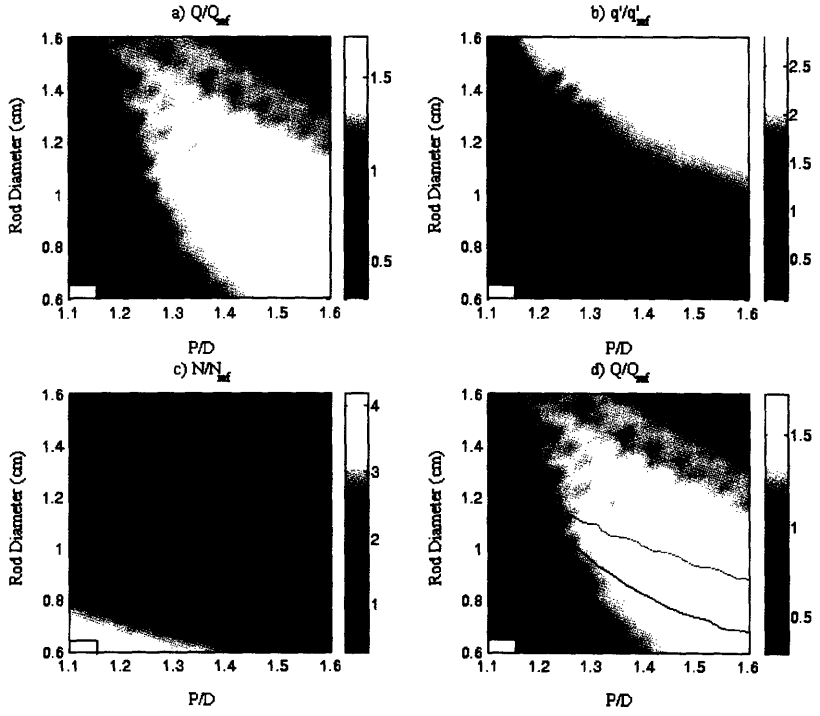

Figure 4.40: Case Hyd-NewCore-ES: Power, LHGR and Number of Rod Ratios Between the Examined Hydride Core Configurations and the Reference ESBWR Core
(continuous lines represent unity ratios)

Consistent with that was found for Case Ox-Backfit-ES, the high power region also includes the bottom region of the map, i.e. where $D<0.75$. For BWR/5-type reactors such a region has always been found to be vibration-limited, with a power lower than that of the reference BWR/5. Instead, the large power/flow ratio characterizing a natural circulation core like the ESBWR yields relatively small flow rates, even for the highest power level. Figure 4.41 shows that the maximum flow rate is 17158 kg/s, a value which is below the maximum flow rate found for Case Hyd-NewCore-5, i.e. 20557 kg/s (see Figure 4.23).

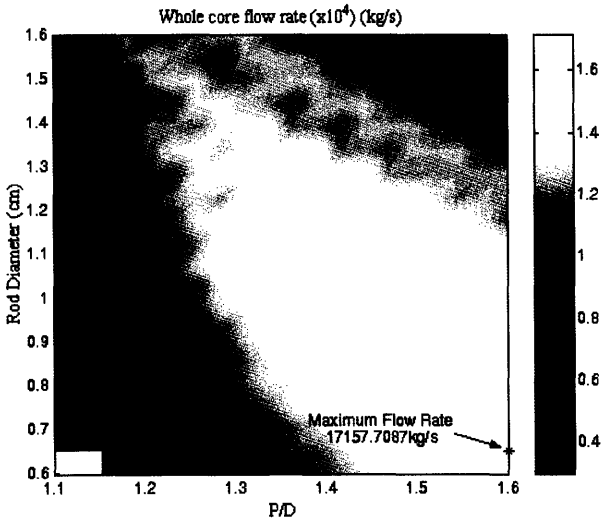

Figure 4.41: Whole Core Flow Rate (Case Hyd-NewCore-ES)

4.5.2 – Fuel Matrix and Structural Constraint

The fuel lattice size, i.e. the so-called fuel matrix, associated with each assembly configuration is shown Figure 4.42. The reference *D-P/D* pair is associated with a matrix 11×11, while that yielding the maximum power with a matrix 14×14. As for case Hyd-NewCore-5, the matrix index does not vary smoothly over the whole geometry range, but shows several discontinuities located mostly in the upper part of the map. Again, they are due to the core construction approach used, i.e. the NewCore approach, and in particular to the criteria used to choose the fuel matrix index to associate to each *D-P/D* pair (see Section 3.3.2). The large matrix index characterizing the bottom left hand corner of the map is a consequence of the structural constraint applied to this case. In fact, the exclusion of smaller matrix indexes for the *D-P/D* pair located in this region was not due to the fact that the resulting triplets *D-P-n* would have yielded lower power, but simply to

the excessive number of bundles that would have been resulted from that choice. In fact, it should be recalled that, for the same rod pitch, a smaller matrix index corresponds to a smaller bundle width and therefore to a larger number of bundles.

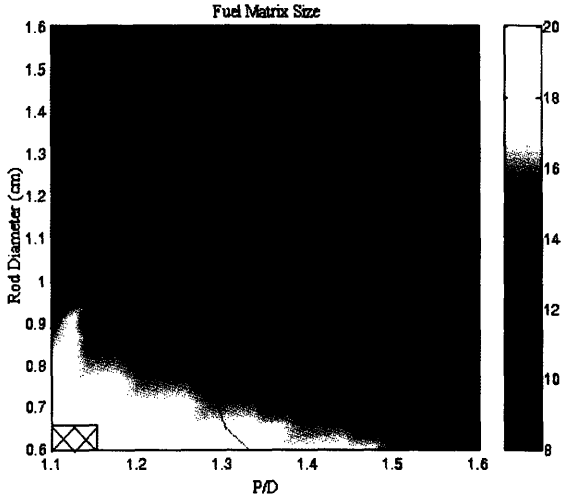

Figure 4.42: Fuel Matrix ($n \times n$) Size (Case Hyd-NewCore-ES)
(the colored scale indicates the matrix index n; green line encloses the high power region)

As described in Section 2.2.2, Case Hyd-NewCore-ES uses a single structural constraint, represented by the total number of bundles contained in the core. Figure 4.43 show that none of the assembly configurations exceed the maximum allowed value, i.e. $1.6 \times N_{bundles}^{ref\_BWR/5}$.

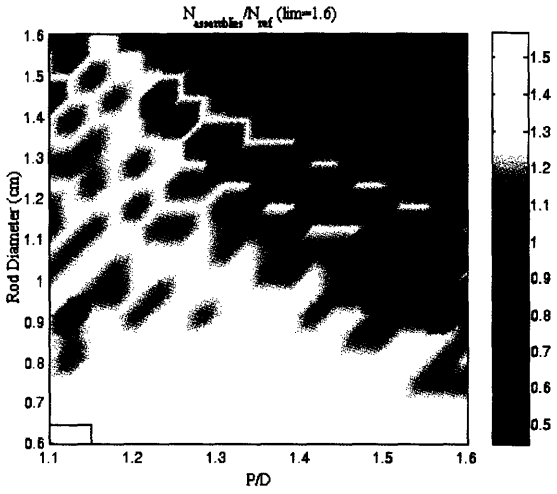

Figure 4.43: Structural Constraint (Case Hyd-NewCore-ES)

Conversely, the bundle weight, which played the role of structural constraint in Case Hyd-NewCore-5, in this case is no longer constrained, and therefore is allowed to assume

any value. For this reason, some configurations are associated with bundles whose weight exceeds the value used as limit in case Hyd-NewCore-5, i.e. $1.4 \times M_{bundle}^{ref\_BWR/5}$. The continuous line in Figure 4.44 separates the assembly configurations that exceed this limit from those that do not.

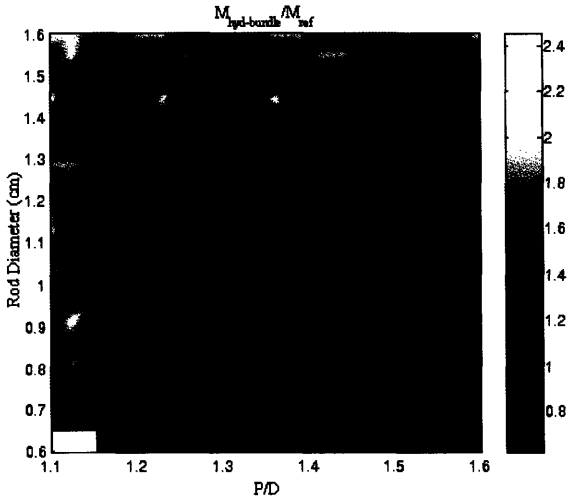

Figure 4.44: Bundle Weight Ratio (Case Hyd-NewCore-ES)

4.5.3 – Constraints on Achievable Power

The limiting effect exerted by the power constraints is shown in Figure 4.45. Again, whenever a parameter limits the power the plots appear white. The pressure drop and the MCPR are the most limiting constraints, while the maximum fuel temperature limits the power of a restricted number of assembly configurations having very large *D* and *P/D*. Conversely, clad temperature and vibration ratio are never limiting. The areas of influence of the limiting parameters are clearly shown in Figure 4.46.

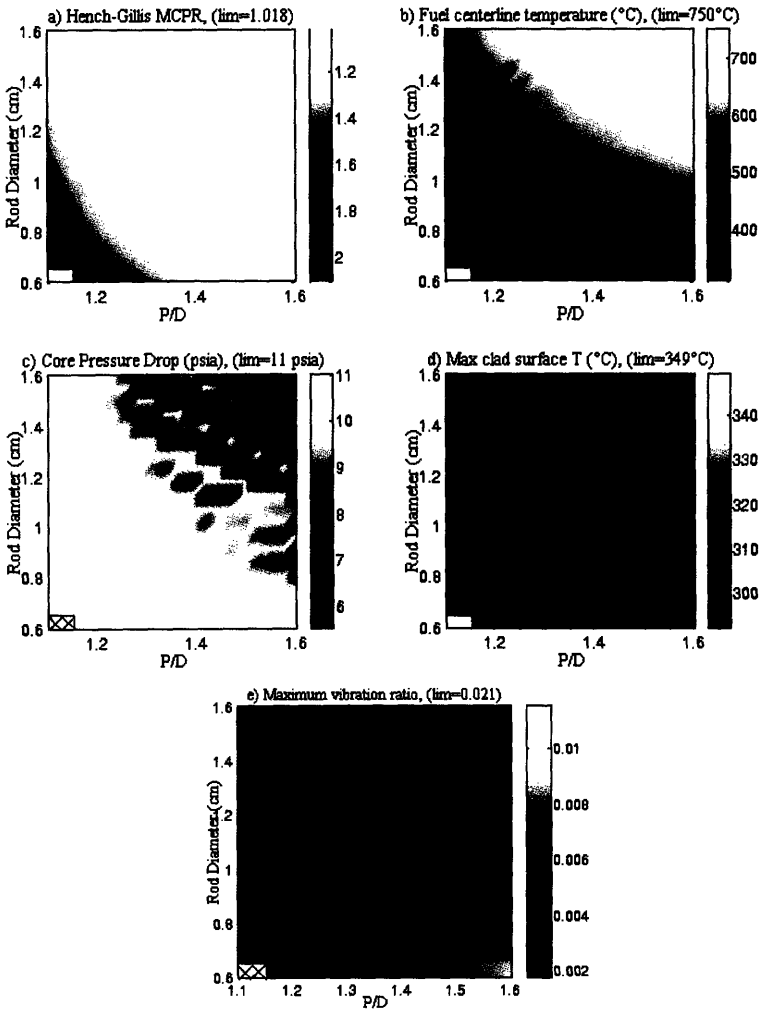

Figure 4.45: Limiting Effect Exerted by Power Constraints (Case Hyd-NewCore-ES)

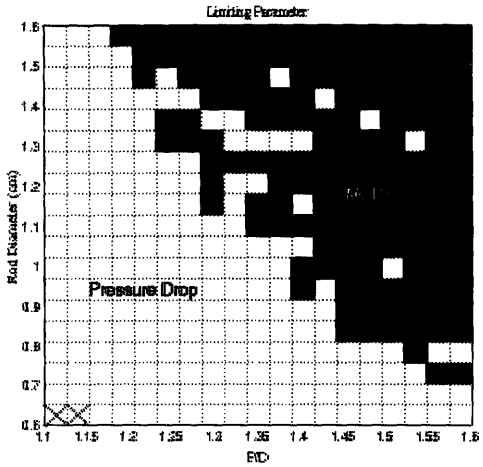

Figure 4.46: Areas of Influence of Limiting Constraints (Case Hyd-NewCore-ES)

4.5.4 – Quality

The constraint which relates core power and flow rate together with the absence of bypass channels and the flat radial power distribution (except for the hot bundle) make the core average exit quality and the hot bundle exit quality quite constant over the whole geometry range. In particular, the former is around 24.2%, while the latter around 33%.

4.6 – Comparison Between Cases

The comparison between the power-related performances of hydride and oxide cores is performed for each *D-P/D* pair by dividing the value assumed by a certain parameter in the hydride configuration by the value that the same parameter assumes in the oxide configuration. Should two cores under examination be of the "backfit" type, each *D-P/D* pair will be coupled with a matrix index n that is common to both cores. Conversely, if the comparison is made between a "backfit" core and a "new core", the same *D-P/D* pair in the two cores may not be coupled with the same matrix index.

4.6.1 – Case Ox-Backfit-5 and Case Hyd-Backfit-5

The ratio between the power of the hydride core configurations and the power of the oxide core configurations is shown in Figure 4.47. In both maps the green line corresponds to a unity ratio. Thus, it divides the powermaps into two regions: that where the hydride cores deliver a higher power (power ratio >1), and that where the oxide cores deliver a higher power.

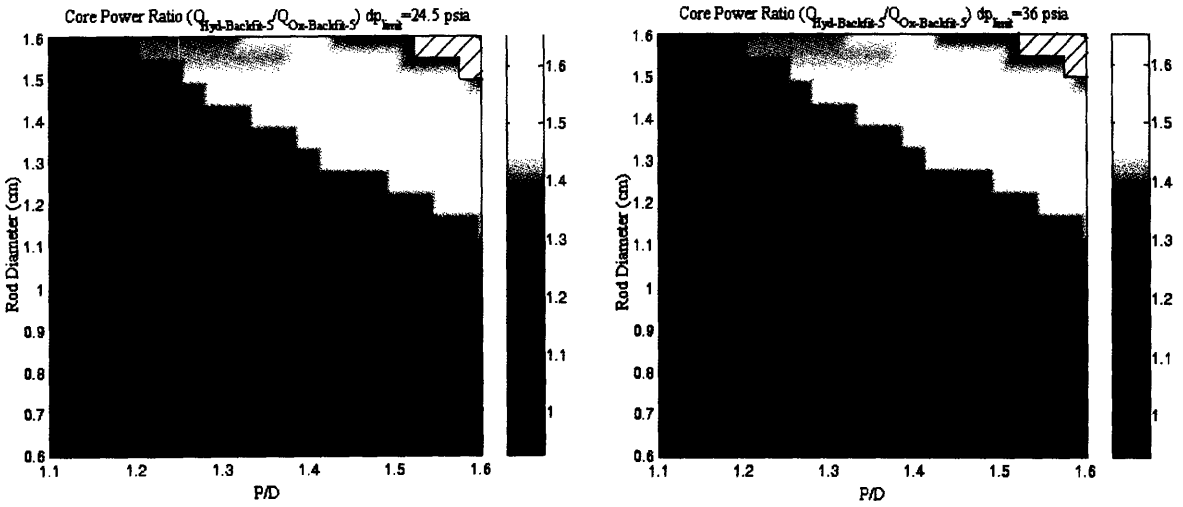

Figure 4.47: Power Ratio: Hyd-Backfit-5 / Ox-Backfit-5 (Left: Δp_{limit} = 24.5 psia; Right: Δp_{limit} = 36 psia)

By comparing Figure 4.47 with Figure 4.18 and Figure 4.8 it can be noticed that the hydride fueled cores deliver a lower power only within the pressure drop limited region, i.e. where the core pressure drop is the parameter that actually limits the power. Since the location of such a region is the same in Case Ox-Backfit-5 and in Case Hyd-Backfit-5, the larger number of rods contained in the hydride bundles results in a slightly larger pressure drop. However, such an effect is not very significant, and the power ratio is only slightly below unity. Conversely, in the rest of the map the power ratio is significantly above unity, and increases as the rod pitch increases[33]. Figure 4.48 shows that this is due both to the larger LHGR and to the larger number of fuel rods characterizing the hydride cores. In particular, while a few less than one half of the hydride configurations have lower LHGR (*D-P/D* pairs located under the unity line in the left plot), all have a larger number of fuel rods. This is a logic consequence of the water rod elimination.

[33] It should be noticed that, in spite of the large power ratios shown in the top right hand corner, this region of the powermap is characterized by very low power levels for both cores (see Figure 4.1 and Figure 4.11).

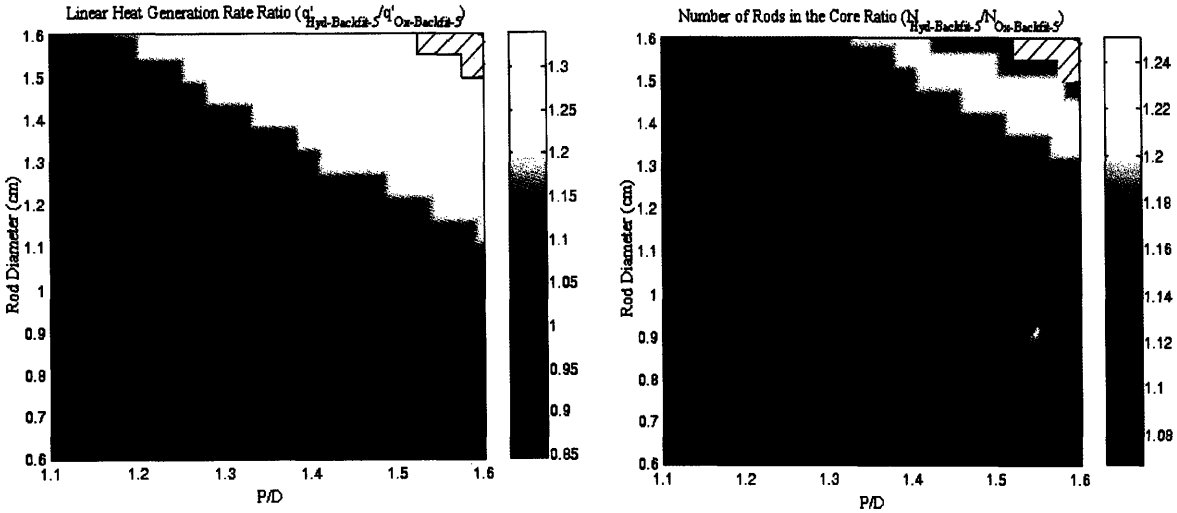

Figure 4.48: LHGR Ratio and Number of Rod Ratio (Hyd-Backfit-5 / Ox-Backfit-5)[34]

Finally, Figure 4.49 shows the plots deriving from the superposition of the LHGR ratio unity line on the two plots of Figure 4.47.

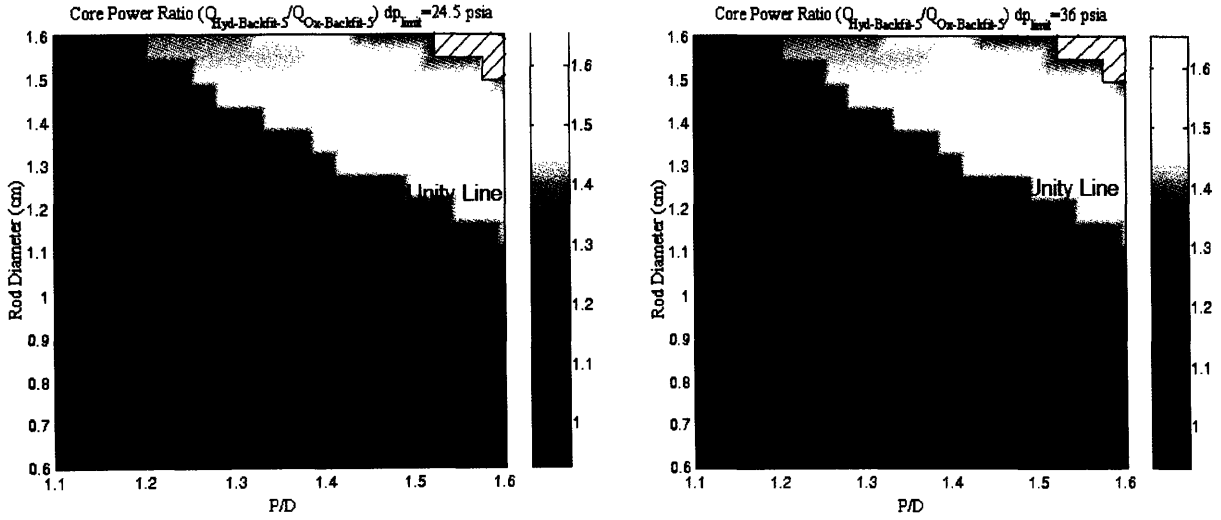

Figure 4.49: Core Power Ratio and LHGR Unity Line
(Left: Δp_{limit} = 24.5 psia; Right: Δp_{limit} = 36 psia)

[34] The plot on the left refers to the upper pressure drop limit, i.e. 36 psia. That referred to the lower pressure drop is qualitatively very similar and therefore is not displayed. The only difference is a larger area of the dark spots located at the bottom left hand corner, as a consequence of the lower pressure drop limit adopted. Instead, being independent from thermal-hydraulic parameters, the plot on the right is in common to both pressure drop limits.

4.6.2 – Case Ox-Backfit-5 and Case Hyd-NewCore-5

The ratio between the power of the hydride core configurations and the power of the oxide core configurations is shown in Figure 4.50. Again, the green line corresponds to a unity ratio.

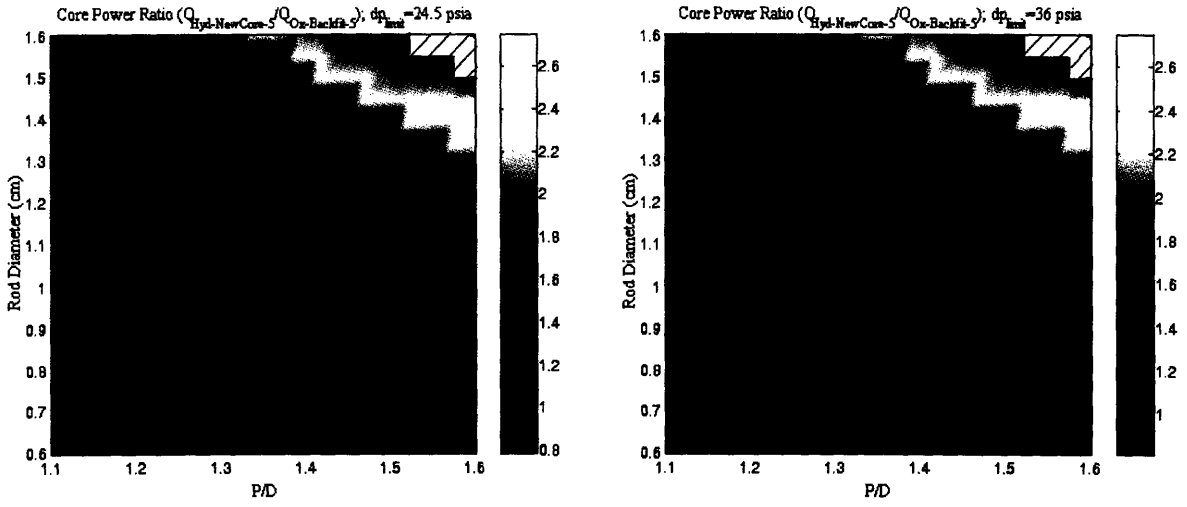

Figure 4.50: Core Power Ratio: Hyd-NewCore-5 / Ox-Backfit-5
(Left: $\Delta p_{limit} = 24.5$ psia; Right: $\Delta p_{limit} = 36$ psia)

Regardless of the pressure drop limit adopted, the great majority of the hydride new core configurations deliver a higher power than the oxide backfit ones. Although the power ratio reaches values up to 2.5, for the *D-P/D* pairs yielding the maximum power (see Figure 4.20) such a ratio is around 1.4, which is still considerably high. Only few hydride configurations, located within the pressure drop limited region, are characterized by a slightly lower power. Again, this is the consequence of the larger number of fuel rods contained in a hydride bundle with respect to an oxide fueled bundle having same *D* and *P*.

The significant gain in power resulting from the implementation of the hydride fuel in a "new core" structure is mainly due to a larger number of rods. This is evident from the right plot of Figure 4.51, which shows that the ratio between the number of fuel rods contained in the two types of core is quite large and always above unity. The contribution given by a larger number of fuel rods is able to recover the slightly lower LHGR that characterize the hydride configurations located below the unity line in the left plot. For example, in the region where the highest power is achieved (see Figure 4.20), the number

of rod ratio ranges between 1.3 and 1.4, while the LHGR ratio is roughly constant and equal to 0.85. Since $\frac{1}{0.85} \approx 1.18 < 1.3$, the contribution provided by the larger number of rods prevails.

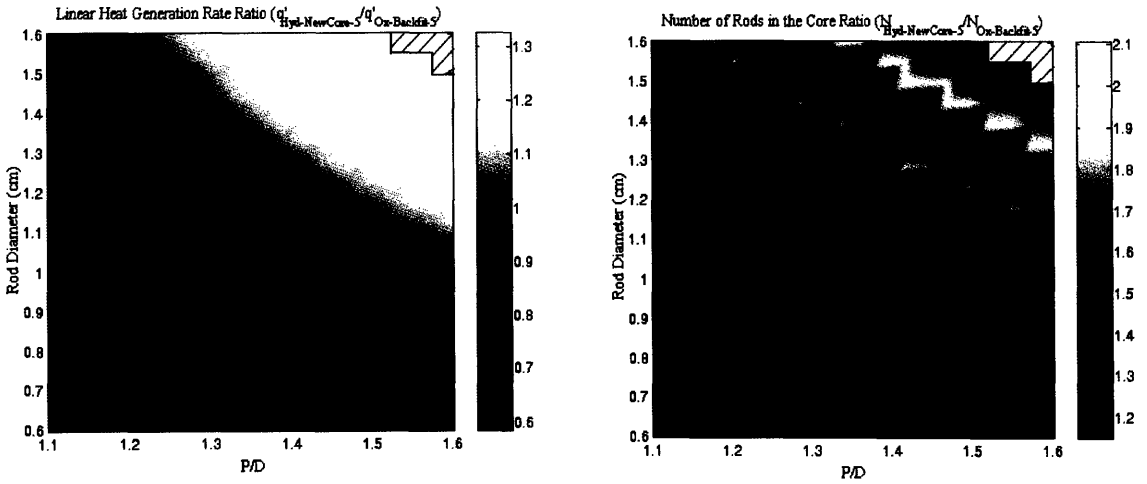

Figure 4.51: LHGR Ratio and Number of Rods Ratio (Hyd-NewCore-5 / Ox-Backfit-5)[35]
(continuous lines represent unity ratios)

Figure 4.52 shows the plots derived from the superposition of the LHGR ratio unity line on the two plots of Figure 4.50.

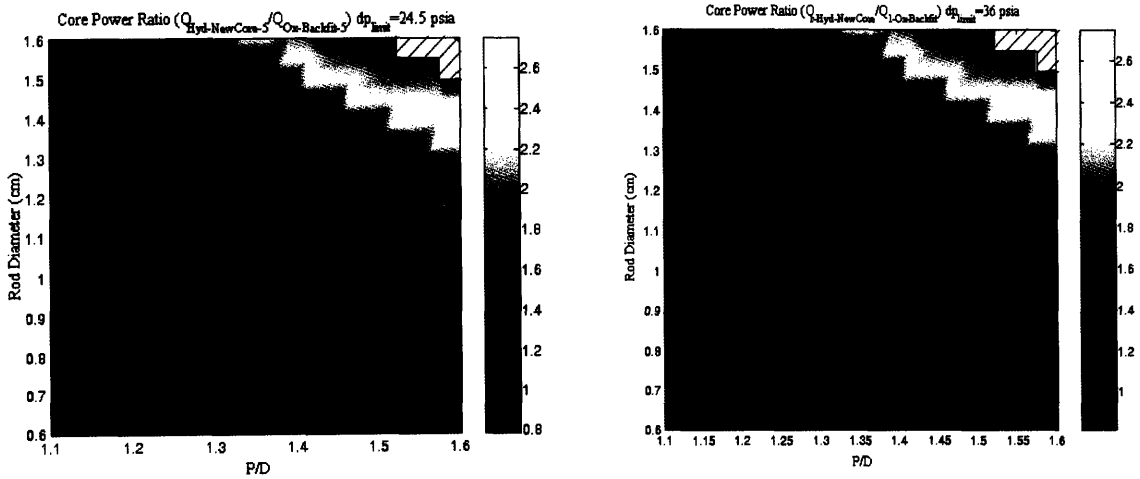

Figure 4.52: Core Power Ratio and LHGR Unity Line (Hyd-NewCore-5 / Ox-Backfit-5)
(Left: $\Delta p_{limit} = 24.5$ psia; Right: $\Delta p_{limit} = 36$ psia)

[35] Both plots refer to the upper pressure drop limit, i.e. 36 psia. Since those corresponding to the lower limit are almost identical, they are not displayed.

Although the power comparison is performed between a backfit core and a new core having the same vessel size, the greater design freedom that characterizes the latter may induce one to think that the two cores do not have the same total cross sectional area. In fact, while all the "backfit" *D-P/D* pairs have the same bundle width, i.e. the reference bundle width, some "new core" *D-P/D* pairs are associated with bundles smaller than the reference one (see Figure 4.26). In these cases the space available for the core is occupied more efficiently, i.e. a smaller "unoccupied" space is left between the outermost bundle ring and the core shroud. It has been demonstrated that this difference is quite small for most of the core configurations. Figure 4.53 shows that the ratio between the core cross sectional areas ranges between 0.85 and 1.03 and that for the core configurations of interest this ratio is practically unity.

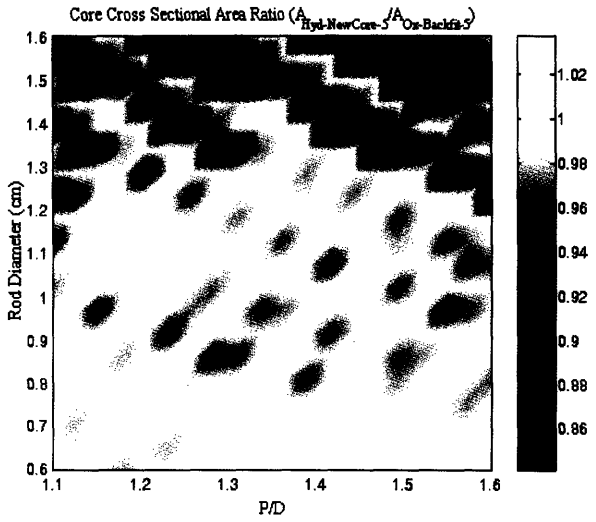

Figure 4.53: Core Cross Sectional Area Ratio (Hyd-NewCore-5 / Ox-Backfit-5)

Since the methodology used to construct the hydride "new core" is completely different from that used for the oxide core, some maps are affected by discontinuities. This is evident in the second plot of Figure 4.51 as well as in Figure 4.52, where the LHGR unity line is actually composed of more than one line. Again, this is due to the greater design freedom characterizing the new core approach. In fact, while for the oxide cores the matrix variation over the geometry range is quite smooth (see Figure 4.5), for the hydride cores (see Figure 4.24) it is not. As a consequence, two hydride assembly configurations located very close together in the map, may have significantly different matrix indexes.

For the same reason, a hydride new core configuration characterized by a certain *D-P/D* pair may have a different matrix index than an oxide backfit configuration characterized by the same *D* and *P*. Figure 4.54 shows that the ratio between the matrix indexes is above unity for most configurations. The green line encloses the regions characterized by a ratio lower than 1.

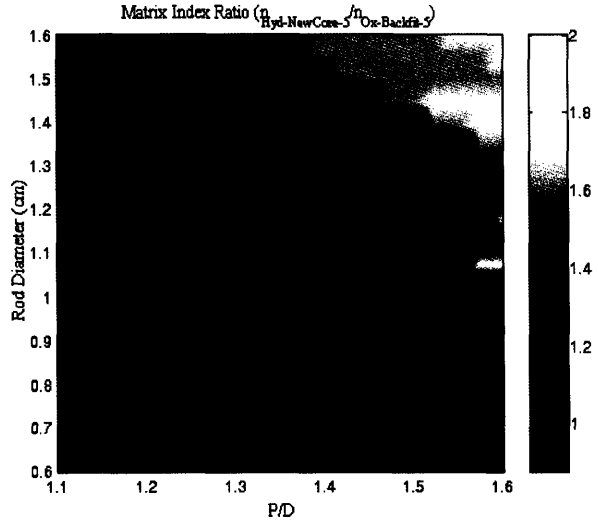

Figure 4.54: Matrix Index Ratio (Hyd-NewCore-5 / Ox-Backfit-5)[36]

4.6.3 – Case Ox-Backfit-ES and Case Hyd-NewCore-ES

Figure 4.55 compares the power performance of the assembly configurations examined in Case Hyd-NewCore-ES to those examined in Case Ox-Backfit-ES. It shows, for each *D-P/D* pair, the ratio between the maximum powers achievable with the two approaches[37]. Except for very tight configurations, i.e. small *P/D*, the power ratio is everywhere above

[36] The plot refers to the upper pressure drop limit, i.e. 36 psia. Contrary to the backfit cases, in the new core approach the methodology used to choose the matrix index to associate to each *D-P/D* pair does not depend on geometric considerations only, but also on the power constraints (through the "maximum power criterion", see Section 3.3.2). For this reason, the plot showing the matrix index ratios for the case adopting 24.5 psia as pressure drop limit is not the same as that shown in Figure 4.54. However, the differences are negligible, and therefore such a plot is not displayed.

[37] The dashed region at the top right hand corner of the powermap is a consequence of the "unsolved region" characterizing Case Ox-Backfit-ES. It has to be recalled, however, that such a region is "unsolved" under the thermal-hydraulic viewpoint only, in that VIPRE was not able to analyze the core configurations located in that region. The geometric characteristics of these core configurations have instead been determined, and for this reason the plots showing geometric parameters are not affected by the upper dashed region. Instead, the absence of data in the bottom left hand corner is due to the structural constraint applied to Case Hyd-NewCore-ES, i.e. the maximum number of bundles (see Section 4.5.1). Since the *D-P/D* pairs located in this narrow region systematically exceed the mentioned constraint, they are not associated with any allowed core geometry. Thus, the lack of data concerns both geometric and thermal-hydraulic parameters.

unity, and ranges between 1.2 to 1.4 for most configurations. As found by comparing Case Ox-Backfit-5 to Case Hyd-NewCore-5, the highest power ratios refer to configurations having very large pitch, i.e. P>1.7 cm, which are not interesting since, for both cases, they deliver low power (see Figure 4.31 and Figure 4.39).

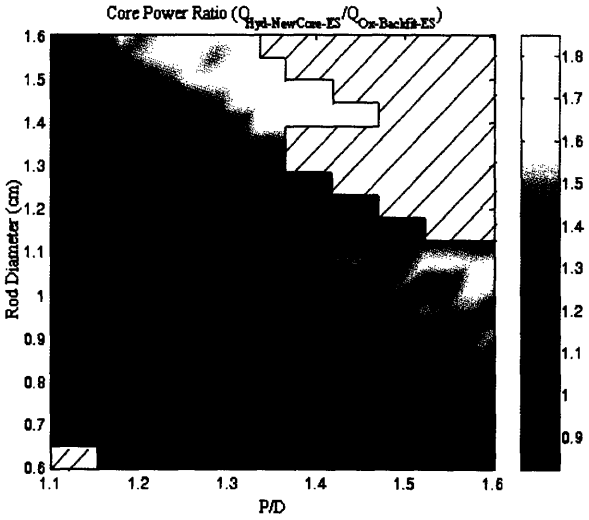

Figure 4.55: Core Power Ratio: Hyd-NewCore-ES / Ox-Backfit-ES
(the green line represents unity ratio)

The reason for these large power ratios lies mainly in the larger number of fuel rods characterizing the "new core" structures, as evident from the right plot of Figure 4.56. It shows that for most configurations the ratio between the number of fuel rods in the two cases ranges between 1.3 to 1.6. In contrast, a smaller contribution is given by the LHGR ratio, which is even below unity for about half of the core configurations, as shown in the left plot of Figure 4.56.

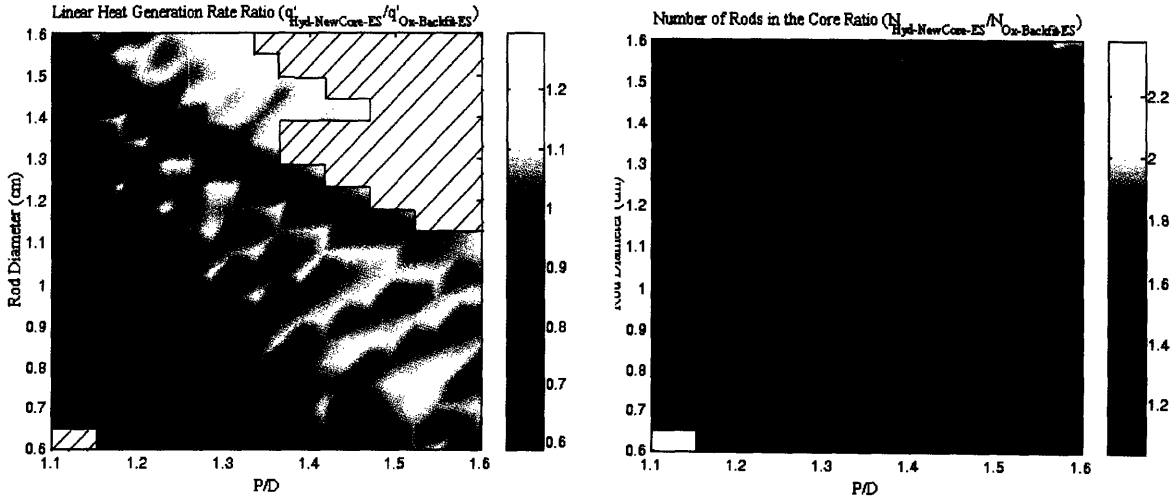

Figure 4.56: LHGR Ratio and Number of Rods Ratio (Hyd-NewCore-ES / Ox-Backfit-ES)

As for the comparison between Case Ox-Backfit-5 and Case Hyd-NewCore-5, it has been verified that the gain in power resulting from the "new core" approach is not due to a better utilization of the "empty" region located between the core shroud and the outermost bundle ring, i.e. the core cross sectional area is substantially the same regardless of the core construction methodology used ("backfit" or "new core").

Chapter 5: Conclusions

The power-related advantages deriving from the implementation of the hydride fuel have been quantitatively proven. The bypass channel and/or the water rod elimination result in a larger volume available for fuel, and therefore in a higher achievable power.

Table 5.1 and Table 5.2 present the results of the whole core analysis. In particular, Table 5.1 shows the key characteristics of the assembly configurations yielding the overall maximum power, i.e. the maximum power achievable for each case over the whole geometry range. In contrast, Table 5.2 compares the power performance of different types of cores when the *D-P/D* pair is fixed at the values corresponding to the reference assembly configuration[38].

The last column of each table shows the power difference percentage, $\Delta\dot{Q}\,\%$, with respect to the maximum achievable power calculated for the reference core/bundle, i.e. 3324 MW_t for the reference BWR/5, 4500 MW_t for the reference ESBWR.

[38] The term "assembly configuration" identifies the coupling "rod diameter-rod pitch" characterizing the bundle design under examination. In particular, the reference assembly configuration for the cases modeling a BWR/5 core is different than that used for the cases modeling an ESBWR core. See Figure 1.2 for the two reference bundles.
Because of the wide geometry spectrum considered throughout the analysis, the quantitative conclusions that can be drawn from the comparisons Oxide-Hydride and Backfit-NewCore in Table 5.2 can not be blindly extended to all the *D-P/D* pairs. The power performance comparison for each *D-P/D* pair can be correctly performed by locating the assembly configuration of interest in the powermaps presented in Chapter 4.

Table 5.1: Overall Maximum Achievable Power Not Accounting for Neutronic Constraints

Case	Vessel Size	Core Structure	Fuel	Δp_{limit} (psia)	*D* (mm)	*P/D*	Fuel Lattice Matrix	$\dot{Q}_{core}$ (MW_t)	$\Delta\dot{Q}_{core}$ %
0 (Ref. BWR/5)	BWR/5	Backfit	Ox	NA*	PrD**	PrD	9×9	3324	0
Ox-Backfit-5	BWR/5	Backfit	Ox	24.5	8.105	1.5737	10×10	3717	+11.8
				36	7.579	1.3632 1.3895 1.4158	12×12	3875	+16.6
Hyd-Backfit-5	BWR/5	Backfit	Hyd	24.5	8.105	1.6000	9×9	3910	+17.6
				36	8.105	1.3895 1.4158 1.4421	11×11	4109	+23.6
Hyd-NewCore-5	BWR/5	NewCore	Hyd	24.5 36	8.105	1.4684	11×11	4997	+50.3[39]
0 (Ref. ESBWR)	ESBWR	Backfit	Ox	N.A.	10.26	1.2622	10×10	4500	0
Ox-Backfit-ES	ESBWR	Backfit	Ox	11	6.000	1.6000	13×13	5621	+24.9
Hyd-NewCore-ES	ESBWR	NewCore	Hyd	11	6.526	1.6000	14×14	7719	+71.5

* NA≡ Not Applicable since Case 0 is used to set the pressure drop limit, i.e. the pressure drop is not imposed as a limit.
** PrD≡ Proprietary Data

Table 5.2: Maximum Achievable Power for the Reference Assembly Configurations

Case	Vessel Size	Core Structure	Fuel	Δp_{limit} (psia)	Fuel Lattice Matrix	$\dot{Q}_{core}$ (MW_t)	$\Delta\dot{Q}_{core}$ %
Ox-Backfit-5	BWR/5	Backfit	Ox	24.5 36	9×9	3324	0
Hyd-Backfit-5	BWR/5	Backfit	Hyd	24.5	9×9	3254	-2.1
				36		3559	+7.1
Hyd-NewCore-5	BWR/5	NewCore	Hyd	24.5 36	8×8	4303	+29.4
Ox-Backfit-ES	ESBWR	Backfit	Ox	11	10×10	4500	0
Hyd-NewCore-ES	ESBWR	NewCore	Hyd	11	11×11	5344	+18.8

[39] This power gain percentage would decrease to +46.4% if a larger thickness was assumed for the gap separating adjacent bundles. See point 6) in the conclusions following Table 5.3 for more details.

Table 5.3 shows the results, again in the form of maximum achievable power, derived from the subchannel analysis described in Appendix A[40]. Unlike the previous two tables, the power performance comparison presented in this last table considers hydride and oxide bundle designs that have been analyzed in detail not only from the thermal-hydraulic point of view, but also (separately) from the neutronic view ([2]). The bundle power chosen as reference is that of the reference oxide bundle, i.e. 6567.7 kW.

Table 5.3: Maximum Achievable Power (Subchannel Analysis, Appendix A)

Bundle Design	*D* (mm)	*P/D*	Limiting Parameter	$\dot{Q}_{bundle}$ (kW_t)	$\Delta\dot{Q}_{bundle}$ %
Oxide 9×9 (reference)	PrD*	PrD	MCHFR	6567.7	0
Oxide 10×10 (WC)**	10.260	1.2622	MCHFR	7319.2	+11.4
Hydride 10×10 (BC-4)	11.176	1.300	Pressure Drop	9917.8	+51.0
Hydride 12×12	9.281	1.300	Pressure Drop	9703.7	+47.7

* PrD≡ Proprietary Data

** The designations WC and BC-4 are used in the subchannel analysis to identify the bundle designs. See Appendix A for details.

The key considerations arising mainly from Table 5.1 are the following:

1) Since the power gain percentages $\Delta\dot{Q}_{core}$ shown in Table 5.1 result from the application of thermal-hydraulic constraints only, they can not be defined as "final gain percentages", i.e. they do not represent the actual maximum power benefits that would derive from the implementation of the hydride fuel in a BWR core. In contrast, they represent the maximum power gains if the thermal-hydraulic constraints were the only constraints to be applied. Only the coupling of these results with those deriving from a neutronic feasibility analysis would yield the power benefits actually achievable by using the hydride fuel. A preliminary neutronic analysis based on the application of reactivity and fuel burnup constraints to $UZrH_{1.6}$ 5% enriched, loaded into bundles suited for a "NewCore"

[40] The results presented in Table 5.3 refer to the comparison designated, in Appendix A, as "Comparison 1" (see Table A.4). Although this Appendix compares the various bundle designs under different sets of assumptions designated as "Comparison 1", "Comparison 2", etc., "Comparison 1" best illustrates the different achievable powers. It compares the various bundle designs on a fair basis since they have the same inlet and outlet conditions, i.e. same inlet enthalpy and same exit quality, and none of the hard or soft constraint is exceeded.

structure (no bypass channels), ([29]) shows that, regardless of the fuel rod diameter, the geometry spectrum $1.1 \leq P/D \leq .6$ can be divided in 3 regions:

- feasible region: $1.1 \leq P/D \leq .2$. In this region there are no limitations due to the reactivity coefficients, and the theoretical burnup can be achieved;
- feasible region but with limited burnup: $1.2 < P/D \leq .35$. These geometries can safely reach only a fraction of the theoretical burnup;
- non feasible region: $P/D > 1.35$. These geometries are not feasible due to limitations on the reactivity coefficients.

If these neutronic limitations were applied to the thermal-hydraulic "NewCore" analysis, and a 5-mm gap was assumed to separate adjacent bundles (in place of the 2-mm gap), the overall maximum powers would no longer be those shown in Table 5.1, but those shown in Table 5.4.

Table 5.4: Overall Maximum Achievable Power for Hydride NewCore Cases Accounting for Preliminary Neutronic Results

Case	Vessel Size	Δp_{limit} (psia)	Neutronic feasibility region	D (mm)	P/D	Fuel Lattice Matrix	$\dot{Q}_{core}$ (MW_t)	$\Delta\dot{Q}_{core}$ %
Hyd-NewCore-5	BWR/5	24.5	Feasible	11.789	1.2053[41]	8×8	3909	+17.6
			Feasible BU limited	8.632	1.3368	11×11	4413	+32.8
		36	Feasible	9.684	1.2053	11×11	4149	+24.8
			Feasible BU limited	8.105	1.3105	14×14	4764	+43.3
Hyd-NewCore-ES	ESBWR	11	Feasible	14.947	1.2053	8×8	5625	+25.0
			Feasible BU limited	1.0211	1.3105	11×11	6250	+38.9

It follows that, for a BWR/5-size vessel provided with a 5-mm inter-bundle gap, the application of thermal-hydraulic AND neutronic constraints would yield a maximum power gain percentage ranging between 17.6 to 24.8%, depending on the pressure drop limit adopted. However, if a lower burnup was considered acceptable, the gain percentages would be higher, ranging between 32.8% to

[41] Although the feasible region has been defined as $1.1 \leq P/D \leq .2$, the preliminary nature of the neutronic calculations allows accepting a margin in the limits. For this reason, the assembly configurations having P/D=1.2053 are considered feasible and able to achieve the theoretical burnup.

43.3%. Likewise, for an ESBWR-size vessel, the power gain percentages would range from 25% to 38.9%, depending on the burnup level considered acceptable.

2) Unlike Table 5.1, the neutronic constraints do not have a significant[42] influence on the power gain percentages shown in Table 5.2 and Table 5.3. In fact, these tables refer to bundle designs that:
   - coincide with those chosen as reference, whose feasibility is clearly proven, or
   - have been separately analyzed under the neutronic viewpoint, or
   - have lattice parameters, i.e. *D* and *P*, very close to those corresponding to the bundle designs mentioned at the two previous points. Thus, their neutronic feasibility can be inferred.

The remaining considerations refer explicitly to the thermal-hydraulic analyses performed without neutronic constraints and with the inter-bundle gap of 2 mm.

3) With respect to the reference core geometry, a significant increase in power would be reachable even without changing the type of fuel but significantly reducing the rod diameter and slightly increasing the pitch. In particular, for a BWR/5 core the increase in power would range between 11.8% and 16.6% (Case Ox-Backfit-5), depending on the pressure drop limit adopted. For the ESBWR core such an increase is even higher, reaching +23.4% (Case Ox-Backfit-ES). However, the choice of fabricating smaller rods should be carefully made in consideration of the short fuel constant time impact on two-phase instability and the mechanical feasibility of the new rods. Should these aspects be acceptable, the extracosts that would be necessary to manufacture the new rods may be compensated by the gain in power. Moreover, the core structure modifications

[42] Based on the feasibility regions described at point 1), the hydride bundles having *P/D* of 1.3 fall in the region designated as "feasible but burnup limited". Although the neutronic analysis revealed that *P/D* of 1.15 offers the maximum hydride fuel discharge burnup ([2]), the thermal-hydraulic analysis suggested that higher power could be generated with an increase in *P/D*. The reduction in achievable burnup can be recovered by increasing the fuel enrichment to 7.70%: in this way it is possible to obtain a cycle as long as that of the reference oxide fuel with the 10x10 high power density hydride fuel bundle ([30]).

that would be required in case of changing from oxide to hydride fuel are avoided, with a consequent economic saving.

4) For a BWR/5, if the implementation of the hydride fuel is performed maintaining the ex-bundle core structure unchanged, i.e. maintaining the bypass channels for the cruciform control rod insertion, the maximum gain in power would range between 17.6% to 23.6% (Case Hyd-Backfit-5), again with respect to the reference BWR/5 core. In agreement with point 1), besides the change in fuel type the maximum gain in power would be achievable by reducing the rod diameter and slightly increasing the pitch. However, by comparing these power gain percentages with those mentioned at point 1), it can be concluded that outside the pressure drop limited region[43] a hydride backfit core delivers about 5.8-7% more power than an oxide core having roughly the same *D-P/D* pair (from comparison between Case Hyd-Backfit-5 and Case Ox-Backfit-5: 5.8%=17.6-11.8; 7%=23.6-16.6).

5) The greater design freedom allowed in the "NewCore" approach yields the construction of hydride cores able to deliver powers significantly higher than those corresponding to the cores chosen as reference. In particular, for BWR/5-size reactors the maximum gain in power is 50.3% (Hyd-NewCore-5), while for ESBWR-size reactors it is even higher, i.e. 71.5% (Hyd-NewCore-ES). This difference in power gain percentage, i.e. 50.3% versus 71.5%, is due to the larger fuel rod ratio for the *D-P/D* pair yielding the maximum power in Case Hyd-NewCore-ES[44] versus that yielding the maximum power in Case Hyd-NewCore-5. However, this is not due to better space utilization of Case Hyd-NewCore-ES, but to the absence of the limiting effect on the power that is usually exerted by the vibration ratio on core configurations located in the bottom right hand corner of

[43] See Figure 4.47 for the location of the pressure drop limited region, i.e. where a hydride backfit core delivers a lower power than an oxide one having the same *D-P/D* pair.

[44] The reference BWR/5 and the reference ESBWR contain 56536 and 104144 fuel rods respectively. Instead, the core configuration yielding the maximum power for Case Hyd-NewCore-5 contains 89980 rods, while that yielding the maximum power for Case Hyd-NewCore-ES contains 196560 rods. Thus, the number of rod ratio is equal to 1.59 (=89980/56536) for the comparison referred to Case Hyd-NewCore-5, while it is 1.89 (=196560/104144) for the comparison referred to Case Hyd-NewCore-ES. Since the LHGR ratio is roughly the same for both comparisons (0.945 for the former comparison and 0.990 for the latter), the parameter responsible for the different power gain percentage is the number of fuel rods.

the powermaps, i.e. where the configuration yielding 7719 MW_t is just located. When such an effect is present, i.e. in Case Hyd-NewCore-5, the vibration ratio of these core configurations matches the maximum allowed value, while the MCPR is well above the minimum allowed value[45].

6) The power gain percentages delivered by the Hydride NewCore configurations would be reduced if a different choice of the thickness of the gap that separates adjacent bundles was made[46]. Such a gap was optimistically fixed at 2 mm, a value which is about 1/3 of the thickness remaining after subctracting the cruciform control rod thickness from the gap of the reference BWR/5. It has been verified that, if the gap was fixed at the larger value of 5 mm, the assembly configuration characterized by the maximum power gain percentage of Case Hyd-NewCore-5 would change. It would no longer have P/D=1.4684, but P/D=1.3105, while the rod diameter would remain the same, i.e. 8.105 mm. In spite of this change in geometry, the maximum gain in power would be only slightly affected, since it would decrease from +50.3% to +46.4%.

   Although these considerations are also valid for Case Hyd-NewCore-ES, the assembly configuration yielding the maximum power gain percentage for this case, i.e. +71.5%, would not be affected by the mentioned change in inter-bundle gap thickness. This is because, in the case of a 2 mm gap, the "empty" space separating the outermost bundle ring from the core shroud is wide enough to allow the change in gap thickness without cause the peripheral bundles to touch the core shroud.

7) As for Case Hyd-Backfit-5, also for Case Hyd-NewCore-5 the maximum gain in power is achievable by reducing the rod diameter and by increasing the rod pitch, with respect to the reference *D-P/D* pair. However, even for the same *D-P/D* pair,

---

[45] For example, in Case Hyd-NewCore-5 the core configuration having D=6.526 mm and P/D=1.6 (same *D-P/D* pair as the Hyd-NewCore-ES configuration yielding 7719 MW_t) is characterized by a MCPR of 1.3480>>MCPR limit=1.015.

[46] All the NewCore configurations are characterized by a certain gap between the outermost bundle ring and the core shroud. Should the larger gap thickness cause the outermost bundle ring to touch the core shroud, the triplet *D-P-n* under examination would yield a reduced number of bundles, and therefore a lower power. However, such a lower power may be not the final power that VAMPIRE associates with the *D-P/D* pair under examination. A higher power (but lower than that corresponding to the case of an unchanged gap thickness) may result from the coupling of the pair *D-P/D* to a different matrix index *n*.

the comparison Backfit-NewCore presented in Table 5.2 shows that the rearrangement of the core allowed by the NewCore design technique yields a significant gain in power. For the reference assembly configuration it is of 29.4% (Hyd-NewCore-5 in Table 5.2), while the same *D-P/D* pair in a Backfit core delivers only 7.1% more power for the upper pressure drop limit, and even 2.1% less power for the lower pressure drop limit (Hyd-Backfit-5 in Table 5.2).

8) The higher power achievable with the hydride fuel is a consequence of the larger amount of fuel that can be fit into the core. For the same *D-P/D* pair, the extra-amount of fuel is quite significant (+30÷40%) if the hydride fuel implementation is performed following a NewCore approach, while is lower (~+15%) when the Backfit structure of the core is maintained. This is shown in the right plot of Figure 4.48 and Figure 4.51. In contrast, for most of the *D-P/D* pairs, it was found that the absence of water rods inside the bundles seems to slightly reduce the critical heat flux, making the LHGR for hydride fuel pins slightly less than for pins in the typical oxide assembly provided with water rods. The left plot of Figure 4.48 and Figure 4.51 show the complete LHGR ratio map, while Appendix G investigates this phenomenon for the reference BWR/5 assembly configuration.

9) As regards Table 5.1 and Table 5.2, the assumption of neglecting the presence of the Partial Length Fuel Rods (PLFRs) in the reference oxide cores yields an over-estimate of the power gain. It has been separately demonstrated, by means of a subchannel analysis, that the presence of the PLFRs would allow getting about 6% more power, without exceeding the limit fixed for the MCPR. Thus, assuming that the hydride bundles will be designed without this feature, which instead characterizes the more recent BWR oxide bundles, the power gain percentages referred to the Hydride Backfit cases should be reduced by about 6%. Conversely, for the Hydride NewCore cases, such a reduction although still present would be counterbalanced, and even overwhelmed, if a different and more careful choice of the number of control fingers per hydride bundle had been performed. In fact, the algorithm used to choose the number and location of the control fingers in each hydride bundle (see Figure 3.9) is not based on a neutronic optimization of the bundle itself, and the resulting number of control fingers is much higher than that

demonstrated to be sufficient to guarantee sufficient power control. The 10×10 hydride bundles presented in Appendix A, which are designed based on a neutronic optimization, contain only 4 control fingers, that is 12 less than those contained in the 10×10 hydride bundles modeled in the whole core analysis (see Table D.1). Should such an optimization be implemented in the whole core analysis, the 10×10 Hydride NewCore configurations would yield about 14% more power (96/84=1.14), and the 6% loss in power gain due to having neglected the PLFRs in the oxide bundles would be more than fully recovered.

10) It should be observated that there is consistency between the whole core analysis results referred to Case Hyd-NewCore-5 in Table 5.1 and the subchannel analysis results of Table 5.3. The two hydride geometries in Table 5.3 have power gains comparable to that of the Hyd-NewCore-5 configuration achieving the maximum power (all about 50%). This consistency is however more a coincidence than a rational conclusion since the whole core and subchannel analyses are based on several differing assumptions. For example, the "NewCore" and the subchannel analysis use:

- a different number of control fingers per bundle;
- a different modeling of the Partial Length Fuel Rods;
- a different pin-by-pin power distribution for the hydride bundles.

Even more important is that, while the geometry range investigated by the whole core analysis is large enough to include all the reasonable geometries ($0.6 \leq D \leq 1.6$ cm, $1.1 \leq P/D \leq 1.6$), the subchannel analysis is focused on a limited number of bundle geometries. Therefore, the maximum achievable power delivered by the former is the <u>overall</u> maximum achievable power, while that delivered by the latter may increase if a larger number of bundle designs was analyzed.

Chapter 6: Future Work

The final objective of the comparison between the two fuel types is focused not only on power performance, but on the assessing if any economic advantage is derived from the implementation of the new fuel. In fact, the significant power levels which the present analysis proved to be achievable, under the thermal-hydraulic constraints applied during normal operational conditions, are not a sufficient proof of the hydride configurations economic advantage. This means that the achievement of the final objective requires a close examination of aspects, not directly related to the power performance but having an economic impact as well. However, before undertaking this task, it is necessary to complete the power performance study by adding a transient analysis, as described in the next paragraph.

Once completed, the transient and steady state results can be put together and used to compile an economic analysis. The one already performed by Shuffler for PWRs ([31]) can be used as useful model.

6.1 Transient Power Performance Analysis

The results presented in this report are specifically referred to normal operational conditions and the power levels labeled as "achievable" satisfy steady state requirements only. In the transient analysis the limits of MCPR, fuel centerline temperature and all the other parameters listed in Table 2.3 will be maintained, but at the same time other parameters need to be applied as new power limiting constraints. Given a core geometry configuration, the maximum achievable power obtained in the steady state analysis may result in exceeding the limit values fixed for the operational transients. For example, the LOCA performance analysis is usually evaluated by considering the time history of the peak clad temperature following the pipe break. Though the control rods are driven in with some inherent small time delay to stop the nuclear reaction, decay of fission products (which depends on the steady state power) provides a continued heat source that must be removed to protect the integrity of the clad and fuel. For many geometry configurations, power levels which satisfy the steady state constraints would result in an

excessive clad temperature in case of LOCA. Therefore, such designs can be made acceptable by reducing the steady-state power in the core.

However, since LOCA is not the only transient to be considered, the transient power performance analysis should be preceded by a careful study aimed at identifying the most limiting transients, for which the maximum allowable power may be lower than that delivered by the steady state analysis.

6.2 Analysis of Other Economics-related Issues

For economic purposes, the power performance analysis cannot be defined as complete until a transient-powermap is available. Once this result is achieved, the main power performance-related input to the economic analysis will be the superimposition of the two powermaps, such that for each core geometry the minimum power between the two available (steady state power and transient power) is chosen.

As highlighted by Shuffler ([31]), besides the power performance already mentioned and partly analyzed, the primary inputs to the economics analysis also include:

- maximum achievable burnup calculation from the neutronics and fuel performance studies;
- specific unit cost estimates for front and back end components of the fuel cycle, operations and maintenance activities, and plant capital.

The first study is required to get the maximum burnups for hydride and oxide fuels that can guarantee criticality preservation as well as protection of fuel pin integrity during irradiation. This study also provides the range of geometries with acceptable (negative) fuel and moderator temperature coefficients. The purely economics aspects have to be accounted for in the second study: in particular, they include the calculation of the extra-costs required to adjust the plant components to the higher power achievable with the new fuel.

Only after having performed the analyses listed above, can the two fuel types be rationally compared under the economic point of view. In this way, the analyst will be able to decide whether the implementation of the hydride fuel in an existing plant is economically beneficial or, vice versa if the power increase is not sufficient to overcome

the extracosts required to update the plant components. Moreover, as already highlighted in Chapter 5 (point 3), the final analysis results may even drive the decision making process to a better oxide core modeling, aimed at achieving a higher power without change of the type fuel.

Appendix A

A1. Comparison Between Oxide and Hydride Bundles Via Subchannel Analysis

A1.1. Motivation for the Analysis

To simplify the programming and limit the computational time, the wide spectrum of core geometries examined in the whole core analysis required the elaboration of several simplifying assumptions (see Chapter 3). The decision to model the Partial Length Fuel Rods (PLFRs) as Full Length Fuel Rods (FLFRs), together with the use of a simplified algorithm to place control fingers inside the hydride bundles are the most important examples. Moreover, except for the reference oxide bundles, which are used in current plants and therefore there is a valid proof of their feasibility, none of the other assembly geometries has been subjected to neutronic calculations. For this reason, the bundle designs examined in the whole core analysis can not be defined as "optimized", either from the thermal-hydraulic point of view, or the neutronic one.

The present Appendix is aimed at investigating the power performance of a very limited number of bundle designs for which a neutronic analysis together with the related "optimization" has also been separately performed. The main consequence of the optimization consisted of a significant reduction in the number of control fingers, i.e. for a 10×10 hydride bundle the number dropped from 16 (number used in the whole core analysis) to only 4. Moreover, concerning the bundle thermal-hydraulic modeling, the inherent nature of the subchannel analysis allows accounting for geometric details that are neglected in the whole core approach. The most important of these is the presence of the PLFRs in the oxide bundles.

A1.2. Analysis Objective

This analysis is aimed at comparing the power performance of different hydride and oxide bundles with those of the oxide GE11 bundle, which is chosen as reference. All the Bundle Units[47] examined occupy the same cross sectional area, regardless of the fuel type

[47] A Bundle Unit is composed of the bundle itself (canister plus rods) and the bypass channel that surrounds it. Since the channel is shared by adjacent bundles, only half has been modeled and included in the bundle

and the lattice type. The comparison is performed by calculating the maximum bundle power that does not exceed any thermal hydraulic constraint. The VIPRE code is used to perform the analysis, which consists of a subchannel analysis of the bundles of interest.

A1.3. Reference Bundle Design

The GE11 is the same bundle design chosen as reference for the BWR/5 whole core analysis (see Figure 1.2). However, while the whole core analysis assumed that all the 74 fuel rods contained in the bundle were Full Length Fuel Rods (FLFRs), the subchannel analysis is performed accounting for the 8 Partial Length Fuel Rods (PLFRs) actually contained in the GE11 bundle[48]. Such a reference bundle is assumed to operate under the conditions characterizing the hot bundle of the reference BWR/5 core. In particular:

- bundle thermal power: 6567.7 kW[49];
- axial power profile common to that used in the analysis of the BWR/5 core[50] (see Figure 3.3);
- local peaking factors shown in Figure A.1;
- operating pressure: 1035 psia;
- coolant inlet temperature: 278.3 °C;
- total flow rate: 16.98 kg/s, of which 86% is active flow, 4% flows through the Water Rods (WRs), and 10% through the bypass channel that surrounds the bundle box[51].

---

layout. For the oxide bundles, the presence of two wings of the adjacent cruciform control rod is accounted for by reducing the effective bypass coolant flow area.

[48] The possibility to account for the PLFRs is a consequence of two main factors. First, contrary to the CPR correlation used in the whole core analysis, the CHFR correlation used in the subchannel analysis allows this design feature to be modeled, and is able to capture its power-related benefits. Second, the more restricted number of bundle geometries examined in the subchannel analysis allows the modeling of each bundle more realistically.

[49] Given the thermal power, the maximum core radial peaking factor and the total number of bundles of the reference BWR/5 (3323 MW, 1.51 and 764 respectively, see Table 1.1 and Figure 3.4), the hot bundle power results to be: $\frac{3323 \cdot 1000}{764} \cdot 1.51 = 6567.7\,\text{kW}$.

[50] The axial power profile of the PLFRs is the same as that of the FLFRs up to the top of the rods. Above this level it is set to 0.

[51] The active flow rate assumed for the reference bundle corresponds to the hot bundle active flow rate derived from the whole core analysis of the reference BWR/5 core.

For such operating conditions, the subchannel analysis delivers an exit quality[52] of 26.8%.

A1.4. Bundles Examined

The bundle designs examined are listed as follows:

- reference oxide 9×9 (GE11);
- oxide 10×10 (similar to the GE14);
- several 10×10 hydride bundles;
- hydride 12×12 bundle;

Geometric key characteristics are summarized in Table A.2.

A1.5. Thermal Hydraulic Constraints

The thermal hydraulic constraints are distinguished between "hard" and "soft" constraints. The former must not be exceeded, either because this would result in some failure mechanisms or because the plant does not have the capability to sustain certain operating conditions. Conversely, exceeding the "soft" constraints does not necessarily result in a failure mechanism, even though the decision to operate under such conditions should be preceded by a careful investigation aimed at excluding the occurrence of any of these phenomena. Table A.1, which summarizes the constraints used, is followed by a brief description of each.

[52] Throughout the whole subchannel analysis, the term exit quality is used to identify the subchannel-averaged exit quality, i.e. the value obtained by averaging the exit quality of the subchannels only; the flow through water rods, control rod channels and control rod guide tubes is not accounted in the averaging procedure.

Table A.1; Subchannel Analysis Thermal Hydraulic Constraints								
	MCHFR	**Pressure drop (psi)**	**Fuel centerline T (°C)**		**Fuel avg T (°C)**		**Clad surface T (°C)**	**Exit quality (%)**
Fuel	Both	Both	Oxide	Hydride	Oxide	Hydride	Both	Both
Numerical Value	1.158	22.6 34.0	2805	750	1400	N.A.	349	26.8
Type of Constraint	HARD	HARD	HARD		HARD		HARD	SOFT

N.A. ≡ Not Applied

- Minimum Critical Heat Flux Ratio (MCHFR): 1.158. This value results from the use of the EPRI-1 correlation ([4]) in the subchannel analysis of the reference GE11 bundle. Although it is a critical heat flux correlation and not a critical power correlation, it has been demonstrated that it gives even a more accurate prediction of the critical bundle power (via critical heat flux) than the Hench-Gillis correlation ([32]).
- Pressure drop: two different limits are used: 22.6 psia is the pressure drop of the reference GE11 bundle, while the upper limit, i.e. 34 psia, derives from the assumptions that a 50% pressure drop increase with respect to the reference bundle is a reasonable estimate of the maximum value that could be achieved in the near future. Although such an assumption is the same as that made in the whole core analysis, the two numerical values slightly differ from those used for the whole core, i.e. 24.5 psia and 36 psia. This is due to having modeled the PLFRs, which gives a lower contribution to the friction losses than the FLFRs.

The numerical values of the remaining hard constraints are the same as those used in the whole core analysis. For this reason, related considerations can be found in Section 2.2.1.

- Fuel centerline temperature: the maximum allowed temperatures are 2805 °C for UO_2 (to prevent from melting) and 750 °C for $UZrH_{1.6}$ (to prevent excessive hydrogen release).
- Average fuel temperature for oxide fuel: 1400 °C (to limit fission gas release below 5% ([17]).

- Clad surface temperature: 349°C (to assure enough margin between the oxide thickness that unavoidably tends to form during normal operation and the 17% limit in oxide thickness referred to the severe LOCA accidents).

Besides the constraints just described, a "soft" constraint is also considered. It is represented by the subchannel averaged exit quality, whose maximum value has been set equal to the subchannel averaged exit quality of the reference bundle, i.e. 26.8%. Such a parameter has a significant influence on the thermal-hydraulic stability of the bundle channel, which is usually expressed by means of the Decay Ratio (DR). However, since the DR is also a function of the time constant of the fuel and especially of the channel inlet orificing coefficient, exceeding the mentioned maximum quality does not necessarily cause exceeding of the maximum allowed DR[53]. This reason, together with the fact that the present analysis was not aimed at the inlet orificing optimization, justifies the choice to allow the exit quality to exceed the mentioned value. However, since the quality in the channel has also an important effect on the neutron moderation, whenever the reference exit quality is exceeded it will be well highlighted.

A1.6. Operating Conditions and Pin-by-Pin Power Distributions

The comparison between bundle performance is performed assuming system pressure, coolant inlet temperature and axial power profile identical to those used for the reference bundle. Moreover, consistent with the assumption made in the whole core analysis, the fuel-clad gap conductance has different values for oxide fueled rods and hydride fueled rods:

- oxide fueled rods $\rightarrow h_g^{He} = 5.6826$ kW/K m^2 (helium-filled gap[54])

[53] The maximum allowed channel Decay Ratio usually ranges from 0.55 to 0.8, depending on the value of the Core Decay Ratio (Figure 4.4-3 of [7]). As an example, according to the Preliminary Safety Analysis Report of Lungmen 1 and 2 ([7]), the channel Decay Ratio of these plants is predicted to be 0.12. In spite of the strong influence that the inlet orificing has on the DR, such a parameter was not used as a constraint for two reasons: first, the code used in Appendix C to provide an estimate of the DR is still in a development phase since it does not account for all the form pressure losses present along the bundle. Second, the simplifying assumption made for the orificing coefficients of the various bundles examined would be inconsistent with the choice of such a parameter as a constraint, since such a choice would require an optimization procedure of the inlet orificing.

[54] See Section 3.2.2, point a) of "Other assumptions and considerations" for details concerning the numerical value used for the gap conductance.

- hydride fueled rods → $h_{LM} = 2k_{LM}\,[D_{fo}\,\ln(D_{ci}/D_{fo})]^{-1}$ (liquid-metal bonded gap), where k_{LM} is the liquid metal conductivity (see Table Table J.1), D_{fo} is the pellet diameter, D_{ci} is the clad inner diameter.

Regarding the in-bundle power distribution, one distribution is considered for the oxide reference 9×9 bundle, while two are considered for the oxide 10×10 bundle and for most of the hydride bundles, namely "Worst Case" (WC) and "Best Case" (BC). They are shown in the following tables, where colors are used to identify:

- unoccupied positions resulting from the presence of the water rods: blue;
- PLFRs: red;
- Control Rod Guide Tubes (CRGTs): grey.

REFERENCE OXIDE 9×9

1.16	1.28	1.27	1.24	1.23	1.24	1.27	1.28	1.17
1.28		1.03	0.45		0.45	1.03		1.28
1.28	1.03	0.43	0.88	1.02	0.93	0.44	1.04	1.28
1.24	0.45	0.88	1.15			0.94	0.46	1.24
1.23		1.02				1.01		1.22
1.25	0.46	0.95			1.13	0.86	0.45	1.23
1.29	1.03	0.44	0.94	1.02	0.88	0.44	1.02	1.26
1.27		1.03	0.45		0.45	1.02		1.28
1.15	1.27	1.27	1.25	1.23	1.24	1.27	1.26	1.16

Figure A.1: Pin by Pin Power-to-Average Power Ratio for Fresh Bundle Oxide Fuel with Gd (from Figure 4 of [2], re-normalized to 74 rods)

OXIDE 10×10 (WC)

1.16	1.28	1.27	1.24	1.23	1.23	1.24	1.27	1.28	1.16
1.28		0.50		0.90	0.90		0.50		1.28
1.28	0.46	0.97	0.50	0.98	1.15	1.00	0.97	0.46	1.28
1.24		0.96	0.97	1.00			1.00		1.24
1.23	0.90	0.50	1.00				1.00	0.90	1.23
1.23	0.90	1.00				1.00	0.50	0.90	1.23
1.24		1.00			1.00	0.97	0.96		1.24
1.28	0.46	0.97	1.00	1.15	0.98	0.50	0.97	0.46	1.28
1.28		0.50		0.90	0.90		0.50		1.28
1.16	1.28	1.27	1.24	1.23	1.23	1.24	1.27	1.28	1.16

Figure A.2: Pin by Pin Power-to-Average Power Ratio for 10×10 oxide bundle (Power distribution of Figure A.1 arbitrarly extended to 10×10 lattice)

OXIDE 10×10 (BC)

1.05	1.04	1.03	1.02	1.02	1.02	1.02	1.03	1.04	1.05
1.02		1.01		1.00	1.01		1.01		1.02
1.03	0.99	0.97	0.97	0.98	1.00	1.00	0.97	0.99	1.03
1.02		0.96	0.96	1.00			1.00		1.02
1.02	0.98	0.98	1.00				1.00	0.98	1.02
1.02	0.98	1.00				1.00	0.98	0.98	1.02
1.02		1.00			1.00	0.96	0.96		1.02
1.03	0.99	0.97	1.00	1.00	0.98	0.97	0.97	0.99	1.03
1.02		1.01		1.01	1.00		1.01		1.02
1.05	1.04	1.03	1.02	1.02	1.02	1.02	1.03	1.04	1.05

Figure A.3: Pin by Pin Power-to-Average Power Ratio for 10×10 oxide bundle, ("Best Case" of Figure A.5 arbitrarily[55] extended to an oxide 10×10 bundle)

HYDRIDE 10×10 (WC)

1.24	1.20	1.17	1.12	1.07	1.07	1.11	1.17	1.21	1.24
1.21	1.18	1.14	1.04	0.91	0.91	1.03	1.14	1.18	1.19
1.18	1.15		0.95	0.51	0.51	0.94		1.14	1.17
1.12	1.02	0.94	0.89	0.81	0.81	0.89	0.94	1.03	1.12
1.08	0.89	0.50	0.81	0.89	0.89	0.81	0.51	0.90	1.07
1.07	0.91	0.51	0.81	0.90	0.90	0.81	0.50	0.89	1.06
1.13	1.04	0.95	0.89	0.81	0.80	0.90	0.94	1.03	1.10
1.16	1.15		0.94	0.51	0.51	0.95		1.14	1.16
1.21	1.19	1.13	1.04	0.91	0.90	1.03	1.15	1.17	1.20
1.25	1.21	1.17	1.11	1.07	1.07	1.11	1.16	1.20	1.25

Figure A.4: Pin by Pin Power-to-Average Power Ratio for Fresh Bundle Hydride Fuel with Gadolinia (from Figure 13 of [2])

HYDRIDE 10×10 (BC)

1.04	1.02	1.02	1.01	1.01	1.00	1.01	1.02	1.02	1.05
1.02	1.02	1.03	1.00	0.98	0.98	1.00	1.03	1.02	1.03
1.01	1.03		1.02	0.97	0.97	1.02		1.03	1.02
1.00	1.00	1.01	0.98	0.96	0.97	0.99	1.01	1.00	1.01
1.00	0.98	0.97	0.96	0.96	0.95	0.97	0.97	0.97	1.01
1.00	0.97	0.97	0.96	0.95	0.96	0.96	0.97	0.98	1.00
1.00	0.99	1.01	0.98	0.96	0.97	0.98	1.02	1.00	1.01
1.01	1.03		1.01	0.97	0.97	1.02		1.04	1.03
1.01	1.00	1.02	0.99	0.98	0.98	1.00	1.03	1.01	1.03
1.04	1.02	1.01	1.00	1.00	0.99	1.01	1.02	1.02	1.05

Figure A.5: Pin by Pin Power-to-Average Power Ratio for Fresh Bundle Hydride Fuel with IFBA (from Figure 40 of [2])

[55] While the other power distributions derive from neutronic calculations performed on the bundles to which they are referred, an oxide 10×10 bundle has been assumed to have this power distribution in order to compare its maximum achievable power to that of the hydride 10×10 bundle for which such a distribution was actually calculated. However, that such a flat pin-by-pin power distribution is hard to obtain for an oxide bundle.

HYDRIDE 12×12

1.05	1.03	1.02	1.01	1.01	1.01	1.01	1.01	1.02	1.02	1.03	1.05
1.03	1.02	1.03	1.00	0.99	0.99	1.00	1.03	1.00	1.03	1.02	1.03
1.03	1.04		1.02	0.98	0.97	0.98	0.99	1.03		1.04	1.02
1.00	1.00	1.02	0.99	0.96	0.97	0.99	0.97	0.99	1.02	1.00	1.00
1.00	0.98	0.98	0.98	0.96	0.95	0.97	0.97	0.98	0.98	0.98	1.00
1.02	0.99	0.98	0.96	0.95	0.96	0.96	0.97	0.98	0.97	0.99	1.01
1.01	1.00	0.97	0.98	0.96	0.97	0.98	0.98	0.97	0.97	0.98	1.00
1.01	1.03	0.99	1.01	0.97	0.97	0.96	0.97	0.97	0.99	1.00	1.01
1.01	1.00	1.02	0.98	0.98	0.98	0.98	0.98	0.99	1.02	1.00	1.01
1.02	1.04		1.03	0.98	0.98	0.97	0.98	1.02		1.04	1.03
1.03	1.02	1.03	0.99	0.98	0.99	0.98	1.01	1.00	1.03	1.02	1.03
1.05	1.03	1.02	1.01	1.01	1.01	1.01	1.02	1.02	1.02	1.03	1.05

Figure A.6: Pin by Pin Power-to-Average Power Ratio for Hydride 12×12 Bundle ("Best Case" of Figure A.5 arbitrarily extended to 12×12 lattice)

A1.7. Bundle Geometry Assumptions

Geometric data applied in the analysis of the oxide GE11 and to the oxide 10×10 bundles are the same as those used in the whole core analysis for the reference BWR/5 bundle and for the reference ESBWR bundle respectively, with few exceptions:

- both bundles are modeled accounting for the presence of PLFRs;
- the heated and total length of the oxide 10×10 bundle are assumed to be the same as those of all the other bundles examined. Moreover, the length of its PLFRs is assumed to be the same as that of the PLFRs contained in the reference GE11 bundle;
- the rods of the oxide 10×10 bundle are assumed to be supported by 7 grid spacers, and not 8 as in the GE14 bundle used to modeled the reference ESBWR.

Other important assumptions referred to all the bundles examined are described below.

- All the bundles are modeled with the same form losses: inlet orificing[56], Lower Tie Plate (LTP), 7 grid spacers, Upper Tie Plate (UTP). They are also assumed to be located at the same axial positions, regardless of the bundle design. Such axial locations are those used in the whole core analysis for the reference BWR/5

[56] Oxide and hydride bundles are modeled with 3 inlet orificing coefficients. They are applied to the active flow area, to the bypass channel, and to the water rods or to the Control Rod Guide Tubes depending on whether the bundle is oxide or hydride fueled.

bundle[57] (see Table E.1). The numerical values used for the form losses are those used in the whole core analysis to model the reference BWR/5 bundle. In particular:

$C_{active\_flow\_area} = 21.089$

$C_{grid} = 1.1040$

$C_{LTP} = 9.4609$

$C_{UTP} = 0.3751$

(see Section E1.2. in Appendix E for details about the relations used to obtain such numerical values). For the oxide bundles, the other inlet orificing coefficients, i.e. for WRs and bypass channels, are chosen such that 4% of the total flow is diverted through the WRs and 10% through the bypass channel. These percentages are typical of BWR oxide fueled cores ([24]). In contrast, for the hydride bundles, the orificing coefficients for the CRGTs and bypass channels are chosen such that 2.5% of the total flow is diverted though the former, and about 1.0% through the latter. These percentages are estimates of the flow required to remove the small amount of energy generated from nuclear reactions in these absorbers and of the flow which will necessarily pass through the bypass region which has been sized as small as judged possible.

While the active flow area orificing coefficient is maintained constant through the whole analysis regardless of the exit quality and the type of bundle, those for WRs, bypass channel and CRGTs are varied to preserve the above specified flow split percentages.

- Except for the reference oxide bundle, which is fully described in [12], and for the hydride 10×10 bundles described in [33], for all the other bundles the clad and fuel-clad gap thicknesses are calculated by means of the same scaling relations used in the whole core analysis, which are fully described in Section E1.3. of Appendix E (see point b) of "Bundle structure assumptions").

[57] Except for the Upper Tie Plate (UTP), which is modeled in its actual axial position, i.e. 162 inches. In fact, the use of the EPRI-1 correlation allows modeling the bundles with a heated length that differs from the total length. Thus, the reduction of the axial location of the UTP, which characterized the whole core analysis, is no longer needed.

All the geometric data are summarized in Table A.2. The most relevant data are listed again within the tables of the results. In this way, the differences in the output parameters can be easily related to the differences in geometry.

Table A.2: Bundle Key Geometric Parameters

	Ox 9×9	Ox 10×10	Hyd 10×10 (WC-1)*	Hyd 10×10 (WC-4)	Hyd 10×10 (BC-1)	Hyd 10×10 (BC-2)	Hyd 10×10 (BC-3)	Hyd 10×10 (BC-4)	Hyd 12×12
Fuel Rod Diameter (cm)	Proprietary	1.0260	1.2413	1.1176	1.2413	1.1176	1.16256	1.1176	0.9281
Fuel Rod Pitch (cm)	Proprietary	1.2950	1.42748	1.45288	1.42748	1.42748	1.42748	1.45288	1.2065
Bottom Act. Flow Area ($\times 10^{-3}$ m^2)	Proprietary	9.3000	9.18534	11.38541	9.18534	11.38541	10.61249	11.38541	11.4859
Top Act. Flow Area ($\times 10^{-3}$ m^2)	Proprietary	10.4575	9.18534	11.38541	9.18534	11.38541	10.61249	11.38541	11.4859
P/D	Proprietary	1.2622	1.1500	1.3000	1.1500	1.2773	1.2279	1.3000	1.3000
Clad Thickness (cm)	Proprietary	0.0760	0.08928	0.08164	0.08928	0.08164	0.08441	0.08164	0.06990
Fuel Pellet Diameter (cm)	Proprietary	0.8600	1.06079	0.91640	1.06079	0.91640	0.95421	0.91640	0.75709
Water Rod Outer Diameter (cm) Water Rod Inner Diameter (cm) Water Rod Pitch (cm) (Number of Water Rods)	Proprietary	2.6218, 2.4694, 3.6628, (2)	NA	NA	NA	NA	NA	NA	NA
CRGT Outer Diameter (cm) CRGT Inner Diameter (cm) (Number of CRGTs)	NA	NA	1.3894, 1.2108, (4)	1.3894, 1.2108, (4)	1.3894, 1.2108, (4)	1.3894, 1.2108, (4)	1.3894, 1.2108, (4)	1.3894, 1.2108, (4)	1.2000, 1.0214, (4)
Canister Thickness (cm)	Proprietary	0.3048	0.2540	0.2540	0.2540	0.2540	0.2540	0.2540	0.2540
Bundle Unit Side Length[58] (cm)	15.2400	15.2400	15.2400	15.2400	15.2400	15.2400	15.2400	15.2400	15.2400
Canister Outer Width (cm)	Proprietary	14.0208	15.1400	15.1400	15.1400	15.1400	15.1400	15.1400	15.1400
Gap Thickness between Bundles (cm)	Proprietary	1.2192	0.1000	0.1000	0.1000	0.1000	0.1000	0.1000	0.1000
Active Bundle Length (m)	3.7079	3.7079	3.7079	3.7079	3.7079	3.7079	3.7079	3.7079	3.7079
Total Bundle Length (m)	4.1800	4.1800	4.1800	4.1800	4.1800	4.1800	4.1800	4.1800	4.1800
# of Active Fuel Rods per Bundle	70.67	86.17	96	96	96	96	96	96	140
Number of PLFRs / length (m)	8 / 2.3175	14 / 2.3175	NA	NA	NA	NA	NA	NA	NA
Number of Grid Spacers	7	7	7	7	7	7	7	7	7
Grid Spacer Loss Coefficient	1.1040	1.1040	1.1040	1.1040	1.1040	1.1040	1.1040	1.1040	1.1040
Lower Tie Plate Loss Coefficient	9.4609	9.4609	9.4609	9.4609	9.4609	9.4609	9.4609	9.4609	9.4609
Upper Tie Plate Loss Coefficient	0.3751	0.3751	0.3751	0.3751	0.3751	0.3751	0.3751	0.3751	0.3751
Active Flow Area Orificing Coeff.	21.089	21.089	21.089	21.089	21.089	21.089	21.089	21.089	21.089

* To distinguish between the hydride 10×10 bundles having same local peaking factor distribution but different geometry, they are named as: Hyd 10×10 (xC - #), where "xC" identifies the power distribution: "WC" (Worst Case) or "BC" (Best Case), while # is a number identifying the combination *P-D* of the bundle under examination. Regardless of the power distribution, if two hydride 10×10 bundles have same # they have the same geometry.

[58] The Bundle Unit Side Length is defined as the canister width plus the thickness of the gap that separates adjacent canisters.

A1.8. Comparisons Performed

The comparison of the bundle types has been performed under different sets of assumptions. The key features for each comparison are summarized in Table A.3, which is followed by some comments and considerations useful to motivate the passage from one comparison to the next.

Table A.3: Bundle Comparison Basis

Comp. #	Constraints Imposed	Constraints Exceeded	Exit Quality	Note on the Constraints	Table #
1	All	None	Fixed at 26.8%	None is exceeded and one matches the limit	A.4
2	All	None	Not fixed, but can not exceed 26.8%	Pressure drop has to match the limit: $\Delta p = 34$ psia	A.5
3a	All	None	Not constrained	None is exceeded and 2 have to match the limits: MCHFR = 1.158 $\Delta p = 34$ psia	A.6
3b	All	None	Not constrained	None is exceeded and 2 have to match the limits: MCHFR = 1.158 $\Delta p = 22.6$ psia	A.7
4	Only MCHFR	Pressure drop for Hydride "Best Cases"	Fixed at 26.8%	The MCHFR matches the limit: MCHFR = 1.158	A.8

Among the comparisons using the upper pressure drop limit, i.e. 34 psia, Comparison 1 is the most conservative since the bundles do not exceed any constraint and, at the same time, must have the same exit quality. However, Table A.4, which presents results from Comparison 1, illustrates that for the oxide bundles and for the Hydride 10×10 Worst Cases, having fixed exit quality at 26.8% causes such bundles to be MCHFR limited, while the pressure drop is still quite far from the upper limit. Conversely, all the remaining hydride bundles are pressure drop limited. Such an observation suggests that the constraint of fixed exit quality be relaxed and that the maximum achievable bundle powers be compared when all the bundles are pressure drop limited. Since all the Hydride

"Best Case" examined in Comparison 1 are already pressure drop limited, only the oxide bundles and the Hydride 10×10 Worst Cases have been analyzed again but now relaxing exit quality constraint. The results, which constitute "Comparison 2", are shown in Table A.5. Relaxation of the constancy of the exit quality implies that the GE11 bundle is analyzed under operating conditions which differ from those taken as "reference": for this reason, the new case for the oxide bundle is named Oxide 9×9 "34 psia" and no longer Oxide 9×9 "reference". Based on what has been stated so far, Comparison 2 shows the maximum achievable power that each bundle would have if exceeding the exit quality limit was not allowed.

Comparisons 3a (Table A.6) and 3b (Table A.7) deliver the maximum achievable power that each bundle would have if exceeding the exit quality limit was allowed. As a consequence, the analysis is aimed at searching the bundle operating conditions which are MCHFR and pressure drop limited[59].

Finally, Table A.8 shows a bundle comparison where the MCHFR is the only constraint applied and all the bundles have the same exit quality. This means that, since the inlet enthalpy is constant, the bundles have the same boiling length and the same margin to the critical condition. This yields a comparison between the heat removal effectiveness of each bundle, with only the MCHFR constraint applied.

A1.9. Results

Results are summarized in several tables, presented in the order shown in Table A.3. Each is based upon a particular set of assumptions, which are specified again in the table title. To convey the results more effectively, the following cell coloring technique is applied to the tables of the results:

Green cell → the parameter in the cell matches the limit value

Orange cell → the "soft" constraint, i.e. the exit quality, exceeds the max. allowed value

Red cell → the parameter in the cell, which is a "hard" constraint, exceeds the limit value

[59] An exception concerns the Oxide 9×9 "34 psia" bundle. In fact, before the CHFR reaches the minimum allowed value, the fuel average temperature reaches its limit value. Therefore, the power of this bundle is double-limited by the pressure drop and the fuel average temperature.

Table A.4: Bundle Comparison 1 (same x_{out} = 26.8%). None of the constraints are exceeded.

	Ox. 9×9 "ref"	Ox. 10×10 (WC)	Ox. 10×10 (BC)	Hyd 10×10 (WC-1)	Hyd 10×10 (WC-4)	Hyd 10×10 (BC-1)	Hyd 10×10 (BC-2)	Hyd 10×10 (BC-3)	Hyd 10×10 (BC-4)	Hyd 12×12
Fuel Rod Diameter (cm)	Proprietary	1.0260	1.0260	1.2413	1.1176	1.2413	1.1176	1.16256	1.1176	0.9281
Fuel Rod Pitch (cm)	Proprietary	1.2950	1.2950	1.42748	1.45288	1.42748	1.42748	1.42748	1.45288	1.2065
Bottom Active Flow Area ($\times 10^{-3}$ m^2)	Proprietary	9.3000	9.3000	9.18534	11.38541	9.18534	11.38541	10.61249	11.38541	11.4859
Top Active Flow Area ($\times 10^{-3}$ m^2)	Proprietary	10.4575	10.4575	9.18534	11.38541	9.18534	11.38541	10.61249	11.38541	11.4859
P/D	Proprietary	1.2622	1.2622	1.1500	1.3000	1.1500	1.2773	1.2279	1.3000	1.3000
Clad Thickness (cm)	Proprietary	0.0760	0.0760	0.08928	0.08164	0.08928	0.08164	0.08441	0.08164	0.06990
Fuel Pellet Diameter (cm)	Proprietary	0.8600	0.8600	1.06079	0.91640	1.06079	0.91640	0.95421	0.91640	0.75709
Fuel-Clad Gap Conductance (kW/m^2 K)	5.6826	5.6826	5.6826	3593.042	188.3926	3593.0420	188.3926	180.7238	188.3926	228.87893
Total Flow Rate (kg/s)	16.9751	18.8698	19.8450	14.6059	17.4182	17.2686	22.7911	20.8656	22.8614	22.3852
Water Rod Flow Rate (kg/s) (Percentage of Total Flow)	0.6777 (4.0)	0.7557 (4.0)	0.7956 (4.0)	NA	NA	NA	NA	NA	NA	NA
CRGT Flow Rate (kg/s) (Percentage of Total Flow)	NA	NA	NA	0.3701 (2.5)	0.4354 (2.5)	0.4354 (2.5)	0.5679 (2.5)	0.5225 (2.5)	0.5715 (2.5)	0.5606 (2.5)
Bypass Channel Flow Rate (kg/s) (Percentage of Total Flow)	1.6992 (10.0)	1.8942 (10.0)	1.9922 (10.0)	0.1488 (1.0)	0.1742 (1.0)	0.1760 (1.0)	0.2250 (1.0)	0.2050 (1.0)	0.2232 (1.0)	0.2232 (1.0)
Bundle Active Flow Rate (kg/s)	14.5982	16.2199	17.0572	14.0870	16.8086	16.6572	21.9982	20.1381	22.0667	21.6014
Bundle Pressure Drop (Max. Allowed Value) (psia)	22.6 (34.0)	26.7 (34.0)	29.1 (34.0)	25.8 (34.0)	21.4 (34.0)					
Max. Fuel Temperature (Max. Allowed Value) (C)	2014.4 (2805)	1858.3 (2805)	1914.9 (2805)	494.7 (750)	542.2 (750)	493.9 (750)	568.4 (750)	544.1 (750)	568.1 (750)	480.9 (750)
Max. Average Fuel Temperature (Max. Allowed Value) (C)	1269.6 (1400)	1194.0 (1400)	1227.0 (1400)	It is not a constraint	It is not a constraint	It is not a constraint	It is not a constraint	It is not a constraint	It is not a constraint	It is not a constraint
Max. Outside Clad Temperature (Max. Allowed Value) (C)	313.3 (349)	312.5 (349)	310.0 (349)	302.6 (349)	307.8 (349)	303.1 (349)	309.5 (349)	307.0 (349)	310.1 (349)	306.5 (349)
MCHFR (Min. Allowed Value)						1.222 (1.158)	1.192 (1.158)	1.206 (1.158)	1.218 (1.158)	1.294 (1.158)
Subchannel-Averaged Exit Quality (%)										
Bundle Power (kW)	6567.7	7319.2	7697.5	6332.6	7556.4	7487.8	9888.0	9046.5	9917.8	9703.7
Power Diff. % with Respect to Ox. 9×9 "ref"	0	+11.4	+17.2	-3.6	+15.0	+14.0	+50.6	+37.7	+51.0	+47.7

Table A.5: Bundle Comparison 2 (same pressure drop = 34.0 psia). None of the constraints are exceeded.

	Oxide 9×9 "34 psia"	Ox. 10×10 (WC)	Ox. 10×10 (BC)	Hyd 10×10 (WC-1)	Hyd 10×10 (WC-4)	Hyd 10×10 (BC-1)	Hyd 10×10 (BC-2)	Hyd 10×10 (BC-3)	Hyd 10×10 (BC-4)	Hyd 12×12
Fuel Rod Diameter (cm)	Proprietary	1.0260	1.0260	1.2413	1.1176	1.2413	1.1176	1.16256	1.1176	0.9281
Fuel Rod Pitch (cm)	Proprietary	1.2950	1.2950	1.42748	1.45288	1.42748	1.42748	1.42748	1.45288	1.2065
Bottom Active Flow Area ($\times 10^{-3}$ m^2)	Proprietary	9.3000	9.3000	9.18534	11.38541	9.18534	11.38541	10.61249	11.38541	11.4859
Top Active Flow Area ($\times 10^{-3}$ m^2)	Proprietary	10.4575	10.4575	9.18534	11.38541	9.18534	11.38541	10.61249	11.38541	11.4859
P/D	Proprietary	1.2622	1.2622	1.1500	1.3000	1.1500	1.2773	1.2279	1.3000	1.3000
Clad Thickness (cm)	Proprietary	0.0760	0.0760	0.08928	0.08164	0.08928	0.08164	0.08441	0.08164	0.06990
Fuel Pellet Diameter (cm)	Proprietary	0.8600	0.8600	1.06079	0.91640	1.06079	0.91640	0.95421	0.91640	0.75709
Fuel-Clad Gap Conductance (kW/m^2 K)	5.6826	5.6826	5.6826	3593.0420	188.3926	3593.0420	188.3926	180.7238	188.3926	228.87893
Total Flow Rate (kg/s)	22.5621	22.2355	22.0676	17.6904	23.8140	17.2686	22.7911	20.8656	22.8614	22.3852
Water Rod Flow Rate (kg/s) (Percentage of Total Flow)	0.8963 (4.0)	0.8918 (4.0)	0.8827 (4.0)	NA	NA	NA	NA	NA	NA	NA
CRGT Flow Rate (kg/s) (Percentage of Total Flow)	NA	NA	NA	0.4463 (2.5)	0.5969 (2.5)	0.4354 (2.5)	0.5679 (2.5)	0.5225 (2.5)	0.5715 (2.5)	0.5606 (2.5)
Bypass Channel Flow Rate (kg/s) (Percentage of Total Flow)	2.2562 (10.0)	2.2190 (10.0)	2.2099 (10.0)	0.1760 (1.0)	0.2395 (1.0)	0.1760 (1.0)	0.2250 (1.0)	0.2050 (1.0)	0.2232 (1.0)	0.2232 (1.0)
Bundle Active Flow Rate (kg/s)	19.4096	19.1247	18.9750	17.0681	22.9776	16.6572	21.9982	20.1381	22.0667	21.6014
Bundle Pressure Drop (Max. Allowed Value) (psia)										
Max. Fuel Temperature (Max. Allowed Value) (C)	2215.7 (2805)	1999.4 (2805)	2004.4 (2805)	517.4 (750)	587.1 (750)	493.9 (750)	568.4 (750)	544.1 (750)	568.1 (750)	480.9 (750)
Max. Average Fuel Temperature (Max. Allowed Value) (C)		1279.3 (1400)	1281.6 (1400)	It is not a constraint	It is not a constraint	It is not a constraint	It is not a constraint	It is not a constraint	It is not a constraint	It is not a constraint
Max. Outside Clad Temperature (Max. Allowed Value) (C)	313.0 (349)	313.5 (349)	310.8 (349)	304.0 (349)	310.7 (349)	303.1 (349)	309.5 (349)	307.0 (349)	310.1 (349)	306.5 (349)
MCHFR (Min. Allowed Value)	1.179 (1.158)					1.222 (1.158)	1.192 (1.158)	1.206 (1.158)	1.218 (1.158)	1.294 (1.158)
Subchannel-Averaged Exit Quality (%)	21.8	24.1	25.0	24.4	22.7					
Bundle Power (kW)	7239.4	7858.6	8050.0	7036.8	8908.8	7487.8	9858.0	9046.5	9919.8	9703.7
Power Diff. % with Respect to Ox 9×9 "ref"	+10.5	+19.6	+22.6	+7.1	+35.6	+14.0	+50.6	+37.7	+51.0	+47.7
Power Diff. % with Respect to Ox 9×9 "34 psia"	0.0	+8.2	+10.9	-3.1	+22.7	+3.1	+36.2	+24.6	+36.6	+33.7

Table A.6: Bundle Comparison 3a (same pres. drop = 34.0 psia + another hard constraint matched). No limit for x_{out}.

	Oxide 9×9 "34 psia"	Ox. 10×10 (WC)	Ox. 10×10 (BC)	Hyd 10×10 (WC-1)	Hyd 10×10 (WC-4)	Hyd 10×10 (BC-1)	Hyd 10×10 (BC-2)	Hyd 10×10 (BC-3)	Hyd 10×10 (BC-4)	Hyd 12×12
Fuel Rod Diameter (cm)	Proprietary	1.0260	1.0260	1.2413	1.1176	1.2413	1.1176	1.16256	1.1176	0.9281
Fuel Rod Pitch (cm)	Proprietary	1.2950	1.2950	1.42748	1.45288	1.42748	1.42748	1.42748	1.45288	1.2065
Bottom Active Flow Area ($\times 10^{-3}$ m^2)	Proprietary	9.3000	9.3000	9.18534	11.38541	9.18534	11.38541	10.61249	11.38541	11.4859
Top Active Flow Area ($\times 10^{-3}$ m^2)	Proprietary	10.4575	10.4575	9.18534	11.38541	9.18534	11.38541	10.61249	11.38541	11.4859
P/D	Proprietary	1.2622	1.2622	1.1500	1.3000	1.1500	1.2773	1.2279	1.3000	1.3000
Clad Thickness (cm)	Proprietary	0.0760	0.0760	0.08928	0.08164	0.08928	0.08164	0.08441	0.08164	0.06990
Fuel Pellet Diameter (cm)	Proprietary	0.8600	0.8600	1.06079	0.91640	1.06079	0.91640	0.95421	0.91640	0.75709
Fuel-Clad Gap Conductance (kW/m^2 K)	5.6826	5.6826	5.6826	3593.0420	188.3926	3593.0420	188.3926	180.7238	188.3926	228.87893
Total Flow Rate (kg/s)	22.5621	22.2355	22.0676	17.6904	23.8140	16.9329	22.5893	20.5662	22.4759	21.5097
Water Rod Flow Rate (kg/s) (Percentage of Total Flow)	0.8963 (4.0)	0.8918 (4.0)	0.8827 (4.0)	NA	NA	NA	NA	NA	NA	NA
CRGT Flow Rate (kg/s) (Percentage of Total Flow)	NA	NA	NA	0.4463 (2.5)	0.5969 (2.5)	0.4300 (2.5)	0.5679 (2.5)	0.5189 (2.5)	0.5625 (2.5)	0.5389 (2.5)
Bypass Channel Flow Rate (kg/s) (Percentage of Total Flow)	2.2562 (10.0)	2.2190 (10.0)	2.2099 (10.0)	0.1760 (1.0)	0.2395 (1.0)	0.1742 (1.0)	0.2250 (1.0)	0.2050 (1.0)	0.2232 (1.0)	0.2214 (1.0)
Bundle Active Flow Rate (kg/s)	19.4096	19.1247	18.9750	17.0681	22.9776	16.3287	21.7964	19.8423	21.6902	20.7494
Bundle Pressure Drop (Max. Allowed Value) (psia)										
Max. Fuel Temperature (Max. Allowed Value) (C)	2215.7 (2805)	1999.4 (2805)	2004.4 (2805)	517.4 (750)	587.1 (750)	502.3 (750)	574.9 (750)	552.3 (750)	579.7 (750)	498.2 (750)
Max. Average Fuel Temperature (Max. Allowed Value) (C)		1279.3 (1400)	1281.6 (1400)	It is not a constraint	It is not a constraint	It is not a constraint	It is not a constraint	It is not a constraint	It is not a constraint	It is not a constraint
Max. Outside Clad Temperature (Max. Allowed Value) (C)	313.0 (349)	313.5 (349)	310.8 (349)	304.0 (349)	310.7 (349)	303.4 (349)	309.9 (349)	307.4 (349)	310.7 (349)	307.7 (349)
MCHFR (Min. Allowed Value)	1.179 (1.158)									
Subchannel-Averaged Exit Quality (%)	21.8	24.1	25.0	24.4	22.7					
Bundle Power (kW)	7259.4	7858.6	8050.0	7036.8	8908.8	7804.8	10124.2	9345.6	10344.0	10605.3
Power Diff. % with Respect to Ox. 9×9 "ref"	+10.5	+19.6	+22.6	+7.1	+35.6	+18.8	+34.2	+42.3	+57.5	+61.5
Power Diff. % with Respect to Ox. 9×9 "34 psia"	0.0	+8.2	+10.9	-3.1	+22.7	+7.5	+39.5	+28.7	+42.5	+46.1

Table A.7: Bundle Comparison 3b (same pres. drop = 22.6 psia, same MCHFR = 1.158). No limit for x_{out}.

	Oxide 9×9 "reference"	Ox. 10×10 (WC)	Ox. 10×10 (BC)	Hyd 10×10 (WC-1)	Hyd 10×10 (WC-4)	Hyd 10×10 (BC-1)	Hyd 10×10 (BC-2)	Hyd 10×10 (BC-3)	Hyd 10×10 (BC-4)	Hyd 12×12
Fuel Rod Diameter (cm)	Proprietary	1.0260	1.0260	1.2413	1.1176	1.2413	1.1176	1.16256	1.1176	0.9281
Fuel Rod Pitch (cm)	Proprietary	1.2950	1.2950	1.42748	1.45288	1.42748	1.42748	1.42748	1.45288	1.2065
Bottom Active Flow Area ($\times 10^{-3}$ m^2)	Proprietary	9.3000	9.3000	9.18534	11.38541	9.18534	11.38541	10.61249	11.38541	11.4859
Top Active Flow Area ($\times 10^{-3}$ m^2)	Proprietary	10.4575	10.4575	9.18534	11.38541	9.18534	11.38541	10.61249	11.38541	11.4859
P/D	Proprietary	1.2622	1.2622	1.1500	1.3000	1.1500	1.2773	1.2279	1.3000	1.3000
Clad Thickness (cm)	Proprietary	0.0760	0.0760	0.08928	0.08164	0.08928	0.08164	0.08441	0.08164	0.06990
Fuel Pellet Diameter (cm)	Proprietary	0.8600	0.8600	1.06079	0.91640	1.06079	0.91640	0.95421	0.91640	0.75709
Fuel-Clad Gap Conductance (kW/m^2 K)	5.6826	5.6826	5.6826	3593.0420	188.3926	3593.0420	188.3926	180.7238	188.3926	228.87893
Total Flow Rate (kg/s)	16.9751	16.7832	16.6199	13.2996	18.0896	12.6781	17.0554	15.4814	16.9782	16.1391
Water Rod Flow Rate (kg/s) (Percentage of Total Flow)	0.6777 (4.0)	0.6786 (4.0)	0.6695 (4.0)	NA	NA	NA	NA	NA	NA	NA
CRGT Flow Rate (kg/s) (Percentage of Total Flow)	NA	NA	NA	0.3320 (2.5)	0.4572 (2.5)	0.3175 (2.5)	0.4300 (2.5)	0.3865 (2.5)	0.4228 (2.5)	0.4046 (2.5)
Bypass Channel Flow Rate (kg/s) (Percentage of Total Flow)	1.6992 (10.0)	1.6810 (10.0)	1.6602 (10.0)	0.1361 (1.0)	0.1832 (1.0)	0.1324 (1.0)	0.1724 (1.0)	0.1597 (1.0)	0.1742 (1.0)	0.1651 (1.0)
Bundle Active Flow Rate (kg/s)	14.5982	14.4236	14.2902	12.8307	17.4492	12.2282	16.4530	14.9352	16.3812	15.5694
Bundle Pressure Drop (Max. Allowed Value) (psia)										
Max. Fuel Temperature (Max. Allowed Value) (C)	2014.4 (2805)	1756.3 (2805)	1762.7 (2805)	484.2 (750)	547.2 (750)	470.4 (750)	536.1 (750)	515.1 (750)	540.1 (750)	468.1 (750)
Max. Average Fuel Temperature (Max. Allowed Value) (C)	1269.6 (1400)	1135.3 (1400)	1138.2 (1400)	It is not a constraint	It is not a constraint	It is not a constraint	It is not a constraint	It is not a constraint	It is not a constraint	It is not a constraint
Max. Outside Clad Temperature (Max. Allowed Value) (C)	313.3 (349)	311.8 (349)	308.6 (349)	301.9 (349)	308.1 (349)	301.4 (349)	307.3 (349)	305.1 (349)	308.1 (349)	305.2 (349)
MCHFR (Min. Allowed Value)										
Subchannel-Averaged Exit Quality (%)					26.3					
Bundle Power (kW)	6561.7	6946.0	7120.8	6008.6	7706.9	6633.6	8790.8	8017.9	8916.5	9072.0
Power Diff. % with Respect to Oxide 9×9 "ref"	0	+5.8	+8.4	-8.5	+17.5	+1.0	+33.9	+22.1	+35.9	+38.3

Table A.8: Bundle Comparison 4 (same x_{out} = 26.8%, same MCHFR = 1.158). MCHFR is the only constraint.

	Oxide 9×9 "reference"	Ox. 10×10 (WC)	Ox. 10×10 (BC)	Hyd 10×10 (WC-1)	Hyd 10×10 (WC-4)	Hyd 10×10 (BC-1)	Hyd 10×10 (BC-2)	Hyd 10×10 (BC-3)	Hyd 10×10 (BC-4)	Hyd 12×12
Fuel Rod Diameter (cm)	Proprietary	1.0260	1.0260	1.2413	1.1176	1.2413	1.1176	1.16256	1.1176	0.9281
Fuel Rod Pitch (cm)	Proprietary	1.2950	1.2950	1.42748	1.45288	1.42748	1.42748	1.42748	1.45288	1.2065
Bottom Active Flow Area ($\times 10^{-3}$ m^2)	Proprietary	9.3000	9.3000	9.18534	11.38541	9.18534	11.38541	10.61249	11.38541	11.4859
Top Active Flow Area ($\times 10^{-3}$ m^2)	Proprietary	10.4575	10.4575	9.18534	11.38541	9.18534	11.38541	10.61249	11.38541	11.4859
P/D	Proprietary	1.2622	1.2622	1.1500	1.3000	1.1500	1.2773	1.2279	1.3000	1.3000
Clad Thickness (cm)	Proprietary	0.0760	0.0760	0.08928	0.08164	0.08928	0.08164	0.08441	0.08164	0.06990
Fuel Pellet Diameter (cm)	Proprietary	0.8600	0.8600	1.06079	0.91640	1.06079	0.91640	0.95421	0.91640	0.75709
Fuel-Clad Gap Conductance (kW/m^2 K)	5.6826	5.6826	5.6826	3593.0420	188.3926	3593.0420	188.3926	180.7238	188.3926	228.87893
Total Flow Rate (kg/s)	16.9751	18.8698	19.8450	14.6059	17.4182	19.4594	24.1315	22.7254	25.3109	28.1776
Water Rod Flow Rate (kg/s) (Percentage of Total Flow)	0.6777 (4.0)	0.7557 (4.0)	0.7956 (4.0)	NA	NA	NA	NA	NA	NA	NA
CRGT Flow Rate (kg/s) (Percentage of Total Flow)	NA	NA	NA	0.3701 (2.5)	0.4354 (2.5)	0.4881 (2.5)	0.6042 (2.5)	0.5679 (2.5)	0.6314 (2.5)	0.7022 (2.5)
Bypass Channel Flow Rate (kg/s) (Percentage of Total Flow)	1.6992 (10.0)	1.8942 (10.0)	1.9922 (10.0)	0.1488 (1.0)	0.1742 (1.0)	0.1978 (1.0)	0.2395 (1.0)	0.2268 (1.0)	0.2504 (1.0)	0.2794 (1.0)
Bundle Active Flow Rate (kg/s)	14.5982	16.2199	17.0572	14.0870	16.8086	18.7735	23.2878	21.9307	24.4291	27.1960
Bundle Pressure Drop (Max. Allowed Value) (psia)	22.6 (34.0)	26.7 (34.0)	29.1 (34.0)	25.8 (34.0)	21.4 (34.0)					
Max. Fuel Temperature (Max. Allowed Value) (°C)	2014.4 (2805)	1858.3 (2805)	1914.9 (2805)	494.7 (750)	542.2 (750)	519.4 (750)	584.6 (750)	566.4 (750)	597.3 (750)	529.8 (750)
Max. Average Fuel Temperature (Max. Allowed Value) (°C)	1269.6 (1400)	1194.0 (1400)	1227.0 (1400)	It is not a constraint	It is not a constraint	It is not a constraint	It is not a constraint	It is not a constraint	It is not a constraint	It is not a constraint
Max. Clad Surface Temperature (Max. Allowed Value) (°C)	313.3 (349)	312.5 (349)	310.0 (349)	302.6 (349)	307.8 (349)	304.6 (349)	310.5 (349)	308.4 (349)	311.9 (349)	310.3 (349)
MCPR (Min. Allowed Value)										
Subchannel-Averaged Exit Quality (%)										
Bundle Power (kW)	6567.7	7319.2	7697.5	6332.6	7556.4	8437.7	10469.5	9852.8	10980.4	12214.7
Power Diff. % with Respect to Oxide 9×9 "ref"	0	+11.4	+17.2	-3.6	+15.0	+28.5	+59.4	+50.0	+67.2	+86.0

Table A.9 summarizes the gains in power, expressed as the percentage difference from the reference Oxide 9×9 bundle power. Again, the red cells indicate those cases where "hard" constraints have been exceded.

Table A.9: Power Difference Percentages With Respect to the Oxide 9×9 reference case

	Oxide 9×9	Ox. 10×10 (WC)	Ox. 10×10 (BC)	Hyd 10×10 (WC-1)	Hyd 10×10 (WC-4)	Hyd 10×10 (BC-1)	Hyd 10×10 (BC-2)	Hyd 10×10 (BC-3)	Hyd 10×10 (BC-4)	Hyd 12×12
Comp. 1	0.0	+11.4	+17.2	-3.6	+15.0	+14.0	+50.6	+37.7	+51.0	+47.7
Comp. 2	+10.5	+19.6	+22.6	+7.1	+35.6	+14.0	+50.6	+37.7	+51.0	+47.7
Comp. 3a	+10.5	+19.6	+22.6	+7.1	+35.6	+18.8	+54.2	+42.3	+57.5	+61.5
Comp. 3b	0.0	+5.8	+8.4	-8.5	+17.3	+1.0	+33.1	+22.1	+35.8	+38.1
Comp. 4	0.0	+11.4	+17.2	-3.6	+15.0					

The following conclusions arise from these subchannel analysis results:

1) the flat pin-by-pin power distribution together with the open lattice characterizing the bundle designated as Hyd 10×10 BC-4 yields a 50% power gain percentage, with respect to the oxide bundle chosen as reference. Such a significant gain in power can be achieved as long as the maximum allowed pressure drop is fixed at 1.5 times the pressure drop of the reference bundle. Should this limit be reduced and fixed at the value corresponding to the pressure drop of the reference bundle, the power gain percentage would decrease to 36%, which still represents a significant gain in power.

2) The MCHFR and pressure drop are the two most limiting power constraints. As shown in Table A.4, when the pressure drop is allowed to increase above the lower pressure drop limit, i.e. 22.6 psia, the oxide bundles and the hydride WC bundles are MCHFR limited, while the BC hydride bundles, together with the 12×12 bundle, are pressure drop limited.

3) The limiting effect of the MCHFR can be reduced by flattening the pin-by-pin power distribution. This is evident by comparing Hyd 10×10 WC-1 to Hyd 10×10 BC-1 in Table A.4: although they have the same geometry, the different power distribution causes the former to be MCHFR limited, while the latter is pressure drop limited. The gain in power resulting from having adopted a flatter power distribution is of the order of 18% (7487.8 kW vs 6332.6 kW). The same verification can be made by comparing, in the same table, Hyd 10×10 WC-4 to

Hyd 10×10 BC-4. In this case, however, the gain in power is much larger: 9917.8 kW vs 7556.4 kW corresponding to a 30% gain. Thus, it seems there is a dependence of the power gain percentage resulting from changing the power distribution and the bundle geometry.

4) For the same fuel and lattice size, the limiting effect of the pressure drop can be reduced by increasing the ratio between pitch and fuel rod diameter. This is evident by comparing Hyd 10×10 BC-1 to Hyd 10×10 BC-2: while they have the same rod pitch, the latter design is characterized by smaller rods, resulting in a larger flow area. Table A.4 shows that such a geometry difference allows Hyd 10×10 BC-2 to achieve 30% more power.

5) For the same exit quality, the 12×12 bundle does not yield any gain in power with respect to Hyd 10×10 BC-4 (see Table A.4, Table A.5). Although both have a flat power distribution and P/D=1.3, the more significant friction losses characterizing the former (it contains 44 more rods) do not allow it to gain in power. As a consequence, except for the cases in which the exit quality is not the same[60], the hydride 12×12 bundle delivers a higher power than Hyd 10×10 BC-4 only when the pressure drop is not a constraint, i.e. in Comparison 4 shown in Table A.8. By comparing the pressure drops of the BC hydride bundles to that of the 12×12 bundle, the larger friction losses are quite evident.

[60] In order to perform a fair comparison between the power performance of different bundles, they have to be characterized by the same inlet and outlet conditions. Under BWR operating conditions, this translates into equal inlet enthalpy and equal exit quality.

Appendix B

B1. Rod Vibration Magnitude in Two-phase Flow: Development of the Corrected Païdoussis Correlation

Although the increase in coolant flow rate is advisable to make the core heat removal more efficient, it is actually limited by two main factors which may induce failure mechanisms or exceed pump flow and head capability. These factors are the following:

- pressure drop increase
- rod vibration enhancement

While several two-phase pressure drop correlations are available in the literature, the rod vibration mechanism in two-phase flow is still a relatively unexplored field. Therefore, the need to add the vibration phenomena to the thermal-hydraulic constraints listed in has first required an investigation to choose a correlation able to predict the rod vibration amplitude. At the same time, the unexplored nature of the two-phase vibrations field has also required the choice of a reasonable vibration limit.

Since the purpose of the present work is not focused on a thorough investigation of the vibration mechanisms that occur in the core, the study presented is a simplified approach. The reason is that the main goal of the present vibration study is not the development of a model able to predict the real in-core structure motions, but a conservative estimate of them. Even if conservative, the model used has to clarify the dependence of the vibration motions on the main thermal-hydraulics parameters, as well as predict their magnitude with a good accuracy.

Correlations examined and vibration limit value

Most of the considerations and conclusions here are based on the studies carried out separately by M.P. Païdoussis [19] and Y. Tsukuda [20]. Both these sources have been examined in order to develop a consistent methodology to conservatively calculate the vibration amplitude to which rods are subjected in a BWR.

The parameter chosen to express the vibrations magnitude is called "vibration ratio", and is defined as the ratio between the maximum peak vibration amplitude and the rod

diameter (y/D). Both the mentioned studies focus partly or entirely on the calculation of this parameter. However, the choice of a parameter which effectively represents the vibration magnitude is undoubtedly influenced by the nature of the analysis: other choices could concern for example the vibration frequency or the energy dissipated by means of the wear mechanism.

The following discussion describes the correlations used to build an effective vibrations calculation strategy. Most of the comments will be addressed to the Païdoussis approach, which is the one actually implemented in the analysis. The study carried out by Tsukuda will be presented in less detail, assigning to it a comparison and validation role.

Païdoussis correlation

In his book [19], Païdoussis states: "*Païdoussis (1965b, 1966c) conducted many experiments with a single cylinder in a channel, as well as with a 19-cylinder bundle, (...). To these were added the experimental data of Burgreen et al. (1958), SOGREAH (1962), Quinn (1962), Rotström (1964) and Rotström & Andersson (1964a,b), the last group involving hot and cold water, two-phase flows and superheated steam. All these were put together (by systematic trial and error, and with the benefit of physical understanding), and the following correlation has been obtained*":

$$\frac{y_{max}}{D} = \Gamma^{-4}\left(5\cdot 10^{-4} K\right)\cdot\left[\frac{u^{1.6}\varepsilon^{1.8}\,\mathrm{Re}^{0.25}}{1+u^2}\right]\cdot\left(\frac{D_h}{D}\right)^{0.4}\left(\frac{\beta^{2/3}}{1+4\beta}\right) \qquad \text{(B-1)}$$

The parameters that appear in this empirical correlation, to which we will refer to as the "Païdoussis correlation", are defined as follows.

y_{max} : max peak vibration amplitude (m). The peak value is about two to three times the root mean square amplitude y_{rms}. Since our approach aims to develop a conservative analysis, this peak value is calculated.

D: rod outer diameter (m)

Γ: 4.73 for rods clamped at both ends

K: 5 for turbulent flow

$u = VL\sqrt{\frac{\rho A}{EI}}$ dimensionless velocity, where: (B-2)

V is the coolant velocity (m/s), directly computed by VIPRE

L is the distance between two grid spacers (0.4953 m, taken as typical average value, compare with grid spacer elevations listed in Table E.1)

ρ is the coolant density (kg/m^3), directly computed by VIPRE

$A = \pi\frac{D^2}{4}$ is the rod cross sectional area (m^2)

E is the Zircaloy Young's modulus (8.0468e10 Pa, see Table J.1)

I is the clad inertia momentum: $I = \frac{\pi}{2}\cdot\left[\left(\frac{D}{2}\right)^4 - \left(\frac{D_{ci}}{2}\right)^4\right]$ with D_{ci} is the inner clad diameter (m)

$\varepsilon = L/D$ (B-3)

$\mathrm{Re} = \frac{\rho V D_h}{\mu}$ Reynolds number, where: (B-4)

D_h is the equivalent diameter of the channel in which the assembly subchannels have been lumped (m)

μ is the coolant mixture viscosity: $\mu = \mu_g \cdot \alpha + \mu_l \cdot (1-\alpha)$ where α is the void fraction directly computed by VIPRE

$\beta = \frac{\rho A}{\rho A + m_l}$ where m_l is the mass per unit length of rod (kg). (B-5)

The present analysis neglects the presence of the fuel inside the rods. This was done essentially for two reasons. First and foremost a lighter rod is subjected to larger vibrations, and therefore this is consistent with the conservative nature of the present analysis. Second, neither the Païdoussis correlation nor the few others available in literature were developed for rods having a structure more complex than that of a single hollow tube or a solid homogeneous rod. Taking into account the presence of the fuel

would introduce uncertainties in the definition of some parameters that the correlations require (m, E, I), as well as further assumptions needed to model the non trivial coupling of clad-fuel. In fact, it is well known that under steady state conditions the fuel doesn't touch the clad, at least at the beginning of life. However, fuel swelling due to irradiation, fission gas release and the occurrence of vibrations may make the non-contact assumption no longer acceptable. Hence the mentioned assumption is not only conservative, but also advisable.

A quick glance at the correlation is sufficient to illustrate that many parameters are involved in the vibration ratio estimate, and each one has an own influence on the amplitude vibrations. Attention need be focused only on those parameters that are subjected to time or spatial variations, within the environmental conditions which are typical of a boiling reactor. Investigations on the dependence of the vibration ratio on the rod mass or on the distance between grid spacers could be useful in other studies, characterized by different objectives or different environmental conditions. Instead, focus upon the influence that the coolant flow rate or the flow quality exerts on the vibrations magnitude is much more consistent with the features of the present analysis.

Figure B.1[61] is useful for this purpose: it shows that the vibration ratio predicted by the Païdoussis correlation increases as the flow rate and quality increase. This is nothing else than an analytical proof of what had been previously stated, that is the limiting behavior exerted by the vibration mechanism on the coolant flow rate increase.

Likewise, the fact that larger quality implies larger vibrations induces us to focus the analysis on the hot assembly, which is characterized by the highest void fraction of the whole core. More precisely, the analysis will be focused on the upper part of the hot assembly, that is on the last 20 inches at the top of the bundle (20 inches is approximately the average distance between two grid spacers).

[61] This figure, together with all the others presented in this Appendix, derives from calculations performed on the reference BWR/5 assembly configuration (see Figure 1.2).

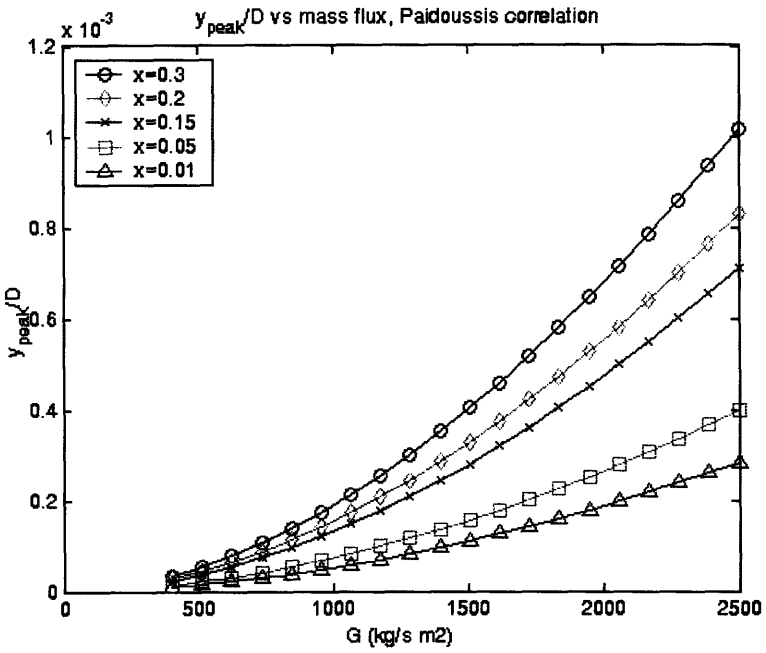

Figure B.1: Peak Vibration Ratio Dependence on Quality and Mass Flux, Païdoussis Correlation

As proof of validation, Païdoussis compared the data obtained using his own correlation with the measurements performed by the authors previously mentioned. The complete picture of this comparison is shown in Figure 8.42 of [19]. Based on this comparison, he stated that the agreement is within one order of magnitude.

For the present study, the most interesting comparison is between the Païdoussis correlation and the data collected by Quinn (1962). In fact, while the other authors performed experiments under environmental conditions far from the ones we are examining, Quinn dealt just with vibrations in two-phase flow. For this reason, Figure 8.42 of [19] has been partly modified, such that the comparison with Quinn's data appears more clearly. This is shown in Figure B.2. If the Païdoussis correlation was exact, the experimental points that Quinn collected would lie on the central straight line. Instead, as previously stated, the empirical correlation has an accuracy of one order of magnitude, and therefore a mismatch between the points was predictable. In particular, it has to be highlighted that the Païdoussis correlation does not always overpredict the vibration ratio. The figure shows that when the parameters combination used in the correlation would seem to drive to very small vibration ratios (close to 10^{-4}), the experimental measurements show instead larger values for the ratio *y/D*. A strict

comparison between predicted and measured data shows that the worst mismatch occurs for the data tail on the left, where the Païdoussis correlation underpredicts the vibration ratio of a factor 15.

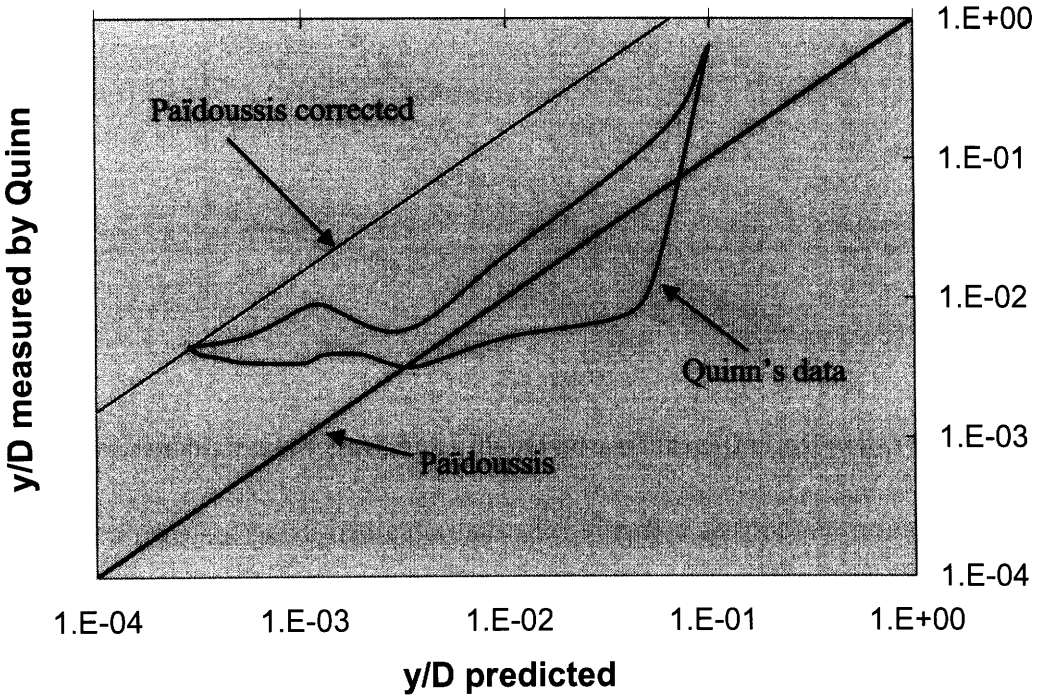

Figure B.2: Païdoussis Correlation – Quinn's Data Comparison

Because of the nature and the objectives of the present analysis it is self evident that the need of a conservative (but realistic) estimate of the vibration mechanism is more important than an exact calculation of the vibration ratios. For this reason, in the thermal-hydraulic analysis herein presented, the vibration ratios are calculated using a correlation obtained by a crude but simple modification of the Païdoussis correlation, that is multiplying it by 15. As a consequence, the predicted vibration ratios would be represented by the upper straight line in Figure B.2, to which the name, "Païdoussis corrected" correlation, has been assigned. A quick glance at the two straight lines is sufficient to make the reader aware that such a correction implies a loss in matching data but a gain in conservativism.

In conclusion, the present thermal-hydraulic analysis implements the vibration magnitude calculation by using the following correlation:

$$\frac{y_{max}}{D} = 15 \cdot \Gamma^{-4}\left(5 \cdot 10^{-4} K\right) \cdot \left[\frac{u^{1.6} \varepsilon^{1.8} \mathrm{Re}^{0.25}}{1+u^2}\right] \cdot \left(\frac{D_h}{D}\right)^{0.4} \left(\frac{\beta^{2/3}}{1+4\beta}\right) \tag{B-6}$$

Tsukuda correlation

The correlation developed by the Japanese team derives from a series of hydraulic vibration tests performed using two full-scale test assemblies simulating real 9×9 BWR fuel assemblies.

The two test assemblies differ from each other in their geometrical characteristics; specifically, Type-A has a partial length rod and two large water rods, while Type-B has a rectangular water channel. A complete description of the test assemblies and the experimental procedure which led to the empirical correlation is provided in [20].

The correlation developed has the following form:

$$\frac{y_{rms}}{D} = 0.189 \cdot G^{0.31} \frac{L^{3.5}}{EI\sqrt{\varsigma \cdot 10^{-2}}} \sqrt{8.35 \cdot 10^{-4} \cdot f_{rn}^{-2.44} \cdot f_n \cdot \frac{D \cdot D_h}{V^{0.5}}} \tag{B-7}$$

The nomenclature used is consistent with that previously described for the Païdoussis correlation. Therefore, only the parameters not yet defined are listed as follows:

y_{rms} : root mean square vibration amplitude (m)

G : coolant mass flux (kg/s m^2)

$f_n = \frac{\pi}{2L^2} \cdot \sqrt{\frac{EI}{\rho_r A}}$: natural frequency of the rod in air (Hz), where ρ_r is the rod density (kg/m^3) (B-8)

$$f_{rn} = \frac{f_n \cdot D_h}{V^{0.5}} \tag{B-9}$$

ζ : damping ratio (%). Its calculation needs a careful description. In fact, the Tsukuda paper does not mention the correlation used to compute it. Fortunately, this parameter is not property of the hydraulic tests performed by the Japanese team, but is a well known quantity often described in the vibration literature. To calculate it, the correlations suggested in the Welding Research Council (WRC) Bulletin 389 [34] were used. They compute the total damping ratio (ζ, expressed in percent) as

sum of three partial damping ratios, namely two-phase damping (ζ_{TP}) , viscous damping (ζ_V) and support damping (ζ_S):

$$\zeta = \zeta_{TP} + \zeta_V + \zeta_S \tag{B-10}$$

where:

$$\zeta_{TP} = 5F_\alpha \cdot \left(\frac{\sigma_T}{\sigma_{20}}\right) \cdot \left(\frac{\rho_l D^2}{m_l + m_h}\right) \cdot \left[\frac{1+R^{-3}}{\left(1-R^{-2}\right)^2}\right] \quad \text{with} \tag{B-11}$$

$$F_\alpha = \begin{cases} \dfrac{\alpha}{0.4} & \text{if } \alpha \leq 0.4 \quad (\alpha \text{ is the void fraction}) \\ 1 & \text{if } 0.4 < \alpha \leq 0.7 \\ 1 - \dfrac{\alpha - 0.7}{0.3} & \text{if } \alpha > 0.7 \end{cases} \tag{B-12}$$

σ_T : water surface tension at the temperature of interest (N/m)

σ_{20} : water surface tension at 20°C (0.073 N/m)

ρ_l : density of liquid water at the temperature of interest (kg/m^3)

$$R = \left(1.07 + 0.56\frac{P}{D}\right) \cdot \frac{P}{D} \quad \text{where } P \text{ is the rod pitch}^{62} \text{ (m)} \tag{B-13}$$

$$m_h = \left(\frac{\rho \pi D^2}{4}\right) \cdot \frac{R^2+1}{R^2-1} \quad \text{is the hydrodynamic mass}^{63} \text{ (kg/m)}$$

Instead, for the viscous damping:

---

[62] In case of triangular lattice, this relation should be slightly modified, becoming: $R = \left(0.96 + 0.5\frac{P}{D}\right) \cdot \frac{P}{D}$

[63] The hydrodynamic mass computed here is slightly different from the one somehow "hidden" in the Païdoussis correlation. In fact, the Païdoussis correlation contains the hydrodynamic mass as the product ρA, which corresponds to the term here in brackets.

$$\zeta_V = \frac{100\pi}{\sqrt{8}} \cdot \left(\frac{\rho D^2}{m_l + m_h} \right) \cdot \left(\frac{2 \cdot \nu}{\pi \cdot f_{TP} \cdot D^2} \right)^{0.5} \left[\frac{1 + R^{-3}}{\left(1 - R^{-2}\right)^2} \right] \qquad \text{(B- 14)}$$

where ν is the two-phase kinematic viscosity (m^2/s), computed as follows:

$$\nu = \frac{\nu_l}{1 + \left(\frac{\nu_l}{\nu_g} - 1 \right) \cdot \alpha}$$

(ν_l and ν_g are referred to the liquid and the steam at saturation corresponding to the pressure of interest)

$$f_{TP} = f_n \cdot \left(\frac{m_l}{m_l + m_h} \right)^{0.5}$$

is the natural frequency of the tube in the two-phase mixture (Hz)

Finally, assuming conservatively the grid spacers as dry supports, i.e. ignoring a possible squeeze-film damping which tends to enhance the damping effect, the support damping ratio is computed as follows:

$$\zeta_S = 5 \cdot \frac{N-1}{N} \cdot \left(\frac{t}{L} \right)^{0.5}$$

where N is the number of spans (8 in our case), while t is the support thickness[64] (10^{-2} m)

The information provided so far is sufficient to compute the vibration ratio using the Tsukuda correlation.

Comparing the predicted results with the empirical measurements, the Japanese team assigned an accuracy of ±30% to their own correlation.

[64] "Vibration Damping of Heat Exchanger Tube Bundles" in WRC Bulletin 389 ([34]) deals with heat exchangers, which have rods supports structurally much simpler than the grid spacers typical of LWRs. These latter, in fact, do not have only a structural function, but at the same time are designed to enhance the coolant turbulence, such that the thermal performances can be improved. Therefore, the use of the actual grid thickness (of the order of 40 mm) is judged as a useless fussiness, since it would be coupled with the crude approximation of neglect of the presence of the springs. The thickness used in the analysis, i.e. 10 mm, is such that the resulting support damping ratio has a reasonable value, or at least comparable to that one calculated in the article for the heat exchanger (t_{WRC}=15 mm → ζ_S = 0.55%, $t_{PRESENT\ CASE}$=10mm → ζ_S = 0.61%).

Figure B.3, which shows the predicted Tsukuda trends of mass flux and quality on the vibration ratio, is discussed in the next paragraph.

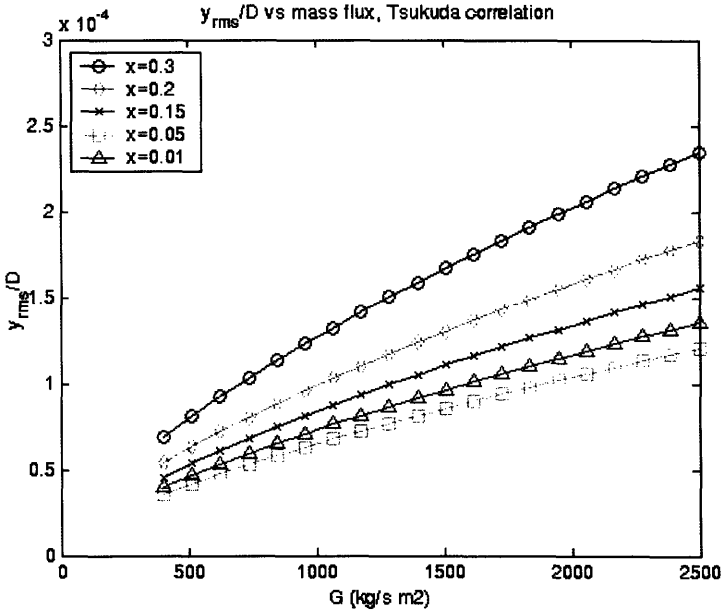

Figure B.3: Rms Vibration Ratio Dependence on Quality and Mass Flux, Tsukuda Correlation

Païdoussis-Tsukuda comparison

Two observations arise from Figure B.3. The first concerns the variation of the vibration ratio with the mass flux and the quality. As previously verified by means of the Païdoussis correlation (Figure B.1), the Tsukuda correlation also shows an increase of the vibration motions as the mentioned parameters increase. Thus the two correlations agree, at least about the vibration ratio's general dependences. However, given a quality, the vibration ratios predicted by the Tsukuda correlation are larger or lower than those deriving from the Païdoussis correlation depending on the value of the mass flux. This is evident from Figure B.4 which compares the two correlations. Rather interesting is that, for each quality, there is a value of mass flux above which the oscillations predicted by Païdoussis are larger than those deriving from Tsukuda, and below which the opposite trend occurs. Moreover, this "transition mass flux value" decreases as the quality increases.

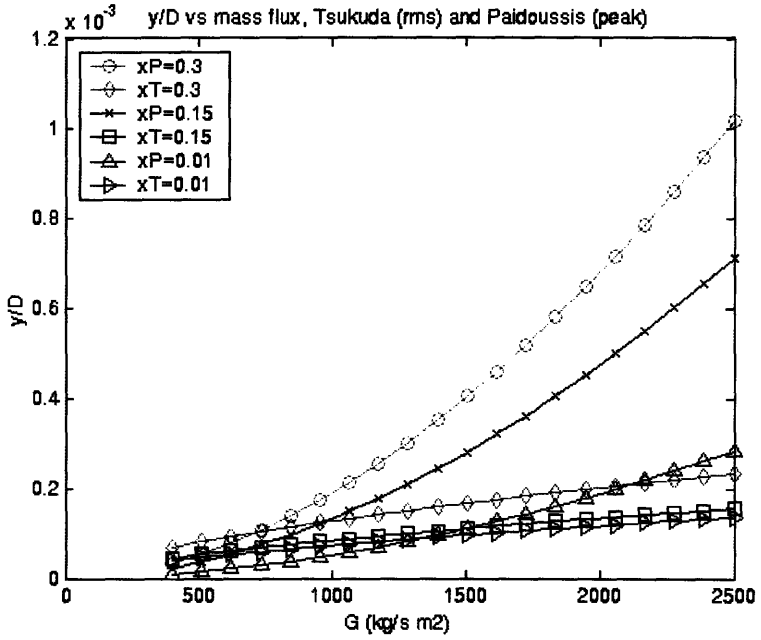

Figure B.4: Païdoussis - Tsukuda Vibration Ratio Comparison

For simplicity and consistency with the present analysis it is advisable to restrict the range of comparison above 1000 kg/sm^2 and at high quality. In such a way the attention is focused on conditions more typical of a BWR, which is the subject of this study. Figure B.5 presents results in the BWR range.

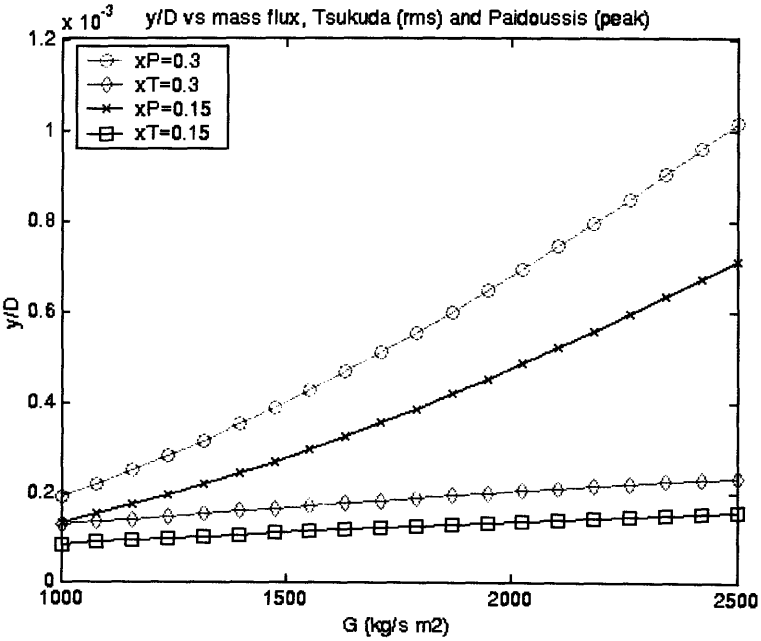

Figure B.5: Païdoussis - Tsukuda Vibration Ratio Comparison (Restricted G Range)

It can be noticed that the Tsukuda correlation delivers vibration ratios from 1.5 to 4.5 times lower than those predicted by Païdoussis. However, it has to be recalled that the vibration ratios computed by the two correlations are not exactly the same: Tsukuda provides the root mean square ratio, Païdoussis the peak value. As previously stated, $y_{peak} \approx 2 \div 3\ y_{rms}$. Taking 2.5 as the average ratio between the peak value and the rms value, and multiplying the Tsukuda correlation by this number, the two correlations tend to approach each other, as shown in Figure B.6.

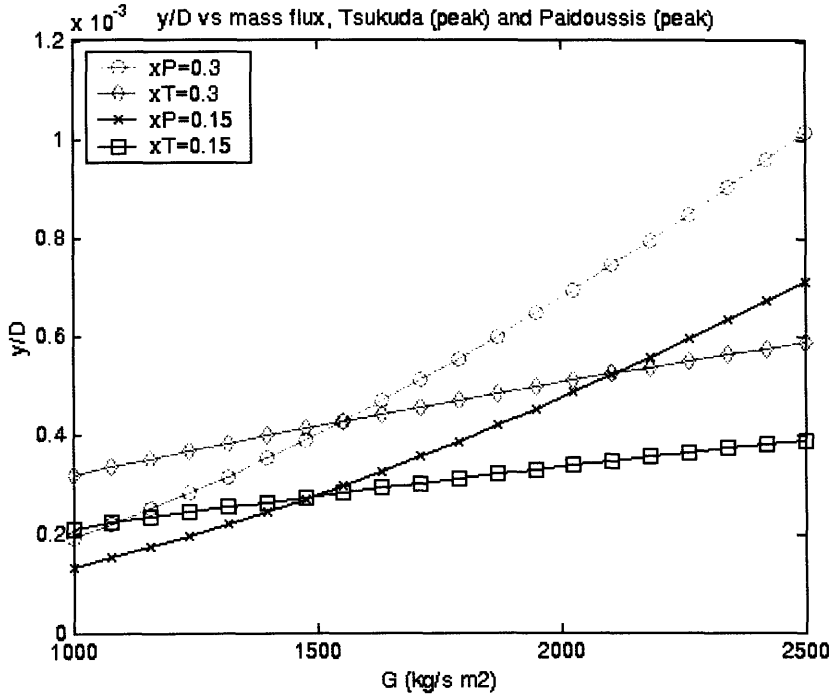

Figure B.6: Païdoussis - Tsukuda Vibration Ratio Comparison (Restricted G Range)

Vibration limit value

The last step in the vibration analysis consists of the choice of a reasonable limit value for the vibration ratio. The final choice is based on two literature references, [20] and [35], of which [20] has already been introduced, i.e. the hydraulic vibration tests carried out by the Japanese team. In order to develop the empirical correlation, they collected experimental data. These data have to be considered, even if not very numerous (they come from a single source), quite reliable; in fact, they were collected rather recently, and are from full-scale test assemblies tested under environmental conditions existing in a

BWR. Figure 5 of [20] shows the vibrations peak amplitude measured for the two 9×9 assemblies[65], for exit quality equal to 15%. As predictable, the peak values increase as the flow rate increases, reaching a maximum of about 16 μm for one of the rod inside the Type A assembly, for a flow rate of 70 t/h, corresponding to a mass flux of about 2140 kg/sm^2. Since the rod diameter for the assembly Type A is 11.2 mm, the maximum measured vibration ratio is about 1.43×10^{-3}.

This value, together with the other three maximum[66] peak vibration ratios measured in the assembly TypeA have been plotted in Figure B.7 as the line titled "Exp.max.peaks, x=15%"). The same figure contains also the vibration ratios predicted by the Païdoussis correlation, the Tsukuda correlation and the Païdoussis corrected correlation. The upper straight line, corresponding to the equation y/D = 0.021, derives from the second literature reference previously mentioned. In fact, reference [35] states: "*For PWR fuel rods, a maximum amplitude of 0.2 to 0.25 mm is generally accepted as design criterion for vibrations*". Taking conservatively the lower end of the suggested range, and using D = 9.5 mm as rod diameter (average value for PWR rods):

$$\frac{y}{D}=\frac{0.2}{9.5}\approx 0.021 \qquad \text{(B-15)}$$

Comparing this value with the profile of the predictive correlations it is evident that this value is a reasonable choice for the vibration ratio limit. In particular, notice the consistent position of the Païdoussis corrected correlation curve: above the two empirical correlations and the experimental measuments, but below the limit value. Rather interesting is its almost asymptotic trend toward the limit value for very high mass fluxes.

[65] The Japanese team also performed measurements on a high-burnup 8×8 fuel assembly, which delivered peak amplitudes about 25% larger than those referred to the 9×9 assemblies. However, in this analysis only data referred to the TypeA&B assemblies will be accounted for since the reference geometry in this study is 9×9.

[66] The adjective "maximum" would seem redundant, it being close to the word "peak". In actuality, under each flow rate condition the rods monitored within the same assembly are subjected to different oscillations. Therefore, each one shows a peak value. The largest peak value is here referred as the maximum peak value.

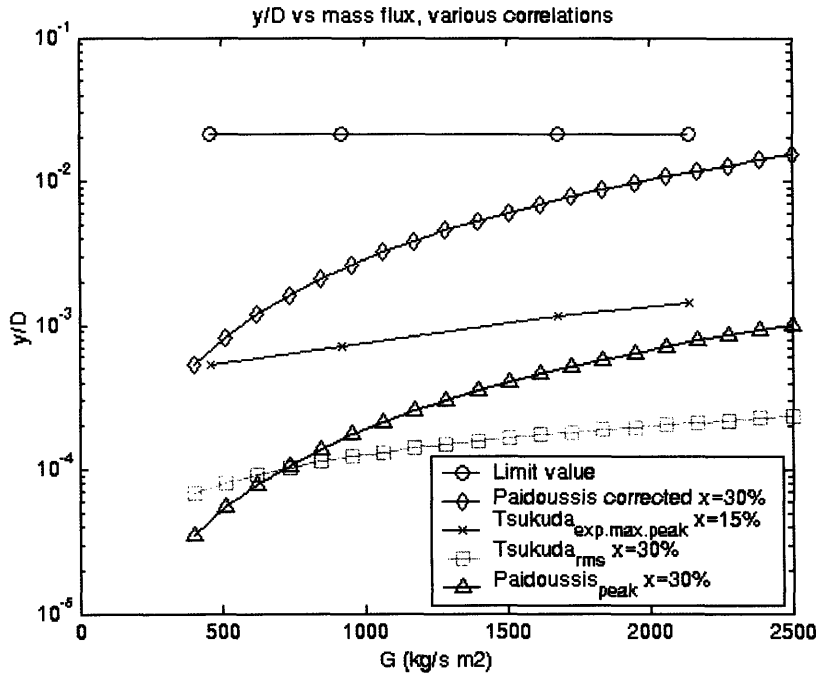

Figure B.7: Final Vibration Ratio Comparison

However, as already stressed, all the graphs presented in this Appendix were derived from calculations performed on the reference assembly configuration. As a consequence, while the vibration ratio limit is maintained fixed throughout the whole analysis, the assembly configurations change and for some of them the vibration ratio at high mass flux may exceed the limit. This phenomenon especially concerns rods having small diameter: in fact, because of the lower weight they are obviously subjected to more significant vibrations (see for example Figure 4.8)

Conclusions

The investigation performed on the vibrations prediction in two-phase flow, based on the few correlations available in literature, can be summarized in the following brief points:

a) the calculation of vibrations in two-phase flow is a research field still little explored and therefore often undefined.

b) The ratio between the transversal vibration amplitude and the rod diameter has been chosen as the vibration parameter upon which all the calculations have been based. This parameter has been called "vibration ratio".

c) Two empirical correlations have been examined and compared: the Païdoussis correlation and the Tsukuda correlation. The first was developed based on a large amount of experimental data, some of which is representative of environmental conditions far from those of the present project. The second was developed more recently based on experimental data referred to environmental conditions specific to a BWR. Taking into account the uncertainties that always accompany the development of empirical correlations, as well as the complexity of the vibration phenomenon in two-phase flow, the two correlations have been found to give comparable results.

d) Based on the need to perform a conservative analysis, the Païdoussis correlation has been modified and used to calculate the vibration ratios in the present thermal-hydraulic analysis. To this "new" correlation the name *Païdoussis Corrected Correlation* has been assigned.

e) Based on experimental data, common design criteria, and comparison with the results delivered by the Païdoussis corrected correlation, the vibration ratio limit chosen is $(y/D)_{LIM} = 0.021$.

Appendix C

C1. Investigation of the Influence of the Ratio Between Core Power and Coolant Flow Rate on the Maximum Achievable Power

As specified in Section 2.2.1, the whole analysis was performed maintaining the ratio $\dot{Q}/\dot{m}$ constant, and equal to the value characteristic of the reference plants, that is 243.07 kW/(kg/s) for the cores assumed to be loaded in a BWR/5 vessel, and 449.87 kW/(kg/s) for those loaded in an ESBWR vessel. This means that, given a *D-P/D* pair, each one of the power levels iteratively examined during the procedure shown in Figure 1.1 was coupled with a unique flow rate, given by the following relations:

$$\dot{m} = \frac{\dot{Q}}{243.07} \quad \text{or} \quad \dot{m} = \frac{\dot{Q}}{449.87} \tag{C-1}$$

depending on the case under examination. Therefore, no freedom in varying the $\dot{Q}/\dot{m}$ ratio has been allowed. Consequently, given a BWR/5 core configuration, for example, for which the maximum achievable power was found to be $\dot{Q}_1$, with $\dot{Q}_1/\dot{m}_1$ = 243.07 kW/(kg/s), another power-flow rate pair ($\dot{Q}_2$ and $\dot{m}_2$) may exist, such that:

$$\dot{Q}_2 > \dot{Q}_1 \quad \text{and} \quad \frac{\dot{Q}_2}{\dot{m}_2} \neq 243.07\,\text{kW/(kg/s)}$$

This Appendix is aimed at demonstrating that even allowing the power/flow ratio to vary, the "overall" maximum achievable power would not significantly differ from that obtained by setting the ratio at the values previously mentioned. To do this, six BWR/5 oxide assembly configurations have been subject to a search for the "actual" maximum achievable power over a range of 12 power/flow ratios (n_1 =290,..., n_6 =243.07,..., n_{12} =190). The first "relative" maximum achievable power ($\dot{Q}^{rel}_{1-max}$) has been determined among all the possible power-flow combinations which satisfy the relation $\dot{Q}/\dot{m} = n_1$, where n_1 is the first and higher value assumed by the power/flow ratio in the mentioned range. Then, the same analysis has been performed over all the power-flow combinations which satisfy the relation $\dot{Q}/\dot{m} = n_2$, and so on for all the *n*-values in the range. At this

point, the data collected, i.e. $\dot{Q}^{rel}_{1-max}$, $\dot{Q}^{rel}_{2-max}$,..., $\dot{Q}^{rel}_{12-max}$, are sufficient to state how much the "overall" maximum achievable power $\dot{Q}_{max} = \max\left(\dot{Q}^{rel}_{1-max}, \dot{Q}^{rel}_{2-max}, ..., \dot{Q}^{rel}_{12-max}\right)$ differs from that obtained setting $n_i = n_6 = 243.07$ kW/(kg/s), i.e. from $\dot{Q}^{rel}_{6-max}$.

The six assembly configurations examined in this Appendix are listed in Table C.1.

Table C.1: assembly configurations examined for power/flow ratio investigation

Assembly	*D (cm)*	*P/D*	*Notes*
A	1.1176	1.2773	Reference BWR/5 assembly configuration
B	0.7579	1.4158	This is one of the three assembly configurations associated with the overall maximum achievable power for Case Ox-Backfit-5 (36 psia as pressure drop limit) (see Figure 3.1)
C	0.7500	1.5500	
D	0.8500	1.2000	
E	1.1000	1.5000	
F	1.5000	1.1500	

The positions occupied by these assembly configurations within the powermap are indicated by means of the corresponding letters in Figure C.1. Since the assemblies examined here are oxide BWR/5-type, the reference powermap chosen is that of Case Ox-Backfit-5 shown in Figure 4.1 .

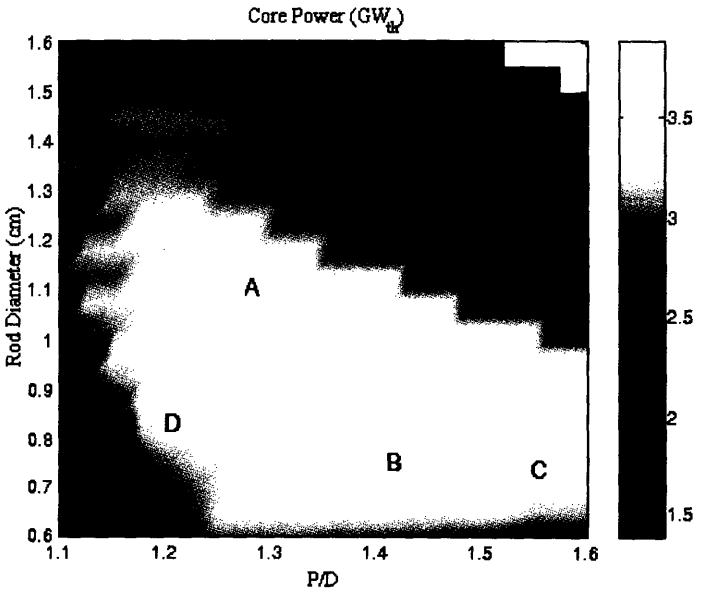

Figure C.1: Locations of the Assembly Configurations Examined for $\dot{Q}/\dot{m}$ Ratio Investigation

The results of the analysis are presented at the end of this Appendix in the form of tables. Each table refers to one of the six assembly configurations, and shows the "relative" maximum achievable powers $\dot{Q}^{rel}_{i-\max}$ associated with each power/flow ratio n_i, together with some additional thermal hydraulic data. In particular, since the ratio power/flow plays an important role in determining the thermal-hydraulic stability of the system, an estimate of the hot bundle decay ratio has been performed[67]. Two main observations arise from the results:

- the hot bundle Decay Ratio (DR) decreases as $\dot{Q}/\dot{m}$ decreases. This reflects the reduced thermal hydraulic stability due to high quality conditions in the channels. In spite of this, all the examined assembly configurations have a decay ratio quite far from the value typically set as maximum limit, i.e. DR=0.5, even for the largest $\dot{Q}/\dot{m}$.

- For each assembly configuration the "overall" maximum achievable power does not differ significantly from the "relative" maximum power $\dot{Q}^{rel}_{6-\max}$. This important conclusion is evident from Table C.2 which extracts the most relevant data from the tables presented at the end of this Appendix and compares $\dot{Q}^{rel}_{6-\max}$ to $\dot{Q}_{max}$ for each assembly configuration examined. The comparison is made easier by calculating a power gain percentage, $Q\%$, defined as:

$$Q\% = \frac{\dot{Q}_{\max} - \dot{Q}^{rel}_{6-\max}}{\dot{Q}^{rel}_{6-\max}} \cdot 100 \qquad \text{(C-2)}$$

and a pressure drop increase percentage, $\Delta p\%$, defined as:

$$\Delta p\% = \frac{(\Delta p)_{i\_\max} - (\Delta p)_6}{(\Delta p)_6} \cdot 100 \qquad \text{(C-3)}$$

where $(\Delta p)_{i\_\max}$ represents the core pressure drop corresponding to $\dot{Q}_{max}$, while $(\Delta p)_6$ is referred to the situation in which $n_i = n_6 = 243.07$ kW/(kg/s). Since the

[67] The DR is a measure of how quickly two-phase instability phenomena tend to die-out. In this analysis it is estimated as 130% of the DR calculated assuming: 1) uniform axial power distribution; 2) inlet orificing coefficient as the only form loss along the channel. The computational model used to perform such a calculation was developed by Zhao in [36].

"overall" maximum power $\dot{Q}_{max}$ can be associated with more than one n_i (sometimes the maximum power calculation is insensitive to the power/flow ratio) the i^{th}-ratio chosen to calculate $Q\%$ is that associated with the lower pressure drop.

Table C.2 : Comparison between "Relative" Maximum Power and "Overall" Maximum Power

Assembly configuration	$\dot{Q}^{rel}_{6-max}$ (MW_t)	$\dot{Q}_{max}$ (MW_t)	n_{i_max} (kW/(kg/s))	$Q\%$ (%)	$\Delta p\%$ (%)
A	3324	3482	200	+4.7	+42.6
B	3875	3898	240	+0.6	+3.2
C	3777	3834	250	+1.5	-1.6
D	3459	3500	250	+1.2	-1.7
E	3377	3482	200	+3.1	+41.6
F	2938	3084	200	+5.0	+41.5

From the table above it is quite evident that even allowing the power/flow ratio to vary, the "overall" maximum achievable power would not significantly differ from the one calculated maintaining the mentioned ratio constant and equal to 243.07 kW/(kg/s). The maximum gain in power is never larger than 5% and, when it approaches such a value, it is coupled with a significant increase in pressure drop.

From the last consideration it can be concluded that the decision to constrain core power and coolant flow rate by means of the fixed ratio $\dot{Q}/\dot{m}$ =243.07 kW/(kg/s) may have prevented the analysis from obtaining the actual maximum achievable power for each assembly configuration. Nevertheless, the difference between the results obtained through the analysis and the "overall" maximum powers is, if actually present, negligible. This justifies the decision to restrict the study range to only the power-flow pairs which satisfy the relation $\dot{Q}/\dot{m}$ =243.07 kW/(kg/s).

The following are the tables which list all the numerical data used to perform the investigation described in this Appendix. In each table, the row highlighted corresponds to the power/flow ratio resulting in the maximum power ($\dot{Q}_{max}$).

Table C.3: "Relative" Maximum Achievable Powers for Assembly A								
i	$\dot{Q}/\dot{m}$ (kW kg^{-1} s)	$\dot{Q}^{rel}_{i-\max}$ (MWt)	$\dot{m}$ (kg/s)	Hot bundle decay ratio	Core pressure drop (psi)	Max. vibr. ratio	Hot bundle exit quality (%)	Limiting parameter
1	290	3020	10412	0.26	16.5	0.0030	33.4	MCPR
2	280	3090	11035	0.23	17.9	0.0033	31.9	MCPR
3	270	3160	11704	0.21	19.4	0.0036	30.5	MCPR
4	260	3225	12402	0.19	21.1	0.0040	29.1	MCPR
5	250	3289	13156	0.17	23.0	0.0044	27.7	MCPR
6	243.07	3324	13676	0.15	24.4	0.0046	26.7	MCPR
7	240	3342	13924	0.15	25.0	0.0048	26.3	MCPR
8	230	3389	14733	0.13	27.2	0.0052	24.9	MCPR
9	220	3430	15589	0.11	29.6	0.0057	23.5	MCPR
10	210	3465	16499	0.10	32.2	0.0063	22.2	MCPR
11	200	3482	17402	0.08	34.8	0.0064	20.8	MCPR
12	190	3394	17866	0.08	36.0	0.0070	19.5	Δp

...

Table C.4 : "Relative" Maximum Achievable Powers for Assembly B								
i	$\dot{Q}/\dot{m}$ (kW kg^{-1} s)	$\dot{Q}^{rel}_{i-\max}$ (MWt)	$\dot{m}$ (kg/s)	Hot bundle decay ratio	Core pressure drop (psi)	Max. vibr. ratio	Hot bundle exit quality (%)	Limiting parameter
1	290	3559	12271	0.16	20.8	0.0133	32.3	MCPR
2	280	3629	12960	0.14	22.6	0.0146	30.9	MCPR
3	270	3705	13723	0.13	24.6	0.0160	29.5	MCPR
4	260	3770	14498	0.12	26.7	0.0174	28.1	MCPR
5	250	3840	15359	0.10	29.1	0.0191	26.8	MCPR
6	243.07	3875	15941	0.09	30.7	0.0203	25.8	MCPR
7	240	3886	16193	0.09	31.3	0.0208	25.4	MCPR
8	230	3767	16377	0.08	31.7	0.0210	24.1	vibr
9	220	3630	16502	0.08	31.7	0.0210	22.8	vibr
10	210	3491	16625	0.06	31.7	0.0210	21.5	vibr
11	200	3351	16753	0.05	31.7	0.0210	20.2	vibr
12	190	3211	16902	0.05	31.8	0.0210	18.9	vibr

...

Table C.5: "Relative" Maximum Achievable Powers for Assembly C								
i	$\dot{Q}/\dot{m}$ (kW kg^{-1} s)	$\dot{Q}^{rel}_{i-\max}$ (MWt)	$\dot{m}$ (kg/s)	Hot bundle decay ratio	Core pressure drop (psi)	Max. vibr. ratio	Hot bundle exit quality (%)	Limiting parameter
1	290	3594	12392	0.09	17.8	0.0146	30.8	MCPR
2	280	3664	13086	0.08	19.4	0.0160	29.5	MCPR
3	270	3723	13788	0.06	20.9	0.0174	28.3	MCPR
4	260	3781	14543	0.06	22.7	0.0190	27.0	MCPR
5	[illegible]	[illegible]	[illegible]	[illegible]	[illegible]	[illegible]	[illegible]	[illegible]
6	243.07	3777	15538	0.05	25.0	0.0210	24.8	vibr
7	240	3737	15572	0.05	25.0	0.0210	24.5	vibr
8	230	3607	15682	0.04	25.1	0.0210	23.2	vibr
9	220	3477	15803	0.04	25.2	0.0210	21.9	vibr
10	210	3345	15927	0.04	25.3	0.0210	20.7	vibr
11	200	3214	16072	0.03	25.4	0.0210	19.5	vibr
12	190	3081	16216	0.03	25.5	0.0210	18.3	vibr

...

Table C.6: "Relative" Maximum Achievable Powers for Assembly D								
i	$\dot{Q}/\dot{m}$ (kW kg^{-1} s)	$\dot{Q}^{rel}_{i-\max}$ (MWt)	$\dot{m}$ (kg/s)	Hot bundle decay ratio	Core pressure drop (psi)	Max. vibr. ratio	Hot bundle exit quality (%)	Limiting parameter
1	290	3166	10917	0.36	24.6	0.0075	35.3	MCPR
2	280	3254	11621	0.32	26.9	0.0083	33.8	MCPR
3	270	3336	12355	0.30	29.5	0.0091	32.3	MCPR
4	260	3418	13146	0.27	32.2	0.0101	30.8	MCPR
5	[illegible]	[illegible]	[illegible]	[illegible]	[illegible]	[illegible]	[illegible]	[illegible]
6	243.07	3459	14230	0.22	36.0	0.0113	28.2	Δp
7	240	3427	14278	0.21	36.0	0.0114	27.7	Δp
8	230	3318	14428	0.19	36.0	0.0114	26.3	Δp
9	220	3201	14551	0.17	36.0	0.0113	24.8	Δp
10	210	3201	14551	0.17	36.0	0.0113	24.8	Δp
11	200	2973	14863	0.13	36.0	0.0114	21.9	Δp
12	190	2852	15013	0.12	36.0	0.0114	20.5	Δp

...

Table C.7: "Relative" Maximum Achievable Powers for Assembly E								
i	$\dot{Q}/\dot{m}$ (kW kg^{-1} s)	$\dot{Q}^{rel}_{i-\max}$ (MWt)	$\dot{m}$ (kg/s)	Hot bundle decay ratio	Core pressure drop (psi)	Max. vibr. ratio	Hot bundle exit quality (%)	Limiting parameter
1	290	3137	10816	0.10	13.2	0.0034	31.2	MCPR
2	280	3195	11412	0.09	14.2	0.0037	29.9	MCPR
3	270	3248	12030	0.08	15.4	0.0040	28.7	MCPR
4	260	3301	12695	0.08	16.6	0.0044	27.4	MCPR
5	250	3348	13391	0.06	18.0	0.0048	26.1	MCPR
6	243.07	3377	13892	0.06	19.0	0.0051	25.3	MCPR
7	240	3389	14119	0.06	19.5	0.0052	24.9	MCPR
8	230	3424	14886	0.05	21.1	0.0057	23.6	MCPR
9	220	3453	15696	0.05	22.9	0.0061	22.4	MCPR
10	210	3471	16527	0.04	24.8	0.0066	21.1	MCPR
11	200	3482	17410	0.04	26.8	0.0072	19.9	MCPR
12	190	3482	18329	0.03	29.2	0.0078	18.7	MCPR

...

Table C.8: "Relative" Maximum Achievable Powers for Assembly F								
i	$\dot{Q}/\dot{m}$ (kW kg^{-1} s)	$\dot{Q}^{rel}_{i-\max}$ (MWt)	$\dot{m}$ (kg/s)	Hot bundle decay ratio	Core pressure drop (psi)	Max. vibr. ratio	Hot bundle exit quality (%)	Limiting parameter
1	290	2668	10000	0.29	13.3	9.2e-4	34.3	MCPR
2	280	2727	9738	0.26	14.3	0.0010	32.9	MCPR
3	270	2785	10315	0.23	15.5	0.0011	31.5	MCPR
4	260	2850	10960	0.21	16.8	0.0012	30.3	MCPR
5	250	2902	11609	0.18	18.3	0.0013	28.6	MCPR
6	243.07	2938	12085	0.17	19.5	0.0014	27.6	MCPR
7	240	2961	12337	0.17	20.0	0.0015	27.2	MCPR
8	230	3008	13077	0.14	21.8	0.0016	25.8	MCPR
9	220	3043	13832	0.13	23.6	0.0018	24.4	MCPR
10	210	3078	14658	0.12	25.7	0.0019	23.0	MCPR
11	200	3084	15420	0.10	27.6	0.0021	21.6	$T_{fuel\_average}$
12	190	3084	16231	0.09	29.8	0.0023	20.2	$T_{fuel\_average}$

Appendix D

D1. Development of a Simplified Relation to Predict the Hydride Bundle Weight

This Appendix describes the procedure followed to obtain equation 2-8, which allows calculation, with good accuracy, of a representative value of the mass of a hydride bundle using the rod diameter D and the bundle matrix n as the only required geometric input data.

The mass of a hydride fueled bundle (fuel channel and grid spacers excluded) can be expressed by means of the following relation:

$$M = M_{UZrH1.6} + M_{Zr} = N_{FR}\frac{\pi}{4}D_{fo}^2 L_H \rho_{UZrH1.6} + N_R\frac{\pi}{4}\left(D^2 - D_{ci}^2\right)L\rho_{Zr} \qquad \text{(D-1)}$$

where D_{fo} is the pellet diameter, L_H and L are the heated and total length, D_{ci} is the inside clad diameter, $\rho_{UZrH1.6}$ and ρ_{Zr} are the densities of hydride fuel and Zircalloy respectively. In particular, N_R is the total number of rods contained in the bundle. Because of the presence of control rod guide tubes: $N_R > N_{FR}$. Moreover, recalling the meaning of the bundle matrix n, it is evident that $N_R = n^2$. By introducing a corrective coefficient $f < 1$ it is possible to express N_{FR} as a function of n:

$$N_{FR} = (n \cdot f)^2 \qquad \text{(D-2)}$$

where $f = \sqrt{N_{FR}}/n$. Based on the VAMPIRE algorithm establishing the control rod guide tube disposition (see Section 3.3.2, point "b" of "Bundle structure assumptions"), it is possible to calculate the number of fuel rods corresponding to different values of n. Such numbers are listed in Table D.1 and shown in Figure D.1.

Table D.1 : Corrective Factor f		
n	$N_{fuelrods}$	f
8	60	0.968
9	72	0.943
10	84	0.916
11	112	0.962
12	128	0.943
13	144	0.923
14	180	0.958
15	200	0.943
16	220	0.927
17	264	0.956
18	288	0.943
19	312	0.930
20	364	0.954

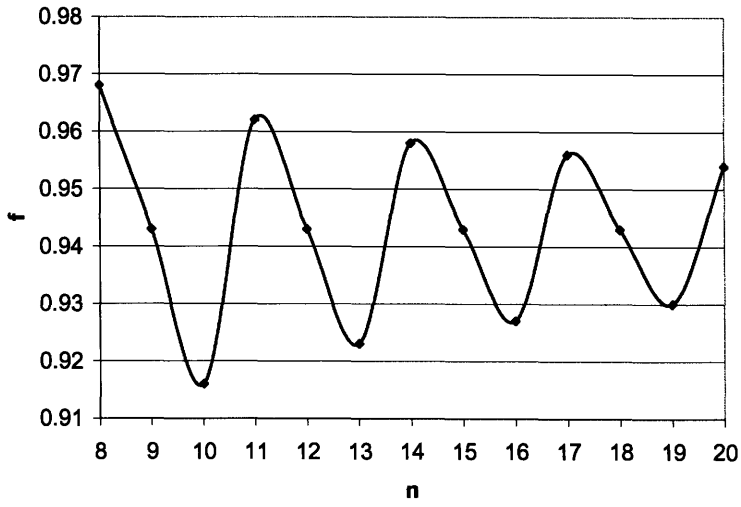

Figure D.1: Corrective Factor f vs n

Since the range of variation of f is quite small, and its oscillatory profile does not suggest any simple function $f = f(n)$, the choice of ignoring the n-dependence and adopting an averaging procedure seems to be the more reasonable. For this reason, the present analysis assigns to the corrective factor the value $\bar{f} = 0.944$, which is the average of the values shown in Table D.1. With this assumption N_{FR} becomes:

$$N_{FR} = \left(n \cdot \bar{f}\right)^2 \tag{D-3}$$

At this point, the scaling relations introduced in Section 3.3.1 (point "b" of "Bundle structure assumptions") have been used to calculate D_{fo} and D_{ci} for several diameters D within the analysis range $6 \leq D \leq 16$ mm. The difference $D^2 - D_{ci}^2$ has been also computed. Numerical results are shown in Table D.2.

Table D.2: Hydride Fueled Rod Geometry					
D [mm]	t_{clad} [mm]	D_{ci} [mm]	t_{gap} [mm]	D_{fo} [mm]	$D^2 - D_{ci}^2$ [mm^2]
6.000	0.584	4.832	0.152	4.527	12.6556
6.526	0.584	5.358	0.152	5.053	13.8855
7.053	0.584	5.884	0.152	5.579	15.1154
7.579	0.594	6.391	0.152	6.086	16.6017
8.105	0.627	6.852	0.135	6.581	18.7478
8.632	0.659	7.313	0.145	7.024	21.0223
9.158	0.692	7.774	0.154	7.467	23.4252
9.684	0.724	8.236	0.163	7.909	25.9565
10.211	0.757	8.697	0.173	8.352	28.6163
10.737	0.789	9.158	0.182	8.795	31.4044
11.263	0.822	9.620	0.191	9.237	34.3209
11.789	0.854	10.081	0.201	9.680	37.3659
12.316	0.887	10.542	0.210	10.123	40.5393
12.842	0.919	11.004	0.219	10.565	43.8411
13.368	0.952	11.465	0.228	11.008	47.2713
13.895	0.984	11.926	0.238	11.451	50.8299
14.421	1.017	12.387	0.247	11.893	54.5169
14.947	1.049	12.849	0.256	12.336	58.3324
15.474	1.082	13.310	0.266	12.779	62.2762
16.000	1.114	13.771	0.275	13.221	66.3485

D_{fo} and $(D^2 - D_{ci}^2)$ are plotted in Figure D.2 and Figure D.3 as functions of the rod diameter D. The corresponding interpolating functions are also displayed together with their mathematical expression. Since the interpolation is very accurate, the two expressions have been recorded and introduced in equation (D-1).

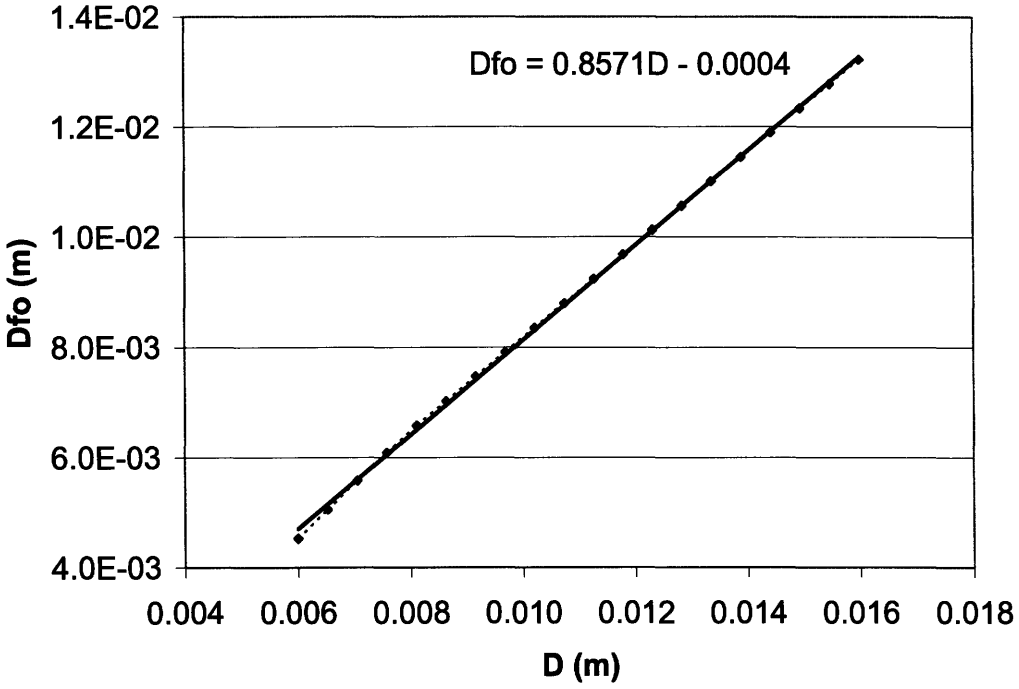

Figure D.2: Pellet Diameter as a Function of D (Hydride Fueled Rod)

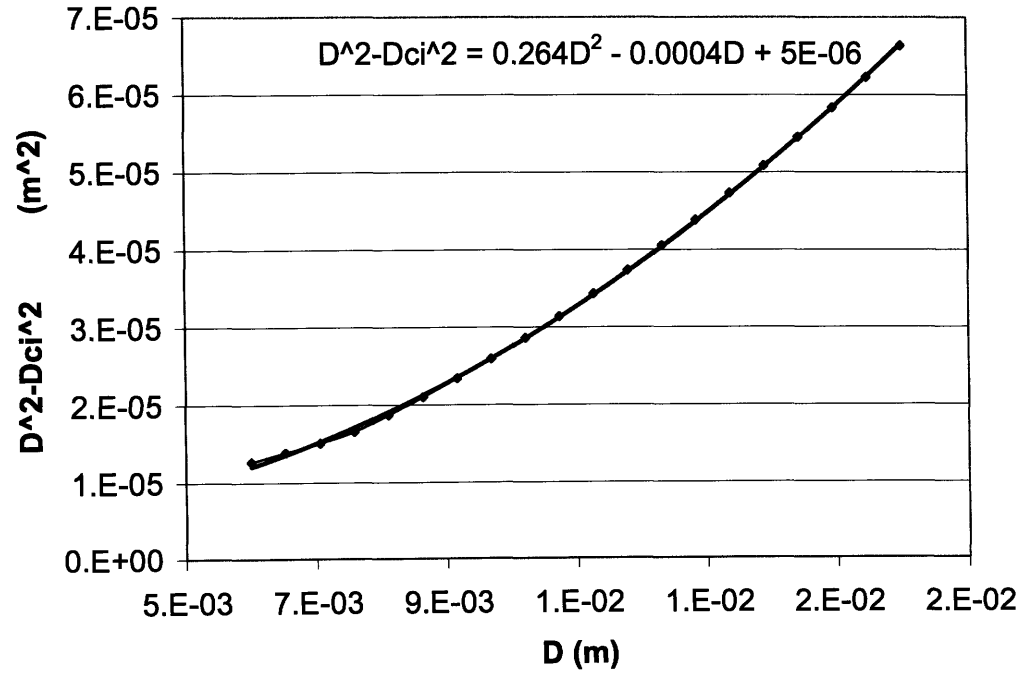

Figure D.3: ($D^2 - D_{ci}^2$) as a Function of D (Hydride Fueled Rod)

$$M = n^2 \bar{f}^2 \frac{\pi}{4}\left(0.8571D - 0.0004\right)^2 L_H \rho_{UZrH1.6} + n^2 \frac{\pi}{4}\left(0.264D^2 - 0.0004D + 5 \cdot 10^{-6}\right) L \rho_{Zr} \qquad \text{(D-4)}$$

Assigning to the parameters present in (D-4) the corresponding values from Table 1.3 and Table J.1, and using the average value $\bar{f} = 0.944$, the expression becomes:

$$M = \left(21416.4D^2 - 23.3D + 0.111\right) \cdot n^2 \qquad \text{(D-5)}$$

Appendix E

E1. Supplemental Comments on Case Assumptions

This Appendix presents supplemental comments and/or justifications concerning assumptions made throughout the analysis which require extended presentation. A complete understanding of the assumptions made for each case, as well as the correct distinction between the assumptions made for a given case and not for the others, require the reading of the relative sections first (Section 3.1, 3.2.2, 3.3.1, 3.3.2). Whenever such sections cite only briefly some assumptions, it is clearly stated and the reader finds here a more detailed description.

The order followed for the assumption description is consistent with the order with which the assumptions were listed in the mentioned sections:

- Common assumptions
- Case 0 (VIPRE Core Modeling Validation)
- Case Ox-Backfit-5, Case Hyd-Backfit-5 and Case Ox-Backfit-ES
- Case Hyd-NewCore-5 and Case Hyd-NewCore-ES

Likewise, the categorization and the numbering with letters are consistent with those used in the mentioned sections. If no comments are needed for a given assumption, the corresponding letter is not displayed.

E1.1. Common Assumptions

Bundle structure assumptions

c) The most recent BWR bundle types are provided with the so-called Partial Length Fuel Rods (PLFRs), whose length is about 2/3^{rds} of the other rod active length. In particular, the GE11 lattice was the first GE bundle geometry developed with this feature and contains eight of these rods. The PLFRs are designed to reduce the two-phase pressure drop in the upper part of the bundles in such a way that the single phase pressure drop due to the orificing can be increased, maintaining the same total pressure drop and so enhancing the two-phase stability. For some designs, the pressure drop gain resulting from the PLFRs use is even sufficient to allow the Debris

Filter Lower Tie Plate (DFLTP) implementation. Contrary to the typical Lower Tie Plate type, this design is provided with a large number of very small holes, through which the coolant flows and enters in the active part of the bundle. For example, besides the 78 holes for the fuel rods and the two holes for the water rods, GE14 10×10 DFLTP is provided with other 444 smaller holes having a diameter of 0.125 inches each ([38]). While the DFLTP is standard with the GE14 design, it is an option for the GE11 through GE13 designs. Consistent with the choice of treating all the rods as full length rods, the Lower Tie Plate examined here is not a DFLTP.

Another important reason for which PLFRs are used is that the larger flow area in the upper part of the bundles results in a reduction of the mass flux. At high quality conditions typical of BWRs this translates in an improved margin to dryout.

Power distribution assumptions

b) The J_1 factor, calculable for each fuel rod, is a function of the peaking factor of the rod to which it is referred and its neighboring ones ([16], [4]). It has a fundamental importance since it is needed for the calculation of the MCPR by means of the correlation chosen for this purpose, i.e. the Hench-Gillis correlation, which is briefly described in this section under "Critical power determination assumptions", and more in detail in [16]. Each J_1 factor can be interpreted as a measure of the degree of non-uniformity of the power distribution among the rods surrounding the one under examination. As a consequence, the maximum J_1 factor of the whole bundle represents the most pronounced local non-uniformity in the rod-to-rod power distribution. Its influence on the MCPR is therefore quite evident. For all the cases examined, regardless of the fuel type, bundle geometry and bundle radial position, the pin-by-pin power distribution shown in Figure E.1 is adopted. The maximum J_1 factor of this power distribution is 1.198, and corresponds to the side rod highlighted in red.

1.15	1.26	1.25	1.22	1.21	1.22	1.25	1.26	1.16
1.26	1.12	1.01	0.44	0.87	0.44	1.01	1.14	
1.26	1.01	0.42	0.87	1.00	0.92	0.43	1.02	1.26
1.22	0.44	0.87	1.14			0.93	0.45	1.22
1.21	0.87	1.00				0.99	0.87	1.20
1.23	0.45	0.94			1.11	0.85	0.44	1.21
1.27	1.01	0.43	0.93	1.00	0.87	0.43	1.00	1.24
1.25	1.14	1.01	0.44	0.89	0.44	1.00	1.12	1.26
1.14	1.25	1.25	1.23	1.21	1.22	1.25	1.24	1.15

Figure E.1: Pin-by-Pin Power Distribution Used for All the Bundle Designs

Such a power distribution is an "elaboration" of an "original" pin-by-pin power map, shown in Figure E.2, deriving from neutronic analysis of a GE11 bundle containing Gadolinium, at Beginning Of Life ([2]).

1.11	1.22	1.21	1.18	1.17	1.18	1.21	1.22	1.12
1.22		0.98	0.43		0.43	0.98		1.22
1.22	0.98	0.41	0.84	0.97	0.89	0.42	0.99	1.22
1.18	0.43	0.84	1.10			0.90	0.44	1.18
1.17		0.97				0.96		1.16
1.19	0.44	0.91			1.08	0.82	0.43	1.17
1.23	0.98	0.42	0.90	0.97	0.84	0.42	0.97	1.20
1.21		0.98	0.43		0.43	0.97		1.22
1.10	1.21	1.21	1.19	1.17	1.18	1.21	1.20	1.11

Figure E.2: Original Pin-by-Pin Power Distribution Used to Obtain Figure E.1

Use of the original map was not considered an appropriate choice, for three reasons:

- it accounts for the presence of Partial Length Fuel Rods (PLFRs, marked in grey), which are instead assumed to be full length rods in this analysis.

- The peaking factors shown are normalized to 70.65, instead of 74, which is the actual number of fuel rods contained in the GE11 bundle[68]. In order to calculate the J_I factors needed for the application of the Hench-Gillis correlations, the

[68] This is because 70.65 is the number of "dummy" Full Length fuel Rods (FLFRs) equivalent to 66 real FLFRs plus 8 PLFRs. In fact, the ratio between the PLFR active length and the FLFR active length is: 85.16/145.98=0.581 (). Therefore, 8 PLFRs are equivalent to: 0.581×8=4.65 "dummy" FLFRs, and 66+4.65=70.65.

peaking factors entered as input should be normalized to the number of fuel rods actually present in the bundle.

- Each peaking factor in Figure E.2 is the ratio between the power of the corresponding rod and the power of the average "equivalent full length rod". The latter, $\overline{\dot{q}}$, is defined as:

$$\overline{\dot{q}} = \frac{\dot{Q}_{bundle}}{70.65} \tag{E-1}$$

where $\dot{Q}_{bundle}$ is the total bundle power. By not accounting for the fact that the power of the PLFRs is generated over a shorter length, the peaking factors shown in Figure E.2 do not reflect the actual unbalance existing between the Linear Heat Generation Rates (LHGRs) of the rods surrounding a PLFR. This piece of information, i.e. the LHGR unbalance, is fundamental for the correct calculation of the J_l factors.

Therefore, it was necessary to re-normalize the pin-by-pin power distribution, such that the peaking factors are normalized to 74 and the ratio between the LHGR of adjacent rods is captured. The method used to perform such a re-normalization is described below for completeness only.

The average LHGR can be calculated as:

$$\overline{q}' = \frac{\dot{Q}_{bundle}}{N_F L_F + N_P L_P} = \frac{\dot{Q}_{bundle}}{L_F\left(N_F + N_P \frac{L_P}{L_F}\right)} = \frac{\dot{Q}_{bundle}}{L_F \cdot 70.65} \tag{E-2}$$

where N_F =66 and N_P =8 are the number of Full Length Fuel Rods (FLFRs) and PLFRs respectively, while L_F and L_P are the corresponding active lengths (145.98 and 85.16 inches, [33]).

Let F_i the i-th rod peaking factor shown in Figure E.2. The power of the i-th rod, $\dot{q}_i$, can be calculated as:

$$\dot{q}_i = \overline{q}' L_F F_i = \frac{\dot{Q}_{bundle}}{L_F \cdot 70.65} L_F F_i = \frac{\dot{Q}_{bundle}}{70.65} F_i \qquad i = 1, \ldots, 74 \tag{E-3}$$

while its linear power (function of the axial location) is:

$$q_i'(z) = \frac{\dot{q}_i}{L_i} \cdot A_i(z) = \frac{\dot{Q}_{bundle}}{70.65} \frac{F_i}{L_i} \cdot A_i(z) \qquad i = 1, \ldots, 74;\ 0 < z < 145.98 \qquad \text{(E-4)}$$

where $A_i(z)$ is the axial peaking factor of the i-th rod at elevation[69] z. Of course, the axial peaking factors of the PLFRs where they are not present are 0.

The rod average linear power, i.e. averaged over all the rods, at the axial locations where all the 74 rods are present and contain fuel is:

$$\overline{q}_L'(z) = \frac{\sum_{i=1}^{74} q_i'(z)}{74} \qquad \text{for: } 6.08 < z < 91.24 \text{ (zone 2)} \qquad \text{(E-5)}$$

while at the remaining axial locations:

$$\overline{q}'_U(z) = \frac{\sum_{i=1}^{74} q_i'(z)}{66} \qquad \text{for: } 0 < z < 6.08 \text{ and } 91.24 < z < 145.98 \text{ (zone 1 and zone 3)} \qquad \text{(E-6)}$$

Now, the pin-by-pin power distribution normalizing to unity can be computed by applying the most well known definition of local peaking factor to each of the 74 rods that form the bundle. This means that the local peaking factor, function of z, is equal to the ratio between the linear power, at z, of the rod under examination and the average linear power at that axial location. Thus, for the generic i-th rod, the "new" local peaking factor at the axial location z within "zone 2", $T_{i,L}(z)$, is equal to:

[69]The axial power profile of the PLFRs coincides with that of the FLFRs where both rod types are present, and is set to zero where the PLFRs are not present (91.24<z<145.98 inches) or, even if present, where they do not contain fuel (in 0<z<6.08 inches) ([33]). Since the axial peaking factors used for each rod must be normalized to 1 over the active length, the axial peaking factors used for the FLFRs in 6.08"<z<91.24" cannot be used for the PLFRs. Even though the axial power shape is the same, the normalization requires conversion of the FLFR peaking factors to new peaking factors adapted to the reduced length.
To be consistent with the calculations that yielded the peaking factors shown in Figure E.2, the FLFR axial peaking factors used in equation E-4 come from the same source, i.e. Figure 9 of [2]. Such an axial power profile was used only for the purpose of calculating the local peaking factors shown in Figure E.1.

$$T_{i,L}(z)=\frac{q_i'(z)}{\overline{q}'_L(z)}=\frac{\dot{Q}_{bundle}}{70.65}\frac{F_i}{L_i}A_i(z)\frac{74}{\sum_{j=1}^{74}q_j'(z)}=$$

$$=\frac{\dot{Q}_{bundle}}{70.65}\frac{F_i}{L_i}A_i(z)\frac{74}{\sum_{j=1}^{74}\left(\frac{\dot{Q}_{bundle}}{70.65}\frac{F_j}{L_j}A_j(z)\right)}=\frac{F_i}{L_i}A_i(z)\frac{74}{\sum_{j=1}^{74}\frac{F_j}{L_j}A_j(z)} \qquad \text{(E-7)}$$

Likewise, for "zone 1" and "zone 3":

$$T_{i,U}(z)=\frac{q_i'(z)}{\overline{q}'_U(z)}=\frac{\dot{Q}_{bundle}}{70.65}\frac{F_i}{L_i}A_i(z)\frac{66}{\sum_{j=1}^{74}q_j'(z)}=$$

$$=\frac{\dot{Q}_{bundle}}{70.65}\frac{F_i}{L_i}A_i(z)\frac{66}{\sum_{j=1}^{74}\left(\frac{\dot{Q}_{bundle}}{70.65}\frac{F_j}{L_j}A_j(z)\right)}=\frac{F_i}{L_i}A_i(z)\frac{66}{\sum_{j=1}^{74}\frac{F_j}{L_j}A_j(z)} \qquad \text{(E-8)}$$

Since in "zone 1" and "zone 3" the PLFR axial peaking factors A_i are 0, they give null contribution to the summation at the denominator. Therefore, the only rods contributing to the summation are the FLFRs. For this reason, equation E-8 can be simplified to the following form:

$$T_{i,U}(z)=F_iA_i(z)\frac{66}{\sum_{j=1}^{74}F_jA_j(z)} \qquad \text{(E-9)}$$

Since the reference BWR/5 bundle has been assumed to contain 74 FLFRs, only "zone 2" has to be considered. Thus, the peaking factors shown in Figure E.1 derive from the application of equation E-7.

Critical power determination assumptions

a) The Hench-Gillis correlation has the general form:

$$x_C=\frac{AZ}{B+Z}(2-J)+F_P \qquad \text{(E-10)}$$

Appendix D of reference [4] provides a concise but essential description of the parameters x_C, A, B, Z and F_P, while a more complete description is presented in [16].

Besides the parameters usually required as input by most of the critical quality-boiling length correlations, the Hench-Gillis correlation requires the knowledge of the *J*-factors, which account for local power peaking in the bundles and depend on the power distribution within the assemblies. Actually, the peaking factor dependence is not directly contained in the J factors, but in the so-called J_1 factors which the user enters as VIPRE input data. The dependence relation for J is the following:

$$J = J(J_1, G) \tag{E-11}$$

where: G : coolant mass flux

$$J_1 = J_1(\textit{geometry, rod peaking factors}) \tag{E-12}$$

The major approximation described here concerns the peaking factor distribution, which is assumed to be constant for all the assemblies, regardless of their location and lattice geometry. In fact, the J_1 factors are computed using equation (E-12) in its full form (see [4]) for all the rods shown in Figure E.1. For each bundle VIPRE requires three values for J_1: the maximum J_1 for corner rods, the maximum J_1 for side rods and the maximum J_1 for central rods. However, since all bundles are assumed to have the peaking factor distribution shown in Figure E.1, the maximum J_1 factor is always associated with a side rod. Therefore a J_1 factor equal to 1.198 referred to a side rod is assigned to all the bundles, regardless of their core radial location, lattice geometry and type of fuel.

E1.2. Assumptions for Case 0 (VIPRE Core Modeling Validation)

Core structure assumptions

b) The assumption to model the cruciform control rods as completely withdrawn is partially justified by the typical operating strategy known as Control Cell Core (CCC), developed in the late 70's by GE. According to this strategy, the control rod movement to offset reactivity changes during power operations is limited to a group of control rods which, coupled with the four surrounding fuel assemblies, comprise a control cell. All the other control rods, which are the majority, are normally completely withdrawn during normal operation. Figure E.3 shows the typical

disposition of the Control Cells in a typical BWR and in the ABWR. It can be seen that in the former about 18% of the control rods are within the Control Cell, while in the latter this percentage drops to 10%.

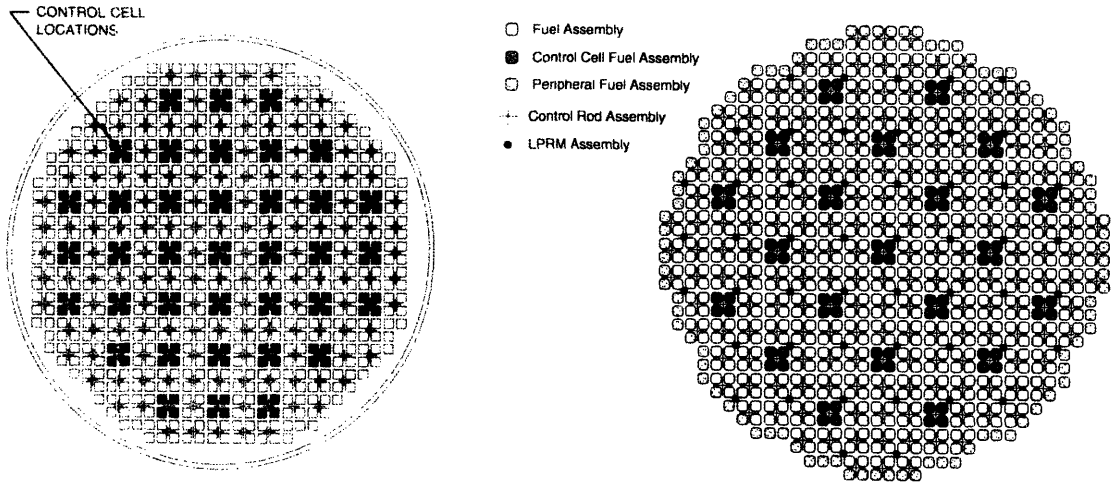

Figure E.3: Typical Control Cell Locations
(Typical BWR on the left ([37]), ABWR on the right ([38]))

Pressure drop assumptions

a) Figure E.4 shows the "central" and "peripheral" bundles for the two reference cores. Such a distinction is important since it identifies the type of orificing applied at the bundle inlet.

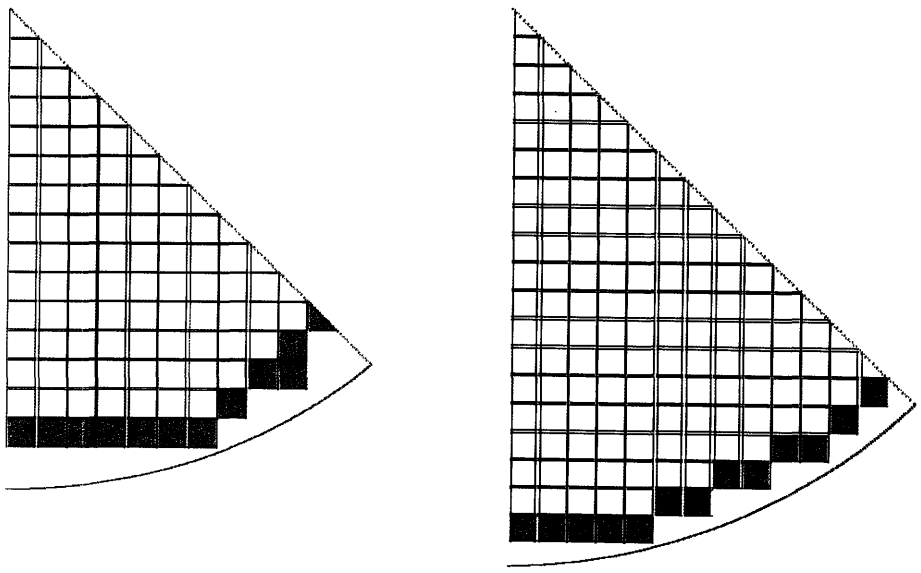

Figure E.4: Central (white) and Peripheral (grey) Bundles in the BWR/5 core (left) and ESBWR core (right)

The orificing coefficients chosen are a function of the bundle flow area. In particular:

$$C_{central} = C_{central}^{10in^2} \cdot \frac{A_f^2}{10^2}$$
$$C_{peripheral} = C_{peripheral}^{10in^2} \cdot \frac{A_f^2}{10^2} \quad \text{(E-13)}$$

where $C_{central}^{10in^2}$ and $C_{peripheral}^{10in^2}$ are the orificing coefficients normalized to an active flow area of 10 in^2 (from [24], see Table E.1), while A_f is the active flow area of the assembly configuration under examination (expressed in in^2), i.e. a proprietary data for the reference BWR/5, 14.4150 in^2 for the reference ESBWR (see Table 1.2).

b) The fuel bundles are modeled using the following form losses:

- inlet orificing ($C_{central}$ or $C_{peripheral}$, see previous point "a");
- lower tie plate ($C_{ltp} = C_{ltp}^{10in^2} \cdot \frac{A_f^2}{10^2}$);
- grid spacers (C_{grid} calculated with In's correlation ([23]). Since this correlation was originally developed for PWRs, the present analysis adjusts it to two-phase flow introducing a corrective factor; see Appendix H for details);
- upper tie plate: ($C_{utp} = C_{utp}^{10in^2} \cdot \frac{A_f^2}{10^2}$).

The coefficients C^{10in^2} (from [24]) and the axial location of each form loss are listed in Table E.1.

Table E.1: Bundle Loss Coefficients			
Type of form loss	***Normalized Value***	***Axial Location (in)***	
		BWR/5	ESBWR
Central region orificing	$C_{central}^{10in^2} = 10.12$	0	0
Peripheral region orificing	$C_{peripheral}^{10in^2} = 87.36$	0	0
Lower tie plate	$C_{ltp}^{10in^2} = 4.54$	7.3[70]	7.3[70]
Grid spacers[71]	Absolute value directly computed using In's correlation (see Appendix H)	19.5; 39.0; 58.5; 78.0; 97.5; 117.0; 136.5. (From [24])	17.7; 33.7; 49.7; 65.7; 81.7; 97.7; 106.1; 113.7
Upper tie plate form	$C_{utp}^{10in^2} = 0.18$	145.3[72]	118[72]

As regards the two-phase friction pressure drop contribution, VIPRE uses the well known relation:

$$\frac{dp}{dz} = f\frac{G^2}{2\rho D_{eq}}\Phi_{lo}^2 \qquad \text{(E-14)}$$

where the friction factor, f, is determined both for the fuel bundles and the bypass channels using an empirical correlation having the general form:

[70] Although the location of the lower tie plate is around 0 inches, it was increased to make VIPRE able to distinguish between the orificing coefficient and the lower tie plate coefficient. In fact, the number of axial nodes chosen to divide the bundle length is 30, with a consequent distance between nodes of about 146/29 ≈5 inches. Paragraph 2.10 of VIPRE manual ([4]) states: "*If the user mistakenly enters two loss coefficient locations in a single node, only the second one will be seen by the code*". To avoid this trouble, the lower tie plate location was arbitrarily increased to 7.3 inches.

[71] Because of the assumption made regarding the total bundle length, i.e. total length = heated length (see Section 3.1, point "a" of "Pressure drop assumptions"), the grid spacer locations in the ESBWR-type cores have been modified with respect to the actual locations found in the literature. In fact, reference [13] provides the axial locations only for the first 6 spacers: 19.7, 39.4, 59.1, 78.7, 92.5, 106.3 inches. Assuming that the 4 upper grid spacers are equally spaced, the two remaining spacers should be located at 120.1 and 133.9 inches respectively. However, since these locations exceed the heated length, all the grid spacer locations have been re-dimensioned, so that all the 8 grid spacers fall within the 120" corresponding to the heated length. This re-dimensioning was not applied to the BWR/5-type cores since the last grid spacer is already located below the top of the heated length.

[72] In a real core the upper tie plate is located well above the top of the heated length, e.g. at elevation 162" in the reference BWR/5, [24]). However, since this analysis is performed assuming the total length equal to the heated length, the upper tie plate location has been arbitrarily set to 145.3" in the BWR/5-type cores, and at 118" in the ESBWR-type cores.

$$f = MAX\left(a_L \, \mathrm{Re}^{b_L} ; a_T \, \mathrm{Re}^{b_T}\right) \qquad \text{(E-15)}$$

The values assumed by the coefficients a and b are listed in Table E.2. In particular, for the fuel bundles they are computed using the Cheng-Todreas friction factor correlation for square arrays having $P/D \geq 1.1$ ([22]). Instead, for the bypass channels the coefficients a and b reflect those characterizing the Blasius correlations for laminar flow, and the McAdams correlation for turbulent flow ([17]).

Table E.2: Coefficients for Frictional Pressure Drop Correlations

Channel type	a_L	b_L	a_T	b_T
Bundles	$35.55 + 263.7\left(\frac{P}{D}-1\right) - 190.2\left(\frac{P}{D}-1\right)^2$	-1	$0.1339 + 0.09059\left(\frac{P}{D}-1\right) - 0.09926\left(\frac{P}{D}-1\right)^2$	-0.18
Bypass channels	64	-1	0.184	-0.2

The two-phase multiplier Φ_{lo}^2 is automatically computed by VIPRE using the Columbia/EPRI correlation (for details see Volume 1 of [4]).

E1.3. Assumptions for Case Ox-Backfit-5, Hyd-Backfit-5, Ox-Backfit-ES

Bundle structure assumptions

a) In the modeling of all the oxide fueled cores, each bundle is modeled assuming it contains a single water rod, called "dummy" water rod. The outer diameter of this rod is chosen such that the ratio k_{flow} of the its inner cross sectional area, $A_{DWR,in}$, to the bundle active flow area $A_{bundle,active}$ is constant and equal to that of the reference bundle assumed perfectly square (k_{flow} = 0.0921 for the BWR/5 oxide core, k_{flow} = 0.1030 for the ESBWR oxide core). The procedure used to calculate the "dummy" water rod outer diameter, D_{DWRo} , was developed by Handwerk [3] and consists of an iterative algorithm which requires, as input, the fuel channel inner width (l_{bi} , constant for a given core type, i.e. BWR/5-type or ESBWR-type) together with the rod diameter D and pitch P. Besides the "dummy" water rod diameter, it delivers also the number of fuel rods contained in a single assembly. The basic feature of this

algorithm consists of placing a central "dummy" water rod that displaces a number of fuel rods equal to:

$$N_{FR}^{displaced} = \left[round\left(\frac{\alpha}{P}\right)\right]^2 \tag{E-16}$$

where α represents the outer width of an imaginary square rod having inner area equal to the "dummy" water rod inner area, while "*round*" is a function which rounds the term in brackets either up or down to the nearest integer The thickness of the walls of the imaginary square rod is the same as the thickness assumed for the wall of all the "dummy" water rods modeled in this analysis, i.e. t_{DWR} = 0.0424". Based on this assumption, the ratio k_{flow} can be written as:

$$k_{flow} = \frac{A_{DWR,in}}{A_{bundle,active}} = \frac{0.25 \cdot \pi \cdot \left(D_{DWRo} - 2t_{DWR}\right)^2}{l_{bi}^2 - \left(n^2 - N_{FR}^{displaced}\right) \cdot 0.25 \cdot \pi \cdot D^2 - 0.25 \cdot \pi \cdot D_{DWRo}^2} \tag{E-17}$$

The fact that equation E-17 contains two unknowns, i.e. D_{DWRo} and $N_{FR}^{displaced}$, motivates the iterative nature of the algorithm.

However, as Handwerk stated, the algorithm provides an approximate result since it assumes that the presence of the "dummy" water rod within a $n \times n$ matrix replaces a single $n_1 \times n_1$ square matrix of fuel rods ($n_1 << n$). Instead, as Figure 1.2 clearly shows, the two water rods contained in a real bundle may replace a number of fuel rods which does not correspond to the square of any integer: in the GE11 design the fuel rods displaced are 7, while in the GE14 design they are 8. None of these numbers correspond to a $n_1 \times n_1$ matrix. Because of this approximation, the number of fuel rods per bundle predicted by the original Handwerk's algorithm does not match the actual value for the two reference bundles. In fact, the predicted number of fuel rods is:

- 77 for the GE11 design, versus 74 which is the actual value
- 91 for the GE14 design, versus 92 which is the actual value

In order to improve the algorithm and make it consistent at least with the reference assembly a small and crude modification was made. Given the number of fuel rods

per bundle predicted by the "original" algorithm, $N_{FR}^{original}$, the corrected relations are the following:

BWR/5 core: $$N_{FR} = N_{FR}^{original} - round\left(3 \cdot \frac{N_{FR}^{original}}{77}\right) \quad \text{(E-18)}$$

ESBWR core: $$N_{FR} = N_{FR}^{original} + round\left(\frac{N_{FR}^{original}}{91}\right) \quad \text{(E-19)}$$

In this way:

- the reference bundles are modeled with the right number of fuel rods
- the other assembly configurations are subjected to a correction in the number of fuel rods which entity increases as $N_{FR}^{original}$ increases.

As specified in Section 3.3.1, the mentioned algorithm and related assumptions are not applied to Case Hyd-Backfit-5 since hydride bundles do not contain water rods.

b) The relations used to calculate the fuel-clad gap and clad thickness for <u>oxide</u> fueled rods are the following ([27]):

Clad thickness:

$$\text{if } D < 0.292 \rightarrow t_{clad} = 0.023$$
$$\text{if } D \geq 0.292 \rightarrow t_{clad} = 0.023 + 0.06176(D - 0.292) \quad \text{(E-20)}$$

Gap thickness:

$$\text{if } D < 0.354 \rightarrow t_{gap} = 0.002$$
$$\text{if } D \geq 0.354 \rightarrow t_{gap} = 0.002 + 0.0152(D - 0.354) \quad \text{(E-21)}$$

where all parameters are expressed in inches.

While the correlation used for the clad thickness is the same also for <u>hydride</u> fueled rods, that for the thickness of the fuel-clad gap is different. In fact, as stated in [27], hydride fuel is subjected to a more significant swelling than the oxide fuel is. As a consequence, for the same rod outer diameter D, a hydride fueled rod must be provided with a thicker gap. The correlation used to calculate such a thickness is provided in [27] as well, and requires rod outer diameter and end Discharge Burnup

as input parameters. In particular, the latter parameter assumes different values on account of the hydride fuel enrichment. For the purpose of the gap thickness calculation, the present analysis considers $UZrH_{1.6}$ 5% enriched. According to [27], the corresponding Discharge Burnup is 48 MWD/t-HM, equivalent to 1.237 at % MET-BU (see Table 1 of [27]). The correlations for the gap thickness have the following form:

$$\text{if } D < 0.30 \rightarrow t_{gap} = 0.006 \tag{E-22}$$

$$\text{if } D \geq 0.30 \rightarrow t_{gap} = -2.131 \cdot 10^{-4} + 7.259 \cdot 10^{-3} D + 8.456 \cdot 10^{-3} D \cdot BU - 9.455 \cdot 10^{-5} BU$$

where D and t_{gap} are both expressed in inches, while BU is in at % MET-BU. Based on the assumption made, the value used for BU is 1.237 at % MET-BU.

Table E.3 shows the difference in fuel pellet diameter resulting from the application of different gap thickness correlations depending on the type of fuel. Such a comparison is made for three representative rod outer diameters, i.e. 0.6, 1.1176 and 1.6 cm.

Table E.3: Fuel Pellet Diameter Comparison for Oxide and Hydride Fueled Rods

	Fuel pellet diameter (cm)		Difference % of hydride fuel pellet D with respect to oxide pellet D
Rod D (cm)	Oxide fueled rod	Hydride fueled rod (5% enriched)	
0.6000	0.4730	0.4527	-4.3
1.1176	0.9375	0.9164	-2.2
1.6000	1.3457	1.3221	-1.8

Other assumptions and considerations

a) While in Case Ox-Backfit-5 and Case Ox-Backfit-ES the fuel-clad gap is assumed to be filled with helium, Case Hyd-Backfit-5 considers fuel rods filled with a liquid metal. In fact, although all the existing LWRs make use of the former, the idea of replacing it with a nonalkaline liquid metal has already been investigated (see [39] and [40]). In particular, Wright ([40]) states that: "*The ability to transfer heat out of the fuel rod can be best influenced by first modifying the fuel pellet to decrease the*

thermal resistance and second reducing the thermal resistance across the gas gap". The present analysis acts in both directions: in fact, the modification concerning the fuel is performed changing its chemical composition from oxide to hydride, while that concerning the gap is implemented using an alloy of 33% wt% lead, 33% wt% bismuth and 33% wt% tin having a thermal conductivity about 100 times that of helium ([39]). By means of these modifications, the heat transfer across the fuel rod is significantly enhanced and consequently the fuel is prevented from reaching the high temperatures typical of oxide fueled – helium gap filled reactor[73]. Moreover, since the lower fuel temperature yields a lower thermal expansion, an accurate initial dimensioning of the gap thickness may even avoid the mechanical stresses resulting from the gap closure, that is from the contact between the fuel and the clad.

E1.4. Assumptions for Case Hyd-NewCore-5 and Case Hyd-NewCore-ES

There are no assumptions specifically referred to these cases requiring a further investigation/description beyond those already discussed in Section 3.3.2.

[73] The experiments carried out by Wright showed that the liquid metal gap implementation yields peak fuel temperatures 400°F lower at beginning of life and 200°F lower at the end of life compared with conventional helium filled gap ([40]). As regard the oxide fuel, since the fission gas release depends strongly on the fuel temperature, it would be expected that the implementation of the liquid metal gap results in a significant mitigation of this gas release. Conversely Wongsawaeng ([39]) proved that, although the fission gas release onset is always delayed by the presence of a liquid metal inside the gap, this delay may be not significant. In particular, the LHGR plays an important role in determining the gas release-related benefits resulting from the liquid metal gap implementation.

Appendix F

F1. Investigation of the Pitch Influence on the LHGR

This Appendix is aimed at finding an approximate relation between the maximum achievable Linear Heat Generation Rate (LHGR) and the rod pitch, so that the profile of the LHGR unity line shown in plot b) of Figure 4.3 can be explained[74]. Although the following considerations can be referred to any of the cases analyzed, Case Ox-Backfit-5 with Δp_{limit}=36 psia was chosen as reference. Therefore, the following considerations are based on the evidence raised by the results obtained for this case.

From plot b) of Figure 4.3 (reproduced for convenience in Figure F.1, left plot) it can be noticed that the LHGR unity line diagonally cuts the map area. This means that only the assembly configurations located above the unity line have better thermal performance than the reference assembly configuration, i.e. a higher LHGR. Above this unity line MCPR is the first limit encountered as the right plot of Figure F.1 shows. The analysis which follows is based upon MCPR being limiting.

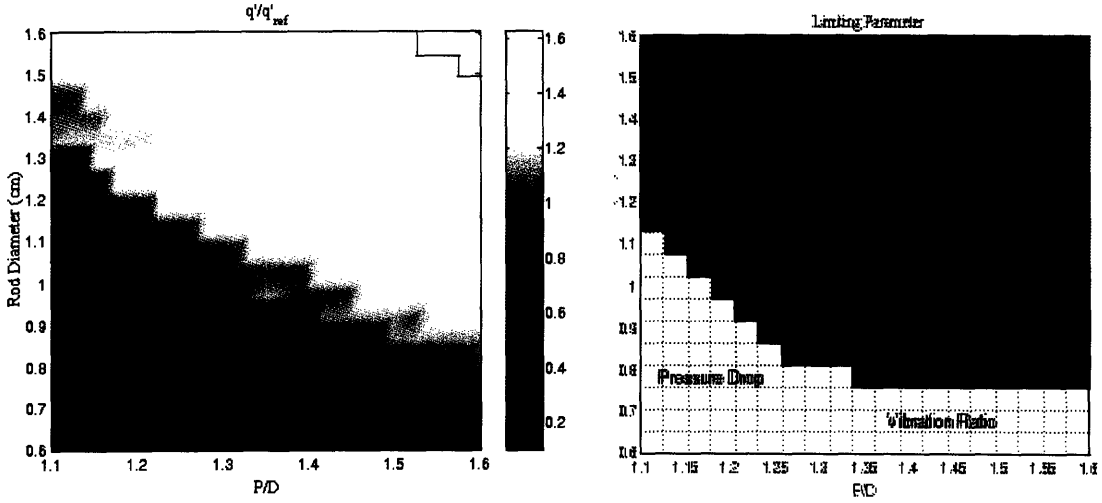

Figure F.1: Left: LHGR Ratio (=LHGR/reference LHGR). Right: Areas of Influence of Limiting Constraints (Case Ox-Backfit-5, Δp_{limit}=36).

[74] Actually, all the plots representing the ratio between the LHGR of the various assembly configurations and that of the reference one show the same profile. See plots b) in Figure 4.12, Figure 4.21 and Figure 4.32.

This can be analytically demonstrated using some simple heat balance relations, referred to the hot bundle. First, assuming that the critical quality is reached near the bundle outlet, the bundle critical power can be written as:

$$\dot{Q}_{bundle,crit} = \dot{m} \cdot h_{fg} \cdot (x_c - x_{in}) \tag{F-1}$$

where $\dot{m}$ is the coolant flow rate, h_{fg} the vaporization heat, x_c the critical quality and x_{in} the inlet equilibrium quality. Also the following relation is approximately[75] valid:

$$\dot{Q}_{bundle,crit} \approx q' \cdot L_H \cdot n^2 \tag{F-2}$$

where q' is the LHGR, L_H is the rod heated length, n is the matrix index. Moreover, the matrix index is related to the fuel assembly inner width l_{bi}, to the rod pitch P and to the rod diameter D through the relation (see equation 3-7 in Section 3.3.1):

$$n = floor\left(\frac{l_{bi} + D - P}{P}\right) \tag{F-3}$$

For simplicity, we can assume that the term in brackets in equation F-3 is an integer, and that $D\text{-}P \ll l_{bi}$. Now, in order to calculate the LHGR ratio $\left(\frac{q'_{actual}}{q'_{ref}}\right)$ which is graphically represented in the left plot of Figure F.1, the three previous relations can be combined as follows:

$$\frac{q'_{actual}}{q'_{ref}} = \frac{\dot{m}_{actual}}{\dot{m}_{ref}} \frac{(x_c - x_{in})_{actual}}{(x_c - x_{in})_{ref}} \frac{\left(\frac{l_{bi}}{P_{ref}}\right)^2}{\left(\frac{l_{bi}}{P_{actual}}\right)^2} = \frac{\dot{m}_{actual}}{\dot{m}_{ref}} \frac{(x_c - x_{in})_{actual}}{(x_c - x_{in})_{ref}} \frac{P_{actual}^2}{P_{ref}^2} \tag{F-4}$$

Therefore the variation of the LHGR ratio is due to three contributions: flow rate, quality and pitch. Each one is examined as follows.

a) *Flow rate contribution*: within the area having the MCPR as limiting parameter the flow rate ratio ranges between about 1.2 and 0.9 (see left plot of Figure F.2),

[75] Actually, the number of fuel rods contained in an assembly is lower than n^2 since the central "dummy" water rod is present.

but its trend is opposite to the LHGR ratio. In fact, whereas the LHGR ratio is high the flow ratio is low and vice versa.

b) Quality contribution: since the MCPR set as limit is very close to unity (1.015), the critical quality can be approximated with the bundle exit quality, that is: $x_c \cong x^{exit}_{hot\_bundle}$. Moreover, from the right plot of Figure F.2 it can be noticed that, within the area having the MCPR as limiting parameter, the ratio $\frac{x^{exit}_{hot\_bundle\_actual}}{x^{exit}_{hot\_bundle\_ref}}$ ranges between 0.9 and 1.1, i.e. the hot bundle exit quality does not vary significantly within the MCPR limited region. These facts, together with the constancy of the inlet equilibrium quality, allow approximating the ratio $\frac{(x_c - x_{in})_{actual}}{(x_c - x_{in})_{ref}}$ as unity.

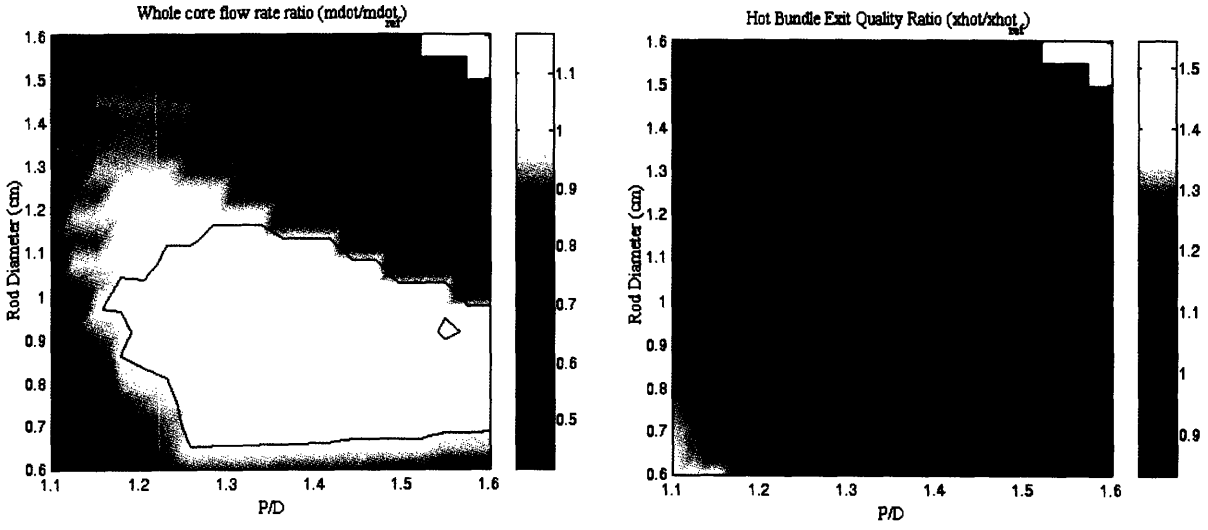

Figure F.2: Left: Whole Core Flow Rate Ratio (flow rate / reference flow rate); Right: Hot Bundle Exit Quality Ratio (quality / reference quality). Case Ox-Backfit-5 (Δp_{limit} = 36 psia)
(continuous lines: unity ratio)

c) Pitch contribution: the assembly configurations enclosed in the MCPR limited region have rod pitch ranging between 1.265 cm to 1.76 cm. This is evident by comparing the right plot of Figure F.1 with the Iso-pitch Line diagram of Figure F.3. Therefore, based on the value of the reference pitch, in the MCPR limited

region the ratio between the squares of the pitches ranges in the interval:

$$0.78 \le \frac{P_{actual}^2}{P_{ref}^2} \le 1.52$$

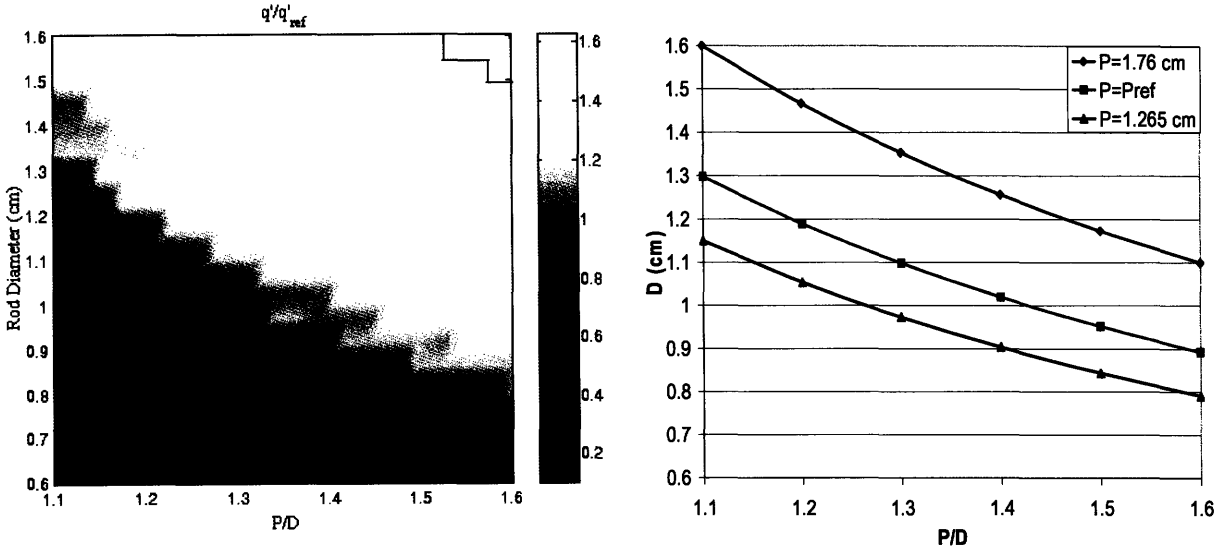

Figure F.3: LHGR Ratio (Case Ox-Backfit-5, Δp_{limit} =36 psia) and Iso-Pitch Lines

Summarizing the results just obtained:

$$\frac{q'_{actual}}{q'_{ref}} \approx \frac{\dot{m}_{actual}}{\dot{m}_{ref}} \frac{P_{actual}^2}{P_{ref}^2} \qquad \text{(F-5)}$$

range: $1.2 \rightarrow 0.9$ range: $0.78 \rightarrow 1.52$

The lower bound of the variation range of the ratio $\left(\frac{q'_{actual}}{q'_{ref}}\right)$ can be obtained by multiplying the two limits above, i.e. 1.2×0.78~0.94, while the upper bound can be obtained by multiplying the the other two limits, i.e. 0.9×1.52~1.37. Thus, in the MCPR limited region, the variation range of the LHGR ratio results to be: $0.94 \le \frac{q'_{actual}}{q'_{ref}} \le 1.37$.

By identifying the MCPR limited region inside the left plot of Figure F.3 it can be seen that the prediction performed is quite accurate.

Moreover, by considering the whole geometry range, i.e. $0.66 \leq P \leq 2.56$ cm, the variation range of the square of the pitch ratio is:

$$0.21 \leq \frac{P_{actual}^2}{P_{ref}^2} \leq 3.2 \qquad \text{(F-6)}$$

which is significantly broader than the variation range of the flow rate ratio, i.e. $0.5 \leq \frac{\dot{m}_{actual}}{\dot{m}_{ref}} \leq 1.2$ (see left plot of Figure F.2). Therefore, using now equation F-5 with these two variation ranges, we can estimate that the major contribution to the variation of the LHGR ratio is due to the difference in pitch. And in fact, from the q'/q'_{ref} plot presented in Figure F.3, it can be noticed that the shading varies almost accordingly to the iso-pitch lines. As the pitch increases (with respect to the reference pitch) the LHGR ratio increases as well.

Appendix G

G1. Investigation of the LHGR of Oxide and Hydride Bundles

G1.1. Motivation for the Analysis

The results derived from the comparison of Case Ox-Backfit-5 to Case Hyd-Backfit-5 show that, for the reference *D-P/D* pair, the presence of water rods inside the oxide bundle seems to have a beneficial effect on the heat removal effectiveness. This effect consists basically in a larger Linear Heat Generation Rate (LHGR) for the oxide assembly with respect to a hydride assembly not provided with water rods. This can be seen in the left plot of Figure 4.48, which shows that the reference assembly configuration (D~1.1 cm, P/D~1.28) is located below the unity line corresponding to the LHGR ratio, i.e. its LHGR ratio hydride/oxide is below 1. This Appendix is aimed at investigating this phenomenon by means of a subchannel analysis performed with VIPRE of the two bundles of interest.

G1.2. Characteristics of the Bundles Examined

The bundles analyzed are the following:

- 9×9 oxide bundle containing 74 full length fuel rods and 2 water rods;
- 9×9 hydride bundle containing 81 full length fuel rods and no water rods.

Except for the different number of rods and for the presence of the water rods in the oxide bundle, all the remaining geometric characteristics are identical and reflect exactly those of the GE11 design shown in Figure 1.2. Moreover, each bundle is surrounded by a narrow bypass region whose orificing coefficient is chosen so that 10.0% of the total flow is diverted through it. Other parameters in common are the following:

- pressure: 1035 psia;
- coolant inlet temperature: 278.3 °C;
- subchannel averaged exit quality[76]: 26.8%;

[76] The subchannel averaged exit quality is defined as the average of the exit qualities of all subchannels, i.e. the flow through water rods and bypass channels is not accounted for in the averaging procedure.

- axial power distribution (see BWR/5 power distribution shown in Figure 3.3).

Each bundle is analyzed twice, i.e. first with a non-uniform and then with a uniform pin-by-pin power distribution. The non-uniform power distribution considered for the oxide bundle is that used in the whole core analysis to get the maximum J_1 factor required as input by the Hench-Gillis correlation. Such a power distribution was described in Section E1.1. of Appendix E and is reproduced in Figure G.1 for convenience. The non-uniform power distribution used for the hydride bundle was obtained from that of Figure G.1 by simply adding 7 unity peaking factors to the 7 central positions that, in the oxide bundle, are unoccupied because of the presence of the water rods.

1.15	1.26	1.25	1.22	1.21	1.22	1.25	1.26	1.16
1.26	1.12	1.01	0.44	0.87	0.44	1.01	1.14	1.26
1.26	1.01	0.42	0.87	1.00	0.92	0.43	1.02	1.26
1.22	0.44	0.87	1.14			0.93	0.45	1.22
1.21	0.87	1.00				0.99	0.87	1.20
1.23	0.45	0.94			1.11	0.85	0.44	1.21
1.27	1.01	0.43	0.93	1.00	0.87	0.43	1.00	1.24
1.25	1.14	1.01	0.44	0.89	0.44	1.00	1.12	1.26
1.14	1.25	1.25	1.23	1.21	1.22	1.25	1.24	1.15

Figure G.1: Non-Uniform Pin-by-Pin Power Distribution Used for Oxide Bundle

The uniform power distribution considered for each bundle consists instead of unity peaking factors for all the fuel rods.

For the oxide bundle, the total bundle power is that corresponding to the hot bundle of the reference BWR/5 core. Likewise, the active flow rate[77] is the same as that delivered by VIPRE in the whole core analysis of the BWR/5, while the total flow rate is simply obtained by dividing this value by 0.86. In fact, the flow rate through the bypass region is 10% of the total flow, while the flow through the water rods is 4%. As done for the bypass channel, the mentioned percentage for the water rods is obtained by varying the corresponding orificing coefficient.

G1.3. Comparisons Performed

Two comparisons are performed:

[77] The active flow rate is equal to the total flow rate reduced by the amount which goes through bypass channels and water rods.

1) oxide bundle – hydride bundle (non-uniform pin-by-pin power distribution);
2) oxide bundle- hydride bundle (uniform pin-by-pin power distribution).

In both cases, the investigation is aimed at comparing the LHGR of the two bundles, when both yield the same MCPR (calculated with the Hench-Gillis correlation). The analysis compares the bundles on a "fair" basis since, other than being equally far from the critical condition, the two bundles have also same inlet and outlet conditions.

G1.4. Results

Results are shown in Table G.1 together with a summary of the key geometric differences between the two bundle designs, i.e. number and type of rods and active flow area.

Table G.1: LHGR Comparison Oxide-Hydride

	Oxide	**Hydride**
Number of Fuel Rods	74	81
Number of water Rods	2	0
Active Flow Area (cm^2)	Proprietary Data (~3% smaller than hydride)	95.999
Non-Uniform Pin-by-Pin Power Distribution		
Total Flow Rate (kg/s)	16.98	17.15
Bypass Channel Flow Rate %	10.0	10.0
Water Rod Flow Rate %	4.0	-
Active Flow Rate (kg/s)	14.60	15.44
Active Mass Flux (kg/m^2 s)	~2.5% lower than hydride	1608.3
Pressure Drop (psia)	22.9	23.9
Subch. Averaged Exit Quality (%)	26.8	26.8
MCPR	1.003	1.003
Bundle Power (kW)	6565.8	6927.2
LHGR (kW/m)	23.93	23.06
Uniform Pin-by-Pin Power Distribution		
Total Flow Rate (kg/s)	16.98	17.43
Bypass Channel Flow Rate %	10.0	10.0
Water Rod Flow Rate %	4.0	-
Active Flow Rate (kg/s)	14.60	15.69
Active Mass Flux (kg/m^2 s)	~4.1% lower than hydride	1634.4
Pressure Drop (psia)	22.8	24.4
Subch. Averaged Exit Quality (%)	26.8	26.8
MCPR	1.212	1.212
Bundle Power (kW)	6565.8	7040.4
LHGR (kW/m)	23.93	23.44

Thus, both with non-uniform and uniform pin-by-pin power distribution, the LHGR ratio hydride/oxide is lower than 1. In particular:

Non-uniform power distribution: LHGRR=0.964

Uniform power distribution: LHGRR=0.980

The reason for the lower LHGR in the hydride bundle is the higher active mass flux characterizing this bundle. As well known, under high quality conditions typical of BWRs, the higher is the mass flux the lower is the margin to the critical condition.

The analysis performed in this Appendix also proves that the results provided by the whole core analysis are indeed correct. For the same *D-P/D* pair, the hydride bundles deliver a higher power, which is consequence of the larger number of rods only. However, the beneficial effect due to the larger number of fuel rods is slightly reduced by a lower LHGR

Appendix H

H1. Grid Spacer Loss Coefficients Calculation: In's Correlation

Given a grid-assembly geometry configuration characterized by:

- rod diameter: D
- rod pitch: P
- grid thickness and height: t and h respectively
- $A_{subch} = P^2 - \pi\frac{D^2}{4}$ (square array)
- no mixing vanes

In's correlation computes the grid spacer loss coefficient C_{grid} as sum of three terms: grid form loss (term A), grid friction loss (term B) and rod friction loss within the spacer region (term C) [23] :

$$C_{grid}^{In} = \left[C_{grid}^{form}\frac{\varepsilon}{(1-\varepsilon)^2}\right]_A + \left[C_{grid}^{fric}\frac{A_{grid,wetted,total}}{A_{flow,bundle}}\frac{1}{(1-\varepsilon)^2}\right]_B + \left[C_{rod}^{fric}\frac{A_{rods,at\_spacer}}{A_{flow,bundle}}\frac{1}{(1-\varepsilon)^2}\right]_C \quad \text{(H-1)}$$

where:

- $C_{grid}^{form} = 2.75 - 0.27\log_{10}\mathrm{Re} = 2.75 - 0.27\log_{10}\left(\frac{GD_{eq}}{\mu}\right) = 2.75 - 0.27\log_{10}\left(\frac{G}{\mu}\frac{4A_{subch}}{\pi D}\right)$ (H-2)
- ε is defined as the ratio between the total projected grid cross section (frontal grid area) and the bundle flow area:

$$\varepsilon = \frac{A_{grid,frontal,total}}{A_{flow,bundle}} = \left(\frac{A_{grid,frontal}}{A_{flow}}\right)_{bundle} \quad \text{(H-3)}$$

Here it is assumed that ε can actually be written in a similar fashion, no longer referred to the whole bundle section but to a single subchannel: in such a way, the numerator becomes the grid frontal area encountered by the coolant flowing in a subchannel while the denominator becomes the subchannel area. However, to move

from the bundle viewpoint to the subchannel one, it is necessary to add a corrective coefficient K:

$$\varepsilon = K\varepsilon_{subch} = K\left(\frac{A_{grid,frontal}}{A_{flow}}\right)_{subch} = K\frac{\left(A_{grid,frontal}\right)_{subch}}{A_{subch}} = 1.815\frac{2Pt-t^2}{A_{subch}} \qquad \text{(H-4)}$$

The value assigned to the corrective coefficient, i.e. 1.815, was calculated using a reverse approach. In fact, Table 1 of [23] provides ε, P, t and the rod diameter D for two grid spacers that In used in his study. Choosing that designated as "Spacer 2" as reference (second column of Table 1 in [23]), it follows that:

$$K = \left[\frac{\varepsilon}{\frac{2Pt-t^2}{A_{subch}}}\right]_{"Spacer2"} = \left[\frac{\varepsilon}{\frac{2Pt-t^2}{P^2-\frac{\pi}{4}D^2}}\right]_{"Spacer2"} = 1.815 \qquad \text{(H-5)}$$

- C_{grid}^{fric} is given as follows:

$$C_{grid}^{frict} = C_{grid,lam}^{frict}\frac{L_t}{h} + C_{grid,tur}^{frict}\frac{h-L_t}{h} = \frac{1.328}{\sqrt{\mathrm{Re}_L}}\frac{L_t}{h} + \frac{0.523}{[\ln(0.06\,\mathrm{Re}_L)]^2}\frac{h-L_t}{h} \qquad \text{(H-6)}$$

where $\mathrm{Re}_L = G\frac{h-L_t}{\mu}$ and $L_t = \frac{30000\mu}{G}$

- $$\frac{A_{grid,wetted,total}}{A_{flow,bundle}} = \frac{A_{grid,wetted,subch}}{A_{subch}} = \frac{4(P-t)h}{A_{subch}} \qquad \text{(H-7)}$$

- $$C_{rod}^{fric}\frac{A_{rods,at\_spacer}}{A_{flow,bundle}} = C_{rod}^{fric}\frac{4h}{D_{eq}} = f\frac{h}{D_{eq}} = 0.184\mathrm{Re}^{-0.2}\frac{h}{D_{eq}} = 0.184\left(\frac{GD_{eq}}{\mu}\right)^{-0.2}\frac{h}{D_{eq}} \qquad \text{(H-8)}$$

H2. Correction of In's Correlation for BWR Application

Since In's correlation was developed for single-phase flow, a corrective multiplier is necessary to allow its applicability under high quality conditions typical of BWRs. According to data provided in [24], for BWRs a typical value for the grid spacer loss

coefficient is 0.53, with respect to a flow area of 10 in^2. Thus, for the reference assembly the grid spacer loss coefficient can be calculated as:

$$C_{grid}^{ref} = 0.53\frac{\left(A_f^{ref}\right)^2}{10^2} \tag{H-9}$$

where the reference bundle flow area is given by (GE proprietary data):

$$A_f^{ref} = l_{bi}^2 - 74\pi\frac{D^2}{4} - 2\pi\frac{D_{WRo}^2}{4} \tag{H-10}$$

Running the code for the reference assembly configuration, ($G_{bundle\_average}$ = 1652.3 kg/s m^2), the value predicted by the In's correlation is 0.7065, which is different from that calculable by means of equation H-9. In particular, In's correlation underpredicts the loss coefficient by a factor around 1.6, which is therefore used as corrective coefficient. In conclusion, the grid spacer loss coefficients for the BWR assemblies in this work are calculated using the relation:

$$C_{grid} = 1.6C_{grid}^{In} \tag{H-11}$$

Appendix I

I1. Channel Numbering for VIPRE Reference Core Modeling

For each "backfit" case examined in the whole core analysis, i.e. Case Ox-Backfit-5, Case Hyd-Backfit-5 and Case Ox-Backfit-ES, a VIPRE input deck was constructed. In each case all the assembly configurations have the same core ex-bundle structure, and therefore the numbering of the channels is the same.

Figure I.1 shows the channel numbering for Case Ox-Backfit-5. Since the only difference between this case and Case Hyd-Backfit-5 consists of the absence of water rods in the latter, the channel numbering adopted for Case Hyd-Backfit-5 is the same. The only exception of the numbering of the water rods that is not performed.

The channel numbering for Case Ox-Backfit-ES is shown in Figure I.2.

The core maps[78] shown in Figure I.1 and Figure I.2 were used to estimate the flow area of the macro-bypass channels, i.e. of the large channels obtained by lumping several bypass channels. The geometric data needed to perform this calculation, i.e. the bundle outer width and the bypass channel width, are known for both cores and are listed in Table 1.2. However, as mentioned in Section 3.2.2 at point b) of "Coolant flow assumptions" the macro-bypass channels shown in Figure I.1 and in Figure I.2 (numbered 2, 8, 9, 19, 20 etc.) are modeled assuming they have a flow area reduced by 50% with respect to the real flow area, and a wetted perimeter equal to 1/8 of the real perimeter. For each macro-bypass channel, Table I.1 shows real flow area and real perimeter, as well as the values used in the modeling of the two cores.

[78] The core maps do not show the real proportion between the size of bypass channels and bundles. To make the latter more visible, the bypass channel width has been significantly enlarged.

Table I.1: Bypass Channel Area and Perimeter				
Macro-Bypass Channel Number	Real flow area (in^2)	Modeled flow area (in^2)	Real Wetted Perimeter (in)	Wetted perimeter (in)
BWR/5				
2	9.8884	4.9442	32.490	4.0612
8,19,35,56,82,107	23.2012	11.6006	75.810	9.4762
9,21,38,60	13.3556	6.6778	43.320	5.4150
20,36,37,57,58,59,83,84,85,86,108,109,110	26.7112	13.3556	86.640	10.8300
126[79]	65	32.5	281.580	35.1975
ESBWR				
2,9,21,38,60,87	13.4792	6.7396	44.16	5.52
8,19,20,35,36,37,56,57,58,59,82,83,84,85,86, 113,114,115,116,117,118,145,146,147,148	26.9584	13.4792	88.32	11.04
119	10.1094	5.0547	33.12	4.14
150,174	20.2188	10.1094	66.24	8.28
149,173	33.698	16.849	110.40	13.8
171,172	40.4376	20.2188	132.48	16.56

[79] As evident in Figure I.1, VIPRE models this channel by lumping the bypass regions highlighted in yellow, some of which are even separated from each other. Although this is not consistent with the real core structure (it was done for convenience), the real flow area actually crossed by the coolant is preserved (before performing the 50% reduction), and the space included between the outermost bundles and the core shroud is assumed to be blocked. In particular, because of the uncertainty concerning the location of the border which separates channel 126 from the region blocked, the real flow area of channel 126 was assumed equal to 65 in^2. As easily verifiable, this value represents a reasonable approximation of the area highlighted in yellow.

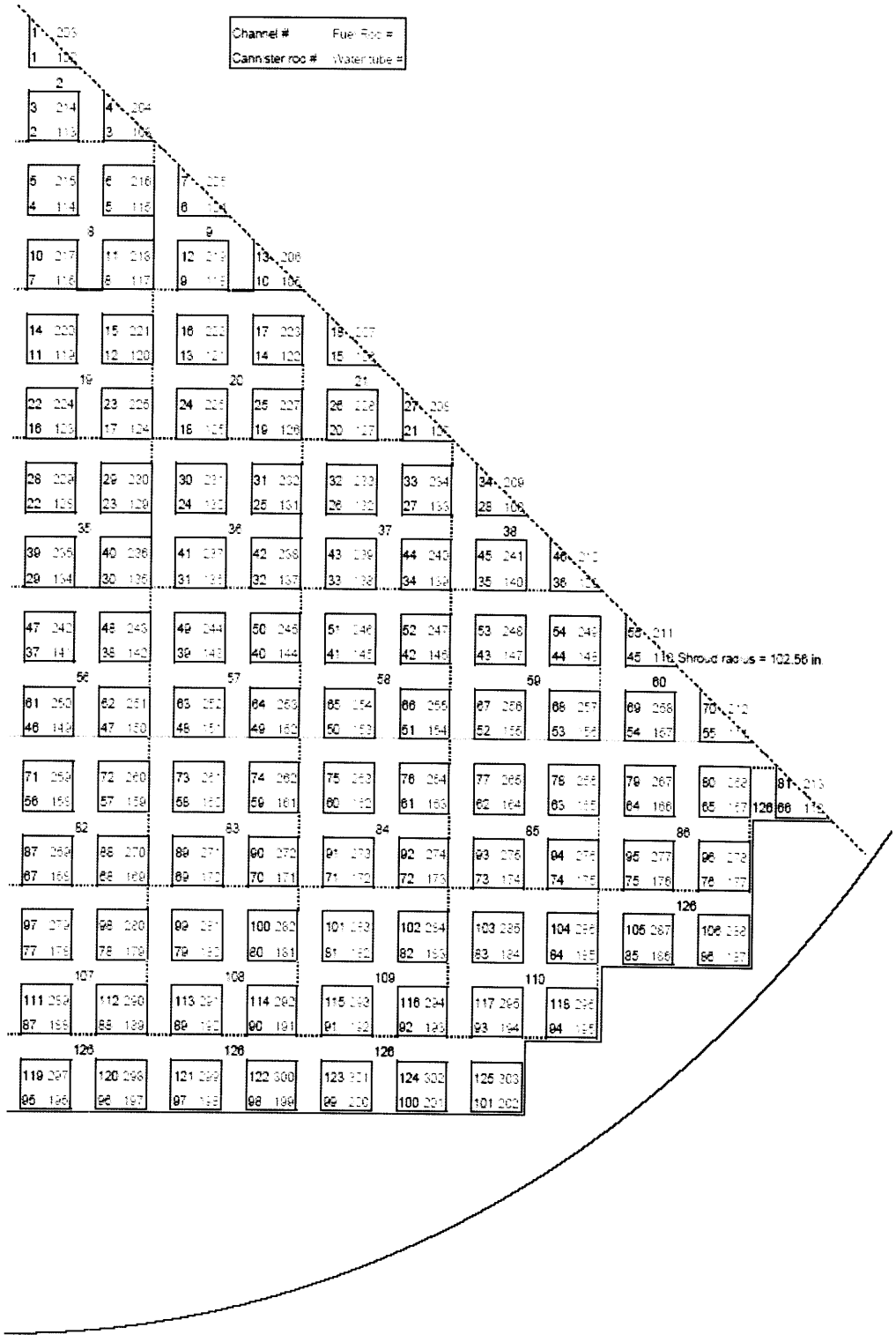

Figure I.1: Reference BWR/5 Oxide Core Modeling Map for VIPRE Input Deck ([3])

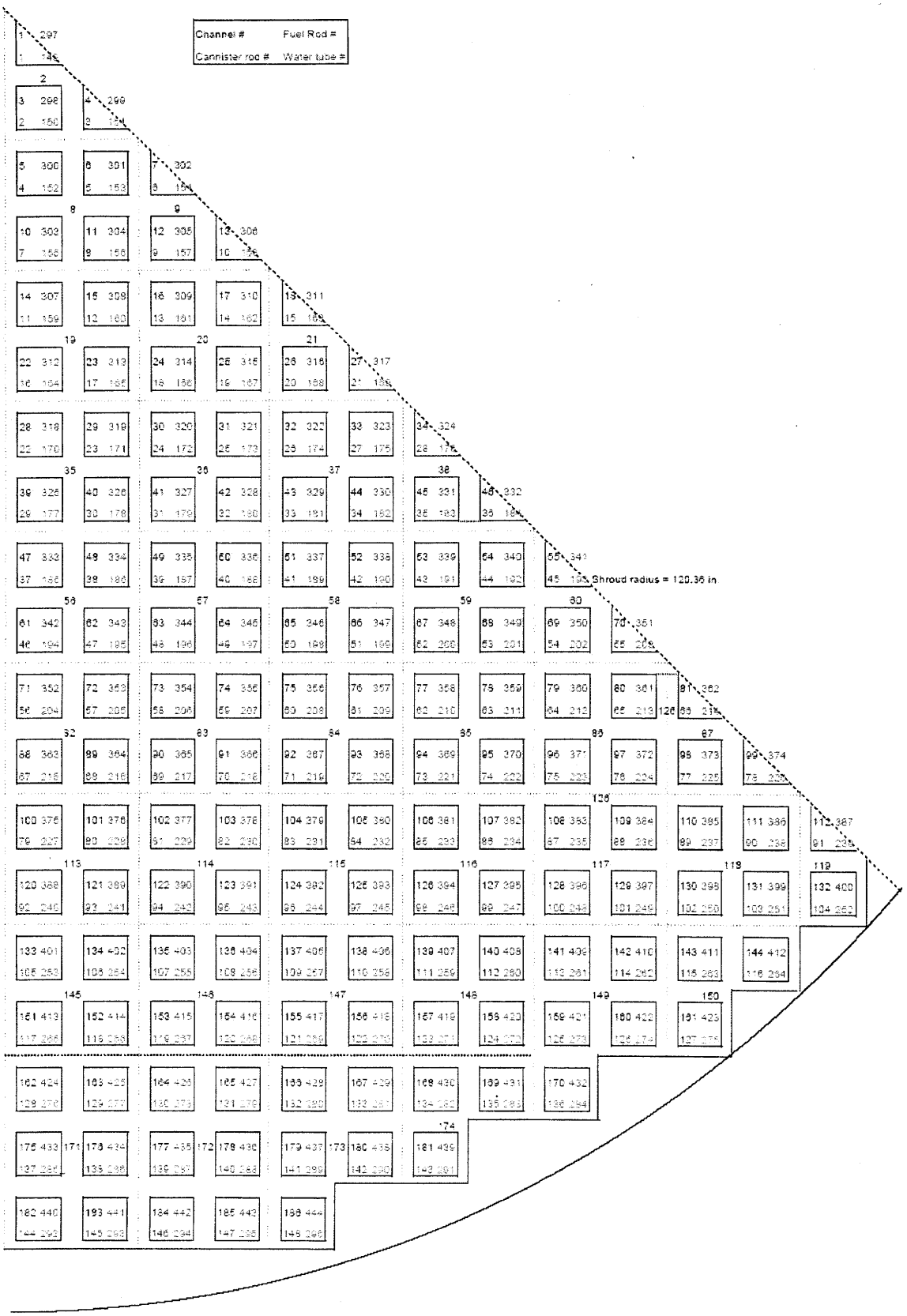

Figure I.2: Reference ESBWR Oxide Core Modeling Map for VIPRE Input Deck

Appendix J

J1. Material Properties

The material properties used through the analysis are listed in Table J.1.

Table J.1 : Material Properties

Parameter	*Value*	*Source*
UO_2 theoretical density (kg/m^3)	10970	[41]
$UZrH_{1.6}$ density (kg/m^3)	8256	5.1.1 in [1]
$UZrH_{1.6}$ thermal conductivity (W/m K)	17.6	5.1.6 in [1]
$UZrH_{1.6}$ specific heat (J/g K)	See below	5.1.5 in [1]
Zircaloy density (kg/m^3)	6550	6.2 in [1]
Zircaloy Young's modulus (Pa)	8.0468e10	6.11 in [1], with T=300°C
Zircaloy heat capacity (J/Kg K)	319.4 (at 350°C)	By interpolation of data from [42]
Zircaloy thermal conductivity (W/m K)	$13.959+9.8522\cdot10^{-3}$T (T in °C)	6.6 in [1]
Liquid metal thermal conductivity (W/m K)	35	Table B-2 in [1]

The specific heat of $UZrH_{1.6}$ is calculated following the directions given in [1]. It is given by the sum of the specific heat of Uranium and the specific heat of $ZrH_{1.6}$, each weighted by the corresponding weight percentage (W_U=0.719; $W_{ZrH1.6}$=0.281):

$$C_{UZrH_{1.6}} = W_U C_U + W_{ZrH} C_{ZrH} \qquad \text{(J-1)}$$

The specific heat of Uranium is the following function of temperature expressed in K ([1]):

For T<938 K:

$$C_U = 104.82 + 5.3686\cdot10^{-3}T + 10.1823\cdot10^{-5}T^2 \ \text{J/kg K} \qquad \text{(J-2)}$$

For 938<T<1049 K: $C_U = 176.41311$ J/kg

while for T>1049 K: $C_U = 156.80756$ J/kg

For the specific heat of $ZrH_{1.6}$ the following relation is used (T in K) ([1]):

$$C_{ZrH_{1.6}} = \frac{1000[0.06976(T - 273.1) + 33.706]}{92.83} \text{ J/kg K}$$

References

[1] H.D. Garkisch, B. Petrovic, "Reference Data and Constraints for Uranium-Zirconium-Hydride and Uranium-Thorium Hydride Fuels for Light Water Reactors", Westinghouse Electric LLC, Rev.6, March 9, 2003.

[2] M. Fratoni, "Burnable Poisons in Hydride Fuel Core", University of California Berkeley, Internal Report, November 2nd 2005.

[3] C. Handwerk, "Preliminary Thermal Hydraulic Analysis of a Hydride Fueled Boiling Water Reactor", NERI02-189-MIT-9, January 2005.

[4] C. Stewart. "VIPRE-01: A Thermal Hydraulic Code for Reactor Cores. Vol.2: User's Manual", August 1989.

[5] S. Blair, "Thermal Hydraulic Performance Analysis of a Small Integral PWR Core", Engineers Thesis, MIT, Department of Nuclear Engineering, September 2003.

[6] J. A. Malen, N. E. Todreas, & A. Romano, "Thermal Hydraulic Design of Hydride Fueled PWR Cores," MIT-NFC-TR-062, MIT Department of Nuclear Science and Engineering Report and associated computer files, March 2004.

[7] Preliminary Safety Analysis Report (PSAR), Lungmen Power Station Units 1 &2. Available on internet at: http://www.nonukesasiaforum.org/lungmen/.

[8] GE Nuclear Energy, "ESBWR Design Control Document", 26A6642AD, Revision 1, January 2006

[9] GE11 BWR-5 Equilibrium Cycle Reload. Personal Communication: R. Fawcett (GNF) to E. Greenspan (University of California Berkeley). November 2004.

[10] GE Nuclear Energy: "ESBWR Design and Technology Reprints of Recent Papers", Volume 3, January 8, 1999

[11] Nine Mile Point Unit 2, Updated Safety Analysis Report (USAR), Rev.16, October 2004

[12] Gerald D. Kvaall, Jr, "Advanced BWR MOX Fuel and Core Design Application Evaluation", Master Thesis, University of California Berkeley, May 1997.

[13] R. Fawcett, "ESBWR Core & Fuel, Core and Fuel Description", September 2005, presentation available at NRC website, ADAMS number ML052840012.

[14] Letter of "Retransmittal of Response to Request for Additional Information for ESBWR Pre-application Review", by A.S. Rao, Project Manager ESBWR, to

U.S. Nuclear Regulatory Commission, September 5, 2003. Available at NRC website, ADAMS number ML032680829.

[15] Fuel Design Data, Nuclear Engineering International, September 2005.

[16] J.E. Hench, J.C. Gillis, "Correlation of Critical Heat Flux Data for Application to Boiling Water Reactor Conditions", EPRI NP-1898, June 1981.

[17] M.S. Kazimi, N.E. Todreas: "Nuclear Systems I, Thermal Hydraulic Fundamentals", Taylor & Francis, third printing, 1993

[18] "Acceptance Criteria for Emergency Core Cooling Systems for Light Water Cooled Nuclear Power Reactors", 10CFR50.46 Appendix K of 10CFR50.

[19] M.P. Païdoussis: "Fluid-Structure Interactions", Academic Press, Inc., 1998-c2004, vol.2, pg. 868-870.

[20] Y.Tsukuda et al.: "BWR 9×9 Fuel Assembly Thermal-Hydraulic Tests (2) – Hydraulic Vibration Test", presented at ICONE 10, April 14-18, 2002, Arlington, VA, USA.

[21] IAEA-TECDOC-1391, "Status of Advanced Light Water Reactor Design 2004", May 2004

[22] S. K. Cheng, N. E. Todreas, "Hydrodynamic Models and Correlations for Wire-wrapped LMFBR Bundles and Subchannel Friction Factors and Mixing Parameters," Nuclear Engineering Design 92:227, 1985.

[23] W.K. In, D.S. Oh, T.H. Chun, "Empirical and Computational Pressure Drop Correlations for Pressurized Water Reactor Fuel Spacer Grids", Nuclear Technology Vol.139, July 2002.

[24] Personal Communication: Russ Fawcett (GNF) to Chris Handwerk (MIT), January 2005.

[25] Personal Communication: R. Fawcett (GNF) to E. Greenspan (University of California Berkeley), July 2005.

[26] F. Ginex, F. Ganda, M. Fratoni, E. Greenspan, "One-Dimensional Neutronic Analysis of BWR Hydride Fuel Bundles", submitted to *Advances in Nuclear Analysis and Simulation*, PHYSOR 2006, Vancouver, BC, Canada, September 10-14, 2006.

[27] H.D. Garkisch, B. Petrovic, "Proposed correlations for cladding thickness and fuel-cladding gap for UO2 and U-ZrH fuel in BWRs" Research Group Internal Report, NERI02-189-WEC-07, December 7, 2004.

[28] D. Carpenter, G. Kohse, "Experimental Determination of the Thermal Conductivity of a Lead Bismuth Eutectic Filled Annulus", MIT-NFC-81, June 2005.

[29] Personal Communication: E. Greenspan (University of California Berkeley) to Paolo Ferroni (MIT), May 2006.

[30] P. Ferroni, M. Fratoni, F. Ginex, F. Ganda, C. Handwerk, E. Greenspan, N. Todreas, "Feasibility of Improving BWR Performance Using Hydride Fuel", ICAPP 2006, Reno, NV, 4-8 June, 2006.

[31] C.A. Shuffler, "Optimization of Hydride Fueled Pressurized Water Reactor Cores", Master Thesis, MIT, Department of Nuclear Science and Engineering, September 2004.

[32] M. S. Kazimi, "TEPCO Research Project Progress Report: Core Design Options for High Power Density BWRs", Center of Advanced Nuclear Engineering Systems, MIT, April 2006.

[33] M. Fratoni, "Performance Comparison Between Oxide and Hydride Fuel in BWR", University of California Berkeley, Internal Report, September 28th 2005.

[34] J.Pettigrew, C.E. Taylor, A. Yasuo, R.D. Blevins, "Vibration Damping of Heat Exchanger Tube Bundles", WRC Bulletin 389, February 1994

[35] A. Preumont, "On the Vibrational Behavior of Pressurized Water Reactor Fuel Rods", Nuclear Technology, Vol.58, September 1982.

[36] Zhao, Jiyun, et. al., "Stability Analysis of Supercritical Water Cooled Reactors", MIT-ANP-TR-108, September 2005.

[37] GE Nuclear Energy: "BWR/6 General Description of a Boling Water Reactor", September 1980.

[38] GE Nuclear Energy: "The ABWR Plant General Description", April 1999.

[39] D. Wongsawaeng, D.R. Olander, "Effect of Replacing Helium With a Liquid Metal in the Fuel-Cladding Gap on Fission Gas Release", Nuclear Technology, Vol.146, pg. 211-220, June 2004.

[40] R.F. Wright, J.S. Tulenko, G.J. Schoessow, "Thermal Bonding of Light Water Reactor Fuel Using Nonalkaline Liquid-Metal Alloy", Nuclear Technology, Vol.115, pg. 281-292, September 1996.

[41] Chemical and Physical properties of elements and compounds available at: http://www.webelements.com/

[42] Zircaloy properties provided by International Nuclear Safety Center, available at: http://www.insc.anl.gov/matprop/zircaloy/